NOVEL PROCESSING OF POROUS BIOCERAMIC STRUCTURES

Dissertation submitted for the degree of

Doctor of Philosophy

June 2009

Anushini Imali Muthutantri

Department of Mechanical Engineering

University College London

Torrington Place

London WC1E 7JE

DECLARATION

I, Anushini Muthutantri, confirm that the work presented in this thesis is my own. Where information has been derived from other sources, I confirm that this has been indicated in the thesis.

Yours sincerely,

Anushini Muthutantri

ABSTRACT

Bone is one of the most commonly replaced tissues in the body. Bone tissue engineering has become one of the key areas of research as a successful treatment option for bone regeneration. Scaffolds are used in tissue engineering to direct tissue development and open pore scaffolds with a pore size range of 100 – 400 μm and porosity >90%, are preferred.

Bioceramics have been used in numerous orthopaedic applications since the 1960s. While bioinert materials such as zirconia have been used in load bearing applications due to their impressive mechanical properties, bioactive materials such as hydroxyapatite (HA) have been used to promote bone growth. Porous bioceramic structures have found uses as scaffolds which act as frameworks to support and guide tissue growth in tissue engineering applications. There is constant demand for new processing methods for producing structures of both graded and uniform porosity.

The current methods used for producing structures of graded porosity involve complex and multiple manufacturing steps. This thesis investigates the feasibility of using electrohydrodynamic (EHD) atomisation to produce foams with graded porosity as a 'one-step' processing method, using zirconia as the ceramic material due to its extensive use in industrial and biomedical applications. Modifications have been made to the electrospraying set–up configuration and a range of suspension concentrations have been utilised to determine the experimental conditions. Control of porosity, pore size

and depth of penetration has been obtained by varying parameters such as spray time, sintering temperature and the sacrificial template.

Secondly, a combination of the traditional slurry dipping method and the EHD method have been introduced and used to process scaffolds with better surface and mechanical properties than using each method individually. For this work, a nano–HA suspension has been used and the scaffolds produced have been characterised by X-ray diffraction, X-ray microtomography, scanning electron microscopy and compression testing.

Due to limitations in the HA suspension, zirconia was used as the ceramic material to produce scaffolds using the EHD method, which was manipulated to enhance its efficiency. The effects of changing and modifying the polymeric template by subjecting the templates to various pre–treatment methods on the microstructure and mechanical properties were investigated. It has been possible to achieve porous scaffolds of mechanical strength within the recommended region for cancellous bone. Finally, these mechanically strong scaffolds have been dipped in a nano–HA suspension and sintered at a lower temperature with an attempt to make the scaffolds bioactive since zirconia is bioinert. These composite structures have been tested for their bioactivity using simulated body fluid (SBF). The SBF results have proved to be favourable and apatite growth has been observed on the composite scaffolds using SEM images, additional apatite peaks on the XRD spectra and the increase in the mechanical properties.

PUBLICATIONS, CONFERENCE PRESENTATIONS AND PRIZES

Publications

1. Muthutantri, A.I., Edirisinghe, M.J. & Boccaccini, A.R. Improvement of microstructural and mechanical properties of bioceramic scaffolds using electrohydrodynamic spraying with template modification (under review)

2. Muthutantri, A., Huang, J. & Edirisinghe, M. (2008) Novel method of preparing hydroxyapatite foams. *J Mater Sci: Mater Med*, **19**, 1485 – 1490

3. Muthutantri, A., Huang, J. & Edirisinghe, M. (2008) Novel preparation of graded porous structures for medical engineering. *J Royal Soc Interface*, **5**, 1459 – 1467

4. Muthutantri, A.I., Huang, J., Edirisinghe, M.J., Bretcanu, O. & Boccaccini, A.R. (2008) Dipping and electrospraying for the preparation of bydroxyapatite foams for bone tissue engineering. *Biomedical Materials*, **3**, Article 025009

Conference Presentations

1. Novel processing method of producing zirconia-nHA composite scaffolds for hard tissue engineering applications; Anushini Muthutantri, Jie Huang & Mohan Edirisinghe

Poster presented at the 8th World Biomaterials Congress in Amsterdam, The Nederlands, from 28th May – 1st June 2008

2. Novel method of preparing hydroxyapatite foams; Anushini Muthutantri, Jie Huang, Mohan Edirisinghe, Jenny Robinson & Serena Best

   Poster presented at the European Society for Biomaterials (ESB) conference 2007 in Brighton, UK

3. Novel method of producing hydroxyapatite foams for bone tissue engineering: replication and electrospraying

   Anushini Muthutantri, Jie Huang & Mohan Edirisinghe

   Poster presented at the UK Society for Biomaterials conference (UKSB) 2007 at King's College, London, UK

Prizes

1. First Prize awarded at the 'UCL graduate school poster competition 2007' (Built Environment, Engineering Sciences, Mathematical & Physical Sciences category)

   Poster title: Novel method of preparing hydroxyapatite foams

2. Award for Best Presentation at the PhD Research Forum 2007 organised by the Department of Mechanical Engineering, UCL

ACKNOWLEDGEMENTS

First and foremost, I would like to thank Professor Mohan Edirisinghe for offering me this research project and great opportunity to further my studies. His guidance, encouragement and support throughout these years are very much appreciated.

I would like to thank the Department of Mechanical Engineering at University College London for the PhD scholarship extended to me. EPSRC grants: GR/S 97880, GR/S 97873 and the Royal Society, UK (Brian Mercer Fund) are acknowledged for partially funding this research.

My collaborators from the Department of Materials Science and Metallurgy, University of Cambridge, Dr. Serena Best and Jenny Robinson are thanked for the constant supply of the aqueous 18 wt% nHA suspension prepared as part of the Nano-top project (collaborating University of Cambridge and UCL) and access to their X-ray microtomography and X-ray diffraction facilities. Dr. Pete Laity (University of Cambridge) is also thanked for his assistance with microtomography imaging.

Collaborators from the Department of Materials at Imperial College London are acknowledged who really assisted me with some of the important analysis work in this research. Professor Aldo R. Boccaccini is gratefully acknowledged for allowing me to access some of the facilities at Imperial College by liaising me with his PhD

and postdoctoral researchers. Oana Bretcanu, who was a postdoctoral researcher, is thanked for assisting me with mechanical testing of the HA scaffolds. PhD research student Darmawati Mohamed Yunos is gratefully acknowledged for her involvement in teaching me the ropes of SBF testing and for assisting me with mechanical testing of the zirconia and composite scaffolds.

Mr. Kevin Reeves at Archaeology Department at UCL is thanked for all his assistance throughout my work with regard to working very hard and tirelessly to obtain good images of my very challenging porous structures using SEM. Dr. Steve Firth from the Department of Chemistry at UCL is thanked for assisting me with the thermogravimetric analysis. Dr. Geoffrey Hyett and Dr. Xuesong Lu also from the Department of Chemistry at UCL are thanked for their time and assistance with the XRD experiments and analysis of the results of my scaffolds.

I would like to express my sincere gratitude to Dr. Qizhi (Judith) Zhou from the Department of Civil, Environmental and Geomatic Engineering at UCL for all her assistance in using the helium pycnometer and data analysis.

I would like to thank my colleagues in the Bio and functional research group for their support and for making the research environment more interesting. I would also like to express a special appreciation to Suren who started off as only a colleague but became one of my close friends for all his support and for being one of my proof readers.

My management at Debenhams Retail Plc is so gratefully acknowledged for giving me employment all through my studies and for creating the opportunity to gain some invaluable skills that cannot be obtained purely from academia.

I would like to thank my extended family *i.e.* my friends for putting up with me through the ups and downs of a research degree and for the constant reminder of life existing outside the lab environment. My closest friends Monique and Lakmal are gratefully acknowledged. Mon, for always being there with the great advice, encouragement that I sometimes desperately needed meant so much to me. Lakmal, throughout the years you have made the miles between us insignificant due to the friendship that we share!

Last but definitely not least, some of the most important people in my life, my parents and my sisters are so lovingly acknowledged. My father, always catching my fall, all your support and endless encouragement is acknowledged. My mother, for all your encouragement and prayers are so much appreciated. My sisters, for always believing in me, even in the times when I did not! You all mean the world to me and I love you!

To my parents and years of hard work…..

CONTENTS

LIST OF TABLES

LIST OF FIGURES

Chapter 1

Introduction

Bone is the most implanted tissue in the human body after blood [Wahl and Czernuszka, 2006]. Even if bone is known for its self–healing abilities, it cannot cope with larger defects. The current treatment methods used to treat bone defects such as transplantation and implantation do not restore the original function of the tissue it replaces. Thus, a tissue engineered solution is considered ideal. The concept of tissue engineering (TE) involves three main components, cells to replace the limited functions of the tissue, growth factors to promote the tissue growth and scaffolds to direct the development of tissue [Langer and Vacanti, 1993, Peters and Mooney, 1997].

Ideally for bone regeneration, pore sizes in the range of 100-400 μm, an interconnected pore network and mechanical properties sufficient to withstand the *in-vivo* loads are considered to be the basic requirements of a successful scaffold structure. Also structures with a porosity gradient are gaining research interest both in the medical and industrial fields [Castillo *et al.*, 2003, Corbin *et al.*, 1999].

Bioceramics have been used in orthopaedics since the 1960s. Based on their tissue response they can be categorised as bioinert, bioactive and bioresorbable. Zirconia is a

popular ceramic with uses extending to biomedical and non–medical industries. As a bioceramic, it is bioinert and is used in load bearing applications such as ball heads for total hip replacements for its impressive mechanical properties. Hydroxyapatite (HA) is an osteoconductive (bioactive) material and has been considered as an ideal scaffold material for bone TE due to its similarity with the inorganic component of bone. HA in the nanometre scale has sparked a recent interest over its macro-scale counterparts as being more bioactive than the latter. Although HA has excellent bioactive properties, it is inherently brittle and is mainly used to produce bioactive coatings on implants and for drug delivery.

Many scaffold fabrication methods have been attempted to produce the 'ideal' scaffold and new methods continue to be invented for producing structures of both graded and uniform porosity. Unlike isotropic ceramic foams, fabricating structures with graded porosity is more sophisticated and requires multiple manufacturing steps [Zeschky *et al.*, 2005]. This is time consuming and does not always produce the desired results.

There is a great interest to improve the mechanical reliability of the porous HA structures while maintaining the other scaffold requirements such as interconnected porosity and pore size. Due to its poor mechanical properties, HA is usually combined with a mechanically stronger material to produce composite scaffolds for the use of bone regeneration.

Replication method (slurry dipping), is the most popular and the simplest method of producing ceramic foam structures. Patented by Schwartzwalder and Somers in 1963, the basic principle of this method involves dipping a sacrificial template in ceramic slurry, squeezing the excess slurry out, then pyrolysis and sintering which will eliminate the template and result in a ceramic scaffold. It has many advantages and it has been possible to obtain the desired properties for bone TE scaffolds, but the mechanical properties still remain poor. The presence of a central void in the foam struts during pyrolysis of the polymeric template has been considered to be the main factor for the poor mechanical properties [Tulliani *et al.*, 1999].

Electrohydrodynamic atomisation (EHDA) or electrospraying has been shown to produce ceramic structures with solid struts [Jayasinghe and Edirisinghe, 2002b] and better mechanical properties [Chen *et al.*, 2006a] than the dipping method. Electrospraying involves the use of a needle through which a ceramic suspension is pumped and when an electric field is applied between the needle and a ground electrode kept below it, the liquid breaks up into fine near-monodisperse charged droplets. In this method, the ceramic slurry is fed through relatively large needles (diameter of a few hundred micrometers) and has the ability of producing fine droplets which are a few micrometers in size [Jayasinghe and Edirisinghe, 2002b]. However, foam preparation by using only the electrospraying method requires well dispersed ceramic suspensions of high concentrations (>60 wt%) [Chen *et al.*, 2006a, Jayasinghe and Edirisinghe, 2002b].

1.1 Aims and objectives

This research is mainly aimed towards the exploration of using electrohydrodynamic (EHD) atomisation to produce scaffold structures of uniform and graded porosity. However, prior to any experimental work, it is important to understand the basic physiology and properties of bone as a familiarisation is required into the background of the tissue in order to find an effective replacement. The scaffold materials especially the uses of bioceramics need to be acknowledged as well as the reasons for choosing the ceramic materials used in the experimental part of this thesis. A detailed study needs to be carried out on the various scaffold processing methods currently used along with their advantages and disadvantages. A thorough literature review is required of the EHDA method, the parameters affecting the process and its application for producing porous ceramic structures.

The initial objective of this research is to investigate the feasibility of using the EHD method to produce ceramic structures with graded porosity. The aim is to be able to easily and efficiently produce structures of graded porosity preferably using a 'one-step' processing method rather than the repetitive measures followed in the literature. Zirconia will be used as the ceramic material due to its variety of use ranging from industry to biomedical applications. A suitable spraying process needs to be optimised, by investigating suitable droplet collection methods, choice of ground electrode and suspension concentration. The effects of parameters such as the spraying time, sintering temperature and the sacrificial template on the control of porosity, pore size and depth of penetration need to be investigated.

EHDA method has been used to produce alumina and zirconia ceramic structures in the literature. However, it has not been attempted to produce HA scaffolds using EHDA which claims to produce better mechanical properties than the dipping method. Therefore, the second objective of this research is to investigate the feasibility of using the EHD method to produce porous HA scaffolds. An aqueous nano–HA (nHA) suspension will be used, its ability to be electrosprayed will be investigated and modifications to the nHA suspension if any, will be carried out. The parameters for the electrospraying set-up need to be optimised, mode selection maps need to be plotted in order to estimate the flow rate and the voltage range for the stable cone–jet mode of atomisation, required for the production of fine near–monodisperse ceramic droplets.

The third objective of this research is to investigate the possibility of manipulating the EHD method in order to enhance its efficiency. The effects of spraying time on the pore size need to be examined both on the sprayed and the interior surfaces of the scaffolds. The effects of modifying the sacrificial templates by subjecting them to pre–treatment methods such as surface hydroxylation and depositing a thin layer of conductive metal coating on the templates will be explored. The effects of pre–treatment methods on the ultimate sintered scaffold structure need to be observed with regard to the pore size, morphology, pore distribution and the mechanical properties. The effects of different template sizes too need to be addressed.

Provided it is possible to obtain zirconia structures with desirable mechanical properties required from a bone tissue engineering scaffold, since the material is still bioinert, the introduction of a nano–HA coating to make these structures bioactive will be investigated. The bioactivity of these composite scaffolds will be investigated using simulated body fluid (SBF) and the structures will be tested after being immersed in SBF over a period of days for their apatite formation and any changes in mechanical properties.

1.2 Content of the thesis

Chapter 1 gives an overview of the content of this thesis. It gives a brief introduction into the main problem which is to find a suitable processing method to produce a scaffold with desirable properties for bone regeneration. This chapter briefly introduces the concept of electrohydrodynamic atomisation in addition to stating the aims and objectives of this research.

Chapter 2 consists of a thorough literature review where the basic physiology and properties of bone are explained as well as the defects and current treatments options. The reasons for a tissue engineered solution are discussed and the concept of TE is explained. The scaffold design requirements, the use of graded porosity, the use of bioceramics and their different types are discussed. Some of the main scaffold processing methods, for producing both uniform and functionally graded pore structures are critically reviewed in this chapter. The main concept of EHDA is introduced and its history on various studies carried out by other researchers is reviewed. Different modes

of atomisation are discussed with special attention given to the cone–jet mode of atomisation which is used for the experimental part of this thesis. Factors that influence the EHDA process are also discussed in addition to its use for the processing of porous structures.

Chapter 3 gives a detailed description of the experimental procedures, the materials, the preparation of zirconia and nano–HA suspensions, and the characterisation methods for the suspensions used in this research. Preparation of simulated body fluid is also described as well as the general equipment set–up used for EHDA. The sample characterisation methods used in this research are also introduced.

Chapter 4 investigates the feasibility of using EHDA to produce ceramic foams with a porosity gradient. The experimental process has been optimised by changing parameters such as the droplet collection method, suspension concentration and the choice of ground electrode, as well as the measurement of the droplets produced by the cone–jet mode. The pores on the sprayed surface, the inner-most surface and length-wise cross-sections, have been analysed, in addition to the change in depth of penetration as a function of spraying time. Control of porosity, pore size and depth of penetration has been obtained by varying parameters such as the spraying time, sintering temperature and the sacrificial template. Scanning electron microscopy has been used extensively and the results obtained in this study are discussed in this chapter.

Chapter 5 investigates the possibility of using EHDA technique for the processing of HA scaffolds. The modifications carried out on the nHA suspension have been investigated and the desired suspension has been characterised. Mode selection maps have been plotted to determine the flow rate and applied voltage range for conducting the experiments. The experimental parameters such as the working distance, ground electrode and sintering temperatures have been optimised experimentally. HA foams have been prepared using replication (dipping), electrospraying and a combination of both dipping and spraying, in an attempt to produce scaffolds with improved mechanical properties. The combined method of dipping and electrospraying has been used in an attempt to overcome the poor mechanical properties of the replication method and to enhance the pore interconnections. A comparison has been made of the surface characteristics such as pore size and distribution, porosity and mechanical properties. The purpose of combining two processing methods to make use of the advantages of each technique and to overcome each others disadvantages are discussed in detail in this chapter.

Based on the results obtained in **Chapter 4**, it was observed that a bone–like structure could be prepared by electrospraying. **Chapter 5** demonstrated the possibility of improving the mechanical properties of the HA scaffolds by combining dipping and electrospraying, however, the mechanical properties were still not sufficient. **Chapter 6** describes an extension of the results obtained in **Chapter 4**. The zirconia suspension has been characterised and zirconia scaffolds have been prepared using electrospraying. This chapter describes how electrospraying has been manipulated to enhance its

efficiency and the effects of spraying time on the pore morphologies and mechanical properties have been investigated. This chapter also investigates the effects of subjecting the polymeric templates to pre–treatment methods and their effects on the scaffold structure and mechanical properties. Finally, this chapter also discusses the introduction of a bioactive component to the bioinert zirconia structures with the attempt of making the structures interact with the cells to promote tissue growth. **Chapter 6** also describes the SBF testing that was carried out to investigate the bioactivity and mechanical properties of these composite structures and comparisons have been made to the zirconia scaffolds which are bioinert.

Chapter 7 points out the conclusions based on the results and discussion of the investigations carried out in **Chapters 4, 5** and **6**. Based on the findings from these investigations, it also gives suggestions for the future work that could be carried out for further exploitation of this rather interesting area of research.

Chapter 2

Literature review

The literature review consists of a general background to bone, its physiology and properties as it is important to be familiar with the main characteristics of bone, in order to effectively find an alternative replacement. This section covers the main bone defects and discusses the main problems in the current treatment methods. The concept of tissue engineering is introduced and the importance of three-dimensional matrices to guide and enhance bone regeneration is addressed. It goes on to discuss the general and specific requirements of scaffolds and pays special attention to the use of bioceramics as a potential material.

The uses of graded porosity in biomedical applications are discussed, as well as the importance of bioactive and mechanically strong scaffolds in tissue engineering applications. The benefits of using hydroxyapatite (HA) for its bioactive properties and the use of zirconia for its favourable mechanical properties are discussed. The numerous scaffold processing methods currently adopted to fabricate porous bioceramic structures and their current limitations, are discussed and comparisons are made to understand the rationale and motivation for the research presented in this thesis.

Finally, electrohydrodynamic (EHD) atomisation is introduced as a processing method for porous ceramic structures, its key features and influencing factors are discussed in this literature review.

2.1 Bone

2.1.1. Physiology

The skeleton forms the basic structural foundation of the body, provides muscle attachment sites and allows for movement of the body. The bones in the skeleton provide protection for organs, house bone marrow and provide the rest of the body with a mineral reservoir [Shea and Miller, 2005]. Bone is considered to be the most complex of all the building materials in the body [Hancox, 1972] and is also a very dense and specialised form of connective tissue [Seal *et al.*, 2001].

Bone is considered to be a volumetrically equivalent mixture of water, protein and cellular matrix and lastly, bone mineral. The water phase includes fluids that fill in the various bone porosities such as, the haversian canals, lacunae, canaliculi and the resorption cavities (enlargements of haversian canals) [Simske *et al.*, 1997]. The organic matrix phase consists of collagenous fibres (type I), which accounts to about 90% and the collagen fibres in turn comprise bundles of much finer fibrils carrying distinctive periodic cross-banding of about 640 Å. This collagen is synthesised by the osteoblasts and is deposited in layers in mature bone, termed lamellae [Shea and Miller, 2005]. The fibres in this orientation allow the tissue to maintain a high density of collagenous filaments. The ground substance of the bone matrix consists of proteoglycans,

glycoproteins and bone cells. Bone mineral constitutes of about 75% of bone tissue by weight, but about 50% by volume [Shea and Miller, 2005]. The mineral is mostly in the form of hydroxyapatite [$Ca_{10}(PO_4)_6(OH)_2$] (HA) and can be found in crystal form, being less than 200Å in size. Bone mineral is responsible for providing the rigidity and strength for load-bearing applications [Shea and Miller, 2005].

The overall structure of bone can be divided into cortical (compact) and cancellous (spongy) bone, and can consist of either woven or lamellar bone [Downey and Siegel, 2006]. The outer region of long bones is of cortical bone, which is a dense structure of high mechanical strength and the interior is filled with cancellous (trabecular) bone [Seal *et al.*, 2001], which provides a porous supporting structural network of struts. The major component of compact bone is termed an osteon, which is composed of a concentric lamellar matrix and creates cylindrical conduits known as haversian canals. The haversian canals contain blood vessels that nourish the tissue, while canaliculi are fine channels that radiate from the lacunae [Lakes, 1993]. Within each trabecula, the osteocytes maintain the bone matrix, osteoclasts degrade regions of existing structure, while the osteoblasts build new sections of bone. Hence, bone continuously undergoes a remodelling process.

As a material, bone can be classified as an organic fibrous material (collagen type I), impregnated with ceramic/mineral crystals of hydroxyapatite. The water and cellular phases do not do much for the bone mechanical strength and stiffness, but contribute by decreasing the brittleness and enhancing the resilience and toughness [Simske *et al.*,

1997]. While the type I collagen is mainly responsible for the bone tensile strength, the embedded mineral in the matrix provides the compressional and torsional strength in bone [Simske *et al.*, 1997].

2.1.2 Properties

Bone is organised in a hierarchical structure (**Figure 2.1**) consisting of (1) the macrostructure: cancellous and cortical bone; (2) the microstructure (10 – 500 µm): haversian systems, osteons, single trabeculae; (3) the sub-microstructure (1 – 10 µm): lamellae; (4) the nanostructure (>100 nm -1 µm): fibrillar collagen and embedded bone mineral; and (5) the sub nanostructure (<100 nm): molecular structure of constituent elements, such as bone mineral, collagen and non-collagenous organic proteins. This arrangement makes the bone both heterogeneous and anisotropic [Rho *et al.*, 1998].

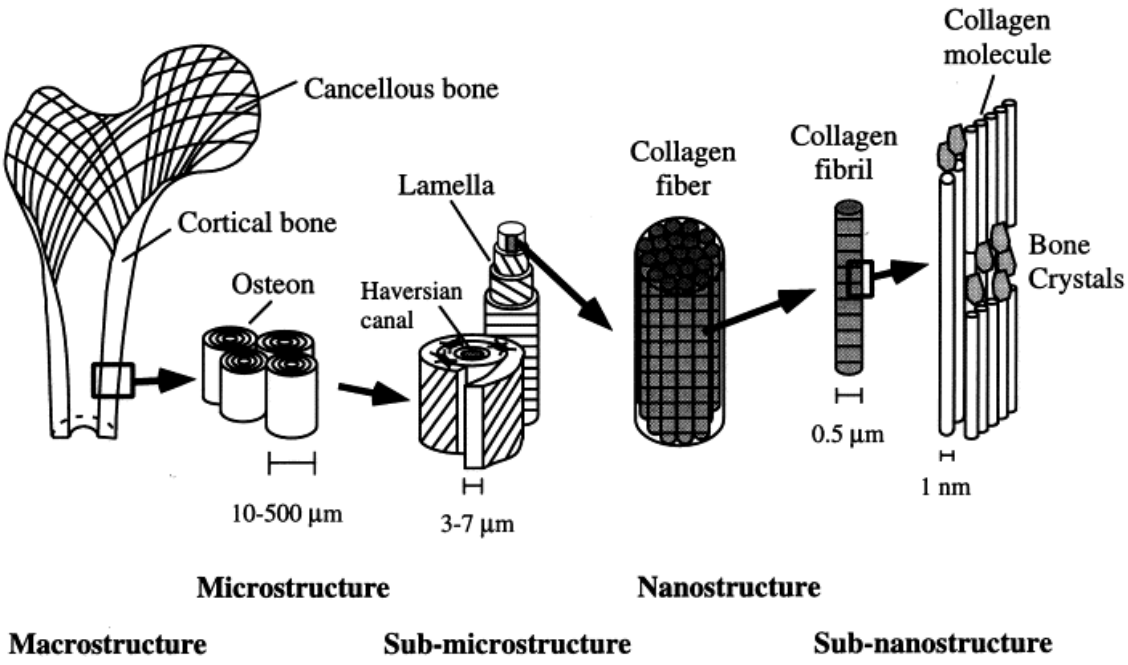

Figure 2.1 Hierarchical structure of bone [Rho et al., 1998]

The compressive moduli of cortical and trabecular bone are approximately 17 GPa and 100 – 200 MPa, respectively, compared to the widely used stainless steel that has a value of 200 GPa [Cullinane and Salisbury, 2004]. The tensile strength of cortical bone is estimated to be about 130 MPa, while for trabecular bone, it is approximately 50 MPa. Bone is a highly anisotropic material: its mechanical properties vary depending on the direction of loading. For example, the tensile strength of cortical bone in longitudinal loading is ~130 MPa, while in transverse loading the tensile strength of cancellous bone is ~50 MPa [Cullinane and Salisbury, 2004]. Cortical bone is known to have an elastic modulus in the range of 3 – 50 MPa and trabecular bone, a value of ~50 MPa [Seal *et al.*, 2001]. Thus bone is a relatively hard material with a relatively high compressive strength and has the ability to support the body.

2.1.3 Defects

The most prevalent bone diseases include osteoporosis and arthritis. It has been estimated that in the US only, osteoporosis affects more than ten million individuals and about another 20 million have low bone mass, which increases the risk of a fracture [Shea and Miller, 2005]. The decrease in bone density and strength is due to the bone resorption occurring much faster than bone regeneration and this can occur due to increasing age, decrease in sex hormone and can also be genetic [Downey and Siegel, 2006]. Other diseases include osteogenesis imperfecta (or brittle bone disease), which is a genetic disease and bone tumours, which can be malignant. Removal of bone in some of these cases results in such large gaps that they cannot be self-repaired.

2.1.4 Current treatment options

Bone is the most commonly replaced tissue in the body [Lu *et al.*, 2003a], with over a million operations involving bone repair annually [Langer and Vacanti, 1993]. The traditional treatment options include autografting and allografting cancellous bone, applying vascularised grafts of the fibula and the iliac crest, and the use of other bone transport techniques [Burg *et al.*, 2000]. However, these standard treatment methods have shortcomings. The avascular bone grafts are dependent on diffusion, the defect size and problems may arise with regard to unpredictable bone resorption prior to complete osteogenesis, especially in the case of large defect sizes [Brown and Cruess, 1982, Enneking *et al.*, 1980]. The use of autografts, where patient's own tissue is removed from a donor site and replaced in the damaged site is popular, but the donor tissue is often scarce, can cause donor site morbidity, anatomical and structural problems, as well as elevated levels of bone resorption during healing [Younger and Chapman, 1989, Glowacki and Mulliken, 1985]. Allografts are used as alternative donor tissue, but can have disadvantages such as the risk of disease and/or infection, bone resorption and rejection. Vascularised grafts require major microsurgical procedures, distraction osteogenesis techniques are considered to be lengthy and laborious, while another procedure, which is the usage of bone fillers is susceptible to infection as the fillers are prepared in the operating room [Burg *et al.*, 2000].

Orthopaedic implants are used for example in total joint replacement surgery in arthritic patients having dysfunctional hip joints. These implants have a limited life-span due to their inability to self-repair, maintain a blood supply, and undergo modification under

mechanical stress [Jones *et al.*, 2006]. It is a necessity that the implantation material maintains its mechanical properties and has similar properties to bone. If the material fails to withstand the *in-vivo* loading, there will have to be repetitive surgery and if the material is too strong, will cause stress shielding in the remaining part of the natural bone and eventually result in bone resorption [Seal *et al.*, 2001].

Most of the implants that are used for stabilising fractures are made from metals such as stainless steel and titanium. These metal implants are widely used in fracture surgery due to properties such as satisfactory mechanical properties, easy handling, ease of processing, availability, and relatively low prices [Patka *et al.*, 1998]. These metal implants also have problems such as stress shielding (due to the moduli differences between the implant and bone), risk of infections and allergies as well as toxic reactions [Van Der Elst *et al.*, 1995]. Therefore it is important to use materials that have similar mechanical properties to bone. In this context, polymeric materials remain attractive candidates, as they can be designed to have a variety of elastic moduli, including values close to that of cortical bone (3–50 MPa), but they still do not have the ability to maintain a blood supply or remodel themselves like natural bone [Seal *et al.*, 2001].

The treatment options that are adopted at present have not been very successful due to donor shortage, surgical reconstruction leading to long-term problems and side effects, as well as being unable to restore original function. There are many clinical reasons to develop bone tissue engineering alternatives, such as the need for better filler materials for use in reconstruction of large orthopaedic defects and the need for orthopaedic

implants that are more suitable to their biological environment [Burg *et al.*, 2000]. Thus, tissue engineering is an important area where intensive research is being carried out in order to possibly obtain a solution that will reduce the complications in the presently used treatment methods.

2.2 Tissue engineering

Tissue engineering (TE) can be defined as an interdisciplinary field that applies the principles of engineering and the life sciences toward the development of biological substitutes that restore, maintain, or improve tissue function [Langer and Vacanti, 1993]. This concept involves the use of three main strategies: the use of isolated cells or cell substitutes to replace limited functions of the tissue, utilisation of tissue-inducing substances such as growth factors and finally, three–dimensional matrices or scaffolds to direct tissue development [Langer and Vacanti, 1993, Peters and Mooney, 1997]. **Figure 2.2** shows an illustration of the basic TE concept.

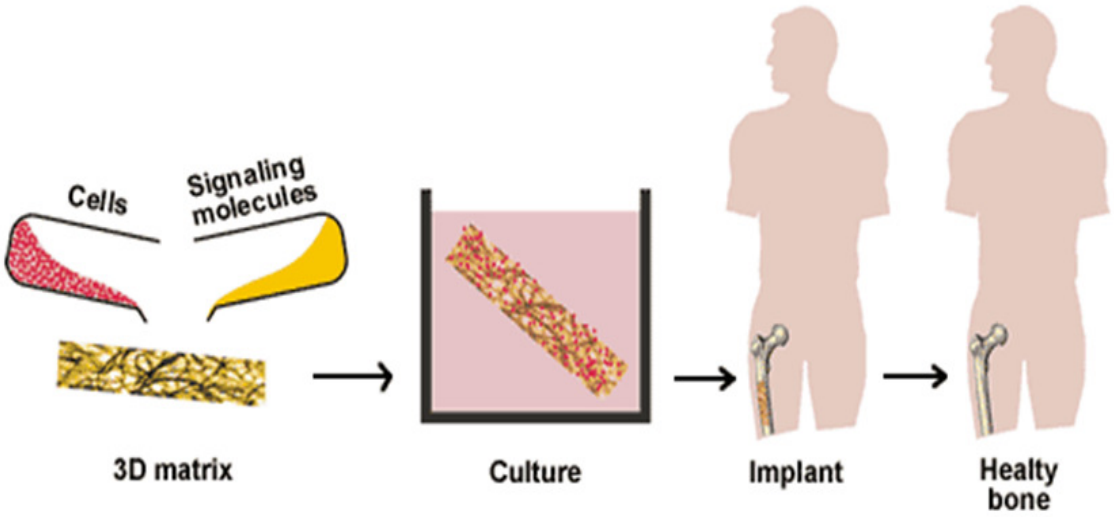

Figure 2.2 Scaffold guided tissue regeneration

[http://www.btec.cmu.edu/reFramed/tutorial/mainLayoutTutorial.html, 2nd March 2009]

2.3 Scaffold design requirements

An ideal scaffold for bone tissue engineering is required to be a matrix that acts as a template that allows cell growth and tissue development, *in-vitro* initially and then eventually *in-vivo* [Jones *et al.*, 2006]. It should be able to mimic the structure and biological function of the native extracellular matrix (ECM) in terms of both chemical composition and physical structure.

A typical scaffold material has to be biocompatible, where the scaffold and its degradation products must not provoke an immunological rejection reaction or influence the normal metabolic activities of the cells [Sittinger, 2003]. It should also exhibit surface properties that promote the adhesion, stimulate proliferation and differentiation of cells as well as provide an environment where the cells can maintain their phenotype and synthesise required proteins and molecules [Vats *et al.*, 2003].

Diverse characteristics such as pore size, pore shape, pore interconnectivity and total porosity of the scaffold are considered important for successful tissue regeneration [Hollister *et al.*, 2002]. A scaffold having an open and interconnected pore network is essential for cell migration, tissue growth, diffusion of nutrients and vascularisation. It has been shown that the pore size is directly related to bone formation, as it provides the surface and space for cell adhesion and bone ingrowth [Mastrogiacomo *et al.*, 2006]. Pore interconnection has been shown to provide the way for cell distribution/migration and to allow efficient *in-vivo* blood vessel formation which is suitable for sustaining bone tissue neo-formation and possibly remodelling [Mastrogiacomo *et al.*, 2006]. High

porosity and large pores are known to enhance bone ingrowth and osseointegration of the implant after surgery [Karageorgiou and Kaplan, 2005].

Pore size has to be of a specific range, neither so small that it will not support vascularity and cell migration or so large, that it will not be completely filled in with bone and will not integrate well with the host bone [Cesarano *et al.*, 2005]. Early work carried out by Hulbert *et al*. established the minimum pore diameter required for bone ingrowth and angiogenesis (formation of blood vessels) into a scaffold to be 100 µm [Hulbert *et al.*, 1970, Klawitter and Hulbert, 1971]. However, subsequent studies have shown better osteogenesis for implants with pores >300 µm [Karageorgiou and Kaplan, 2005]. Relatively larger pores are known to favour direct osteogenesis, allowing vascularisation and high oxygenation, while smaller pores have a tendency to result in osteochondral ossification [Karageorgiou and Kaplan, 2005]. Even though Itala *et al.* (2001) claimed that bone ingrowth occurred in pores as small as 50 µm [Itala *et al.*, 2001], the accepted minimum pore interconnection size remains as ~100 µm. Therefore, for bone TE applications, pore sizes between 100 – 400 µm and porosity greater than 90% is preferred [Klawitter and Hulbert, 1971, Yoshimoto *et al.*, 2003]. It is also important to note that there is an upper limit on the pore size and porosity, usually set by the constraints linked to the mechanical properties [Karageorgiou and Kaplan, 2005]. Increase of porosity results in reduced mechanical strength, which becomes an issue for regeneration in load-bearing bones.

The scaffold material should also be able to release active growth factors (*e.g.* bone morphogenic proteins or BMPs) to enhance tissue regeneration. A suitable scaffold should also facilitate the development and organisation of a 3D structure. It is also necessary that the scaffold exhibits sufficient mechanical properties to resist handling during implantation [Freyman *et al.*, 2001] and to enable tissue regeneration in applications such as bone in load bearing sites [Jones and Hench, 2003]. The ideal scaffold also needs to bond with the host tissue with no scar tissue formation, as well as have the ability to be produced in irregular shapes to match the defect shape. The scaffold must be commercially producible, have a long shelf-life and be sterilisable to conform to the international clinical standards such as the International Standards Organisation (ISO) or Food and Drug Administration (FDA) [Jones *et al.*, 2006].

2.4 Graded porosity in biomedical applications

Functionally graded materials (FGM) provide the advantage to engineer materials with specific structural, compositional, morphological and mechanical properties [Castillo *et al.*, 2003]. In industry, functionally graded materials with a porosity gradient are used to overcome the problems caused by severe discontinuities upon the passage from a ceramic to a metallic medium, by providing a gradual transition [Dariel *et al.*, 2001]. They are used in applications such as, anode supported electrolyte cells to allow for high electrochemical activity at the interface [Holtappels *et al.*, 2006], preforms for liquid metal infiltration [Corbin *et al.*, 1999] and thermal barrier coatings [Steffens *et al.*, 1999].

As the demand for improved advanced porous implant material is increased, the concept of FGM is being increasingly considered for biomaterials [Castillo *et al.*, 2003]. In the case of implants, issues arise due to poor integration of the implant to the tissue surface causing loosening of the implant. In order to overcome this problem, functionally gradient materials where the level of porosity can be graded, have been considered the ideal solution from a highly porous surface layer (which can interact with the tissue) to a dense core, giving the implant suitable strength to withstand the physiological loadings [Becker and Bolton, 1997].

Graded porosity can also find uses in producing artificial spinal cages that could promote the reconstruction of the anterior column after vertebrectomy in tumour and trauma surgery [Lu *et al.*, 2003b]. The present solutions of carbon fibre and metallic cages do not fuse with the internal environment and give rise to stress shielding, while autologous grafting leads to complications at the donor site and risk of tissue rejection and disease transmission [Lu *et al.*, 2003b].

The design of natural bone, how it demonstrates change from a dense, stiff external structure of the cortical bone to light and porous cancellous bone on the interior surface is a perfect example where functional gradation has been used by biological adaptation [Pompe *et al.*, 2003]. This type of structure can optimise the material's response to external loading and a similar feature might prove favourable for an artificial bone implant [Pompe *et al.*, 2003]. The interest in porosity graded implants is to enable a new

functionality of a spatially guided degradation process and cell ingrowth, thus can also find uses in scaffolds for tissue engineering [Pompe *et al.*, 2003].

There is an interest in fabricating implants with different porosities, pore sizes and mechanical properties that could mimic the complex architecture of bone–specific sites, in order to optimise bone tissue regeneration [Karageorgiou and Kaplan, 2005]. It is also believed that scaffolds with gradients in porosity and pore sizes could allow high vascularisation and direct osteogenesis on one side, while promoting osteochondral ossification on the other. This characteristic is found to be appealing in terms of reproducing multiple tissues and tissue interfaces on the same biomaterial scaffold (*e.g.* growth of bone and cartilage on the same scaffold) [Karageorgiou and Kaplan, 2005].

A FGM is obtained by varying the composition from one side of the material to the other side either in a continuous or stepwise manner [Guo *et al.*, 2003]. FGMs are known to allow the achievement of varied properties unlike uniform composites [Guo *et al.*, 2003].

2.5 Ceramics as a scaffold material

Ceramics were introduced to orthopaedics during the 1960s [Murugan and Ramakrishna, 2005]. They have favourable mechanical properties such as high compressive strength and hardness, high biocompatibility, wide availability, shapeability, as well as being tissue responsive, non-toxic and non-immunogenic. Due to their strong ionic, covalent and /or mixed bonding, they cannot be shaped by melting or

casting and can only be produced through high temperature sintering [Ben-Nissan and Pezzotti, 2004]. Sintering is a process of densification where a loose mass of particles (*i.e.* powders) are heated up to approximately two-third of their melting temperature, where they consolidate with the aid of a driving force such as diffusion [Ben-Nissan and Pezzotti, 2004, Bailliez and Nzihou, 2004]. During the densification process, the particles bond together to form necks between the particles, which causes the surface area to reduce and the powders to consolidate [Ben-Nissan and Pezzotti, 2004].

Based on their tissue response, bioceramics can be categorised as; (i) bioinert (e.g. alumina and zirconia), (ii) bioactive (e.g. hydroxyapatite and bioglass) and (iii) bioresorbable (e.g. tri-calcium phosphate).

Bioinert alumina (Al_2O_3) and zirconia (ZrO_2) are predominantly used as femoral heads of total hip joints. This is due to their biocompatibility, hardness, fatigue and corrosion resistance, and good fracture toughness, which allow them to be used in load bearing applications [Murugan and Ramakrishna, 2005]. Being bioinert, these materials do not chemically or biologically react with surrounding tissues and have high thermodynamic stability. Generally, the bioinert implant's biofunctionality relies on tissue integration through a fibrous capsule which forms around it [Ben-Nissan and Pezzotti, 2004].

Calcium orthophosphate (CaP) compounds have been studied as potential bone repair materials for over 80 years. The first *in-vivo* use of tri-calcium phosphate as a stimulus for osteogenesis was performed by Albee and Morrison in 1920 [Albee and Morrison,

1920]. This was followed by injecting various CaP particles into animals to investigate their effects on bone healing [Haldeman and Moore, 1934] and HA has been implanted in rats and guinea pigs to investigate bone regeneration [Ray *et al.*, 1952]. The early studies on using CaPs as hard tissue implants revolved around the hope that the local release of calcium ions would stimulate osteogenesis and there have been contradictory reports where in some cases accelerated healing was observed, while in others little or no healing enhancement was observed [Jarcho, 1981]. However, despite the early interest, it was only in the 1970's that CaPs were synthesised, characterised and applied [Bohner, 2000]. They were prepared by sintering as granules or blocks, porous or dense.

Calcium sulphate ceramics such as plaster of Paris ($CaSO_4 \cdot 2H_2O$) has had a history of clinical use dating back to at least the early 1950s [Peltier *et al.*, 1957]. Calcium sulphates need considerable modification to have practical applications in resolving bone defects, but their reasonable tissue compatibility, availability, low cost, and ease of handling and sterilisation continue to stimulate their study in certain applications [Hollinger and Battistone, 1986]. Coral structures have also been used under the assumption that they consist of a more organised porosity than the random porosity produced in synthetic materials [Hollinger and Battistone, 1986].

Tri-calcium phosphate (TCP) is widely used as a bioresorbable bone graft [Murugan and Ramakrishna, 2005]. Resorbable ceramics provide a temporary framework for the new bone tissue to form and are resorbed leaving the newly formed bone. It is essential that the rate of resorption is identical to the rate of bone growth. However, TCP has an

unpredictable bioresorption rate and gives rise to very poor mechanical properties, thus its uses are limited to low-weight bearing orthopaedic applications [Murugan and Ramakrishna, 2005].

It has been reported by numerous *in–vivo* and *in–vitro* assessments that calcium phosphates in whichever form (bulk, coating, powder or porous) and phase (crystalline or amorphous), will always support the attachment, differentiation and proliferation of cells such as osteoblasts and mesenchymal cells, with HA being the most efficient among them [Rezwan *et al.*, 2006].

Bioactive ceramics such as bioglass, TCP and synthetic hydroxyapatite (HA) have been widely used as fillers, spacers and bone graft substitutes in orthopaedic and maxillofacial applications owing to their biocompatibility and bioactivity [Lee *et al.*, 2006, Pereira *et al.*, 2005]. There has also been much interest in the use of bioceramics in emerging biotechnologies such as tissue engineering applications.

Surface-active glass and glass ceramics are known to bond to bone through an interfacial apatite layer which is collagen-free and consists of fine granular apatite crystals distinct from the structure of bone, suggesting chemical bonding [Neo *et al.*, 1993]. Bioresorbable TCP is known to make direct contact with bone, suggesting mainly mechanical bonding by interlocking [Neo *et al.*, 1993]. HA is known to show intermediate characteristics, *i.e.* by sometimes bonding directly to bone and sometimes through a very thin and indistinct interfacial apatite layer [Neo *et al.*, 1993]. However, in

the review by Jarcho (1981) it is suggested that the CaP implants bond to the surrounding bone due to chemical bonding and without the benefit of an interlock [Jarcho, 1981].

This interfacial layer of calcium phosphate has been observed to be almost independent of the ceramic types (*e.g.* glass, ceramic, polycrystal), the forms (*e.g.* bulk, particulate) and the compositions (*e.g.* phosphate, silicate) [Lee *et al.*, 2006]. It has been assessed by time-dependent animal study that the interfacial layer is formed on the bioactive surface initially and mediates integration of bone matrix to metabolise as a part of tissue [Neo *et al.*, 1993, Ohtsuki *et al.*, 1991]. The calcium phosphate formed on the bioactive ceramics is calcium-deficient solid-solution HA in its nano-crystalline form and contains ions of sodium, magnesium, carbonate and chlorine, and is hybridised with biomacromolecules [Lee *et al.*, 2006]. This calcium phosphate, due to its bone mineral-like characteristics, recruits bone cells and leads them to proliferate, differentiate and produce an ECM with biological calcium phosphate and collagen [Lee *et al.*, 2006]. Therefore, the core mechanism of the surface chemistry of bioceramics lies on the biomineralisation of calcium phosphate nano-crystallites on the bioactive ceramics in the living biological system. The applications of bioceramics are summarised in **Table 2.1**.

Table 2.1 Clinical uses of bioceramics (modified from [Hench, 1998, Murugan and Ramakrishna, 2005])

Application	**Materials**
Orthopaedic	Al_2O_3, Stabilised ZrO_2, HA powders, Bioactive glass powders
Coatings for bioactive bonding	HA, Bioactive glass ceramics
Bone space fillers	TCP, CaP salts, bioactive glass – ceramic composite
Dental implants	Al_2O_3, HA, Bioactive glasses,
Periodontal pocket obliteration	HA, HA-PLA composite, TCP, CaP salts, Bioactive glasses
Alveolar ridge augmentation	HA, HA-autogenous bone composite, Bioactive glasses, TCP
Maxillofacial reconstruction	Al_2O_3, ZrO_2, HA, PE-HA composite, Bioactive glasses
Spinal surgery	Bioactive glass-ceramic, HA
Otolaryngological	Al_2O_3, HA, Bioactive glasses, PE-HA composite

2.5.1 Zirconia

Zirconia (ZrO_2) is a popular ceramic which has been used extensively in both biomedical and non–medical industries. Uses of zirconia range from its low-quality product that can be used as an abrasive, refractory zirconia ceramics used to manufacture parts that can operate in aggressive environments such as extrusion dyes and thermal shock resistant refractory liners [Piconi and Maccauro, 1999]. Due to their good wear properties, zirconia is also used as cutting tools to cut Kevlar and magnetic tapes. These ceramics are also considered suitable as solid electrolytes in fuel cells and in oxygen sensors.

Research on the possibility of using zirconia as a biomaterial began in the late sixties [Helmer and Driskell, 1969]. Introduced as a possible material for the manufacture of ball heads for total hip replacements in the eighties [Christel *et al.*, 1988], bioinert zirconia still remains popular as a biomaterial for load bearing applications [Yoshida *et al.*, 2006].

In comparison to alumina, zirconia has better reliability (high Weibull modulus), higher flexural strength and fracture toughness, lower Young's modulus and the ability to be polished to a superior surface which is required when designing femoral heads [Ben-Nissan and Pezzotti, 2004]. Due to the impressive mechanical properties of zirconia, it has been referred to as 'ceramic steel' [Garvie *et al.*, 1975]. Zirconia ceramics used for surgical implants are of two types: tetragonal zirconia stabilised with yttria (TZP) and magnesium oxide partially stabilised zirconia (MG – PCZ) [Hulbert, 1993]. Most of the

zirconia femoral heads are of TZP consisting of 97 mol% ZrO_2 and 3 mol% Y_2O_3 [Ben-Nissan and Pezzotti, 2004]. Therefore, throughout the thesis, this TZP is referred to as zirconia. It is also important to note that there is a controversy regarding zirconia on the reduction in strength with time when exposed to physiological fluids. The deleterious martensitic transformation from tetragonal to monoclinic phase in TZP due to aging in water and the accompanying reduction in strength seems to be well documented [Hulbert, 1993]. However, tests carried out in simulated body fluids and in animals have shown only slight decreases in fracture strength and toughness [Hulbert, 1993]. It has also been observed in a comparative study that the strength after two years is still much higher in zirconia than in alumina [Hulbert, 1993].

Mechanical stability is an important characteristic in the investigation of a suitable scaffold material for bone tissue engineering applications. Bioactive materials such as HA and bioglass enhance bone regeneration but are inherently brittle, thus its applications are limited when it concerns load bearing issues. Recently, zirconia has sparked an interest as a scaffold material for improved mechanical strength [Kim *et al.*, 2003, Kim *et al.*, 2004a, Kim *et al.*, 2004b, Jun *et al.*, 2006, Malmstrom *et al.*, 2008].

2.5.2 Hydroxyapatite

Hydroxyapatite (HA), is a calcium phosphate-based bioceramic and has been used extensively in medicine and dentistry for over 20 years with its applications extending over a wide spectrum as shown in **Table 2.1**. HA [$Ca_{10}(PO_4)_6(OH)_2$] in its pure form has the stoichiometric Ca to P ratio of 1.67 [LeGeros, 2002]. HA is highly crystalline and is

thermodynamically, the most stable CaP at the pH, temperature and composition of physiological fluids, as well as the most biocompatible CaP [Bohner, 2000, Correia *et al.*, 1996]. HA is the main mineral constituent of teeth and bone. It does not exhibit any cytotoxic effects and is biocompatible with hard tissues, as well as with skin and muscle tissues [Hu and Miao, 2004]. HA also adsorbs protein, the osteopromoting growth factors (BMPs), and the bone matrix substances collagen and proteoglycan [Okii *et al.*, 2001]. HA is known for its osteoconductivity properties and bioactivity both *in-vitro* and *in-vivo* [Hench, 1991], as well as known for its bone-bonding properties [Zhang and Ma, 1999]. HA is resorbed into the body mainly by the action of osteoclasts found in bone.

Most bone substitutes currently available on the market are made of HA [*e.g.* Pro Osteon® (Biomet Inc.); Healos® (DePuy Orthopaedics, Inc.); ApaPore™ (Apatech)]. These products are usually regarded as non-degradable, as their degradation time is estimated in decades and not in years [Bohner, 2000]. HA has been used in dental and orthopaedic surgery as bone defect fillers and as coatings on metallic implant surfaces, to enhance bone regeneration [Kim *et al.*, 2006, Miao *et al.*, 2004]. Due to its similarity to the inorganic component of bone, HA has been investigated as a potential scaffold material for bone tissue engineering applications to promote osteoblast differentiation and proliferation [Shin *et al.*, 2005].

However, HA and related calcium phosphates are also very brittle (*i.e.* lower fracture toughness than bone), have low fatigue properties, low impact resistance, and relatively

low tensile strengths [Jarcho, 1981], thus making them unsuitable to be used on their own for scaffolds in load bearing applications [Baksh *et al.*, 1998]. Therefore owing to the weak mechanical properties, structures made of HA have been limited to non load-bearing applications and reinforcements in polymeric templates [Zhang and Ma, 1999, Wei and Ma, 2004, Thomson *et al.*, 1998, Devin *et al.*, 1996].

2.5.2.1 Hydroxyapatite in the nano–scale (nHA)

There has been an interest in using precipitated nano–scale HA (nHA) particles due to their resemblance to the morphology of the mineral crystals found in bone and hence have the potential to enhance the mechanical properties of implants and their osteoconductivity [Du *et al.*, 1999, Wei and Ma, 2004]. The HA particles between 10 to 100 nm in size have received much attention as they are believed to have superior functional properties over their microscale counterpart with enhanced surface reactivity and ultra–fine structure, which are important characteristics for tissue–graft interaction post–implantation [Murugan and Ramakrishna, 2005]. Nano–HA has been claimed to promote osteoblast cells adhesion, differentiation and proliferation, osteo-integration and deposition of calcium containing minerals than microcrystalline HA leading to enhanced formation of new bone within a short period [Murugan and Ramakrishna, 2005, Webster *et al.*, 2000, Xu *et al.*, 2004]. It is also thought that nano-structured ceramics can be sintered at a lower temperature, thus reducing the problems associated with high temperature sintering [Kalita *et al.*, 2007].

Nano–HA powders exhibit improved sinterability and enhanced densification due to larger surface area, which could improve the fracture toughness as well as other mechanical properties [Kalita *et al.*, 2007]. The surface roughness of the nanophase is increased in comparison to conventional form, due to the reduction in grain size, and the surface wettability (hydrophilicity) is increased which results in an increased adsorption of vitronectin (protein which mediates adhesion of osteoblasts), leading to greater osteoblast adhesion [Webster *et al.*, 2001]. Therefore, nHA is expected to demonstrate better bioactivity than coarser crystals. Nano-HA is used primarily as bioactive coatings on metallic prostheses and for drug delivery [Kalita *et al.*, 2007].

2.6 Scaffold processing methods

There are many processing methods to produce porous ceramic structures as they are extensively used for filtration of molten metal, high–temperature thermal insulation and filtration of hot corrosive gas in various industrial processes [Studart *et al.*, 2006]. These methods have also been researched and used to produce bioceramic porous structures for biomedical applications. Some of the most popular processing methods to produce bioceramic structures are discussed, with an emphasis on the production of HA scaffolds. There is much interest on developing novel processing methods and improvement of existing fabrication methods to produce porous HA structures of controlled porosity and improved mechanical properties.

In 1974, Roy and Linnehan developed a hydrothermal exchange process to derive porous HA from reef building corals [Roy and Linnehan, 1974]. The calcium carbonate

in the coral exoskeleton was converted into HA with the structural pattern of the coral exoskeleton preserved, and the connecting channels of the final HA implant was provided by the architecture of this exoskeleton [Chu *et al.*, 2001]. Another method of producing porous HA involves embedding organic particles such as polyvinyl butyral, naphthalene [Bouler *et al.*, 1996], and acrylic beads [Tsuruga *et al.*, 1997] in HA powder. In this method, the HA powder is dry-pressed with the organic particles and these particles are subsequently pyrolysed, resulting in pores the size of the burnt particle. The green body is then sintered at high temperature. Liu (1997) has produced porous HA structures using polyvinyl butyral (PVB) as a porosifier (**Figure 2.3**). The pore size and structure were determined by the PVB particle size, sintering time and forming pressure (die-pressing technique) [Liu, 1997a]. It was shown that it was possible to obtain porous structures with controlled pore characteristics and compressive strength [Liu, 1997b]. Both these processes do not enable control over the internal porosity, with coralline HA containing only the porous structure provided by the exoskeleton pattern of the harvested coral, while the organic particle method gives rise to undesirable isolated pores, showing poor interconnectivity and non-uniform pores (**Figure 2.3**).

2.6.1 Microsphere sintering

Microsphere sintering is a simple way of producing porous ceramic scaffolds such as HA and it involves sintering the ceramic particles, preferably spheres of equal size [Jones and Hench, 2003]. Compaction of the ceramic particles is achieved by cold isostatic pressing into cylinders at approximately 200 MPa, with the assistance of a

wetting solution such as poly vinyl alcohol [Ota *et al.*, 1997]. The pore diameter decreases with increasing sintering temperature and the mechanical properties increase as the packing of spheres increase. The mechanical properties can be improved by hot isostatic pressing, which will also result in a reduced pore diameter [Jones and Hench, 2003]. However, in this method it is a challenge to maintain the pore diameter within the required range for bone TE scaffolds and the pore interconnectivity is not favoured, which is also a necessity for cell migration.

Microsphere based polymer-ceramic scaffolds have also been prepared using the microsphere sintering method. In this process, microspheres of a ceramic and polymer composite are synthesised using emulsion/solvent evaporation [Rezwan *et al.*, 2006]. The microspheres are then sintered to form a three-dimensional porous scaffold. **Figure 2.4** gives a clear illustration of this process. Polymer-ceramic composite spheres with bioglass and CaP as the ceramic component have been used to produce scaffolds [Lu *et al.*, 2003a, Khan *et al.*, 2004]. However, again, by observing the SEM images (**Figure 2.5**) obtained from these investigations, it is hard to be convinced that the porosity and pore size is favourable and the pore interconnectivity is desirable for bone TE purposes.

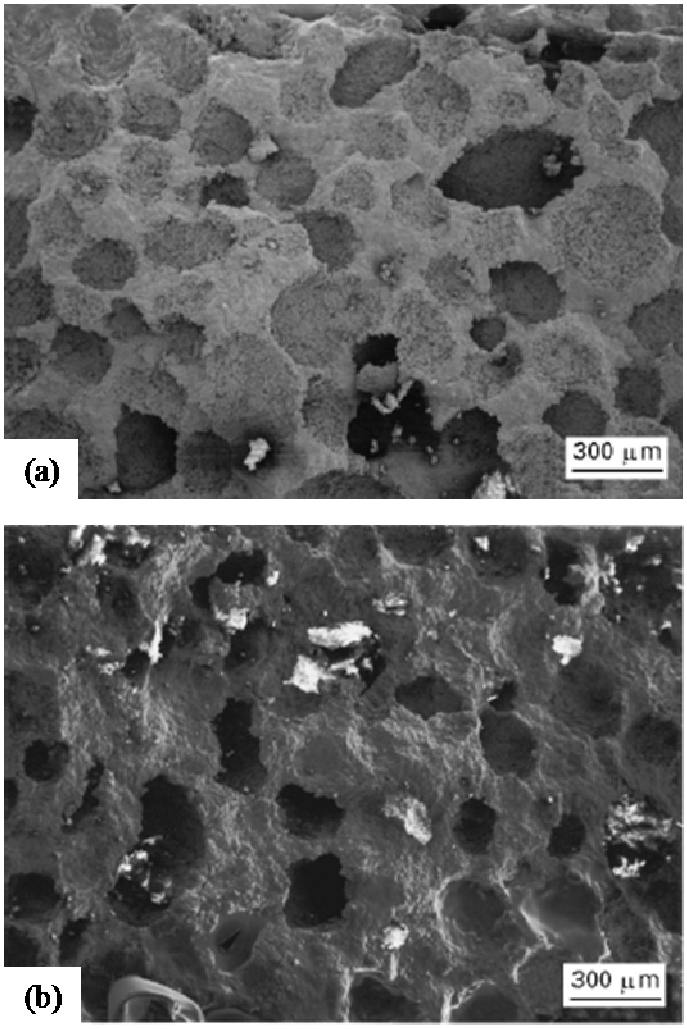

Figure 2.3 SEM of HA scaffolds produced using the die-pressing method. (a) scaffolds prepared using 0.42 mm PVB particles and (b) scaffold prepared by sintering at 1200℃ for 30 hours. Images show poor interconnectivity and non-uniformity of pores. [Liu, 1997a]

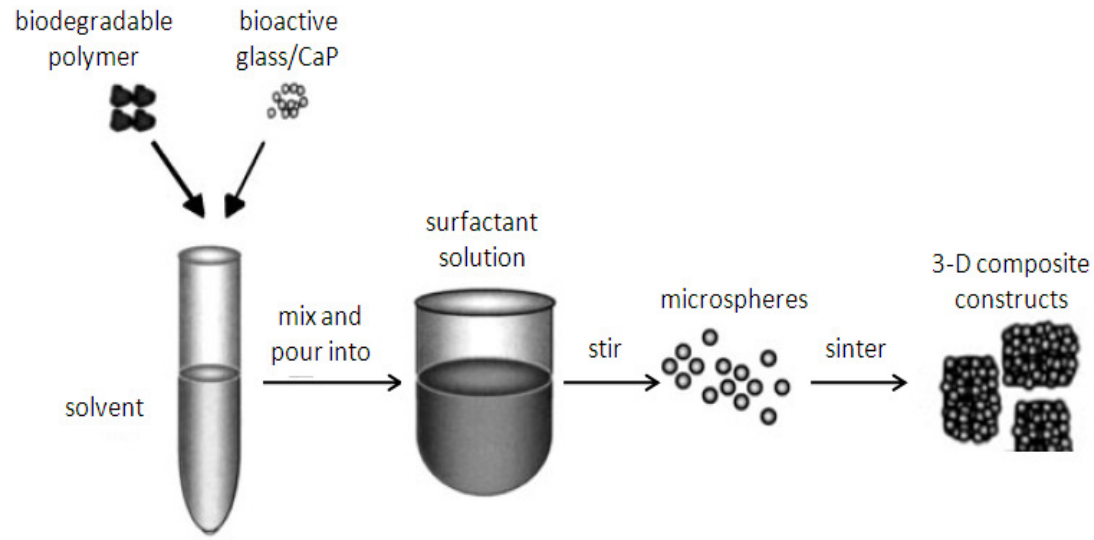

Figure 2.4 Schematic illustrating the microsphere production and scaffold processing [Lu *et al.*, 2003a]

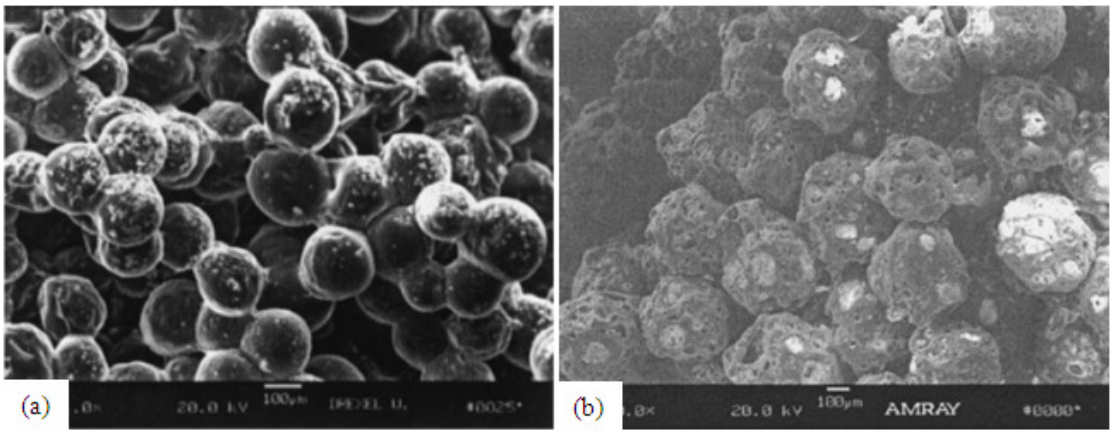

Figure 2.5 Scaffold surfaces prepared using microsphere sintering method: (a) polymer – bioglass microspheres [Lu *et al.*, 2003a] and (b) polymer – CaP microspheres [Khan *et al.*, 2004]. Does not indicate much interconnectivity and the pores are hard to distinguish.

2.6.2 Gelcasting

Gelcasting is considered to be one of the most versatile routes for producing foam structures of complex shapes and good mechanical properties. This method involves preparing a homogeneous suspension that consists of the ceramic powder, water, dispersing agents and a monomer solution. Then, avoiding contact with oxygen, a surfactant is added and the foam is generated. Into this mixture, initiators and catalysts are added to promote polymerisation which starts when the foam has been cast into a mould. The gelled body with a rubbery texture is dried and then fired to remove the polymers [Sepulveda, 1997]. The gel is known to retain the foamed structure preserving both the micro and the macrostructures. Higher strength in the struts has been observed as a result of the tailored microstructure and minimised presence of defects. It has also been observed that it is possible to obtain a fully dense microstructure in the struts by this method unlike the typical hollow struts observed in the replication method. However, this method also has limitations associated with the free radical *in–situ* polymerisation in the setting of the foams [Dhara *et al.*, 2005].

Gelcasting method has also been used to produce porous HA scaffolds to be used as implantable drug delivery systems [Netz *et al.*, 2001]. In this case, it was concluded that at higher porosities, the samples presented an irregular structure which could interfere with drug release. This characteristic could also affect scaffolds prepared for bone TE applications as it is important to maintain a high level of porosity to promote tissue growth.

Sepulveda *et al.* (2000b), has used this technique to produce open-cell HA foams with a relative porosity range of 0.72-0.90. Even though the porosity was in the required range, the pore diameter was in the range of 17-122 μm which is towards the minimum pore size required for bone TE (**Figure 2.6**). However, the elastic modulus of the HA scaffolds was a close match to that of both compact (~11.5-17 GPa) and cancellous (~1.3-14.1 GPa) bone, thus the stress shielding would be prevented [Sepulveda *et al.*, 2000b]. The compressive strength of the HA foams produced varied within the range 1.6-5.8 MPa, increasing with decreasing porosity [Sepulveda *et al.*, 2000b]. Even if this method produces structures of high mechanical strength, the pores are poorly interconnected and it is difficult to obtain a uniform pore size distribution [Sepulveda *et al.*, 2000a].

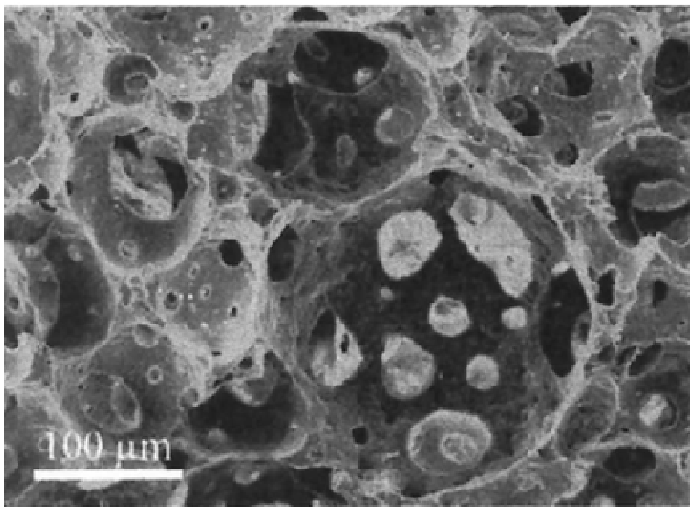

Figure 2.6 SEM of a hydroxyapatite foam produced by gelcasting method [Sepulveda *et al.*, 2000b]

2.6.3 Foaming method

The gas foaming technique has the advantage that it does not involve the use of an organic solvent. Organic solvent residues left behind can elicit an inflammatory response *in-vivo* [Thomson *et al.*, 2000]. Muller *et al*. (2005), produced calcium phosphate bioceramics with interconnective pore structures by foaming of HA and methyl phenyl poly (silsequioxane). The cellular structures of the foams were controlled by foaming parameters and filler load. Porosity of approximately 92% was achieved by decreasing the HA-filler amount and increasing the foaming temperature [Muller *et al.*, 2005].

H_2O_2 is used as a foaming method and has been applied to obtain porous TCP, HA and glass ceramic scaffolds [Yuan *et al.*, 2001]. The porosity of the scaffold structures cannot be controlled and it has been difficult to obtain pore interconnectivity, using the foaming method [LeGeros, 2002]. Almirall *et al*. (2004) used H_2O_2 combined with a low temperature method of preparation of HA through dissolution and precipitation. α-tricalcium phosphate (α-TCP) cement paste was hydrolysed to a calcium deficient hydroxyapatite (CDHA) and foamed to create an interconnected porous structure. The pore size ranged between 50 μm–2 mm and the maximum porosity achieved was 66% which was below the requirement for bone tissue engineering. The compressive strength ranged between 2-9 MPa and could be as a result of its low porosity levels. This method generated two different and well-defined mechanisms: (1) macroporosity, introduced by the foaming agent, and (2) the setting of the CDHA ceramic creating some intrinsic microporosity [Almirall *et al.*, 2004].

Huang and Miao (2007) used a combination of a polyurethane (PU) foam method and a H_2O_2 foaming method to fabricate macroporous HA scaffolds (**Figure 2.7**). However, the results in this investigation does not exhibit any interconnectivity and most of the pores seem to be closed (**Figure 2.7**). After sintering, the ceramic structures were infiltrated with PLGA polymer and the internal surfaces of the macropores coated with PLGA-bioactive glass composite coating. It had been possible to obtain HA scaffolds having porosities of 61-65% (which is relatively low to the desired range) and pore sizes of 200-600 μm. The polymer improved the compressive strength of the structures, while the bioactive glass-PLGA coating improved the bioactivity [Huang and Miao, 2007].

Other foaming agents include citric acid with (bi)-carbonate salts [Li *et al.*, 2002]. Citric acid is present in the body and has been used to prepare macroporous PLGA scaffolds. Yoon and Park in 2001 reported that it was possible to obtain macroporous biodegradable scaffolds by using an ammonium bicarbonate salt which acts as a foaming agent and a porogen additive. The salt particles of ammonium bicarbonate dispersed within a polymer-solvent mixture generate gases of ammonia and carbon dioxide upon contact with hot water, producing a highly porous structure and the porosity in this case is controlled by the amount of ammonium bicarbonate incorporated into the polymer [Yoon and Park, 2001]. Li *et al.* (2002) prepared HA scaffolds by a dual-phase mixing method, where HA slurry and polymethylmethacrylate (PMMA) resin were mixed together. PMMA was eliminated by pyrolysis, but the porosity was limited to 50%. It was attempted to increase the porosity by adding more PMMA, but

the samples collapsed during pyrolysis. The porosity was improved up to 70% by introducing citric acid and (bi)-carbonate salts and it was deduced that only the ammonium bicarbonate system could be used to make HA scaffolds for implants.

Binner and Reichert (1996) have produced HA scaffolds using a foaming method using stirring, introducing stabilising agents and ultrasonics [Binner and Reichert, 1996]. However, these scaffolds did not show well-defined pores due to the thin walls between the pores rupturing and some had a very non-uniform structure. Observing the scanning electron micrographs in the published work it is clear that there was not much interconnection between the pores and the porosities of these structures were not evaluated.

2.6.4 Freeze-drying

Freeze casting is a method where complex-shaped ceramic or polymeric porous structures can be made [Fukasawa *et al.*, 2001]. In this case, the ceramic slurry is poured into a mould and frozen. The frozen solvent acts as the binder and the part is subjected to freeze drying to sublimate the solvent. Freeze drying eliminates the drying stresses and shrinkage leading to cracks during normal drying procedures. Afterwards, the parts are sintered to obtain a porous structure of desired porosity and strength. This procedure results in a scaffold with anisotropic porous microstructure [Deville *et al.*, 2006]. Fukasawa *et al.* (2001), introduced a freeze-drying process using a water-based alumina slurry which in comparison had several advantages over freeze-drying processes using chemical solutions. The advantages included small sintering shrinkage, widely

controllable porosity, relatively good mechanical properties and more environmentally-friendly.

The freeze-drying method was further extended to fabricating bioceramic scaffolds when Deville *et al.* (2006), produced HA scaffolds and were able to obtain porosities ranging between 40-56%. This process involved pouring the ceramic slurry into a Teflon mould placed between two copper cold fingers whose temperature is controlled by liquid nitrogen baths and ring heaters [Munch *et al.*, 2008]. While the ceramic slurry is freezing, the growing ice crystals expel the ceramic particles, which in turn create a lamellar microstructure oriented in a direction parallel to the movement of the freezing front. For slurries of high concentration, a small fraction of particles tend to get entrapped within the ice crystals due to tip-splitting and subsequent healing forming inorganic bridges between the walls [Munch *et al.*, 2008]. A schematic of the freeze casting process is shown in **Figure 2.8**. It was reported that the HA scaffolds produced using freeze casting method had an open and unidirectional porosity which was controlled by modifying the freezing rate of the slurries and the slurry concentration [Deville *et al.*, 2006]. Owing to their lamellar architecture (**Figure 2.9**) the scaffolds exhibited high compressive strength (65-145 MPa), and had the possibility of being considered for some load-bearing applications. However, the porosity was too low and the pore interconnectivity did not meet the bone TE requirement. Fu and co–workers (2008) investigated the compressive strength dependence of freeze–cast HA constructs sintered at different sintering temperatures. A 20 vol% HA content was used, and it was observed that the optimum strengths of the constructs were observed at a sintering

temperature of 1350℃ with no phase change indicated by X-ray diffraction. Even if compressive strengths of 12 MPa (parallel to freezing direction) and 5MPa (perpendicular to freezing direction) were obtained, the porosity (52%) and pore size (5-30 μm) were considered to be too low to support tissue ingrowth [Fu *et al.*, 2008].

Kim *et al*. (2005a), used a mixing, freeze drying and cross-linking method to form HA and gelatin composite foam structures [Kim *et al.*, 2005a]. The gelatin-HA composite solution was poured into plastic dishes, quenched promptly in a freezer at -20°C for 24 hours and freeze dried for another 72 hours. The foams were then cross-linked by immersing into an acetone-water based solution. The cross-linked samples were rinsed twice with ethanol and three times with distilled water to remove the residual chemicals and then vacuum dried for a further 48 hours. The pore sizes were in the hundred micron range, and even with the addition of 30 wt% HA, there was high porosity of approximately 85%. Lee *et al.* (2000) also used a similar technique to form scaffold sponges from a mixture of chitosan and tricalcium phosphate (TCP). These supported the proliferation and differentiation of osteoblast cells [Lee *et al.*, 2000].

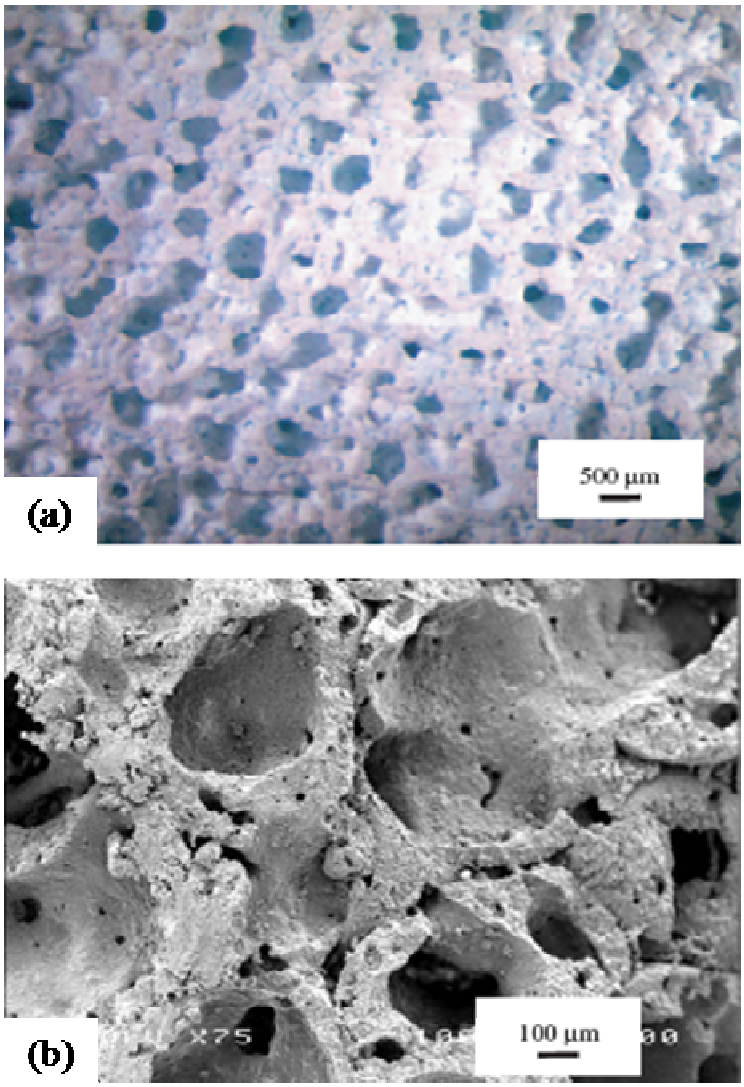

Figure 2.7 Porous HA scaffolds prepared by combining foaming and replication method: (a) a stereozoom optical micrograph and (b) a scanning electron micrograph, showing closed pores and poor interconnectivity. [Huang and Miao, 2007]

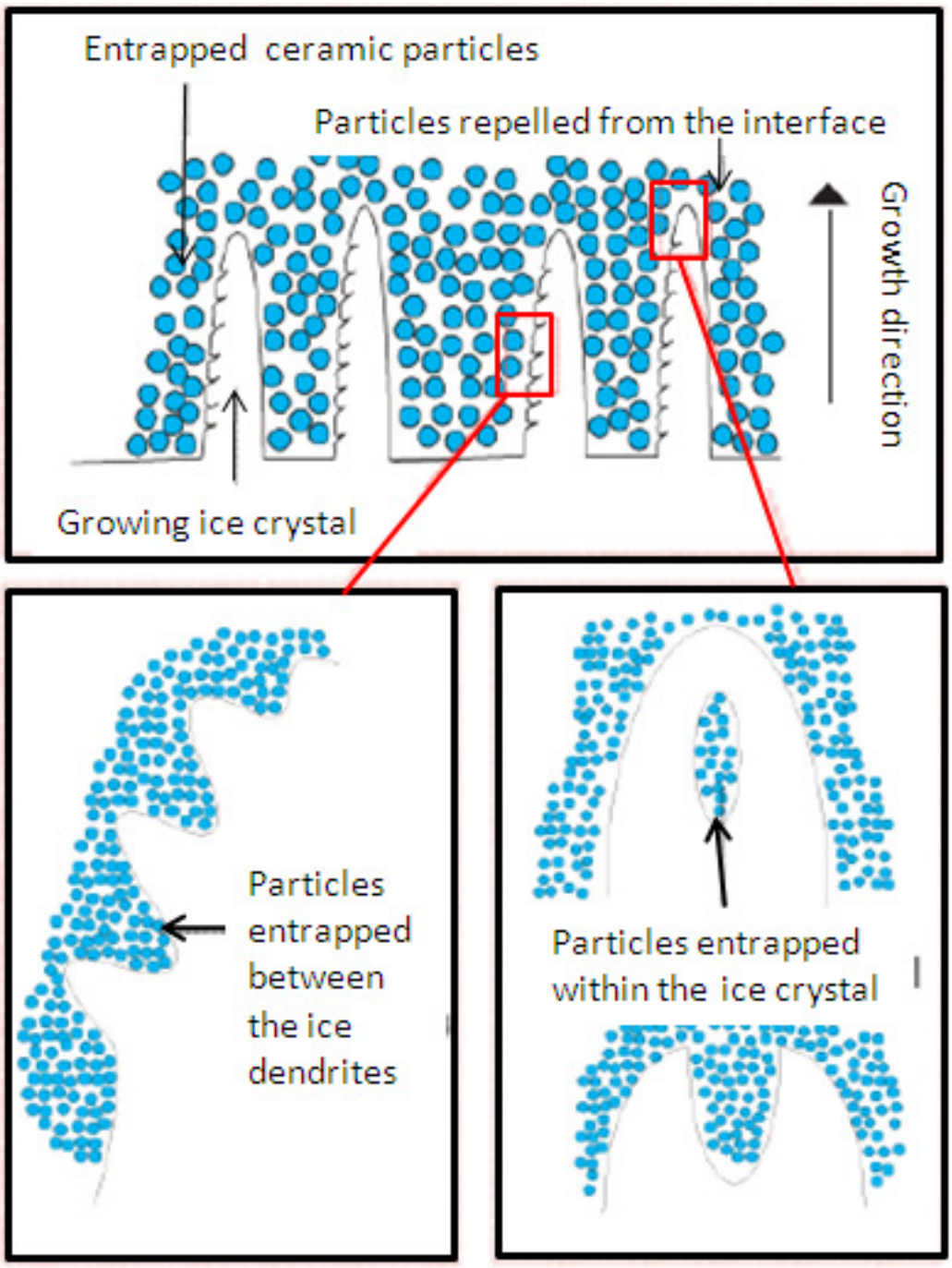

Figure 2.8 Schematic of the freeze casting process [Munch *et al.*, 2008]

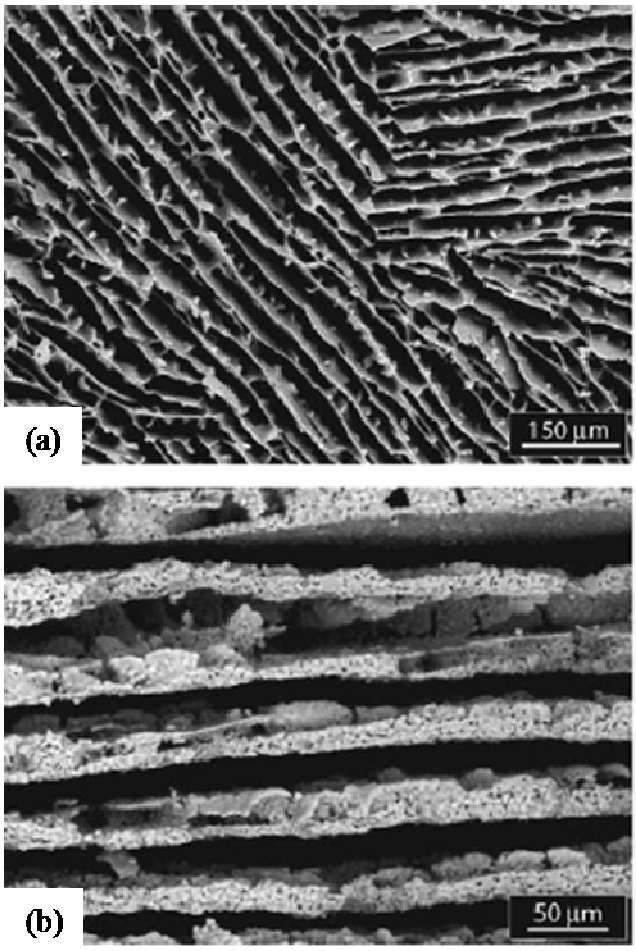

Figure 2.9 Microstructure of HA scaffolds using freeze casting: cross sections (a) parallel to the ice front and (b) perpendicular to the ice front [Deville *et al.*, 2006]

2.6.5 Sol–gel process

Tian *et al.* (2005), prepared porous HA scaffolds using a three-dimensional gel-lamination technology with sodium lauryl sulphate as the foaming agent and lauryl as foam stabilising agent. The gelling system consisted of sodium alginate and calcium chloride, and the foamy HA slurry was gelled layer by layer on the 3-D gel-lamination machine for the preparation of the porous HA scaffold [Tian *et al.*, 2005]. Dong *et al.* (2005), mixed HA powder with particle size in the range of 80-250 nm with binder

(containing acid magnesium and aluminium phosphates) and distilled water to increase the flowability. The sintered scaffolds had an interconnected open pore structure with a porosity of 70-85% and a compressive strength of 10-20 MPa [Dong *et al.*, 2005]. However, the sol-gel process is used to mainly produce macroporous bioglass scaffolds [Jones and Hench, 2004] and the process is described in the flow chart in **Figure 2.10**.

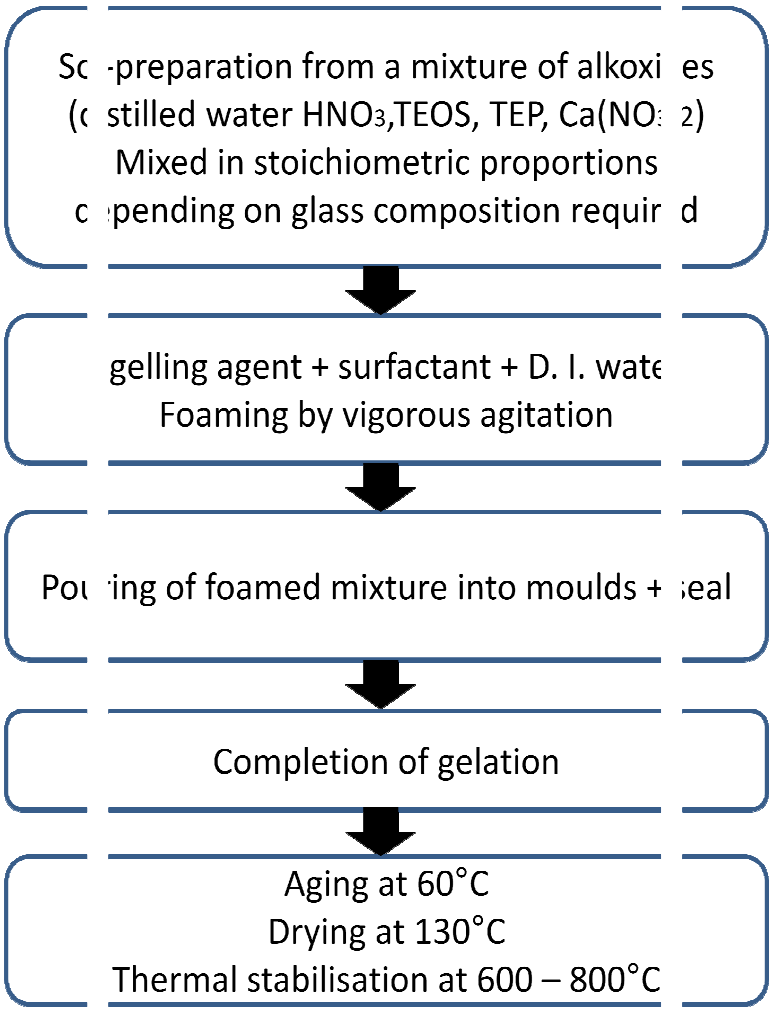

Figure 2.10 Flow diagram of sol-gel foaming process [Jones and Hench, 2004]

2.6.6 Solid free-form fabrication (SFF)

Solid free-form fabrication (SFF), also known as rapid prototyping technology (RP) can be defined as a set of manufacturing processes, capable of producing complex free-form parts directly from a computer-aided design (CAD) model of an object without part specific tooling or knowledge [Hutmacher, 2000]. This technology can be divided into two general categories [Hollister *et al.*, 2004]: (1) utilises material, either powdered or liquid, on a platform, where the material is processed by a device that is moved over the material, and (2) feeds the material directly through a nozzle (using heat) onto a platform. Stereolithography (SL), selective laser sintering (SLS) and 3-D printing belong to the first category and fused deposition modelling (FDM) is the most popular fabrication method in the second category. SFF has been used to directly build structures (direct SFF) and to create moulds that serve as templates (indirect SFF) for the desired structures [Simon *et al.*, 2007]. While precise control over the three-dimensional geometry is the main advantage, high cost of equipment, use of toxic organic binders and difficulty in adapting the method to fabricate biomaterials are a few limitations in the SFF technique [Sachlos *et al.*, 2003].

2.6.6.1 Direct SFF method

Three-dimensional (3-D) printing involves ink-jet printing of binder droplets onto a ceramic powder bed and has been utilised to produce bone scaffolds with minimum feature sizes [Cima and Cima, 1996]. HA scaffolds have been fabricated using 3-D printing [Seitz *et al.*, 2005] (**Figure 2.11**) and when seeded with fibroblasts, there was good cell proliferation [Leukers *et al.*, 2005]. But during the 3-D printing process, the

spreading and wetting of impinging droplets within the porous powder bed results in scaffolds with rough surfaces and limited feature resolution [Michna *et al.*, 2005]. 3-D printing method requires ceramic powder with good flowability, a controlled particle size distribution, and a suitable and strong binder interaction [Seitz *et al.*, 2005].

The SL method has also been used to directly pattern HA scaffolds by laser curing a monomeric resin that is filled with ceramic particles, but the curing efficiency and feature resolution are lower than that for the pure resins, due to the HA filler particles scattering light [Michna *et al.*, 2005]. FDM, which relies on continuous extrusion of a particle-filled, molten polymer filament have been used to create HA scaffolds with relatively smooth features defined by the nozzle size (**Figure 2.12**) [Simon *et al.*, 2007]. However, HA scaffolds produced by either fused deposition or stereolithography often require lengthy heating cycles to successfully remove organic species without introducing defects [Simon *et al.*, 2007].

Direct-write assembly by using concentrated colloidal inks have been considered a new approach for creating 3-D HA scaffolds. The composition and visoelasticity of the ink can be tailored with minimal organic content (~1 wt%) and can eliminate the need for sacrificial support material or mould [Michna *et al.*, 2005]. The 3-D HA scaffolds produced using this method were investigated for their *in-vivo* bone response at 8 and 16 weeks, where it was observed that new trabecular bone was conducted rapidly and efficiently across substantial distances within the structures [Simon *et al.*, 2007]. However for this method to be successful, it is necessary that the HA ink have a high

solid loading (~45 vol%) and high elastic shear modulus (~10^5 Pa) [Michna *et al.*, 2005].

Robocasting, is a freeform fabrication method that utilises computer-controlled extrusion of colloidal pastes, slurries, or inks (**Figure 2.13**). This is different from other extrusion free-form fabrication methods, such that the carrier fluid is a volatile solvent and the transition of the extrudate from a fluid-like state to a solid-like state occurs due to the solvent evaporation rather than the solidification of a thermoplastic material [Cesarano *et al.*, 2005]. This is a rapid and versatile technique which can simultaneously control the rod size and multiscale porosity of the scaffolds [Dellinger *et al.*, 2007]. This method has been used to fabricate HA lattice based scaffolds for possible bone implant applications [Saiz *et al.*, 2007, Cesarano *et al.*, 2005, Dellinger *et al.*, 2007]. It is possible to precisely control the porosity directly by the drawing of successive layers, varying the rod spacing and the rod size, and can be machined into customised implants (**Figure 2.13c**) [Cesarano *et al.*, 2005]. Again, 40-50 vol% of solid loading is used for robocasting [Saiz *et al.*, 2007].

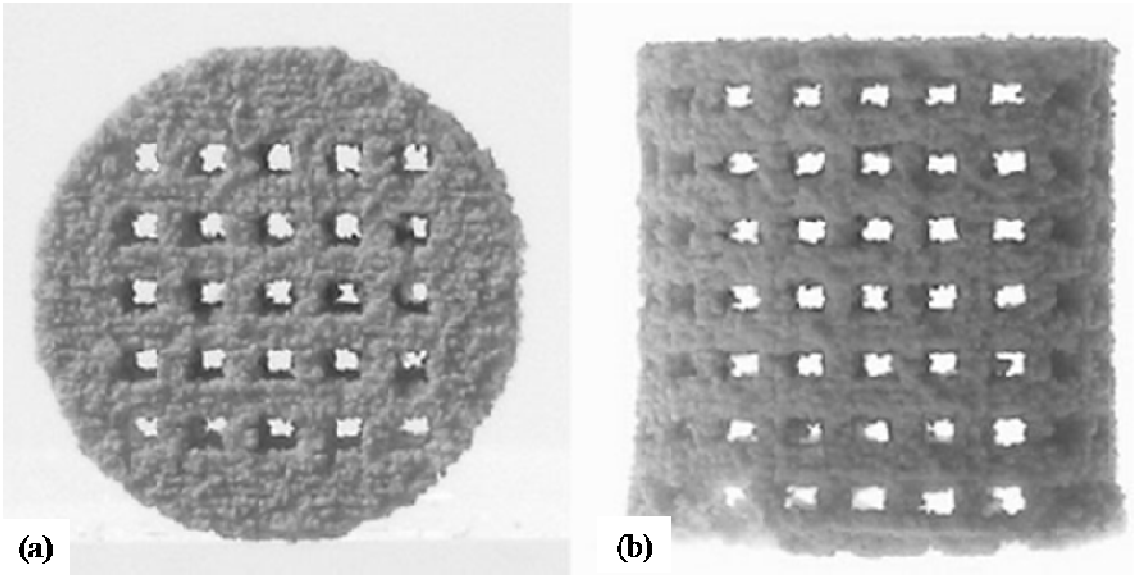

Figure 2.11 HA scaffolds produced using 3-D printing (a) Top view and (b) side view (Diameter of structure = 7.8 mm with channel range of approximately 500 µm in the z-direction and 570 µm in the x-direction [Seitz *et al.*, 2005]

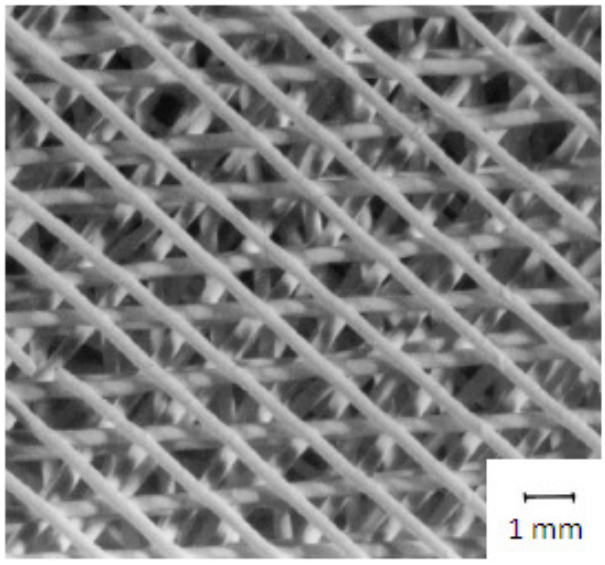

Figure 2.12 HA latticework produced using fused deposition SFF method [de Sousa and Evans, 2003]

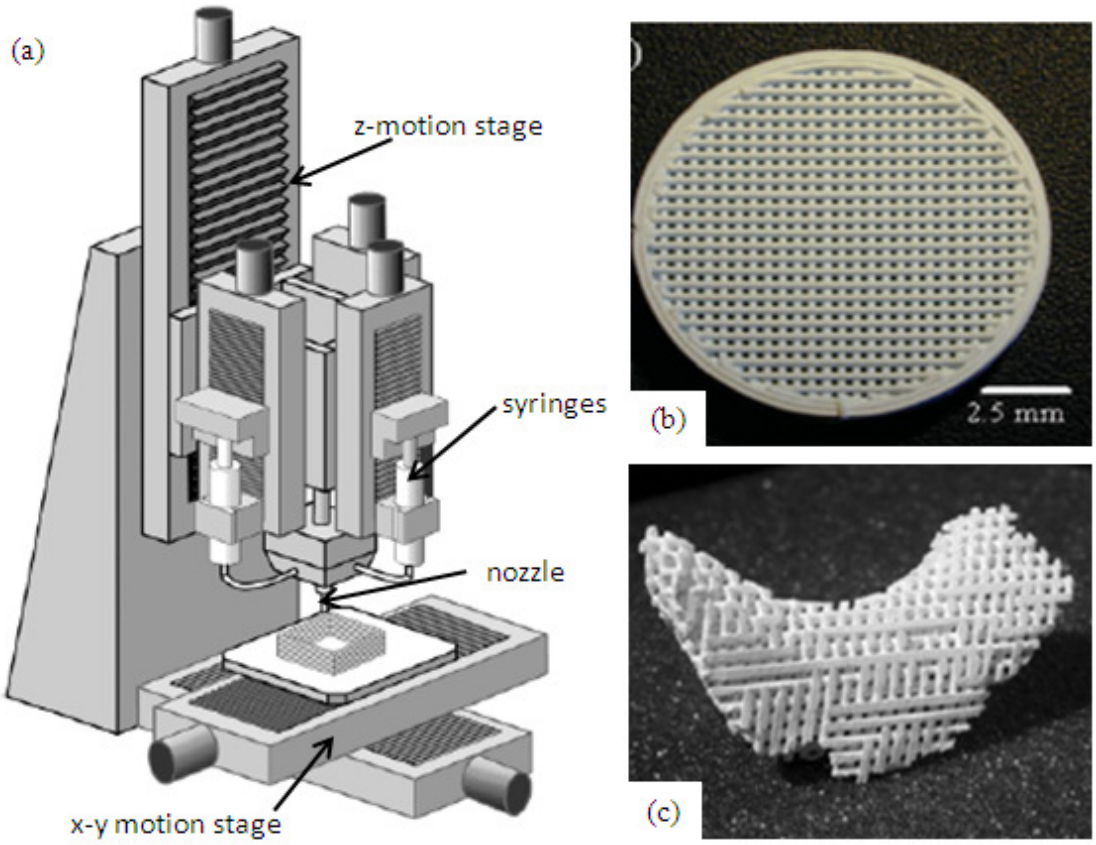

Figure 2.13 Robocasting method: (a) schematic of a robocaster [Cesarano *et al.*, 2005], (b) HA scaffold produced with visible macropores between rods designed by the CAD program [Dellinger *et al.*, 2006] and (c) customised lattice implant [Cesarano *et al.*, 2005]

2.6.6.2 Indirect SFF method

Indirect SFF method is an alternate approach where, SFF is used to fabricate a mould into which biomaterials are cast instead of direct building of the scaffold. This method preserves the three dimensional complexity, while increasing the material selection [Hollister *et al.*, 2004] and provides improved control over scaffold shape, porosity and

pore architecture, including the size, interconnectivity and orientation [Taboas *et al.*, 2003].

Chu *et al*. (2001), introduced a new method of producing porous HA with designed pore channels. The implants were initially designed by a CAD software or computer-tomography (CT) data. This process involved stereolithography (SL) and a highly loaded 'reactive ceramic suspension'. The ceramic suspension needs to be reactive such that the ceramic powder is therefore dispersed in a reactive medium that can be polymerised or cured by heat or radiation [Chu *et al.*, 2001]. A flow chart of the steps involved in the manufacturing process is shown in **Figure 2.14**. The casting moulds for the structures were made from epoxy resin using SL from the negative image of the designed scaffold [Chu *et al.*, 2002b]. HA suspension was cast into these moulds and cured. Then they were pyrolysed to eliminate the mould and binders, and sintered at 1350℃. **Figure 2.15** shows the SEM images of the epoxy mould and the final product obtained from Chu *et al.* (2002b). Even though it is a versatile technique, the porosity created by the channels was 26-52% which is very much below the scaffold requirement for bone TE [Chu *et al.*, 2001]. However, the *in-vivo* study demonstrated biocompatibility and osteoconductivity of the HA scaffolds [Chu *et al.*, 2002a]. It was also observed that the manufacturing process did not impose any adverse effects on the biological properties of HA. The mould removal can be a lengthy process, often requiring days to generate scaffolds that are defect-free [Michna *et al.*, 2005]. Kim *et al*. (2007), used micro-SL method to produce porous HA scaffolds of pore size ~250 μm, and it was observed that the average shrinkage was ~40% [Kim *et al.*, 2007a].

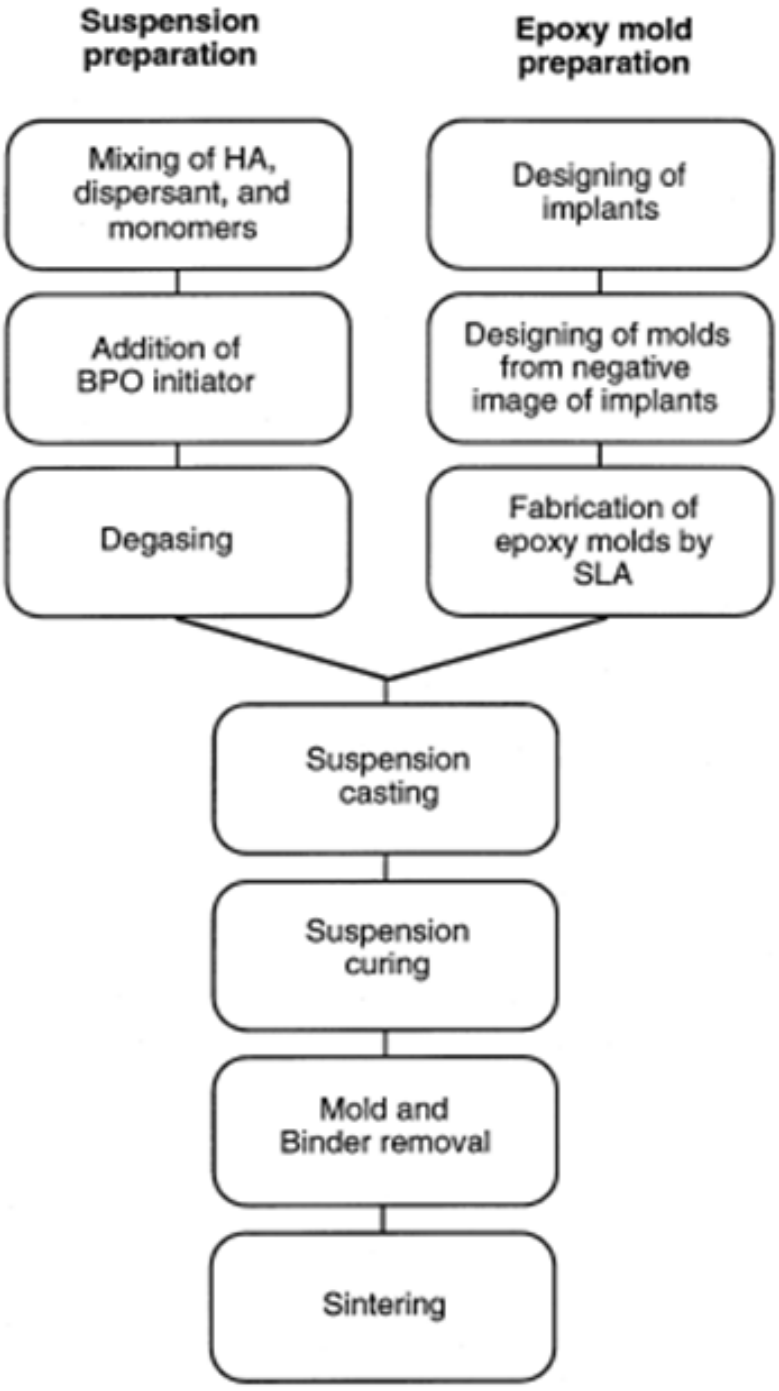

Figure 2.14 Flow chart of HA implant processing using indirect SFF method

[Chu *et al.*, 2001]

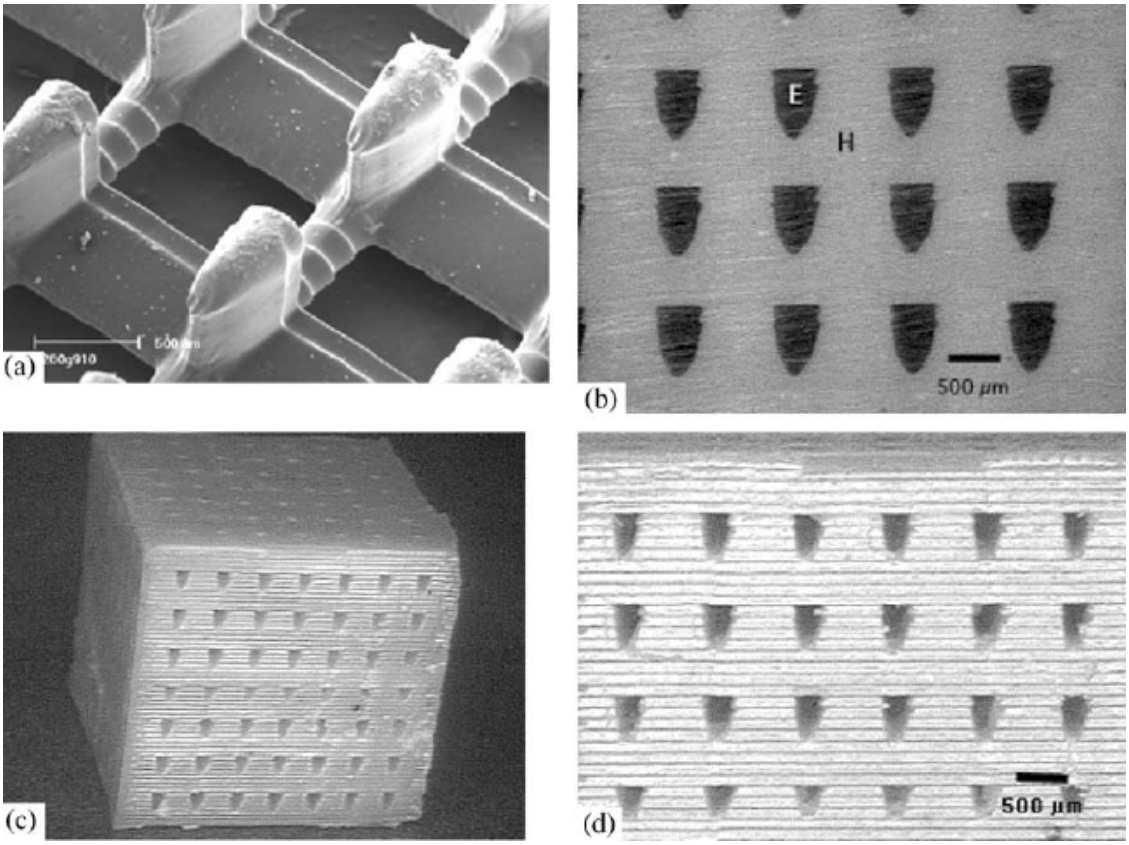

Figure 2.15 SEM images of (a) the epoxy casting moulds for the specimens, (b) cross section of a casting mould showing complete filling of the HA suspension (E: epoxy, H: HA suspension), (c) sintered HA scaffold and (d) the surface of the HA scaffold at higher maginification [Chu *et al.*, 2002b]

2.6.7 Replication method

This technique is also known as the sponge method, slurry dipping method or reticulate method. This is a very popular method of producing ceramic foams owing to its simplicity and efficiency and was patented in 1963 by Schwartzwalder and Somers [Schwartzwalder *et al.*, 1963]. The method involves the use of a polymeric template, usually polyurethane (PU) foam, which is immersed in a slurry mixture that infiltrates the porous structure of the template. Infiltration of the slurry into the polymer sponge is

enabled by repetition of compression/release processes. The pore size, pore wall thickness and the mechanical strength of the scaffolds is dependent on the number of compression/release steps [Thomas *et al.*, 2006]. Excess slurry is squeezed out from the polymeric template, to obtain a homogeneous coating on the foam struts and the foam is allowed to dry either at ambient temperature for 12 hours [Chen *et al.*, 2006a] or at elevated temperatures of approximately 80°C for about 10 minutes [Kim *et al.*, 2004a]. The dried body is heat treated to burn out the polymer template and sintered at higher temperatures to obtain dense structures. The result is a three-dimensional open-cell foam structure of high porosity and interconnectivity (**Figure 2.16**). It also has high commercialisation potential due to its low cost and simplicity, in addition to the characteristic that it can be produced in any irregular shape, hence it is ideal for bone tissue engineering applications (**Figure 2.17**). This technique is usually used to fabricate scaffolds of ceramic materials such as ZrO_2, HA and related calcium phosphates.

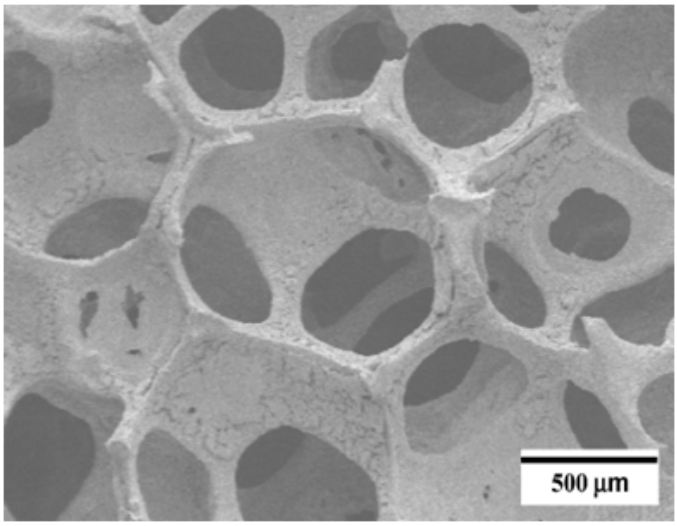

Figure 2.16 HA porous scaffolds prepared using the dipping method [Kim *et al.*, 2005b]

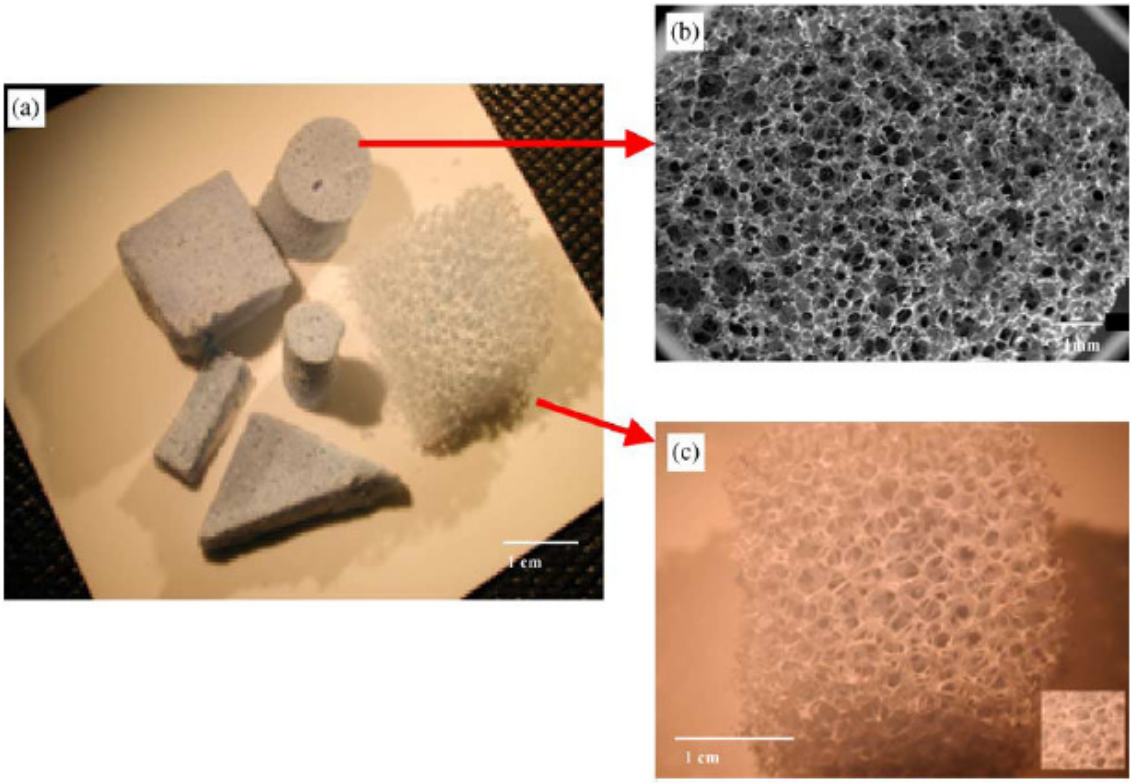

Figure 2.17 (a) HA scaffolds of different shapes, (b) and (c) macroporous structures of HA scaffolds using combined gel–casting and dipping methods.

[Ramay and Zhang, 2003]

Using the replication technique it is possible to obtain scaffolds of high porosity (~90%), pore size of >400–500 µm and pore interconnectivity [Chen *et al.*, 2006a]. The porosity of the body can be controlled by repetition of the dipping and sintering process [Kim *et al.*, 2005b]. The scaffolds prepared using this method have a controllable pore size, pore interconnectivity and desired pore geometry, which is dependent on the polymeric template. The structural properties of the resultant ceramic foam are controlled by the characteristics of the polymeric template such as density, porosity and pore size distribution. For example, Kim *et al.* (2005c) demonstrated a decrease in

porosity, increase in density due to thickened struts by repeating the replication process twice [Kim *et al.*, 2005c].

Tian and Tian (2001), investigated the preparation of porous HA scaffolds using the reticulate method. They varied the porosity of HA by altering the slurry, and the pore size was varied by using different substrates. They were able to obtain up to 80% porous and interconnected structures [Tian and Tian, 2001]. They also deduced that the compressive strength of porous HA has an exponential reduction with porosity. It is important to burn out the polymer template slowly, using an appropriate heating rate, in order to minimise the damage (*e.g.* formation of microcracks) to the ceramic coating [Kim *et al.*, 2004a].

Mastrogiacomo *et al*. (2006), compared HA scaffolds using two different fabrication methods; slurry dipping and foaming. For the latter process, a slurry with surfactants and a high powder concentration (20 wt%) was used and expanded in a known volume (40 – 60 vol% of the total) to achieve a controlled morphology. This resulted in a faster occurrence of bone tissue in the scaffolds obtained from this method than slurry dipping, but the blood vessels formed were smaller due to the smaller pore interconnections than in the other type of scaffolds [Mastrogiacomo *et al.*, 2006]. Min *et al.* (2006), have compared the effect of HA content in the slurry on the pore morphology and size, and density, porosity and mechanical strength of porous HA scaffolds prepared by slurry-dipping method [Min *et al.*, 2006]. As the HA content was increased, the porosity of the scaffold decreased and the density was increased.

However, in the slurry-dipping method, the foam struts have a very high probability of containing micropores and microcracks [Vedula *et al.*, 1999], mainly caused by the non-uniform coating of the slurry on the polymeric template. There exists a central pore in the struts, which is a direct result of burning out the template [Tulliani *et al.*, 1999]. This problem associated with this technique leads to a heavy compromise of the mechanical properties and structural integrity of the scaffold structure. Several attempts have been made to improve the mechanical properties of the porous ceramic foams produced using this method.

Kim *et al*. (2005b), used this reticulate method to fabricate a scaffold-coating system, of porous HA coated with poly (ε-caprolactone) (PCL) polymer and HA hybrid, to be used in hard tissue regeneration [Kim *et al.*, 2005b]. This was an attempt to improve the mechanical properties of porous HA scaffolds and to enhance wound healing by incorporating vancomycin, which is an antibiotic. Callcut and Knowles (2002), used a glass reinforced HA slurry to fabricate porous scaffolds and the foams were coated twice. A significant enhancement of both the scaffold density and mechanical properties was observed and there seemed to be no degradation of the macrostructure by using the PU template [Callcut and Knowles, 2002].

Ramay and Zhang (2003) introduced a method of producing porous HA scaffolds by combining the gel-casting and the replication method (**Figure 2.17 b & c**) [Ramay and Zhang, 2003]. This was an attempt to overcome the disadvantages and to develop a

method to combine the advantages of both methods. It was possible to obtain a pore size range of 200 – 400 μm of interconnected porosity and the elastic modulus obtained was comparable to that of cortical bone (**Figure 2.17b**). These features were more favourable for bone tissue engineering applications than the structures produced only by gel-casting.

2.7 Processing methods used to produce scaffolds with graded porosity

Unlike producing isotropic ceramic foams, fabricating porous ceramics with graded porosity is more sophisticated and usually requires multiple manufacturing steps [Zeschky *et al.*, 2005]. Usually, the processing methods used to produce structures of uniform porosity are modified or the steps are repeated a few times to obtain the desired gradation of porosity.

Graded ceramic foams have been produced by compacting ceramic powders with varying amounts of porosity generating additives, using 3D printing techniques, electrophoretic deposition, stacking tapes with different porosity or by packing ceramic powders to the desired structure and partial sintering of the scaffolds [Zeschky *et al.*, 2005].

The design of porous implant materials with a porosity gradient closely mimicking the bimodal structure of bone (cortical and cancellous) and with a sufficient degree of interconnectivity can be considered a most important challenge [Hing *et al.*, 1999]. Production of implants with graded porosity have been attempted with hydroxyapatite

(HA) using methods such as tape casting [Pompe *et al.*, 2003] and slip casting [Vaz *et al.*, 1999]. The macropores in the outer layers provide access for cells and blood vessels and enhance new bone formation, while the inner dense ceramic structure provides the mechanical stability of the implant.

Slurries for casting porous tapes were prepared by adding porogens (polymer spheres) with different particle size fractions (100-300 μm) and volume fractions (0-40%) [Pompe *et al.*, 2003]. The slurries were cast onto a polymeric carrier tape, allowed to dry at room temperature for 24 hours and the subsequent layer was cast upon the previous sheet. The organic additives and the porogen were burned out in air between 200-500℃, and then sintered for 2 hours at temperatures between 1250-1450℃. Excellent bioactivity was demonstrated due to the macropores in the outer layers, but the mechanical properties still needed improvement. Slip casting produced pores on the external surface that were approximately 100 μm but there was no interconnectivity [Vaz *et al.*, 1999]. Osteoimplants with graded porosity have also been manufactured by multiple tape casting using a water-based HA slurry with porosifier [Werner *et al.*, 2002].

The replication method (*i.e.* slurry dipping) has been used to produce HA structures of graded porosity [Tampieri *et al.*, 2001]. Using multiple and differentiated impregnations, and using slurries that had HA powders with different crystallinity degrees, a reproduction of cortical and cancellous bone was achieved [Tampieri *et al.*,

2001]. Porosity-graded zirconia ceramics have been produced by slurry infiltration with graded pore sizes ranging from 300-1000 μm [Miao *et al.*, 2003].

Pairing different porosities with different geometries for desired mechanical properties has been attempted using computational algorithms such as an image-based optimisation scheme [Lin *et al.*, 2004]. The prototypes of the designed scaffold architectures have been fabricated using solid free-form fabrication (SFF) method [Lin *et al.*, 2004]. However in this case, due to the regenerate tissue within a trabecular structure being negative of the scaffold structure, it does not seem possible to completely match the desired native structure nor the mechanical properties.

2.8 Electrohydrodynamic atomisation

Electrospraying or more appropriately electrohydrodynamic atomisation (EHDA) is explained by Grace and Marijnissen (1994) as 'tiny droplets obtained from the electrically forced (electro) break-up of a moving (dynamic) liquid (hydro)' [Grace and Marijnissen, 1994]. In this process, the liquid flows through a nozzle/needle which is connected to a high voltage power supply. Another electrode, which is usually grounded is held below the needle. When a voltage is applied to the needle, the liquid forms a jet at the needle exit, which subsequently breaks up into fine droplets. The droplets produced are electrically charged, thus enabling them to be guided and focused easily, minimising droplet agglomeration. Generation of very fine droplets with nearly uniform size distribution is an advantage of this process. The droplet size can be controlled by varying either the flow rate of electrospraying or the electrical conductivity of the liquid.

Due to these properties, EHDA has been used for applications such as, producing ceramic powders [Rulison and Flagan, 1994], producing aerosol standards [Meesters *et al.*, 1992], coatings, dispersion of pesticides and mass spectrometry [Fenn *et al.*, 1989].

EHDA of liquids was noted and reported as early as 1600 by Gilbert, but Bose is considered to be the first to describe the process in 1745 [Gañán-Calvo, 1999]. However, it was only many years later that Rayleigh made the earliest observations on the instability due to electric charges on drops and jets [Rayleigh, 1879]. Rayleigh also suggested the conditions for a drop or jet to become unstable, since the stability of the drop/jet is dependent on the balance of forces, *i.e.* the outward electrical stresses tending to disrupt the drop and the counteracting surface tension forces trying to hold the drop together [Rayleigh, 1878, Rayleigh, 1882].

It was only since the early 20^{th} century, that this phenomenon managed to attract a considerable amount of interest from both a fundamental and application viewpoint. It was Zeleny who pioneered the experimental studies of EHDA based on Rayleigh's theories [Zeleny, 1914, Zeleny, 1915, Zeleny, 1917]. He observed different modes of spraying at the exit of the capillary which was exposed to an external electric field. He was able to produce a qualitative description of the process based on parameters such as the liquid flow rate at the capillary exit (Q) and the applied voltage (V), and obtain photographs showing these different modes [Zeleny, 1917]. The experimental features in the apparatus used by Zeleny are still being used by researchers.

The next significant contribution into this field was reported by Vonnegut and Neubauer in 1952. They managed to produce monodispersed aerosol droplets of 0.1 mm diameter by applying a voltage in the range of 5–10 kV using a similar experimental set–up to that used by Zeleny [Vonnegut and Neubauer, 1952]. In the 1960's Taylor noted that for a conducting liquid and jet of a higher viscosity, the liquid did not vibrate prior to spraying, but instead would adopt a conical shape with a sharp apex. This semi-vertical angle of the conical meniscus was calculated to be close to 49.3°. This angle was named the 'Taylor cone' after the creator and describes the angle at which a conical meniscus of a conducting liquid can exist in equilibrium under an applied electric field [Taylor, 1964]. Taylor predicted that the threshold applied voltage of a liquid would be related to the surface tension and the geometry of that liquid [Taylor, 1969]. This prediction was found to be inaccurate later on, as it was found that other liquid properties also have an effect on this process [Michelson, 1990].

In 1965, Carson and Hendrick used a metallic capillary instead of a glass capillary and obtained the current in pulse form. They still managed to obtain similar photographs to that obtained by Taylor using glycerine and octoil [Carson and Hendrick, 1965]. In 1980 it was reported that the droplet size was decreased with increasing applied potential, thus obtaining an important condition for the production of fine droplets by electrostatic atomisation [Nagornyi and Bezrukov, 1980].

There seemed to be a continued interest in the field into the 1980s with Smith (1986) publishing a general discussion of the process with quantitative descriptions on the

influence of liquid properties on the experimental results while others tried an energy approach or a Joule heating mechanism [Smith, 1986]. Hayati and co-workers (1986–1987) carried out a detailed investigation of the mechanisms present in the atomisation process and pointed out that the electrical conductivity of a liquid plays a major role in the electrostatic disruption of the liquid flowing through a capillary [Hayati *et al.*, 1986, Hayati *et al.*, 1987a, Hayati *et al.*, 1987b]. With insulating liquids little disruption occurs due to insufficient free charges available in the bulk of the liquid, while conducting liquids form very unstable streams and tend to discharge at higher electric potential.

After the work by Zeleny and Taylor, the most significant work was the classification of the functional modes of spraying carried out by Clopeau and Prunet-Foch (1990 and 1994) [Cloupeau and Prunet-Foch, 1990, Cloupeau and Prunet-Foch, 1994]. The main modes of EHDA will be explained in **Section 2.8.1**.

Lately, the cone-jet mode of atomisation has attracted the attention of researchers due to its great application potential for its ability to produce near-monodisperse droplets. Researchers have used high ($>10^{-5}$ ml/s) and low ($<10^{-5}$ ml/s) flow rate regimes. Meesters *et al*. (1992) investigated the cone-jet mode atomisation at high flow rates and observed a very high droplet production. Loscertales and Fernandez were able to produce droplets in the nano-meter scale at very low flow rates of 10^{-7} ml/s [Grace and Marijnissen, 1994].

2.8.1 Different modes of atomisation

In electrohydrodynamic atomisation, the shear stress acting on the liquid surface due to the applied electric field causes the liquid meniscus at the exit of the capillary to elongate and form a cone and/or a jet, which later disrupts into droplets because of the mechanical and electrical forces. A few papers have been published regarding the classification of modes in EHDA [Hayati *et al.*, 1987a, Hayati *et al.*, 1987b, Cloupeau and Prunet-Foch, 1990, Grace and Marijnissen, 1994, Grigorev and Shiryaeva, 1994, Shiryaeva and Grigorev, 1995], but the formation of the jet and the disintegration of droplets and the characteristics of each spraying mode was not explained much, as most of them used geometrical forms of the jet and meniscus as the criterion [Jaworek and Krupa, 1999]. The interest in the classification of modes was mainly due to the production of different droplet sizes and their charges, as well as the difference in the obtained spray patterns in each mode of spraying.

In the work done by Jaworek and Krupa (1999) the mode of EHDA spraying was characterised by two criteria:

1. The geometrical form of the liquid at the outlet of the capillary (drop, spindle, jet)
2. The type of jet behaviour in its disintegration into droplets

The first group includes the modes in which only fragments of liquid are ejected from the capillary, and the dripping, microdripping, spindle, multi–spindle belong to this category. The second group includes modes which have a characteristic that the liquid

issues a capillary in the form of a long continuous jet which then disintegrates into droplets only at a distance, usually a few millimetres, from the exit of the capillary. Cone-jet, precession, oscillating-jet, multijet and ramified-jet modes belong to this second category. The meniscus and the jet in this second group can be stable, can vibrate, rotate spirally, around the capillary axis or whip irregularly [Jaworek and Krupa, 1999].

A combination of parameters described in the **Section 2.8.3** gives rise to different modes of spraying, and Jaworek and Krupa (1999) summarised these different modes with their key characteristics. This has been reproduced in this thesis (**Table 2.2**).

Table 2.2 Characteristic features of the modes of EHD spraying [Jaworek and Krupa, 1999]

Mode of spraying	**Forms of liquid**	**Dynamics of meniscus/jet**	**Spray pattern**
Fragments of liquid			
Dripping 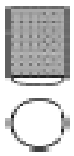	Meniscus: semi – spherical Drop: simple spherical	Axially vibrating	Single drop (with siblings)
Microdripping 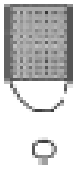	Meniscus: cone/hemispherical Drop: small, simple spherical (in some case with trailing/	Axially stable	Linear series of droplets (accompanied with fine mist)

	leading thread)		
Spindle 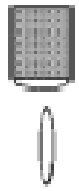	Meniscus: cone/semi-spherical Drop: elongated fragment of liquid (spindle) (with trailing thread)	Axially vibrating	Spindles disrupting into small droplets
Multispindle 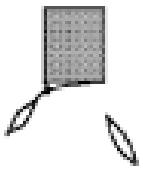	Meniscus: flat/multi-cone Drops: multiple spindles (with trailing thread)	Stable/lateral vibrating	Spindles around the axis disrupting into small droplets
Ramified-meniscus 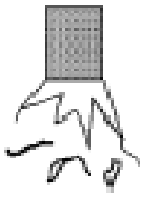	Meniscus: irregular short jets oriented in random directions Drops: irregular fragments of liquids	Irregularly deformed	Fragment of liquids sputtered in different directions
Liquid jets			
Oscillating-jet 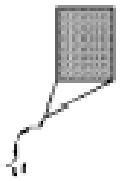	Meniscus: skewed, oscillating cone Jet: linear, oscillating in a plane	Oscillating in a plane, kink instabilities at its end	Droplets sprayed in ellipsoidal-base cone
Precession 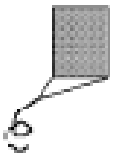	Meniscus: skewed, rotating cone Jet: spiral, rotating around the capillary axis	Rotating around the capillary axis, spiral instabilities	Fine aerosol sprayed in a regular cone

Cone-jet 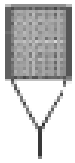	Meniscus: cone (linear, concave, convex, skewed) Jet: simple straight linear	Axially stable, varicose or kink instabilities	Fine aerosol sprayed in regular cone
Multijet 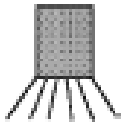	Meniscus: flat, with small cones on the rim Jet: linear, multiple	Stable (usually with kink instabilities)	Fine aerosol sprayed in distinct directions
Ramified – jet 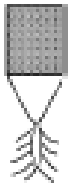	Meniscus: cone Jet: linear, ramified in random directions	Mother jet with randomly changed sub-jets	Droplets sprayed around the capillary axis

However the characteristics given in **Table 2.2** refer only to clear forms of spraying modes and there can be irregularities preventing the classification of the EHD spraying process to a distinctive known spraying mode. These irregularities could occur when one regular mode changes to another with changes to voltage or the flow of the liquid. It is therefore possible to recognise two different spraying modes that occur alternately or simultaneously [Jaworek and Krupa, 1999].

However the cone–jet mode is known to produce fine near–monodisperse droplets at a reasonable production frequency. Therefore in this thesis, the cone–jet mode of the ceramic suspensions subjected to the EHDA process was used for the processing. Therefore emphasis is placed on this spraying mode and its mechanism is discussed in **Section 2.8.2**.

2.8.2 Mechanism of stable cone-jet mode

Due to its ability to produce near-monodisperse droplets, the cone-jet mode is the most popular mode of EHDA. There are three processes involved in the EHDA of the cone-jet mode [Hartman *et al.*, 1999a] and these are described in the following sections.

2.8.2.1 Acceleration of the liquid in the liquid cone

In the stable cone-jet mode, the conical shape was studied by Taylor (1964) and it was realised that the 'Taylor cone' is formed when the outward stress due to an applied electric field balances the inward stress due to the surface tension of the liquid. **Figure 2.18** indicates the forces acting on a Taylor cone as shown by Hartman and co-workers in 1999.

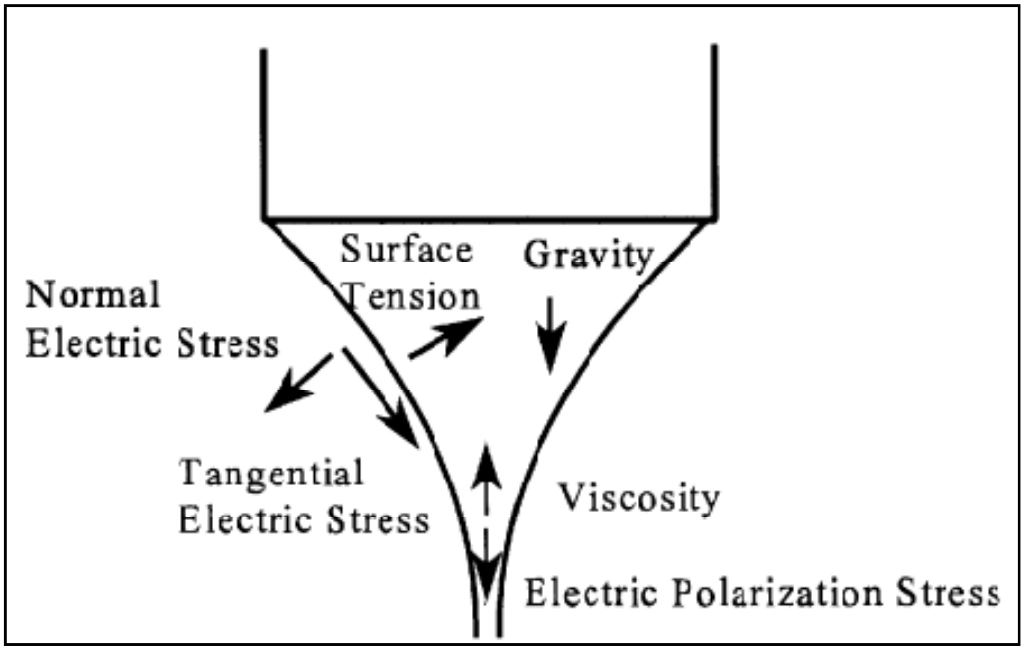

Figure 2.18 Forces in the liquid cone [Hartman *et al.*, 1999b]

In the liquid cone, the charge could be transported through conduction in the liquid due to the electric field and by charge convection. The electric field induces free charge that consists of ions at the liquid surface. Due to this charge at the liquid surface, the normal electric field acting inside the liquid is smaller in comparison to the normal electric field acting outside the liquid. The tangential electric field accelerates the ions on the liquid surface towards the cone apex, where the ions accelerate the surrounding liquid resulting in a thin jet emerging at the cone apex. It was stated by Hartman and co-workers (1999) that this acceleration process and the shape of the liquid cone are a result of the balance of the pressure and surface tension of the liquid, gravity and electric stresses in the liquid surface and of the inertia and viscosity of the liquid [Hartman *et al.*, 1999a].

2.8.2.2 Break–up of the jet into droplets

For each liquid, there exists a minimum flow rate, below which a stable cone–jet mode cannot exist and at this minimum flow rate, the jet breaks up due to axisymmetric instabilities, which are also termed ‘varicose instabilities’. At higher flow rates, the current through the liquid cone increases which in turn increases the surface charge on the jet. Above a certain surface charge, the jet break–up will also be influenced by the lateral instabilities of the jet and these instabilities are called ‘kink instabilities’[Hartman *et al.*, 1999a]. When the influence of these kink instabilities increases, the produced size distribution of the main droplets become wider [Cloupeau and Prunet-Foch, 1989]. While these kink instabilities could also be described as a whipping motion of the jet, it is important to note that above a certain maximum flow rate, a stable cone-jet mode cannot exist [Hartman *et al.*, 1999a]. **Figure 2.19** shows the jet break-up changing from

axisymmetric to kink instabilities. **Figure 2.20** shows the real-time images of the transition from a varicose break-up towards a whipping break-up.

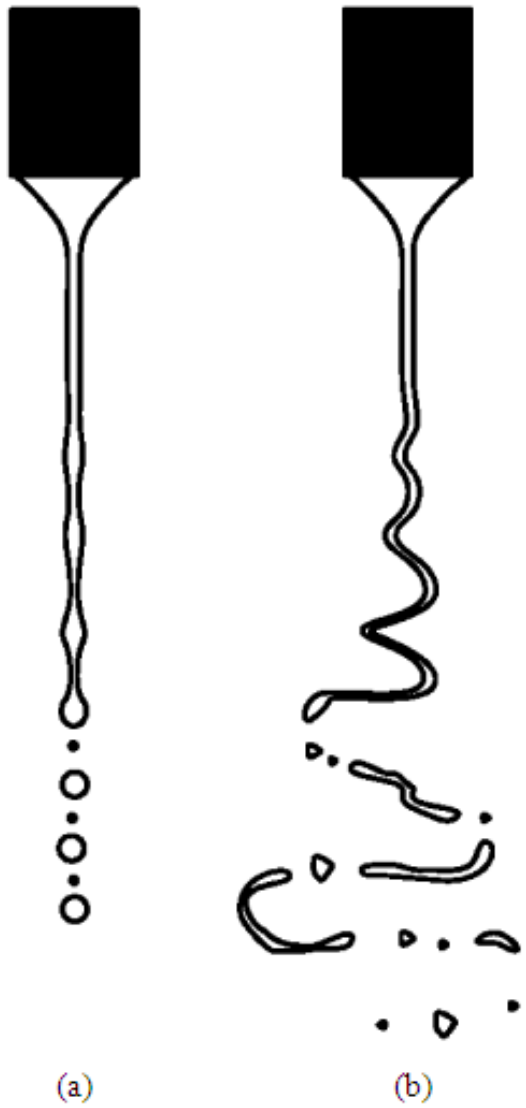

Figure 2.19 Jet break-up modes: (a) the axisymmetric varicose break-up and (b) the lateral kink break-up [Hartman *et al.*, 2000]

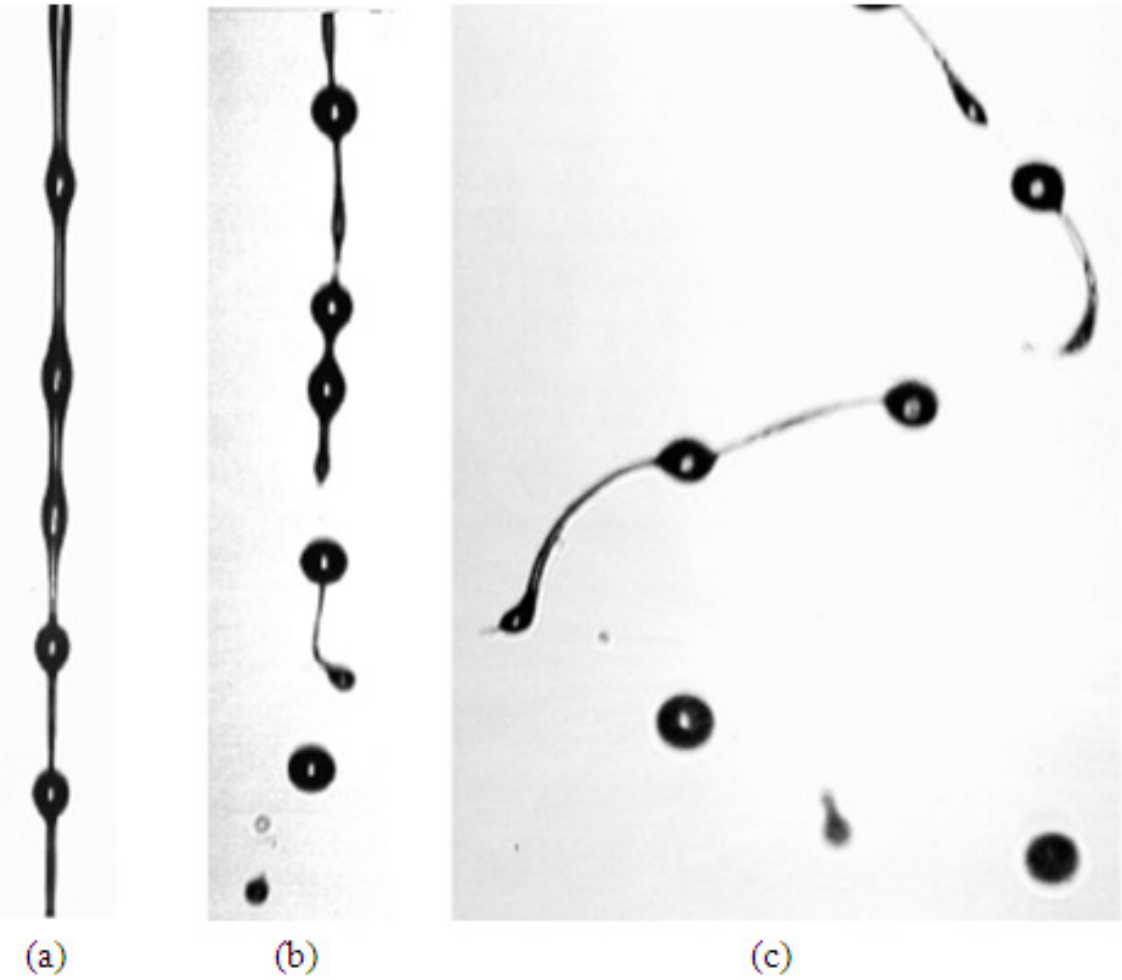

Figure 2.20 (a – c) The transition from varicose break-up toward whipping break-up [Hartman *et al.*, 2000]

2.8.2.3 Evolution of the spray after droplet production

When the jet becomes unstable, it will eventually disintegrate into droplets. The electrical interactions between these highly charged droplets give rise to a size segregation effect. Smaller droplets are found at the edge of the spray and the larger droplets at the centre of the spray [Gañán-Calvo *et al.*, 1994, Hartman *et al.*, 1999a].

2.8.3 Factors influencing EHDA

EHD process is governed by the physical properties of the liquid such as surface tension, viscosity, density, and electrical conductivity as well as on the capillary diameter, applied voltage, and liquid volume flow rate [Jaworek and Krupa, 1999].

The surface tension is the dragging force of the liquid from its surface and needs to be overcome in the EHD process by the electrical forces. Higher surface tension needs higher electrical forces, but has no influence on the droplet size [Gañán-Calvo *et al.*, 1997]. Viscosity makes a major contribution to the jet formation and droplet production [Gañán-Calvo, 1995]. Work undertaken by Jayasinghe and Edirisinghe (2002) deduced that an increase in viscosity results in an increase of the droplet size [Jayasinghe and Edirisinghe, 2002a]. Electrical conductivity is important in producing the jet and a liquid with a very low electrical conductivity cannot be atomised due to the lack of tangential stress by the charges and if the conductivity is too high there arises concern regarding electrical discharge with the surrounding atmosphere [Fernandez de la Mora, 1992]. Density is another parameter which appears in the scaling laws that describe and predict the EHD phenomena and may affect the droplet production.

It has been shown that the capillary size has an effect on electrohydrodynamic processing [Cloupeau and Prunet-Foch, 1989]. It was reported in their work that for a given liquid, the range of possible flow rates varied according to their size and the flow rate was much higher with increase in capillary diameter. Tang and Gomez (1996) showed the droplet diameter to be independent of the needle diameter. They plotted a

graph of droplet diameter against flow rate, and obtained a single curve that correlated to the droplet sizes using different capillaries (**Figure 2.21**) [Tang and Gomez, 1996]. However it was also reported that increase of capillary size would lead to a narrowing of the stable cone-jet domain (*i.e.* it reduces the maximum liquid flow rate for the stable cone-jet). Below the minimum voltage of the domain, the spray operates in the pulsating mode, while above the maximum voltage of the domain, the spray operates in unstable modes and they both tend to be polydisperse.

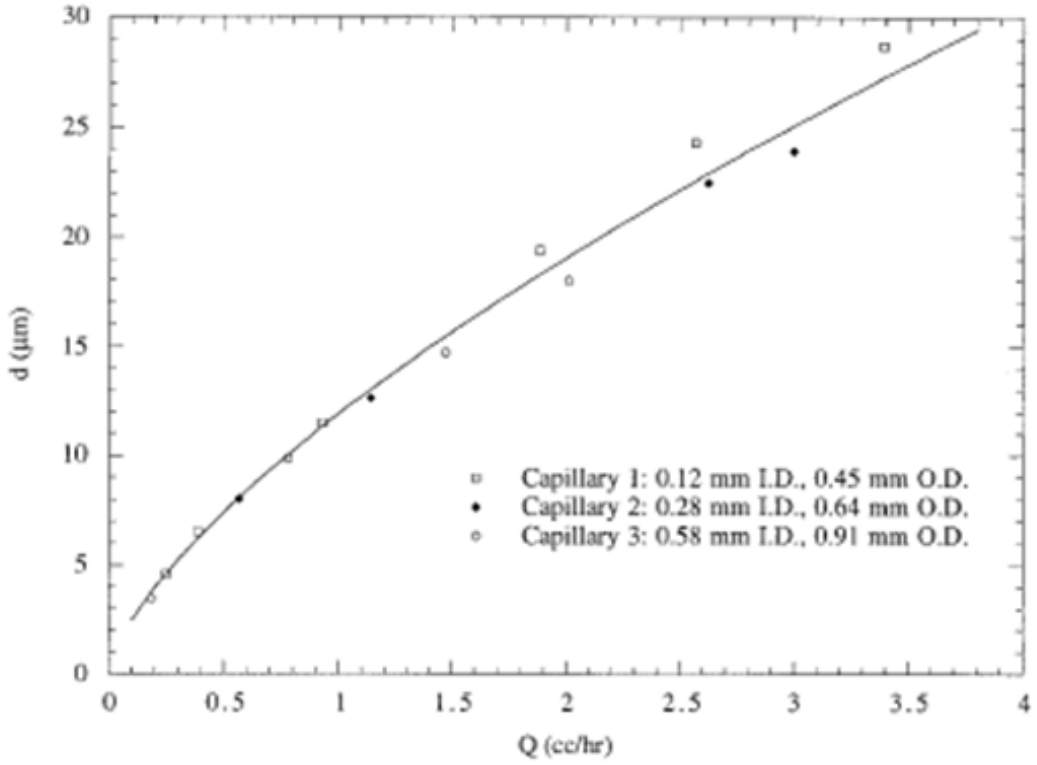

Figure 2.21 Droplet diameter vs liquid flow rate for different capillary sizes [Tang and Gomez, 1996]

The geometry of the ground electrode is known to influence the trajectory of the droplets. A ring shaped ground electrode produces a conical spray with larger droplets

segregated in the central regions and the finest droplets re-circulating about the ring [Gañán-Calvo *et al.*, 1997, Hartman *et al.*, 1999a, Hartman *et al.*, 2000]. **Figure 2.22** shows an electrospray set-up using a ring shaped ground electrode depicting the trajectory of the primary and satellite droplets being ejected from the jet break-up, where the former is found at the centre and latter found towards the edge of the spray. A point-like ground electrode can be used to focus most of the droplets towards a designated area [Jayasinghe and Edirisinghe, 2004] and was found to be useful in electrostatic atomisation printing [Jayasinghe *et al.*, 2002]. **Figure 2.23** shows the trajectory of the droplet moving towards the point-shaped electrode.

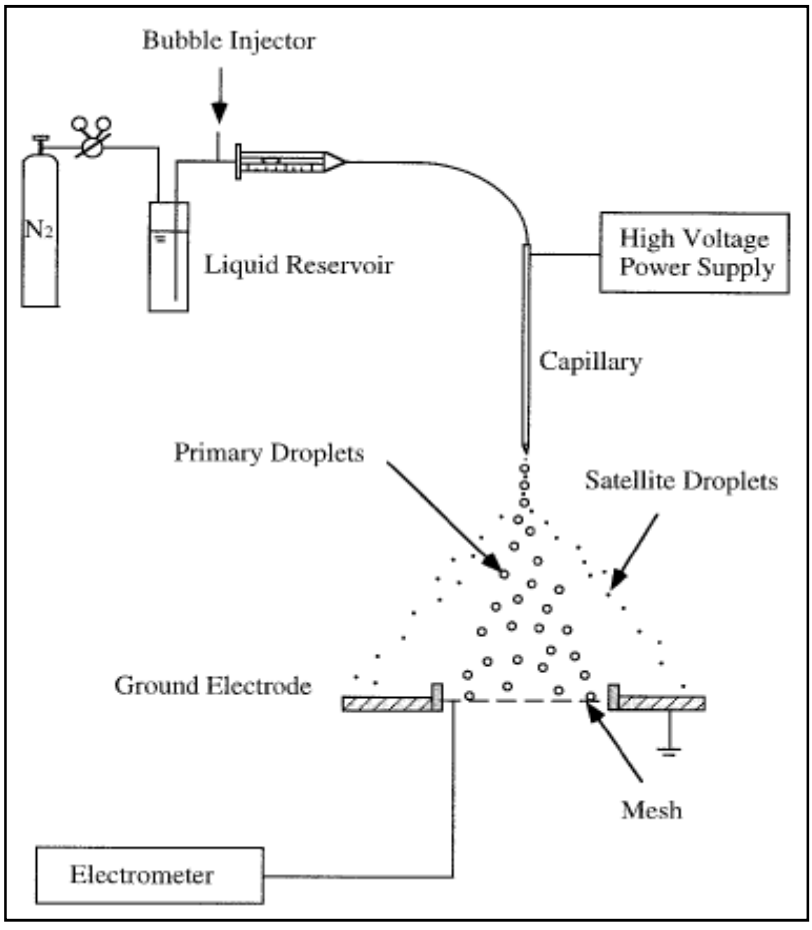

Figure 2.22 Configuration of the electrospray atomisation system

[Tang and Gomez, 1996]

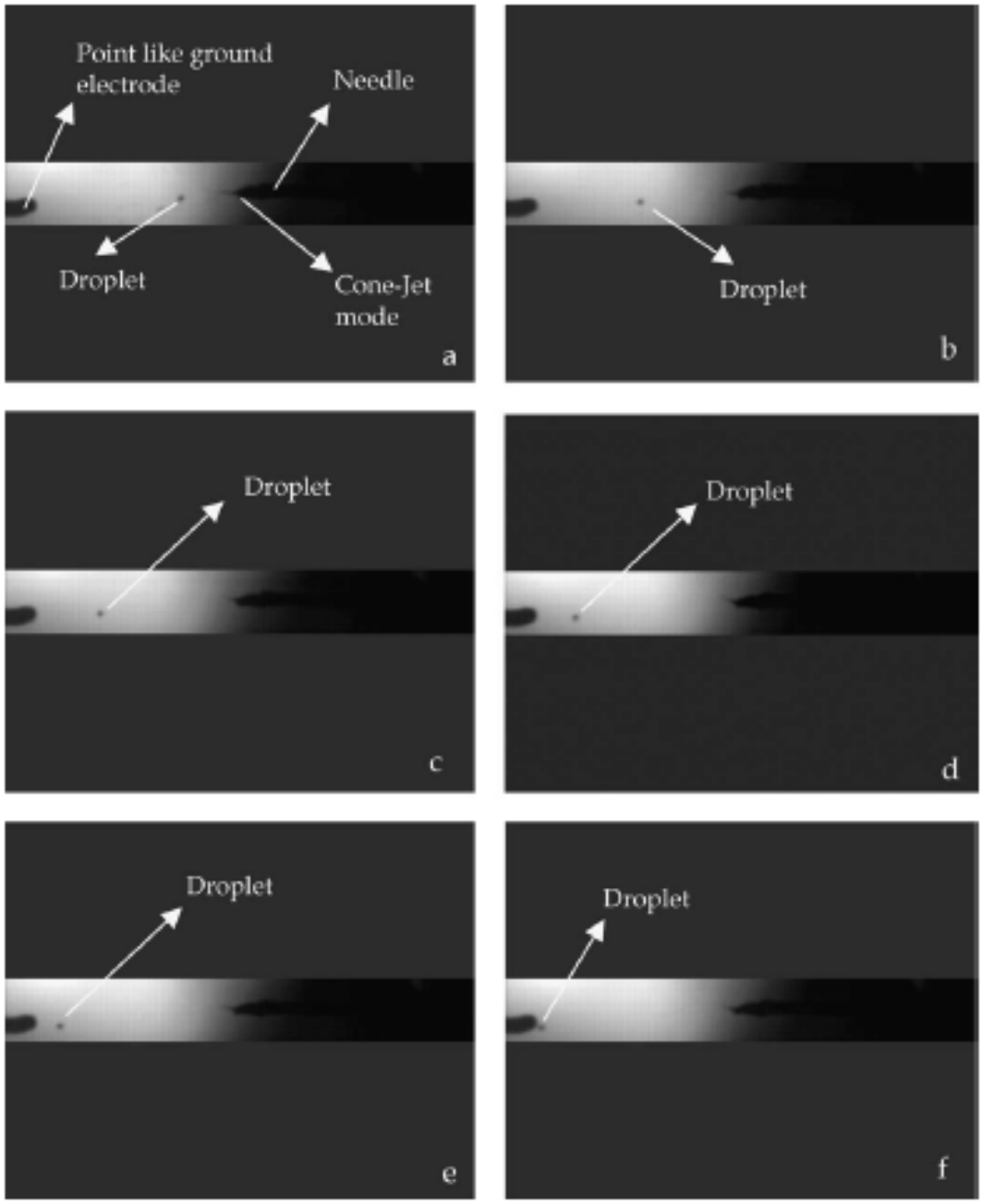

Figure 2.23 Sequence a – f showing a droplet of the suspension moving from the exit of the needle towards the point-like ground electrode [Jayasinghe and Edirisinghe, 2004]

The electrospraying modes are subjected to change when the applied voltage is altered. The applied voltage creates an electric field between the needle and the ground

electrode, and has a major influence on the droplet size and production frequency. When the applied voltage is higher, the electrical field strength is higher, and the electric forces are stronger, which can cause a stronger atomisation effect and a higher droplet production frequency with smaller droplet sizes [Gañán-Calvo *et al.*, 1997].

Flow rate is another parameter that can influence the droplet size and production rate significantly. The flow rate can be adjusted by either changing the cross-sectional area of the tube transporting the liquid or by varying the output of the syringe pump. The cone-jet mode can only occur within a certain range of flow rate and these limits are generally imposed experimentally [Grace and Marijnissen, 1994]. Hartman *et al.* (2000), have observed that at relatively low flow rates, just above the minimum flow rate for a given liquid, monodisperse sprays are produced [Hartman *et al.*, 2000]. At relatively higher flow rates, the droplets tend to become larger, but have a higher production frequency [Grace and Marijnissen, 1994]. Increase in flow rate can also lead to an increase in the polydispersity of the droplets [Higuera, 2003].

2.8.4 Electrohydrodynamic atomisation for the processing of porous structures

Even though the EHDA method itself dates back a few centuries, its possible use as a processing technique for producing porous structures was only investigated in 2002. Jayasinghe and Edirisinghe (2002) utilised electrospraying for producing porous alumina foams. This method can be categorised under the replication method as the process involves coating a sacrificial template. However, unlike in the replication method, it has been possible to obtain solid struts (**Figure 2.24**) and a ceramic coating

with reduced micropores [Jayasinghe and Edirisinghe, 2002b]. Therefore, this method seems to have all the flexibilities (irregular shapes, interconnected pores and controlled porosity) of the dipping method, but has deemed to be more advantageous. Further work was done by Chen *et al.* (2006a), where zirconia porous scaffolds were prepared by EHDA and the morphology of the coating and the mechanical properties were compared with structures prepared using the dipping method [Chen *et al.*, 2006a]. It was observed that the structures prepared by electrospraying demonstrated improved mechanical properties and can be linked to the reduced amount of micropores on the ceramic coating and stronger struts. However, foam preparation by electrospraying only, requires well dispersed ceramic suspensions of high concentrations of 60 – 65 wt% and the templates were electrosprayed for at least two hours for complete coverage of the ceramic coating. Thus even if this method has proved itself successful for suspensions of high particle loading, its eligibility for suspensions of lower particle loading is questionable and the production efficiency could be compromised.

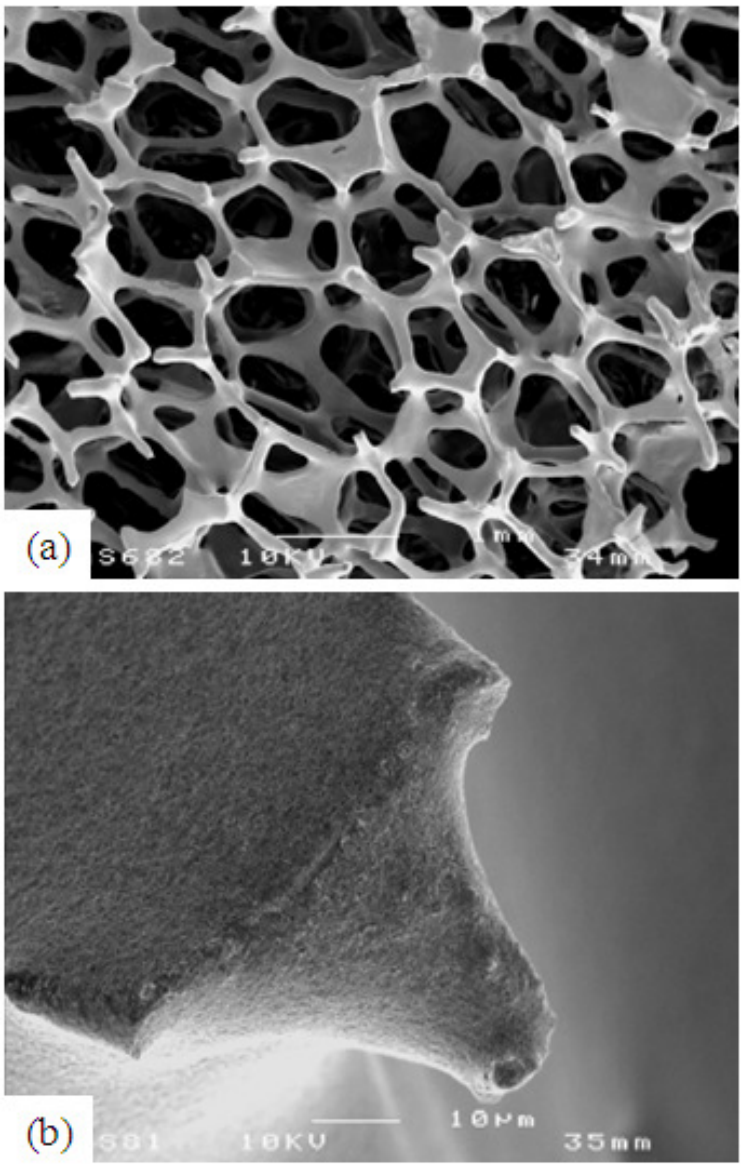

Figure 2.24 Alumina porous foam produced by electrospraying (a) open and interconnected pore network, and (b) image of a solid strut

[Jayasinghe and Edirisinghe, 2002b]

Chapter 3

Experimental details

This chapter is dedicated to explaining the materials used, corresponding suppliers, the product details and the main equipment set-up used for the experiments in this thesis. However, each research chapter involved a change to the basic electrohydrodynamic (EHD) spraying set-up and these changes are described in the respective chapters. The methods followed for the preparation of zirconia and nano-hydroxyapatite (nHA) bioceramic suspensions, the suspension and sample characterisation techniques and heat-treatment programs are described in this chapter. All experiments have been repeated to ensure reproducibility. All equipment that was used has been calibrated and measurements were checked against known values quoted by the supplier or in the literature.

3.1 Materials

3.1.1 Polymeric templates

Polyurethane (PU) templates were obtained from Recticel (Corby, UK). Two types of templates having different porosities were used for the experiments. Both types of foam templates had fully reticulated pore structures and were cut into the required dimensions

depending on the experiment. The main characteristics of the PU templates are shown in **Table 3.1**.

Table 3.1 The main characteristics of the PU templates used in the thesis

Template	Cell range /µm	Window size /µm
60 ppi	740 – 1040	200 – 500
45 ppi	1060 – 1600	400 – 650

Even though the pore structures had a cell size range of 740 – 1040 µm as in the case of 60 ppi (pores per inch) foams, each window size of the cell was 2 to 3 times smaller (~ 200 – 500 µm) than specified in **Table 3.1** and were verified by scanning electron microscopy (**Figure 3.1**).

3.1.2 Preparation of zirconia suspensions

A zirconia suspension of 15 vol% ceramic particle concentration was used for most of the experiments and its preparation will be described in detail in this section. All other concentrations (5, 15 and 20 vol%) were also prepared following the same procedure, with the zirconia and the dispersant content changed accordingly. The amounts are stated clearly in **Chapter 4**.

The zirconia powder (HSY3 Grade), with a mean particle size of 0.47 µm and density 6000 kgm^{-3} was supplied by MinChem Limited, Aldershot, UK. This HSY3 grade has

also been used in the literature [Evis *et al.*, 2006] and consists of tetragonal zirconia (97mol%) and Y_2O_3 (3 mol%). To prepare a 15 vol% zirconia suspension, 57.1 wt% zirconia powder was mixed manually for 10 min in ethanol, which contained 1.5 wt% of EFKA 4401 polymeric dispersant (donated by Stort Chemicals, Bishop Stortford, UK), at ambient temperature in a beaker placed in a cold water bath. The suspension was subjected to ultrasonic agitation for 30 min at 200 W input power. Cold water was replenished every 15 minutes to minimise the evaporation of ethanol. The zirconia content of the suspension was determined by loss-on-ignition by heating up to a temperature of 600°C. The suspension was stored in a plastic bottle and was kept agitated continuously using a roller mixer.

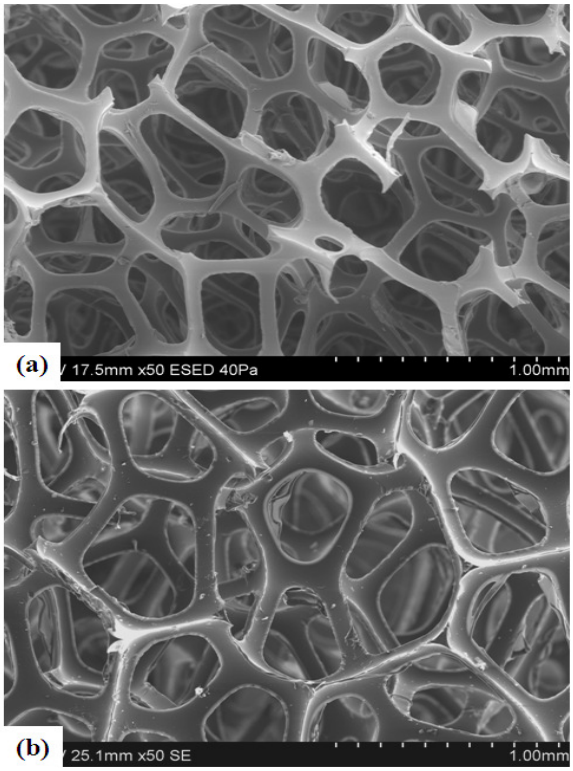

Figure 3.1 SEM of PU foam templates: (a) 60 ppi – cell range of 740 – 1040 µm, showing window size ranging ~200 – 500 µm and (b) 45 ppi – cell range of 1060 – 1600 µm, showing window size ranging ~400 – 650 µm

3.1.3 Preparation of nHA suspension

The original nano-hydroxyapatite (nHA) suspension was prepared in the Department of Materials Science and Metallurgy, University of Cambridge (UK). The suspension was water based and had an nHA solid loading of 18 wt%. This was verified by loss-on-ignition test. Even though the solid content was low, the suspension had a paste-like consistency and was not possible to use in its as-received state for electrospraying. Therefore, the 18 wt% nHA suspension was diluted in ethanol: where the latter is a common solvent used in EHD spraying and is known to produce a stable cone-jet mode. An nHA suspension of 6 wt% was used for the experimental work in **Chapter 5** and thus its preparation is discussed in this section. This suspension was chosen as it was the maximum nHA concentration that was able to produce a stable cone-jet mode to produce a spray of near mono-disperse fine droplets.

50g of original 18wt% nHA water based suspension was weighed using an electronic microbalance. 105g of ethanol (5g extra to compensate for the ethanol evaporation) was added and then was mixed together using a magnetic stirrer. The beaker was covered to prevent contamination and the suspension was stirred for 6 – 8 hours. The suspension was further subjected to ultrasonic agitation for 15 minutes at 200 W input power. The beaker was placed in a cold water bath to minimise the evaporation of ethanol and the water was replenished every 300 s. The suspension was stored in a plastic bottle, which was placed on a roller mixer and was continuously agitated. The suspension

concentration was determined by loss-on-ignition tests and the average concentration was ~6wt% nHA.

3.1.4 Preparation of simulated body fluid

Simulated body fluid (SBF) was used for bioactivity investigation in **Chapter 6**. SBF was prepared as proposed by Kokubo and his colleagues [Tanahashi *et al.*, 1994, Abe *et al.*, 2001].

Table 3.2 Amounts of reagents for preparation of SBF

Order	Reagent	SBF 1000 mL
#0	Ultra-pure water	750 mL
#1	NaCl	7.996 g
#2	NaHCO3	0.350 g
#3	KCl	0.224 g
#4	$K_2HPO_4 \cdot 3H_2O$	0.228 g
#5	$MgCl_2 \cdot 6H_2O$	0.305 g
#6	1kmol/m^3 HCl	40 cm^3
#7	$CaCl_2$	0.278 g
#8	Na_2SO_4	0.071 g
#9	$(CH_2OH_3)CNH_2$	6.057 g
#10	1 kmol/m^3 HCl	Appropriate amount for adjusting pH

The polyethylene bottle of 1000 ml capacity, in which SBF was to be made was cleaned thoroughly with dilute hydrochloric acid solution and then, with ultra-pure water. 750 ml of ultra-pure water was poured into the bottle which was placed in a water bath and was kept stirring at a temperature constant at 36.5℃, using a magnetic stirrer and heater.

Each chemical given in **Table 3.2** was added into the water until #8, one by one following the order in the table, after each reagent was completely dissolved. Reagent #9 was added little by little to avoid local increase in pH of the solution.

A pH meter was calibrated with fresh standard buffer solution. After #9 was added and the solution was stirred, the electrode of the pH meter was placed in the solution. The pH was measured when the temperature was 36.5℃. At this point the pH value is approximately 7.5 and the pH needs to be adjusted to 7.4 or 7.25 at 36.5℃. The pH of the solution is reduced by drop-wise addition and stirring of 1 kmol/m^3 HCl (#10). After the adjustment of pH, ultra-pure water was added to the solution adjusting the total volume of the solution to 1000 ml. The bottle containing SBF was cooled to room temperature (20℃), ultra-pure water was added as necessary to make the total volume of the SBF solution to 1000 ml and was shaken well. The bottle was labelled, and either used straightaway or stored in a refrigerator at 5-10℃ to be used within 30 days [Kokubo and Takadama, 2006].

3.2 Characterisation of the bioceramic suspensions

The physical properties such as density, surface tension, viscosity and electrical conductivity of the suspensions were measured. The equipment was cleaned and dried prior to each measurement and calibrated against the reference data. These measurements were taken at room temperature.

3.2.1 Loss-on-ignition

This is a widely used method for investigating the solid content of a suspension. The weight loss is measured by weighing out the samples before and after heating. Samples of the suspension were heated up to 600℃ in static air to calculate the actual weight loading of the solid, and in this case, the ceramic, and subsequently the samples were cooled down to room temperature in the furnace.

3.2.2 Density

The densities of the nHA and zirconia suspensions were determined by using the standard density bottle. The volume of the density bottle provided by VWR International, UK was 10 ml. Both the weight of the empty bottle and that filled with the suspension were weighed on the balance AND GR300-EC (A&D Instruments Ltd., Japan), which was capable of measuring precise values up to four decimals. The density bottle was calibrated using distilled water and ethanol. Five consecutive measurements were taken and were noticed to have a negligible variation. The average readings of density are reported in this thesis.

3.2.3 Surface tension

Surface tension of the suspensions were measured using Kruss Tensiometer K9 (Du Novy's ring method). The ring was hung from the hook by an eyelet. The suspension was poured into a beaker and the liquid was raised until contact with the surface was registered. The sample was then lowered again so that the liquid film produced beneath the ring was stretched. As the film is stretched, a maximum force is experienced and this is recorded in the measurement and used to calculate the surface tension [www.kruss.info, Feb 2009]. The mean value from a set of 10 recordings was taken and was noticed to have a negligible variation. The instrument was calibrated using ethanol prior to measuring the suspensions and it was thoroughly cleaned and dried before each measurement.

3.2.4 Electrical conductivity

The electrical conductivity of the suspensions was measured using HACH SensION^{TM} 156 dip-probe (Camlab Ltd., Cambridge, UK). The electrode was always cleaned with distilled water and dried before measurements. The electrode was placed in the suspension for 30 s to dislodge any trapped air bubbles inside the cell before recording the values. The probe was calibrated using ethanol and the mean values from a set of 10 recordings were taken for each suspension.

3.2.5 Viscosity

A U-tube viscometer (BS/U type) was used, which was immersed in a water bath maintained at 20℃, to determine the kinematic viscosity (v) of the suspensions. This

was determined by measuring the time (t) taken by the samples to travel between two marked regions in the U-tube viscometer. The time was recorded using a stop watch with millisecond accuracy. The kinematic viscosity is calculated by multiplying the viscometer constant (C) with the time (t).

$$v = Ct \qquad \textbf{(Eq. 3.1)}$$

Then, the dynamic viscosity (η) was calculated by multiplying the kinematic viscosity with the relative density (ρ) of the sample.

$$\eta = v\rho \qquad \textbf{(Eq. 3.2)}$$

Deionised water was used to calibrate the viscometer. However, due to the high particle content in the zirconia suspension in **Chapter 4** and **6** and the nHA suspensions' tendency to agglomerate in **Chapter 5**, it was not possible to use the U-tube as the ceramic particles seemed to block the fine capillary.

Therefore, a rotational viscometer (Visco Easy – L, Camlab Ltd., Cambridge, UK) was used to measure the viscosity of the suspensions. The spindle type was chosen using the viscometer manual and based on the estimated viscosity value, a rotational speed for the spindle was chosen. A viscosity measurement is obtained with reference to the rotational speed of the spindle inside the suspension, which also gives an estimate of its accuracy. L1 spindle was chosen for the measurements. At a rotational speed of 100 rpm and an accuracy >85%, the viscosity of the suspensions were measured. Ten consecutive readings were measured and a mean value was obtained for each suspension. The spindle was always thoroughly cleaned before each measurement.

3.3 General equipment used for electrohydrodynamic atomisation

A schematic diagram illustrating the equipment set-up used for electrospraying is shown in **Figure 3.2a**. The basic equipment set-up consists of a needle, connected to a syringe pump via a silicone tube. The needle is also connected to a high voltage power supply unit supplied by Glassman Europe Ltd., Tadley, UK, which is capable of supplying up to a maximum voltage of 30 kV. The jet behaviour was observed and recorded using a high speed camera (Weinberger AG, Dietikon, Switzerland) and a fibre optic light was used for illumination near the needle exit.

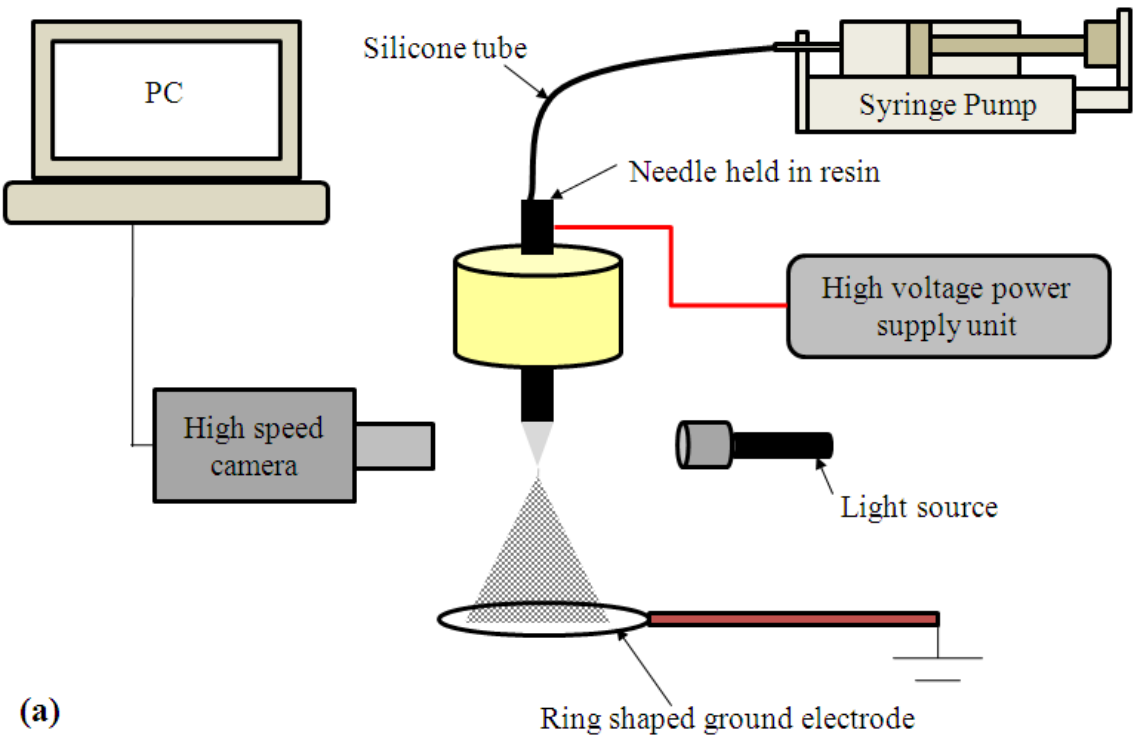

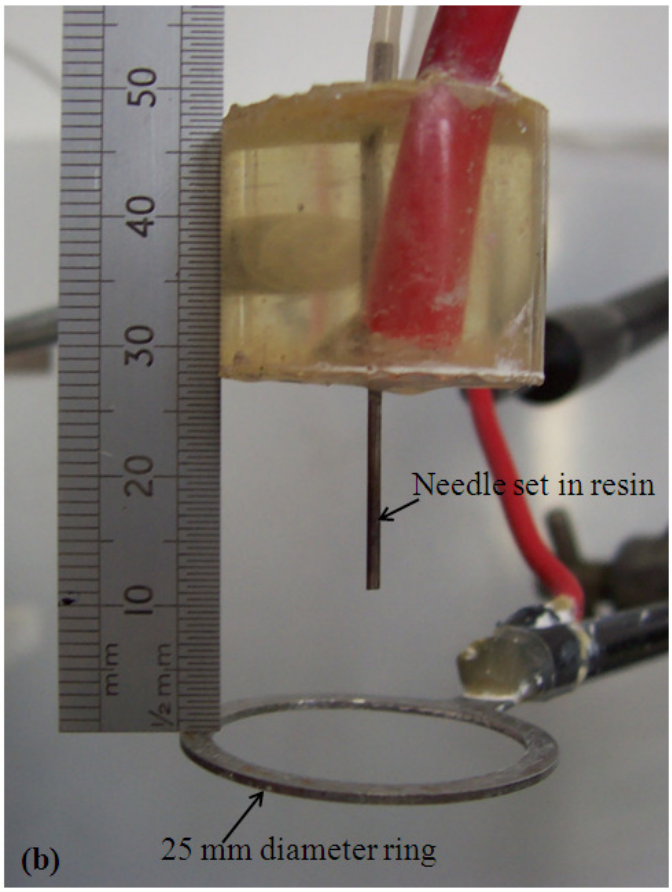

Figure 3.2 (a) schematic diagram illustrating the general electrospraying set–up and (b) photographic image of the needle and the ring electrode with a working distance of approximately 10 mm

3.3.1 Needle and ground electrode configuration

The stainless steel needles used in the electrospraying set-up were held firmly in resin for insulation and rigidity (**Figure 3.2b**). They were also able to be connected to a high voltage power cable. For the research in **Chapters 4** and **5**, needles with outer and inner diameters of 810 µm and 510 µm respectively, were used and experiments were carried out at lower flow rates. In **Chapter 6**, a stainless steel needle of outer and inner diameters 1100 µm and 810 µm respectively, was used.

A series of ground electrodes were used in this thesis. In **Chapter 4**, a selection of ground electrodes, which consisted of stainless steel rings of diameters 15 and 25 mm, a pin electrode set in resin and the mechanical rotating arm were used. In **Chapters 5** and **6**, the mechanical rotating arm was used as the ground electrode.

3.3.2 Syringe pump

In all the electrohydrodynamic experiments carried out in this thesis, the needle set-up was connected to a syringe mounted on a Harvard Apparatus PHD 4400 programmable infusion pump using silicone rubber tubing. For each new experiment, the pump was calibrated for short and long periods of time. Syringes of different capacity were used for investigations, depending on the volume to be processed and the range of flow rates.

3.3.3 High speed camera

The frequency of the droplet production in the stable cone-jet mode is very high, therefore in order to observe the jet break up, a high speed camera was required. SpeedCam MotionBLITZ (Weinberger AG, Dietikon, Switzerland) high speed camera consisting of a high definition digital camera to which a microscopic lens was attached, was used in conjunction with a fibre optic light source provided by the same company.

3.4 Measurement of droplet and relic sizes

3.4.1 Sympatec laser diffraction

The droplets produced from the atomisation process were measured using a computer controlled Sympatec Helos (helium laser optical spectrometer) model Vario KF sizing system (Sympatec Ltd., System-Partikel-Technik, Bury, UK), which recorded and plotted the collected data. The laser system was incorporated in the EHD processing equipment, by placing the 2.2 mm diameter laser beam approximately 10 mm below the exit of the needle, which was the working distance used for most of the experiments.

The Sympatec system is based on the diffraction of light that occurs when a laser beam impinges on the droplet of the spray. The laser beam travels perpendicular to the needle and measurements were synchronised with the appearance of the droplets in the measurement zone by monitoring the decrease in laser light transmission caused by the scattering of droplets. The lens used for the measurements had a droplet detection capability within the size range of 0.5 – 175 µm. The droplet size distribution experiments were repeated many times in order to check the validity of the data.

3.4.2 Optical microscopy

The relics obtained from electrospraying the nano-HA suspension (**Chapter 5**) were collected on a glass microscope slide approximately 10 mm below the exit of the needle, which was also the working distance for the experiments. The relics were observed using an optical microscope (Nikon Eclipse ME 600). A joy stick connected to the table axis of microscope helps to move the table in x and y directions. This microscope had

the ability to alter the magnification lenses and measure dimensions varying from a few micrometers to a few centimetres. The measurements were carried out by means of 'Acquis' digital imaging software (Synoptics Ltd., Cambridge, UK).

3.5 Heat treatment

A Eurotherm 2416 furnace (Elite Thermal Systems Ltd., Leicestershire, UK) which could go up to a maximum temperature of 1600℃ was used for the sintering of the electrosprayed structures.

Figure 3.3 shows an illustration of the heat-treatment programme that was followed to sinter the green bodies. This programme was followed throughout the thesis which consisted of two stages. The bioceramic coated templates were air-dried and heated to 400℃ at 2℃/min and soaked in that temperature for 1hr for the pyrolysis of the polymeric template to occur. This temperature was determined using thermogravimetric analysis (TGA) on the polyurethane template, which indicated decomposition at 400℃. Following pyrolysis, the bodies were sintered to a maximum temperature of 1200℃ and soaked at that temperature for 5 hrs, followed by cooling to room temperature. The heating and cooling rates were set to 2℃/min and 5℃/min respectively.

Only the maximum sintering temperature was adjusted according to the experiment, as 1200℃ (**Chapter 4** and **5**), 1400℃ (**Chapter 4**) and 1450℃ (**Chapter 6**).

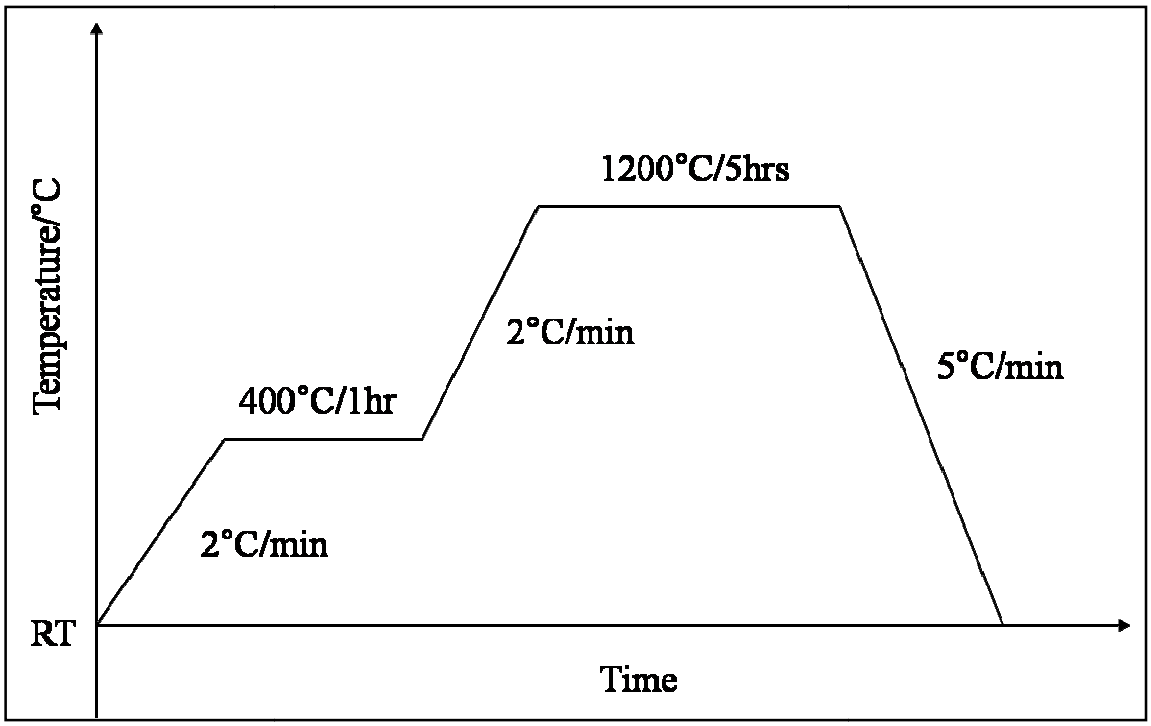

Figure 3.3 Heat-treatment program for the sintering of the green bodies (RT indicates room temperature)

3.6 Scaffold processing methods

Three main processing methods were adopted throughout this thesis; electrospraying, replication method and a combination of both. The electrospraying was the most used method spanning through all the research chapters, with numerous adaptations and modifications applied, depending on the requirement of the experiment. These adjustments to the experimental set-up are described in each research chapter, in addition to the explanations of how deductions were made to optimise the experimental procedure.

The replication or dipping method was used to process HA scaffolds in **Chapter 5**. This forming process along with the hybrid method, combining dipping with electrospraying is described in detail in **Chapter 5**.

3.7 Sample characterisation

3.7.1 Thermogravimetric analysis

Thermogravimetric analysis (TGA) is a type of testing used to determine characteristics of polymers such as degradation temperatures. JUPITER® thermogravimetric analyser, (Netzsch GmbH, Germany) was used to construct the heat treatment programme for the pyrolysis of the sacrificial PU template. The PU templates were burnt in air which was identical to that followed in the furnace for sintering.

3.7.2 X-ray diffraction

X-ray diffraction (XRD) was used for crystal phase identification and two X-ray diffractometers were used as per availability. In **Chapter 5**, XRD was carried out on the HA powder obtained from the sintered foams and was compared to the results of the original HA suspension to investigate any phase changes in the material after sintering. A Philips PW1830 diffractometer with CuKα radiation and scan range (2θ) between 25 – 45˚ was used.

In **Chapter 6**, XRD measurements were made using a Bruker-Axs D8 (GADDS) diffractometer. In this case, the surfaces of the scaffolds were scanned with 0.01° resolution using a CuKα radiation source. A scan range of 25 – 55° was used and the

objective was to observe any apatite formation on the scaffolds. The power used for X-ray excitation was at a voltage and current of 40 kV and 40 mA, respectively.

3.7.3 Porosity measurement

3.7.3.1 Calculation

The total porosity (p) of the foams were calculated by [Gibson and Ashby, 1997b]:

$$p = 1 - \frac{\rho_{foam}}{\rho_{solid}} = 1 - \rho_{relative} \qquad \textbf{(Eq. 3.3)}$$

where ρ_{solid} is the density of the solid material as given by the supplier or a reference and is indicated in the research chapter. The density of the scaffolds (ρ_{foam}) was determined from the mass and dimensions of the sintered structures.

This calculation was used to estimate the total porosity of the HA scaffolds and zirconia scaffolds in **Chapters 5** and **6**, respectively.

3.7.3.2 X-ray microtomography (XμT)

Internal pore networks for the different foam fabricating combinations were compared using Sky-Scan 1072 X-ray microtomograph. The X-ray radiographs were collected at 67 kV/154 μA with 0.5 mm aluminium filter, a pixel size of 8.01 μm, 0.68° angle step (0-180° rotation) and 3-frame averages were acquired for each radiograph. A cone-beam accusation was selected and cone-beam volumetric reconstruction (Feldkamp algorithm) was employed for image reconstruction. During the image reconstruction process, the beam hardening parameter was set to 20%. Each reconstructed image contained

1024×1024 pixels. The porosity of these 3-D images were analysed and calculated using the CTAn software.

This technique was used to image the internal structure of the HA scaffolds and to obtain porosity measurements and are discussed in **Chapter 5**.

3.7.3.3 Helium pycnometry

The helium pycnometer allows the measurement of volume and true density or specific gravity of solid objects. A Micromeritics AccuPyc 1330 pycnometer was used for the research work in **Chapter 6**, where zirconia scaffolds and zirconia-HA composite scaffolds were investigated. This method was used because the porosity was non-uniform in the former and the calculation method could not be used on the latter as it was a composite.

The volume measured in the pycnometer is that volume within the sample chamber which is inaccessible to the gas that was used, *i.e.* the solid volume. This gives the true density of the sample of known mass. The porosity is then calculated using:

$$Porosity\% = 100 - \left[\frac{100 \times Bulk\ Density\ (1 - Moisture\ Content)}{True\ Density}\right] \qquad \textbf{(Eq.3.4)}$$

where the bulk density = mass of sample/ bulk volume of the sample. Moisture content of these samples was assumed to be insignificant as the samples were sintered and kept dry. The bulk volume of the samples was calculated from the dimensions.

3.7.4 Scanning electron microscopy

The morphological characteristics of the sintered foams were observed using a Hitachi S-3400N scanning electron microscope (SEM). The samples were sputter coated with gold (Edwards sputter coater S150 B) for 1–2 minutes and were observed using an accelerating voltage of 20 kV. Both the sprayed and interior surfaces of the sintered bodies were imaged. The Hitachi was useful and easier to use for the low magnification images and was used extensively on this project. It was possible to use a high accelerating voltage and obtain images using environmental secondary electron detector, unlike high vacuum conditions in the field emission SEM.

For much higher magnifications however, a JEOL JSM 6300F field emission SEM was used. This microscope requires very high vacuum conditions and the scaffolds were more prone to charging at high accelerating voltage, so the voltage was reduced to 3-5 kV. The field emission SEM was mainly used to observe any surface changes due to apatite formation on the scaffold surfaces in **Chapter 6**. The elemental distribution map was plotted using INCA software (INCA Instruments, Oxford, UK).

3.7.5 Mechanical testing

Compression testing was carried out using a Zwick/Roell Z010 mechanical tester, using a cell load of 1 kN and a crosshead speed of 0.5 mm/min. This equipment was used to evaluate the mechanical properties of HA scaffolds (**Chapter 5**), zirconia scaffolds (**Chapter 6**) and zirconia–HA scaffolds (**Chapter 6**). During the test, the applied strain was set to a maximum of 70%. Six samples for each category were tested to obtain an

average measurement of compressive strength. Polytetrafluoroethylene (PTFE) layers were used at the two ends of the testing foams to avoid edge effects (*i.e.* sliding) during loading. The compressive stress (σ) at each point for each specimen was calculated by using $\sigma = F/A$, where F = the force at each data point and A = area of cross section. Any specific details referring to each type of scaffold is mentioned in the research chapter.

Chapter 4

Electrohydrodynamic preparation of zirconia foams with graded porosity

---

This chapter investigates the feasibility of using the electrohydrodynamic atomisation process to produce ceramic foams with graded porosity. The gradation of porosity in a biomaterial can be very useful for a variety of medical engineering applications such as filtration, bone replacement and implant development. The importance and uses of materials with a porosity gradient were discussed in the literature review. However, the preparation of such structures is not a technologically trivial task and replication methods do not offer an easy solution. As discussed in the literature review, the processing methods currently used to produce structures with a porosity gradient involve complicated and multiple manufacturing steps.

Zirconia (ZrO_2) was chosen as the ceramic material due to its extensive use in industrial and biomedical applications, which were also explained in the literature review. Modifications have been made to the electrospraying set-up configuration, the ground electrode and a range of suspensions of different concentrations have been utilised in order to determine the appropriate experimental conditions. The pores on the sprayed

surface, the inner-most surface and length-wise cross-sections, have been analysed, in addition to the change in depth of penetration as a function of spraying time. Control of porosity, pore size and depth of penetration has been obtained by varying parameters such as the spraying time, sintering temperature and the sacrificial template. It is the ultimate aim to create porous ceramic foams, using a 'single-step' processing method, where the porosity can be tailored and graded for uses in both industrial and biomedical applications.

4.1 Process optimisation

It is the objective of this investigation to obtain a profile of the porosity of the structure as a function of spray time and depth of penetration. Thus, the optimisation of the experimental parameters such as the suspension concentration, spraying time as well as a suitable droplet collection method to create graded porosity needed to be investigated. A needle having an inner diameter of 510 μm was used for the experiments, as it seemed suitable and would enable suspensions of high particle content to be electrosprayed minimising the blockages which would affect needles of finer diameters. Using needles of smaller inner diameters makes it feasible to use lower flow rates. Low flow rates are known to produce much finer droplets [Jayasinghe and Edirisinghe, 2004].

The ceramic suspension of ~20 vol% (65.4 wt%) was prepared using zirconia powder (Grade HSY3, details can be found in **Chapter 3**), which was suspended in ethanol, containing 1.25 wt% of EFKA 4401 polymeric dispersant. Ethanol was used in the ceramic suspension because it has been known to produce a stable cone-jet that is

essential for the EHD process [Gomez and Tang, 1994]. Polyurethane templates of pore size 60 ppi (pores per inch) with a cell range of 740 – 1040 µm were used for these experiments.

4.1.1 Investigation of a suitable droplet collection method

The charged ceramic droplets produced during the electrospraying process were to be used to coat the polymeric templates, which would then be pyrolysed (to remove the polymeric template) and sintered, resulting in porous foams. Different methods of spraying the foams using the electrohydrodynamic atomisation (EHDA) technique were adopted in order to investigate the most effective method of producing a ceramic foam with a graded porous structure.

The methods were as follows and are illustrated in diagrams shown in **Figure 4.1**:

1. The foam was held stationary, immediately below a 15 mm (diameter) ring which was electrically grounded (ring placed ~10 mm below the needle exit and foam immediately below the ring) **(Figure 4.1a)**
2. Foam was rotated below the 15 mm ring which was grounded (ring placed ~10 mm below the needle exit and foam below it) **(Figure 4.1b)**
3. The mechanical rotating arm was grounded (no ring and the foam was rotated 10mm below the needle exit) **(Figure 4.1c)**
4. Foam was rotated between the needle and a 25 mm diameter ring (ground electrode) [foam was 10 mm from the needle exit and the ring was kept 10 mm below the foam] **(Figure 4.1d)**

5. Foam was rotated at the same level as the ring of 25 mm diameter which was grounded [ring and foam ~10 mm below needle exit] **(Figure 4.1e)**

All ceramic coated templates were sintered to a maximum temperature of 1200℃ using the heat treatment program shown in **Figure 3.3** (**Chapter 3**).

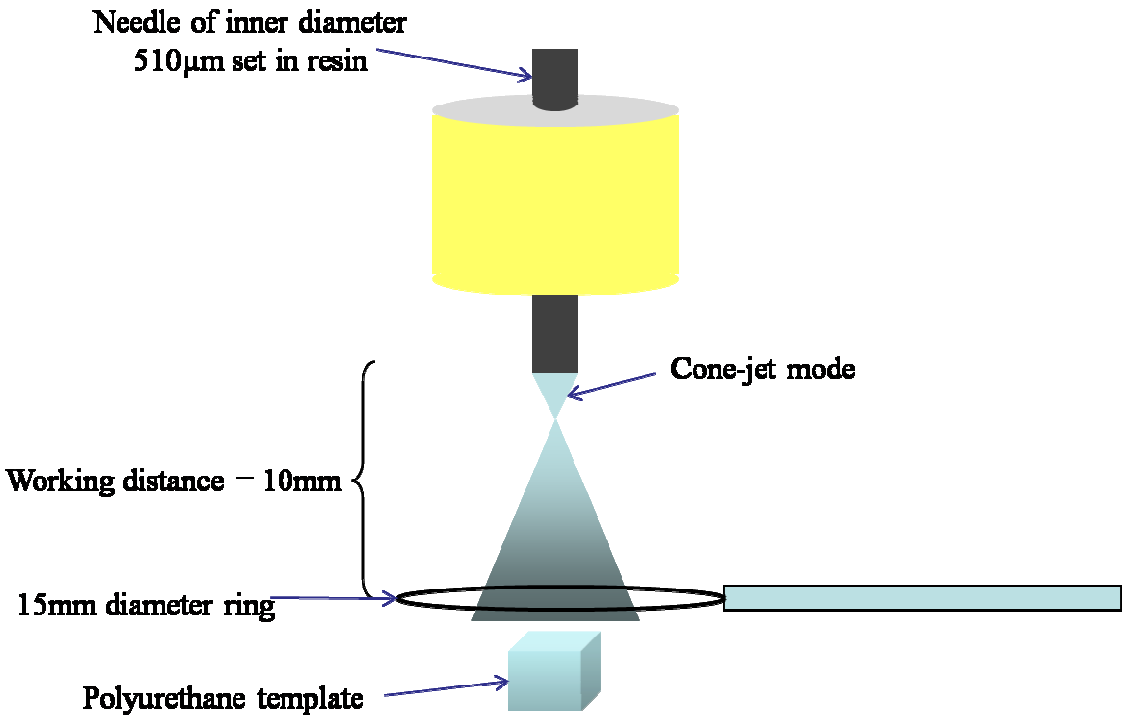

Figure 4.1a

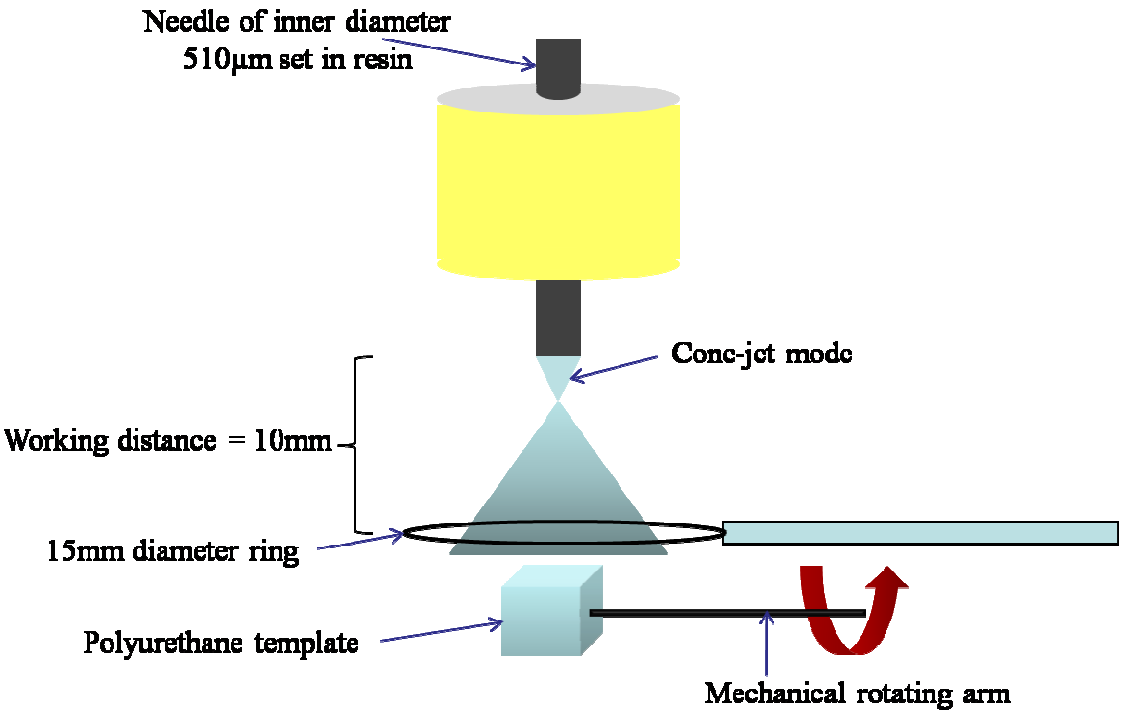

Figure 4.1b

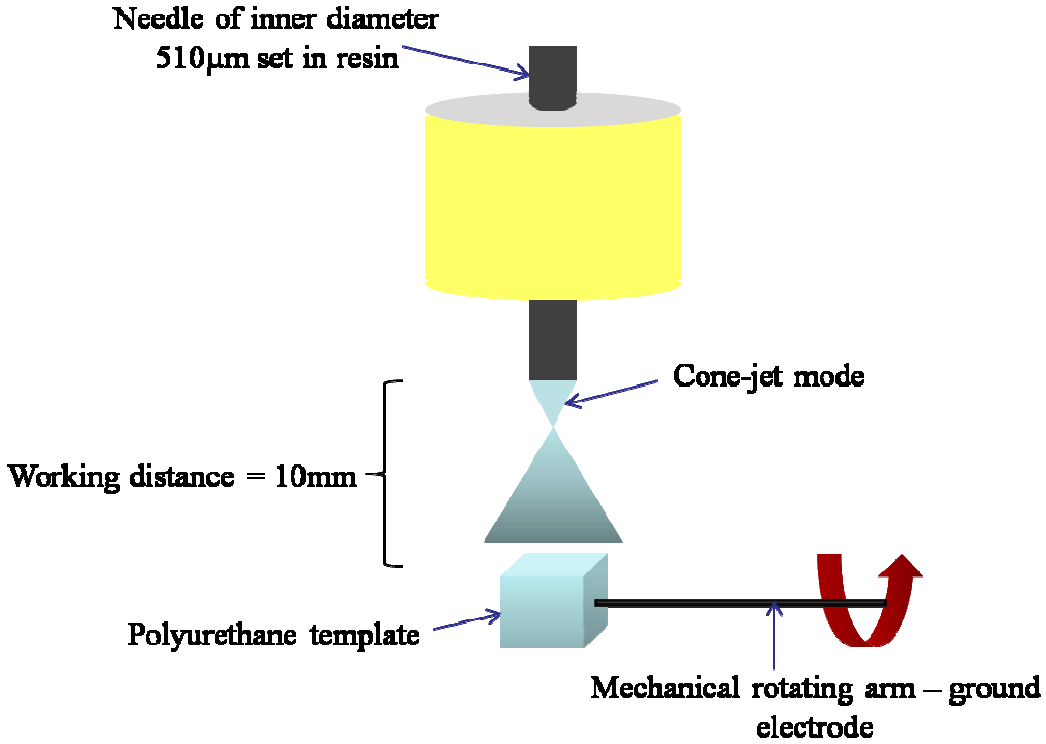

Figure 4.1c

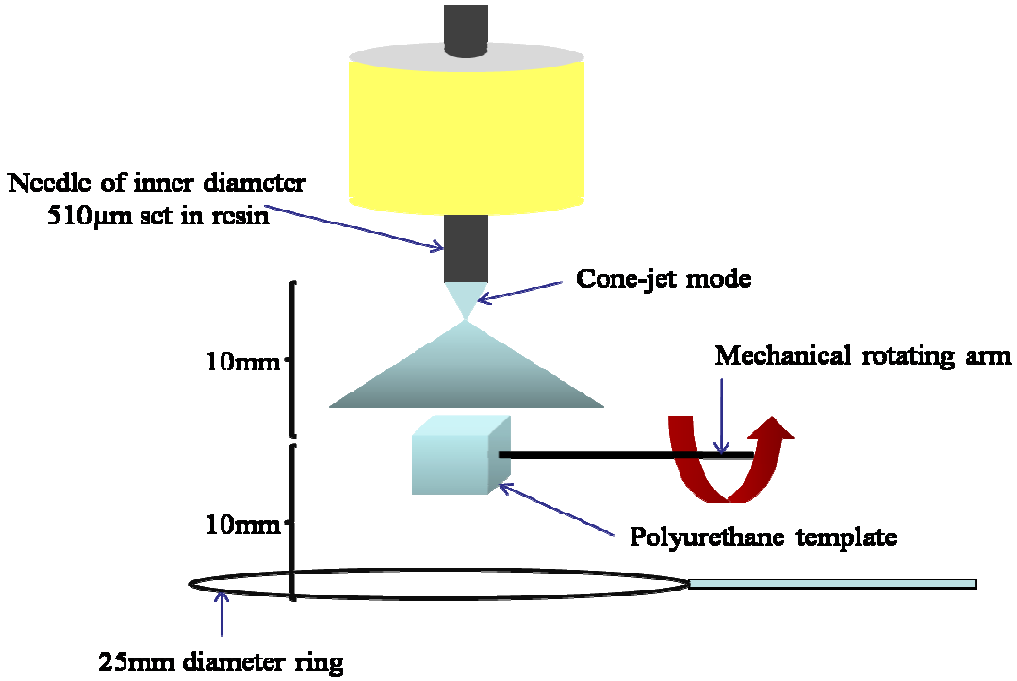

Figure 4.1d

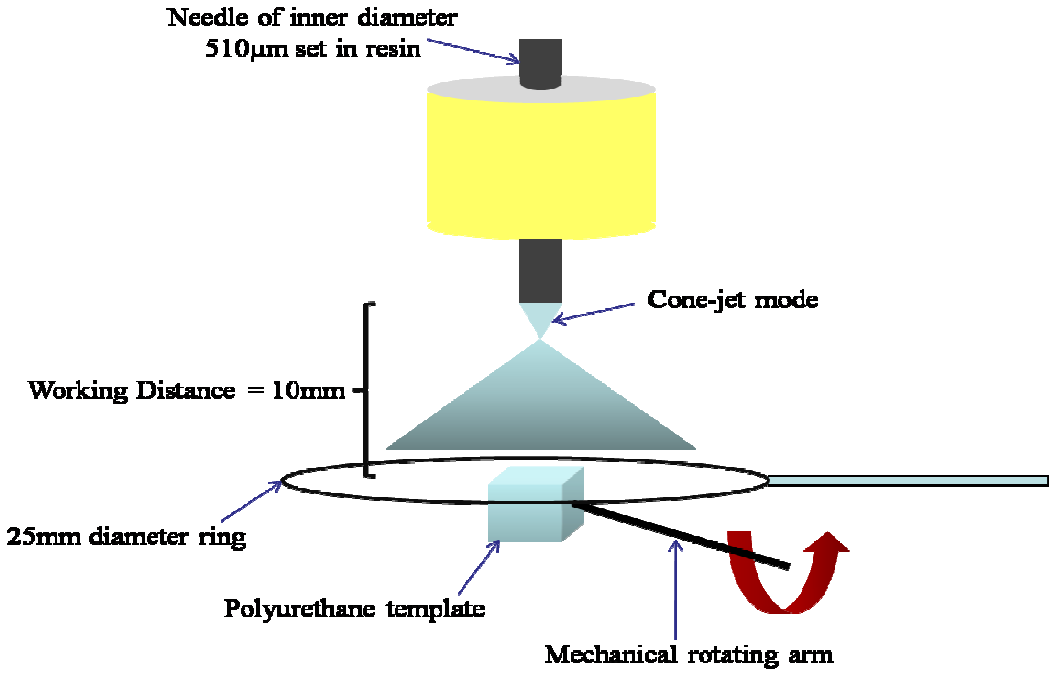

Figure 4.1e

Figure 4.1 Different methods adopted to determine the most appropriate method of spraying in order to obtain foams with graded porosity

Parameters kept constant were:

Flow rate (100 µlmin^{-1}), suspension concentration (20 vol %), sample size (5 mm× 5 mm× 5 mm), needle diameter (inner = 510 µm) and spray time (15 min).

Summary of results and discussion:

SEM (Field emission: JEOL JSM-6301F) was used to image the surface of the sintered structures which were gold coated.

Method	**Results and discussion**
1	The sample crumbled on sintering. This could have been due to insufficient penetration of ZrO_2 into the foam
2	Sintered sample retained the structure but was very fragile, which might improve with increased spray time.
3	The cone-jet was attracted to the rotating arm, but the entire foam was thickly coated and the pores were blocked. Therefore was deduced to be unsuitable.
4	The outside surface of the sample had a very thick coating and few pores, but inside the structure, the pores were interconnected. By comparing the outside and inside surfaces of the foam, even though the penetration into the foam might improve and be able to produce foams with thicker struts, the outside surface would be completely coated with no pores. Therefore, this method was considered to be unsuitable.

5	The structures were densely coated (there were no pores) and the surface that was imaged was the side that was not in direct contact with the spray, which indicated effective penetration into the foam. But this method was considered unsuitable due to the inability to spray as a function of time.

Therefore in conclusion, methods [1] and [2] were considered to be more suitable to investigate the graded porosity as a function of time.

4.1.2 Further investigation of droplet collection method as a function of time

The polymeric templates were further sprayed while some were kept stationary (method 1 in section **4.1.1**) and some were rotated (method 2 in section **4.1.1**), as a function of time to investigate the penetration of the ceramic droplets into the foam. The SEM images and the observations at different experimental conditions and spraying times are shown in **Tables 4.1** and **4.2**.

Table 4.1 SEM images and observations when the templates were held stationary

Spray time	SEM image	Observations
15 min	N/A	The sample crumbled to pieces after sintering
30 min	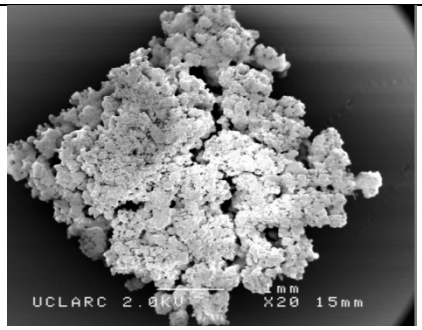 sprayed side 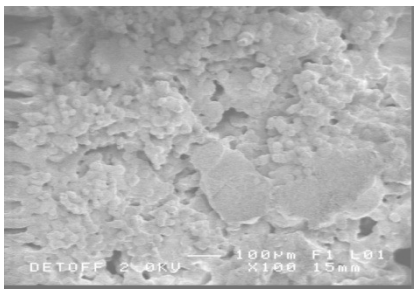 sprayed side showing no pores at higher magnification 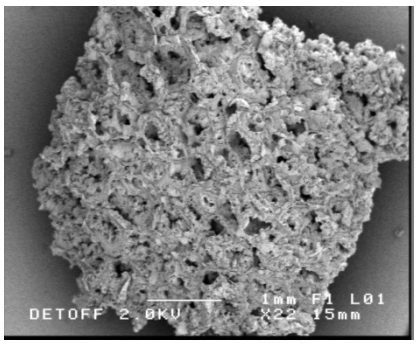 reverse side	1. The sprayed side consisted of very few pores in a size range of <1 µm 2. The reverse side had pores in the 100 µm range but they were not interconnected 3. No visible microcracks were observed on the coating.

	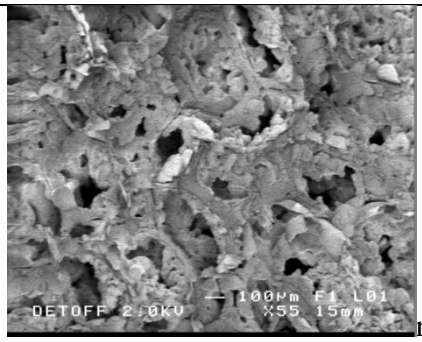 reverse side, showing pores with no interconnectivity	
1 hr	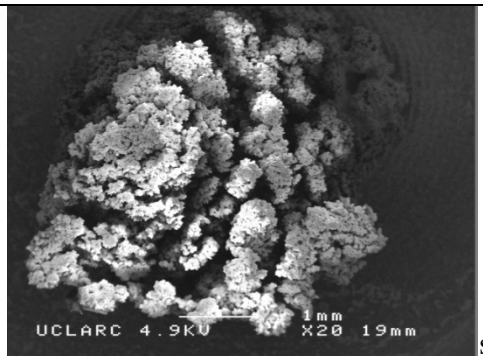 sprayed side 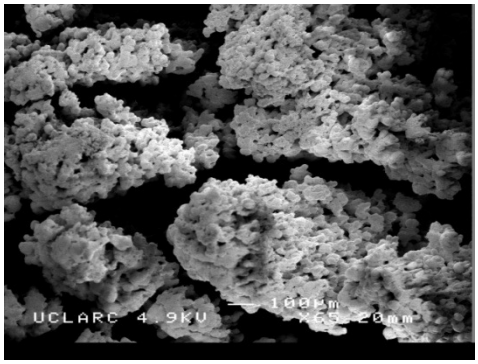 there were no pores, only gaps between the agglomerations	1.ZrO_2 suspension agglomerated on top of the foam and prevented further penetration of suspension into the foam 2. The ZrO_2 deposited on top of the polymer template formed a pyramid shaped structure

When the spraying time was increased, the penetration into the polymer template was extremely poor, therefore the rotation of the foam seemed necessary to ensure uniform coating of the slurry to create a porous structure.

Table 4.2 SEM images and observations when the templates were rotated

Spray time	SEM image	Observations
15 min	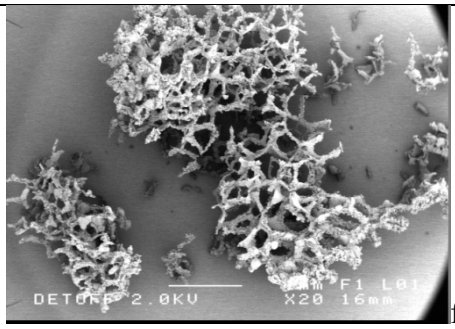 foam overview 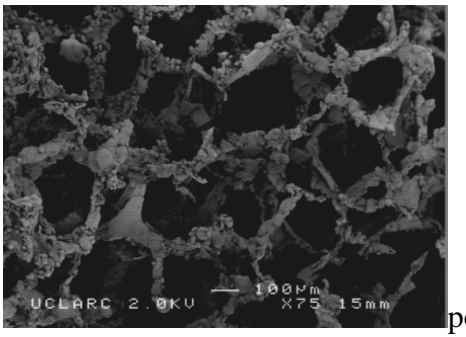 pore network	1. Sample retained the structure on sintering, but was very fragile and fractured slightly on handling 2. The structure showed interconnected pores and pore size seemed >100 µm
30 min	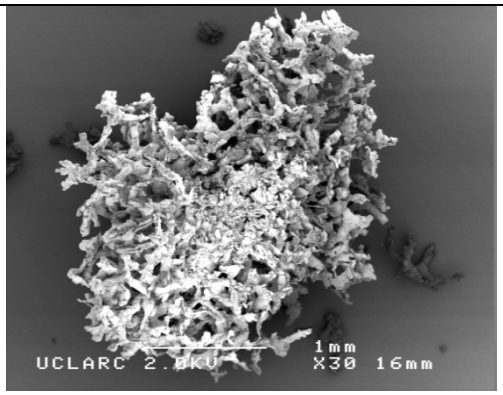 overview	1. The struts had a more dense coating than the 15 min sprayed sample 2. The amount of pores and the interconnectivity seemed less and the pores were in the 100 µm range

	 pore structure	
1 hr	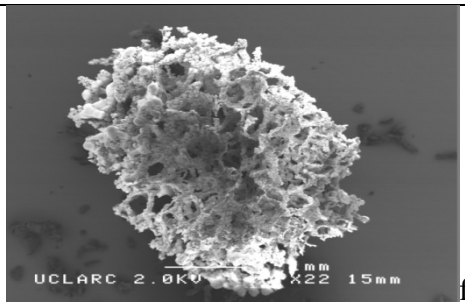 foam overview 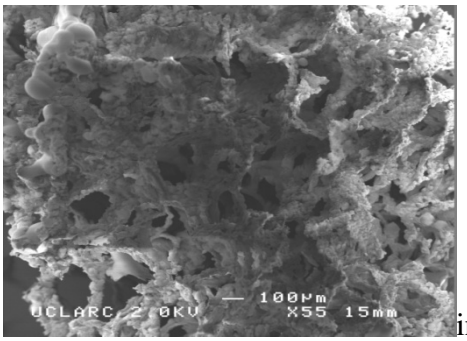 interconnected pore structure	1. In comparison to 30min, the coating was thicker
1hr 30min	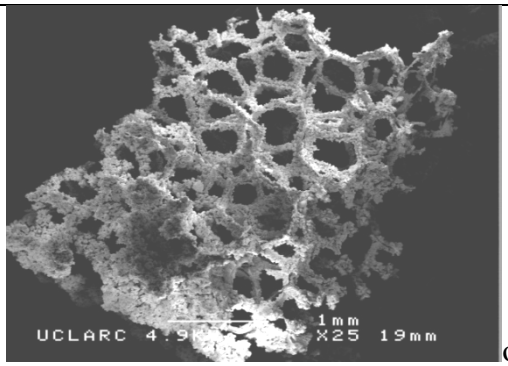 overview	1. The structure fractured on handling 2. The suspension penetration into the foam seemed effective by the presence of an open and

	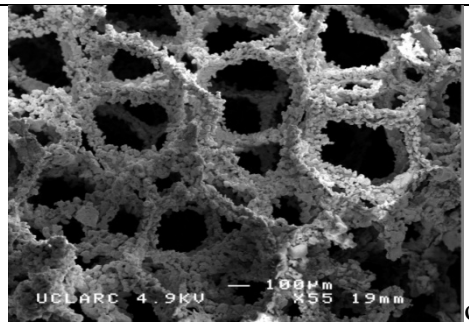 open and inter-connected pores	interconnected pore network
2 hrs	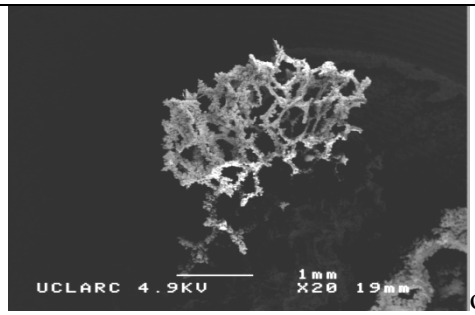 overview 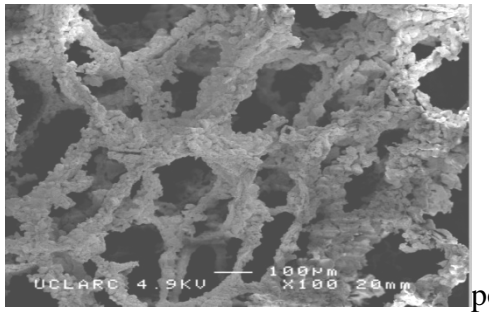 pore network	1. The structure fractured on handling 2. Suspension penetration into the template seemed effective by the presence of an interconnected pore structure

It was observed that by rotating the sample, it was possible to obtain a porous foam with interconnectivity. But these foams were quite fragile and it was not possible to obtain their dimensions or to measure the change in thickness of struts and porosity with depth.

4.1.3 Further optimisations on the experimental set-up and materials

4.1.3.1 Change of ground electrode

It was discussed in the literature how the geometry of the ground electrode is known to influence the trajectory of the droplets. While a ring shaped ground electrode produces a conical spray with larger droplets segregated in the central regions and the finest droplets re-circulating about the ring [Gañán-Calvo *et al.*, 1997, Hartman *et al.*, 2000, Hartman *et al.*, 1999a], a point-like ground electrode can be used to focus most of the droplets towards a designated area [Jayasinghe and Edirisinghe, 2004]. The ring was used initially to disperse the ceramic spray into a larger area in order to produce a more homogeneous coating of the ceramic suspension, but it was observed that the zirconia droplets were attracted to the ring onto which they were deposited in preference to the polymeric template, thus resulting in no observable ceramic coating on the template.

Therefore, it was decided to investigate the influence of using a pin as a ground electrode to which the foam would be fixed (**Figure 4.2**) as an attempt to attract the ZrO_2 droplets towards the foam, which would be stationary. The objective was to spray the foam and to measure the depth of penetration as a function of time.

Foams of dimensions 5 mm × 5 mm × 5 mm, suspension concentration of 20 vol%, flow rate of 100 $\mu l min^{-1}$, needle (inner diameter = 510 µm) and a voltage of 6.7 kV (which was noted to be higher than for the other methods) was used for the experiments. It attempts to spray the foam for 15 min, but within 5 min, the sprayed side was thickly coated with the suspension and the experiment was suspended. There was very slight penetration into the foam (<1 mm).

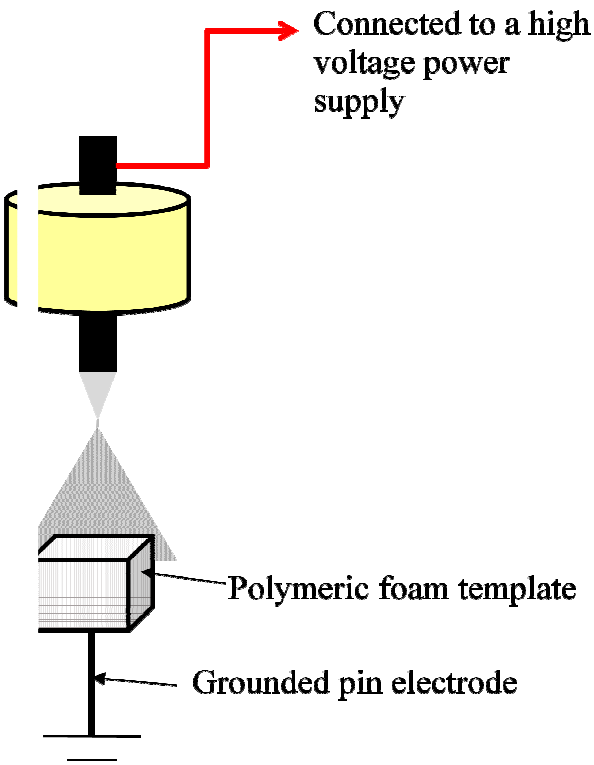

Figure 4.2 Modification to the experimental set-up using a pin electrode

4.1.3.2 Change of suspension concentration

With the use of a pin electrode to attract the charged zirconia ceramic droplets towards the foam, it was observed that the suspension was of too high concentration and therefore, a suspension of lower concentration was considered. Thus, a ZrO_2 suspension of 5 vol% (28.5 wt%) with 0.5 wt% of EFKA dispersed in ethanol was prepared.

Parameters that were kept constant:

Flow rate (20 µlmin^{-1}), suspension concentration (5 vol %), sample size (5 mm× 5 mm× 5 mm), needle diameter (inner = 510 µm) and the distance between the surface of the foam and the needle exit ~10 mm

Initially, the sample was sprayed for 15 min, but there was no visible penetration of the ceramic slurry. The spray time was further increased to 30 min and there seemed to be a coating and the foam seemed to have been infiltrated with the slurry, but upon sintering, the structure was reduced to powder. The spraying time was increased up to 1hr, but again, the structure was reduced to powder on sintering. Therefore, it was deduced that the concentration of the suspension was too low, hence resulting in a longer spray time. Longer spray time is not time efficient and to obtain a detectable structure (*i.e.* the ability to retain its structure upon sintering) with the 5 vol% slurry, the foam might have to be sprayed for at least 2 hours.

ZrO_2 suspension of 10 vol% (45.7 wt%), with 1 wt% of EFKA dispersed in ethanol, was then prepared and the same set-up as for the 5 vol% suspension was used to spray the foams. Foams were sprayed for 30 min, 1hr and 1hr 30 min time intervals. They seemed to be coated better than the foams sprayed using the 5 vol% suspension.

The observations of the green bodies and the sintered structures using the 10 vol% ceramic suspension are shown in **Table 4.3**.

It was concluded from these experiments that even though the 10 vol% ZrO_2 suspension gave a thicker coating than the 5 vol% slurry, the former was still not able to produce porous structures that could be imaged using the SEM and neither was it time efficient.

Table 4.3 Observations of the green bodies and sintered structures (10 vol% suspension concentration)

Spray time	Observations on green body	Observations on sintering
30 min	The slurry seemed to have penetrated ~1 mm into the foam	The structure was reduced to powder
1 hr	The slurry seemed to have penetrated >1mm into the foam and seemed to be thicker than for 30 min spray time	There was a very thin layer of the structure ~1 mm thick, but due to its extreme fragility, it crumbled on handling
1 hr 30 min	The struts seemed to have been coated to a depth of ~1.5 mm	A very thin layer of the ceramic layer remained, but was extremely fragile and fractured on handling

4.1.4 Deductions from optimisation experiments

- From the experiments conducted, it was deduced that fixing the polymeric template on a grounded pin electrode was a better method of attracting the charged zirconia droplets in order to observe any graded porosity.
- A zirconia suspension concentration of 20 vol % was too high and resulted in blocking the pores, while both 5 vol% and 10 vol% were too low and it was not possible to obtain strong sintered structures.
- It was then decided to prepare a ZrO_2 suspension of 15 vol% ceramic particle concentration and carry out the experiments using the pin electrode, which will

act as the ground electrode. Provided there is success in obtaining porous structures, parameters such as thickness of the sintered structure, strut thickness, pore size and their differences with depth could be measured using SEM.

- Polymeric foam templates of dimensions 5 mm × 5 mm × 5 mm were decided to be used for ease of spraying.
- Stainless steel needle (for electrospaying) of inner diameter 510 µm, flow rate of 20 $\mu l min^{-1}$ were decided as these parameters proved sufficient in the above experiments with respect to the stability of the cone-jet mode. The flow rate of 20 $\mu l min^{-1}$ was the lowest stable value for the chosen needle size.
- At a flow rate of 20 $\mu l min^{-1}$, a stable cone-jet mode was established in the voltage range of 4.5 - 5.5 kV for a 15 vol% zirconia suspension.
- The working distance (WD) between the upper surface of the foam and the needle exit was fixed at ~10 mm which seemed to be the minimum distance which would enable maximum coverage and attraction of the charged droplets without interfering with the stability of the cone-jet mode of the ceramic suspension.
- **Figure 4.3** shows a schematic diagram of the optimised equipment set-up to produce ceramic foams with graded porosity.

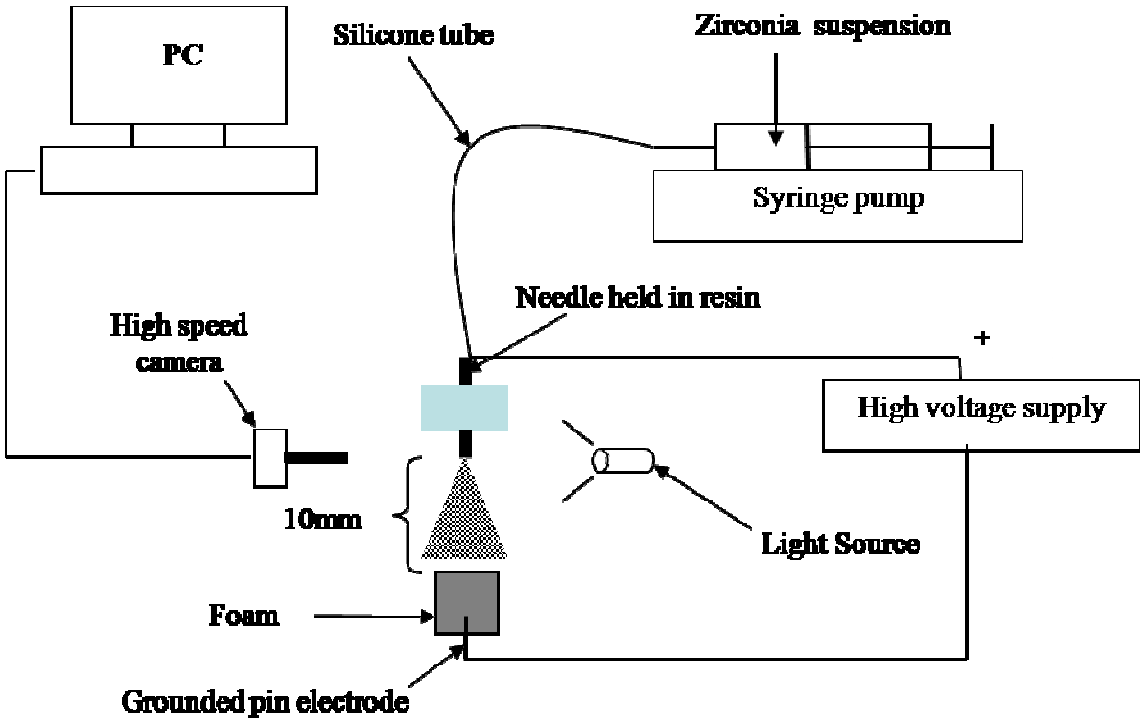

Figure 4.3 Equipment set-up for electrospraying of graded porous structures

4.2 Droplet size measurement

The droplet size distribution resulting from the atomisation of the 15 vol% zirconia suspension at a flow rate of 20 $\mu l min^{-1}$ and voltage of 5.1 kV was measured using a Sympatec sizing system explained in **Chapter 3**, which recorded and plotted the data.

The **Figure 4.4** shows a graph indicating the frequency of the droplets of specific sizes. It shows that the droplets are less than 30 µm in diameter and the majority were 25 µm in size.

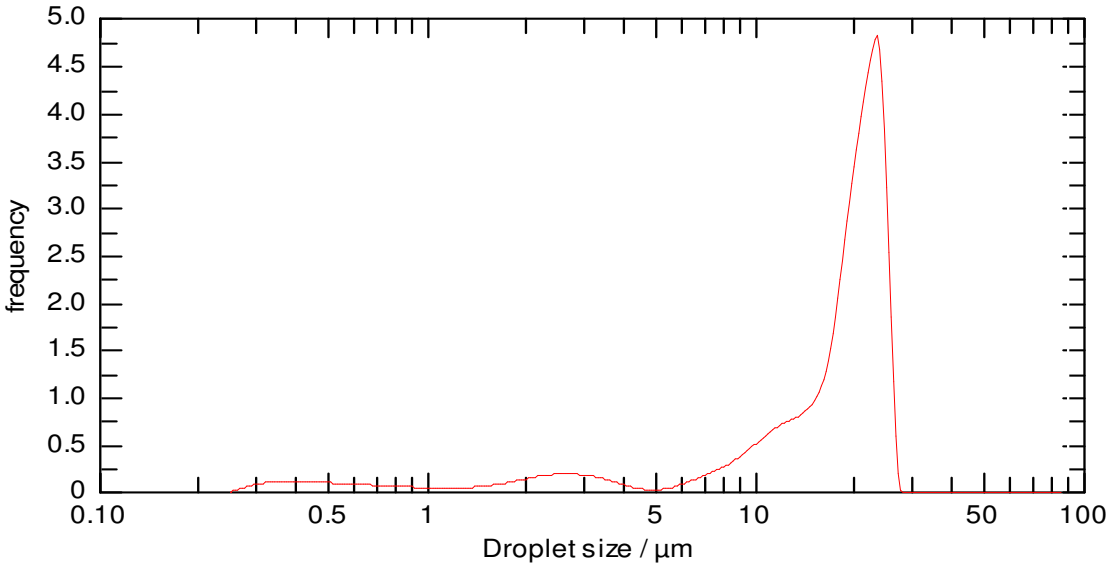

Figure 4.4 Droplet size distribution of the 15vol% ZrO_2 suspension during atomisation at a flow rate of 20 µlmin^{-1} and voltage of 5.1 kV

4.3 Modification of the polymeric template

Initially, the foams were sprayed for 15 and 30 min intervals. There was hardly any penetration of the suspension into the foam. The spraying time was increased to 1hr, 1.5hr, 2hrs and even if there was some penetration of the ceramic suspension into the template, the structures were too weak and were reduced to powder on sintering.

The 60 ppi polymeric templates were then dipped in ethanol and squeezed out, and were immediately followed by electrospraying the zirconia suspension. This simple step of dipping the templates in ethanol produced an instant attraction of the zirconia droplets towards the PU foam and the spraying time was significantly reduced. It was possible to electrospray the PU templates for 1, 3, 5 and 15 min intervals by introducing this step rather than the 2 hrs which was the time taken to produce an observable ceramic coating

on the template without dipping the template in ethanol. Dipping the foams in ethanol prior to spraying, greatly enhanced the efficiency of preparing graded porous structures. This effect could be due to the ethanol improving the attachment of the sprayed ceramic particles by moistening the polymeric surface, in addition to the fact that the ceramic suspension also contains ethanol. The strength of ceramic reticulated foams can be increased by improving the wetting of the polyurethane foam template [Luyten *et al.*, 2005]. Polymeric foams have been pre-treated with ethanol to improve the wettability of the foam [Boccaccini *et al.*, 2003, Mikos *et al.*, 1994]. It has been shown in previous studies that improvements in terms of the degree of infiltration and coating homogeneity have been achieved by pre-treatment of the poly(D-lactic acid) (PDLLA) foam with ethanol as it is believed that ethanol tends to reduce the hydrophobicity of the PDLLA foam [Roether *et al.*, 2002]. Some work has also been carried out on preparing HA foams using the replication method by pre-soaking the polyurethane foam templates in ethanol and an improvement in the ceramic coating has been observed [Robinson *et al.*, 2008].

4.4 Heat treatment

The heat treatment program was set up based on the results of thermogravimetric analysis carried out on the PU foam templates. It was observed that by 400°C, the PU template pyrolyses and does not leave any residue. Therefore, it is fair to assume that the burnout of the template does not have any effect on the final microstructure upon sintering.

The green bodies which were allowed to dry at ambient temperature for at least 12 hrs were heat treated to 400°C, maintained at that temperature for 1hr for the pyrolysis of the template to occur and then sintered to a maximum temperature of 1200°C (**Figure 3.3, Chapter 3**). The sintered samples were maintained at the maximum temperature for 5hrs and then cooled to room temperature. The heating and the cooling rates were 2˚C/min and 5˚C/min respectively.

4.5 Depth of penetration

The green bodies electrosprayed for 1, 3, 5 and 15 min intervals using the 60 ppi templates were sintered to a maximum temperature of 1200°C. The samples were measured for their depth of penetration of suspension using a vernier. For each spray time 5 samples were measured and a mean value was calculated for the depth of penetration and when the spray time was increased, the suspension penetrated deeper into the foam (**Figure 4.5**).

Furthermore, 60 ppi templates were electrosprayed under the same conditions but the maximum sintering temperature was increased to 1400℃. Samples were sprayed for 1, 3, 5 and 7 min intervals as beyond this, there was not much penetration into the foam, since a thick ceramic coating covered the sprayed surface. When the maximum sintering temperature was increased to 1400°C the penetration depth was decreased for the corresponding spraying time than that for 1200°C sintered samples (**Figure 4.6**). This could be due to more shrinkage occurring at higher temperatures. However, the amount of shrinkage seems to be similar when the spraying time is beyond 3 minutes. This could

be due to the thick coating forming on the sprayed surface.

The change in penetration depth was further investigated using different templates having a larger cell range of 1060-1600 μm (45 ppi), which were electrosprayed under the same conditions as that of 60 ppi, and sintered at 1400℃. The 45 ppi templates were also cut into 5mm × 5mm × 10mm samples, then sprayed under the same conditions and sintered at 1400˚C.

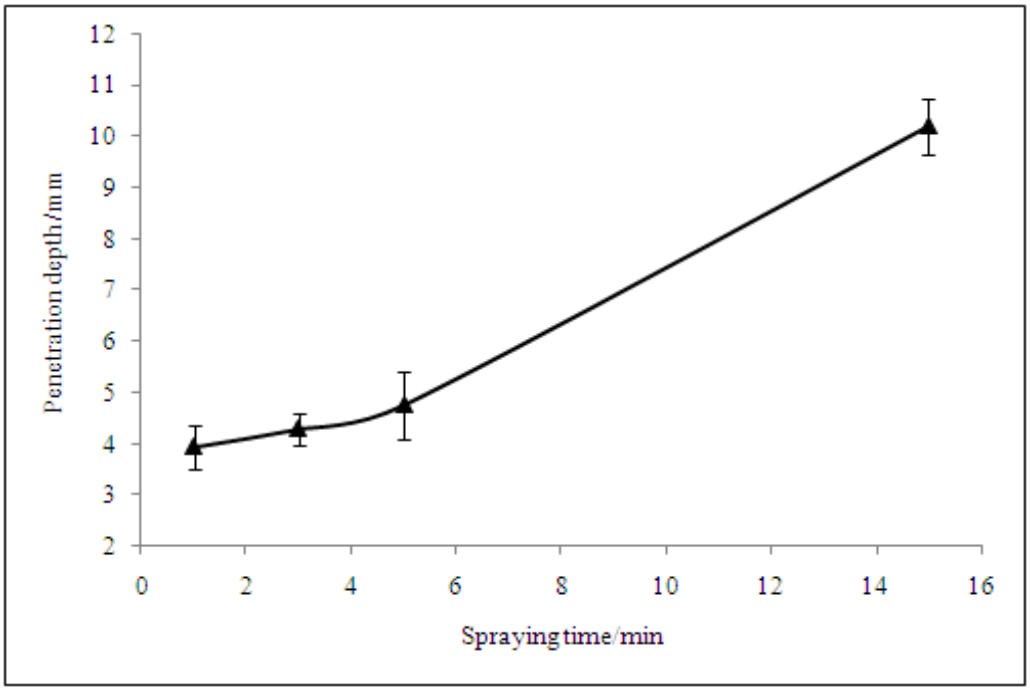

Figure 4.5 The depth of ceramic suspension penetration as a function of spraying time for the structures sintered at 1200°C (60 ppi templates)

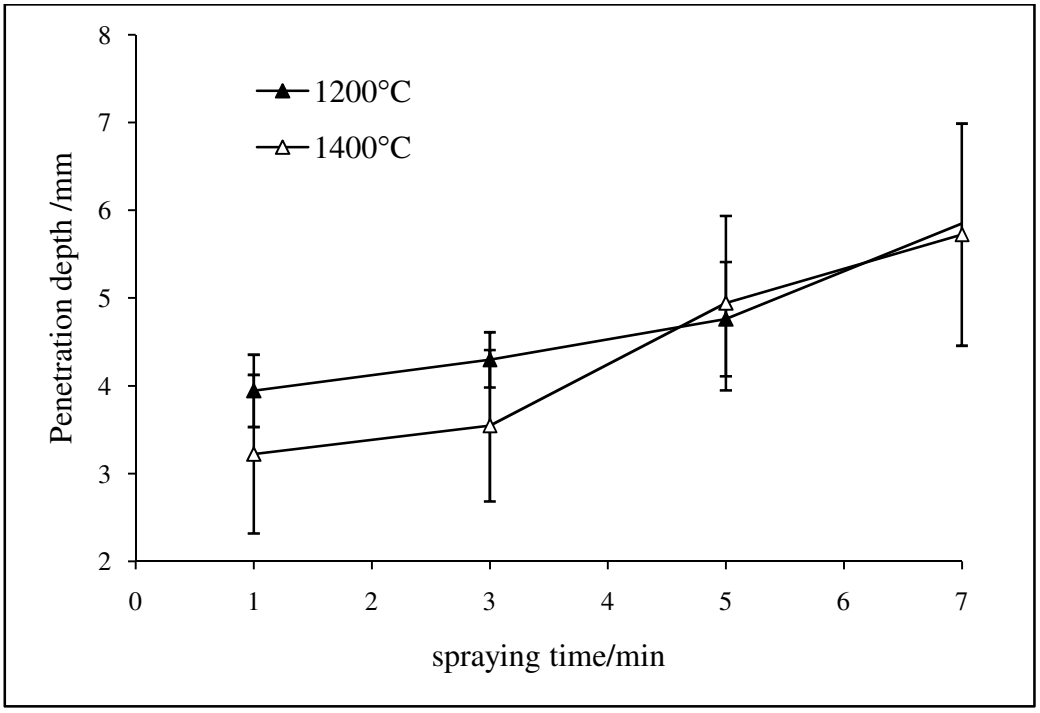

Figure 4.6 Comparison of the penetration depth with varying sintering temperatures (60 ppi templates)

It was observed that the 45 ppi templates had better penetration of the ceramic suspension into the foam than in the case of 60 ppi templates as shown in **Figure 4.7a**. This is expected because with larger pore size, the fine droplets produced in electrospraying can reach further into the template. When the height of the template was increased, there was a slight increase in the depth of penetration of the ceramic suspension (**Figure 4.7b**). This is logical, since with increased height of the template, the particles can penetrate deeper into the foam. However, it can be seen that the depth of penetration was not doubled by increasing the template height by a factor of 2. This could be due to the thick coating forming on the sprayed surface.

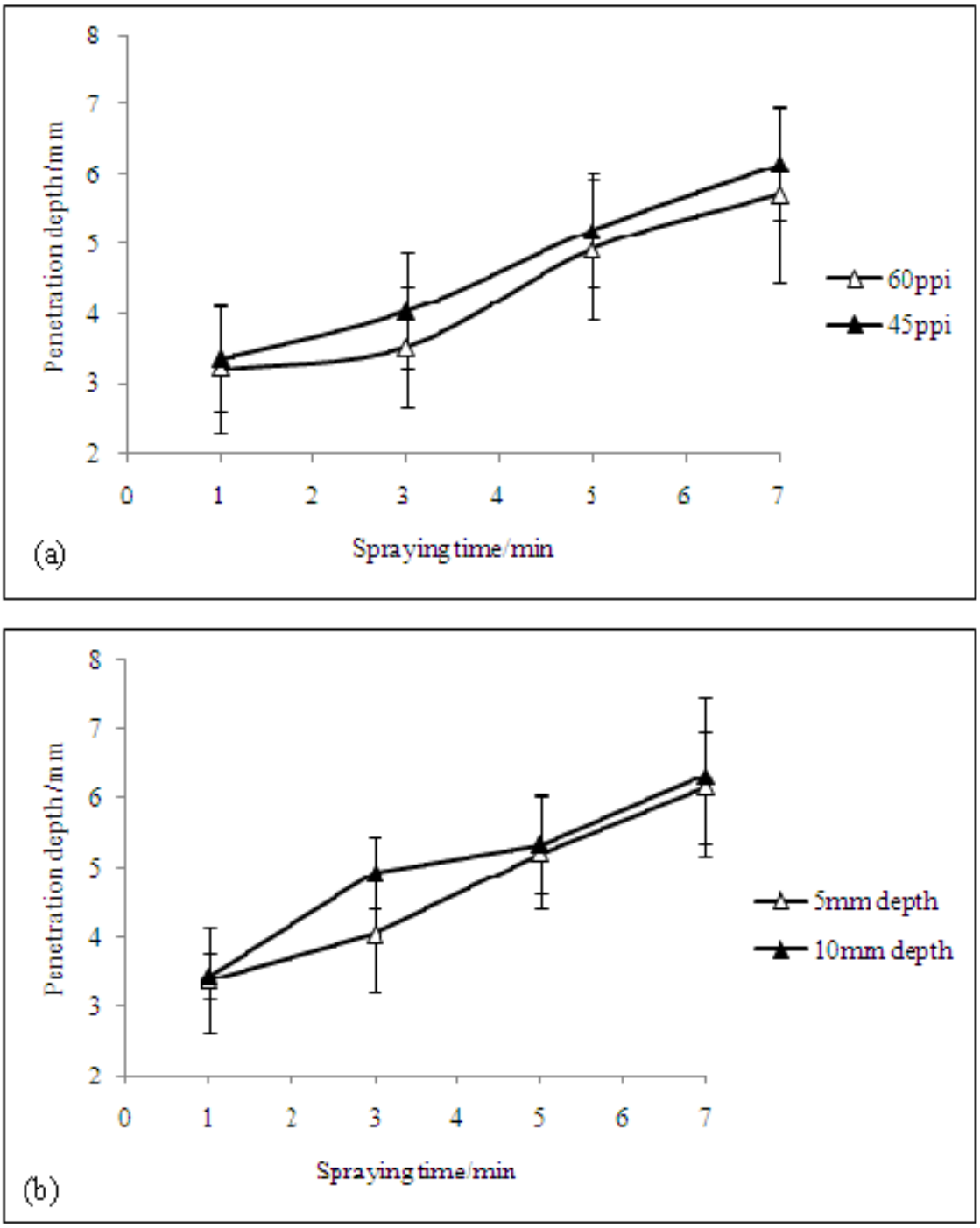

Figure 4.7 Comparisons of penetration depth obtained by (a) using different sacrificial templates and (b) varying the height of the sacrificial template (45 ppi templates)

4.6 Microstructural analysis

The green bodies were initially sintered to a maximum temperature of 1200°C. The samples' outer and inner-most surfaces were observed using the SEM to investigate the variation in pore size. The inner-most surface refers to the surface opposite to the sprayed surface (i.e. the surface furthest away from the sprayed surface). In the case where the template is rotated, the inner surface is the centre of the template which receives the least amount of direct coating. Therefore, in general, the inner-most surface refers to the surface that receives the least direct deposition of the ceramic droplets. The foam structures were not strong enough to be fractured in order to observe the internal cross-section in the hope of investigating any variation in pore size. When the sintering temperature was increased to 1400°C, foams prepared were stronger and it was possible to fracture the sintered structures length-wise to observe their cross-sections. It actually proved to be difficult to fracture them at increased spray time due the thick coating becoming too hard during sintering.

4.6.1 Shape of the sintered structures

The sprayed surface had a thick layer of ceramic suspension (**Figure 4.8a**) and the pores were scattered. It was interesting to note an inverted pyramidal structure (a pyramidal crater from the surface downwards) was formed under all sintering conditions and an example is shown in **Figure 4.8b**. It was expected that pores would get gradually larger in size when deeper into the template as the amount of zirconia particles reaching such locations would be less than that on top of the template, hence resulting in thinner struts and larger pores. However, it was observed that the pores on the inner-most surface

were again smaller and the struts were relatively thinner than observed throughout the sintered structure.

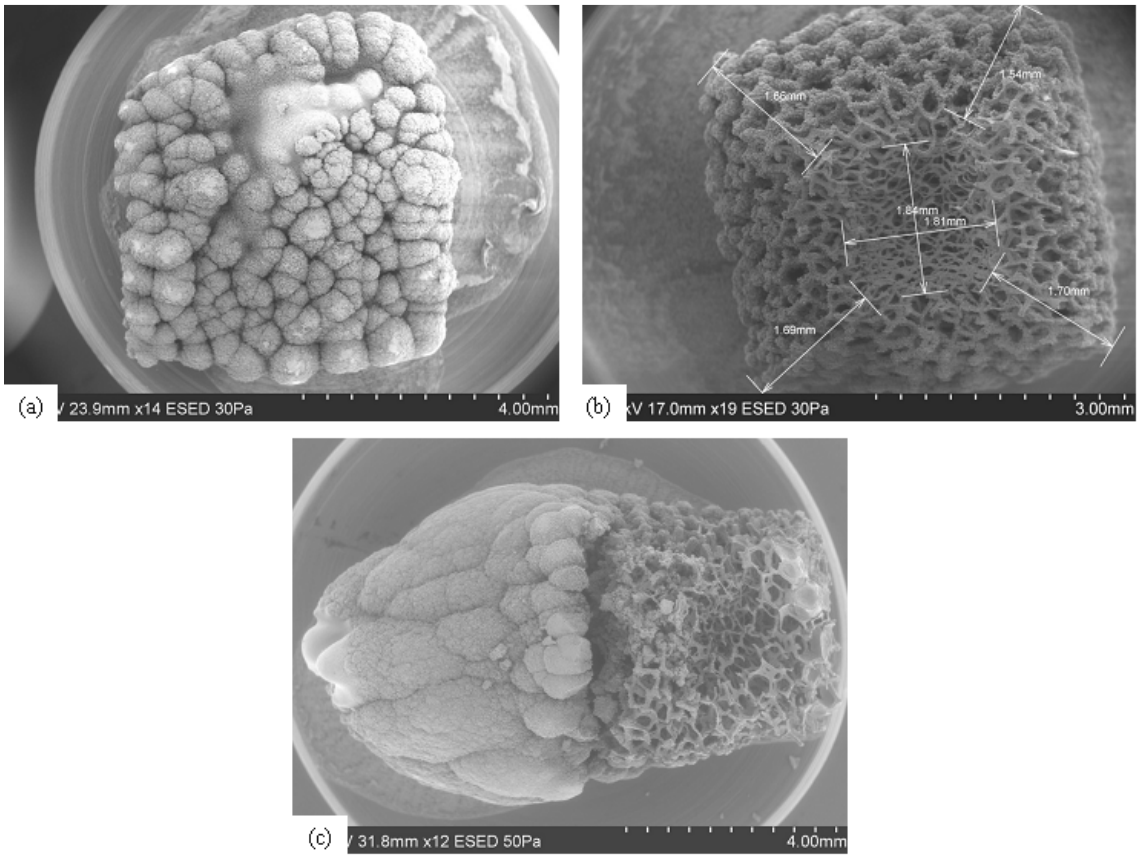

Figure 4.8 Microstructural features. (a) The electrosprayed surface (the 60 ppi template was electrosprayed for 7 min and sintered at a maximum temperature of 1400℃). (b) An example of inverted pyramid shape observed, gradually narrowing towards the innermost surface (the 60 ppi template was electrosprayed for 3 min and sintered at a maximum temperature of 1400℃). (c) The thick ceramic coating forms a pyramidal shape on top of the foam with increased spraying time (60 ppi template). ESED, environmental secondary electron detector.

The inverted pyramidal shape (**Figure 4.8b**) could be due to the particle attraction towards the grounded pin electrode. The amount of ceramic particles penetrating deep into the polymeric template is less in comparison to that on the sprayed surface. It is possible that the particles deep within the template get deposited close to the pin electrode. Therefore, due to both the lack of ceramic particles and the attraction towards the pin electrode, in relation to the rest of the foam (especially the sprayed surface), it can be estimated that the inner-most layer undergoes most shrinkage. This can be a possible explanation of the smaller pores observed on the innermost layer and the pyramidal shape of the sintered structure. Another factor governing the penetration into the template would be that the thick ceramic coating on the sprayed surface prevents the ceramic droplets reaching into the template. This would obviously result in a reduced amount of zirconia particles reaching into the foam resulting in the much smaller pores on the innermost surfaces.

It was also noted that with increased spraying time, the ceramic coating on the sprayed surface became thicker and began to form a pyramid shape structure on top of the foam (**Figure 4.8c**). In the cone-jet mode in electrospraying, the larger droplets are in the centre of the spray and gradually decrease in size with distance from the centre [Grigoriev and Edirisinghe, 2002]. The electrical interaction between highly charged droplets causes a size segregation effect [Hartman *et al.*, 1996]. This results in the smaller droplets to be found at the edge of the spray and the large droplets to be found near the spray centre. The bigger droplets in the centre of the foam block the template pores faster than the much finer droplets that deposit on the sides of the foam. With

continued spraying, since the pores are blocked in the centre of the template, the ceramic droplets start agglomerating on the surface of the template. With the relatively larger droplets still being deposited in the centre of the foam, at a given time, the thickness of the coating at the centre of the foam will be greater than on the sides. This will eventually take the shape of a pyramid.

4.6.2 Analysis of the pores

Images of all the sintered samples were studied at three locations – on the sprayed surface, the inner-most surface and the cross-section. The mean pore size was calculated from approximately 100 measurements for each category. The average pore sizes with their maximum and minimum values have been tabulated in **Table 4.4** for the sprayed surface and in **Table 4.5** for the inner-most surface of the sintered structures.

Table 4.4 The pore size values for the sprayed surface (template used is indicated within brackets) (S.D. = Standard Deviation)

1200°C (60 ppi)				
Spray time/min	**Average pore size/µm**	**S. D.**	**Min pore size/µm**	**Max pore size/µm**
1	300	90	156	481
3	16	8	9	42
5	9	4	4	16
15	3	1	2	5
1400°C (60 ppi)				
1	226	66	144	451
3	260	101	71	425
5	213	61	132	277
7	66	83	2	240
1400°C (45 ppi)				
1	320	102	115	565
3	320	70	176	438
5	10	26	2	108
7	3	0.5	2	4

Table 4.5 The pore size values for the inner-most surface (template used is indicated within brackets) (S.D. = Standard Deviation)

1200°C (60 ppi)				
Spray time/min	**Average pore size/µm**	**S. D.**	**Min pore size/µm**	**Max pore size/µm**
1	222	50	128	346
3	217	66	86	361
5	192	85	57	352
15	277	78	186	530
1400°C (60 ppi)				
1	115	48	42	239
3	200	60	104	330
5	168	70	55	354
7	228	46	138	314
1400°C (45 ppi)				
1	264	84	90	483
3	218	75	92	408
5	250	97	120	572
7	309	103	166	563

The electrosprayed surface shows a thick coating which increased in thickness as a function of spray time. At higher magnification, micropores in the range of 2-10 µm were observed to be scattered throughout the surface of the structure (**Figure 4.9a**). It was also observed that the inner-most surface had an interconnected pore network with pores >100 µm in size (**Figure 4.9b**). The length-wise cross-sections of the sintered structures exhibited the presence of pore interconnectivity throughout its structure (**Figure 4.9c**) and the variation of the pore structure was clearly observed. The interconnected pores towards the centre of the foam were approximately 300 µm in size.

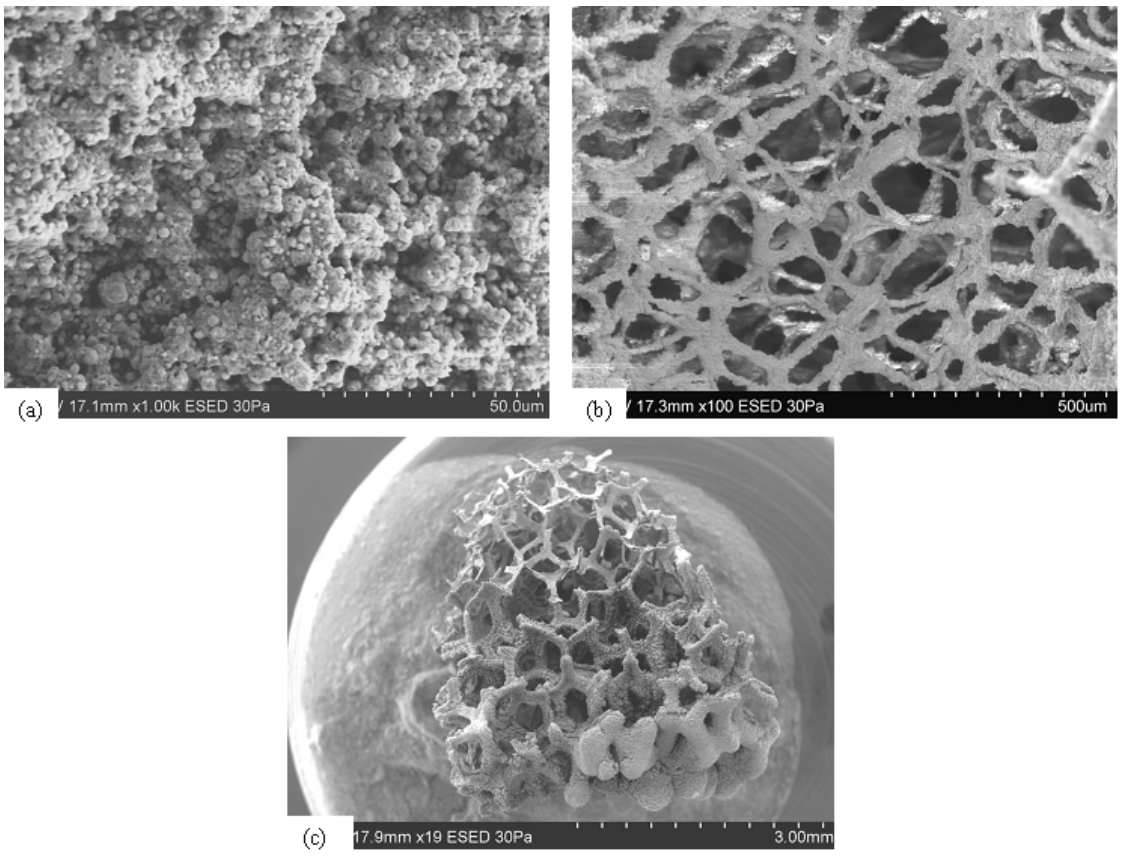

Figure 4.9 Microstructural features. (a) Micropores smaller than 10 µm observed on the electrosprayed surface (45 ppi template, electrosprayed for 5 min and sintered at 1400℃). (b) Interconnected pore network on the innermost surface with pores greater

than 100 µm (60 ppi template, electrosprayed for 3 min and sintered at 1400℃). (c) Lengthwise cross section showing the variation of pores from the sprayed to the inner surface. Interconnected porosity is present throughout the structure (45 ppi template, electrosprayed for 3 min and sintered at 1400℃)

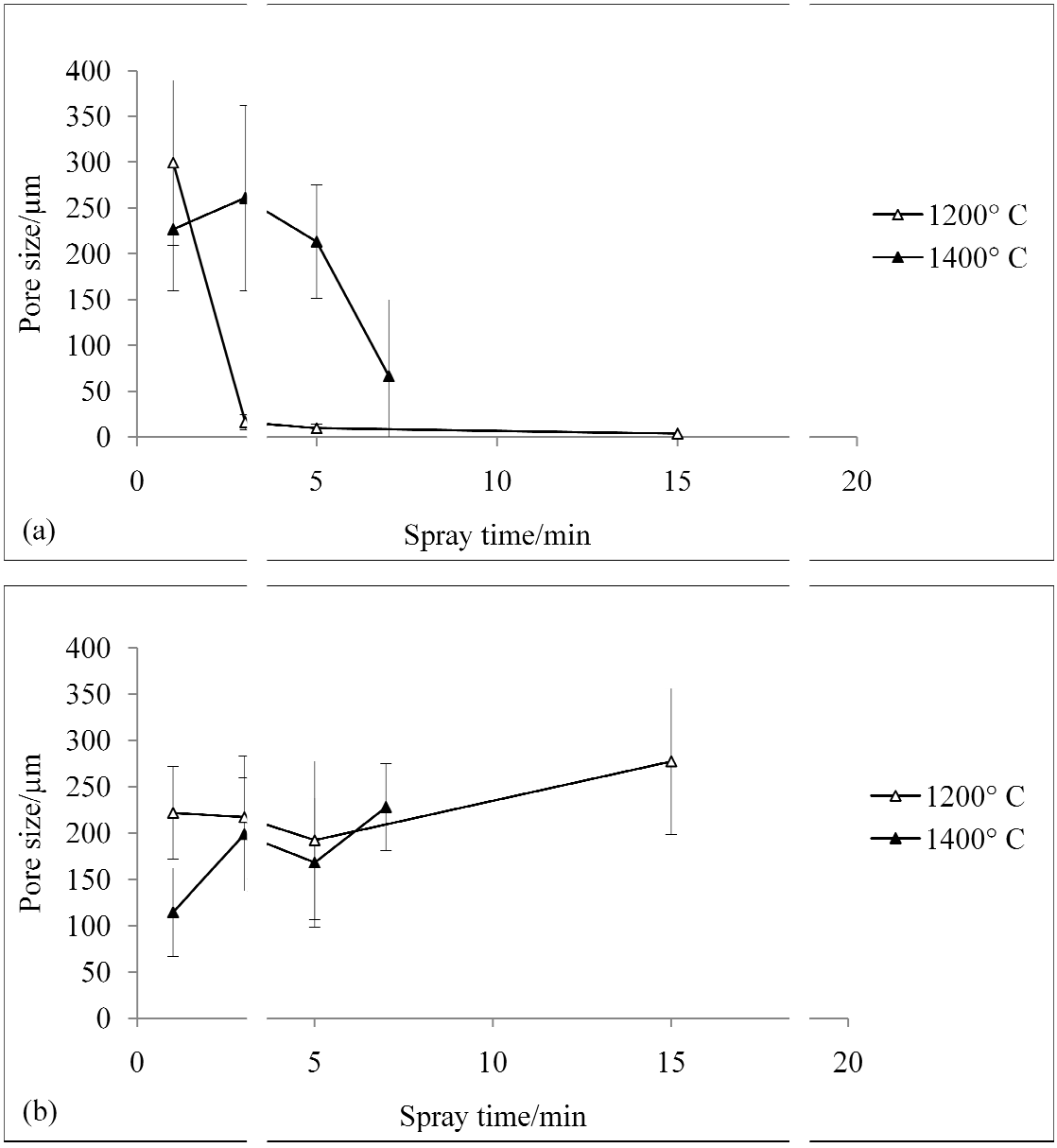

Figure 4.10 Variation of pore sizes observed on the (a) sprayed surface and the (b) inner-most surface as a function of sintering temperature (60 ppi templates)

Figure 4.10 shows the change in average pore size on the sprayed and inner-most surfaces as a function of spray time at different sintering temperatures. It can be seen that in general, on the sprayed surface the pores seem to be larger on the structures that were sintered at a higher temperature (**Figure 4.10a**). This result seemed uncharacteristic, as it was expected that with increased sintering, due to higher shrinkage, smaller pores would result. However, it is also important to note that this graph indicates only the mean value, as the pores on the sprayed surface have a very large distribution of very small pores and much larger but scattered pores. This can be seen in **Table 4.4** where the minimum and maximum of the pore measurements are tabulated. On the inner surface, the structures sintered at the higher sintering temperature show a smaller pore size in comparison to the structures sintered at 1200°C (**Figure 4.10b**). This can possibly be related to a higher shrinkage at the higher sintering temperature. This can be further confirmed by the minimum and maximum pore sizes in **Table 4.5**.

Figure 4.11a shows the change in pore size on the sprayed surface due to changing the template. At 1 and 3 min spray times, the structures prepared using 45 ppi had larger pore sizes. This is expected as the template used has much larger pores than in 60 ppi. However with increased spray time, the mean pore size on the sprayed surface of the 45ppi structures seems to have significantly reduced in comparison to that of 60 ppi. **Figure 4.11b** shows a more consistent set of data on the inner-most surfaces of the sintered structures using templates having a larger cell range (45 ppi). As expected, the

structures prepared using 45 ppi shows a larger mean pore size than the ones prepared by using 60 ppi templates, owing to the larger cell-range of the former template.

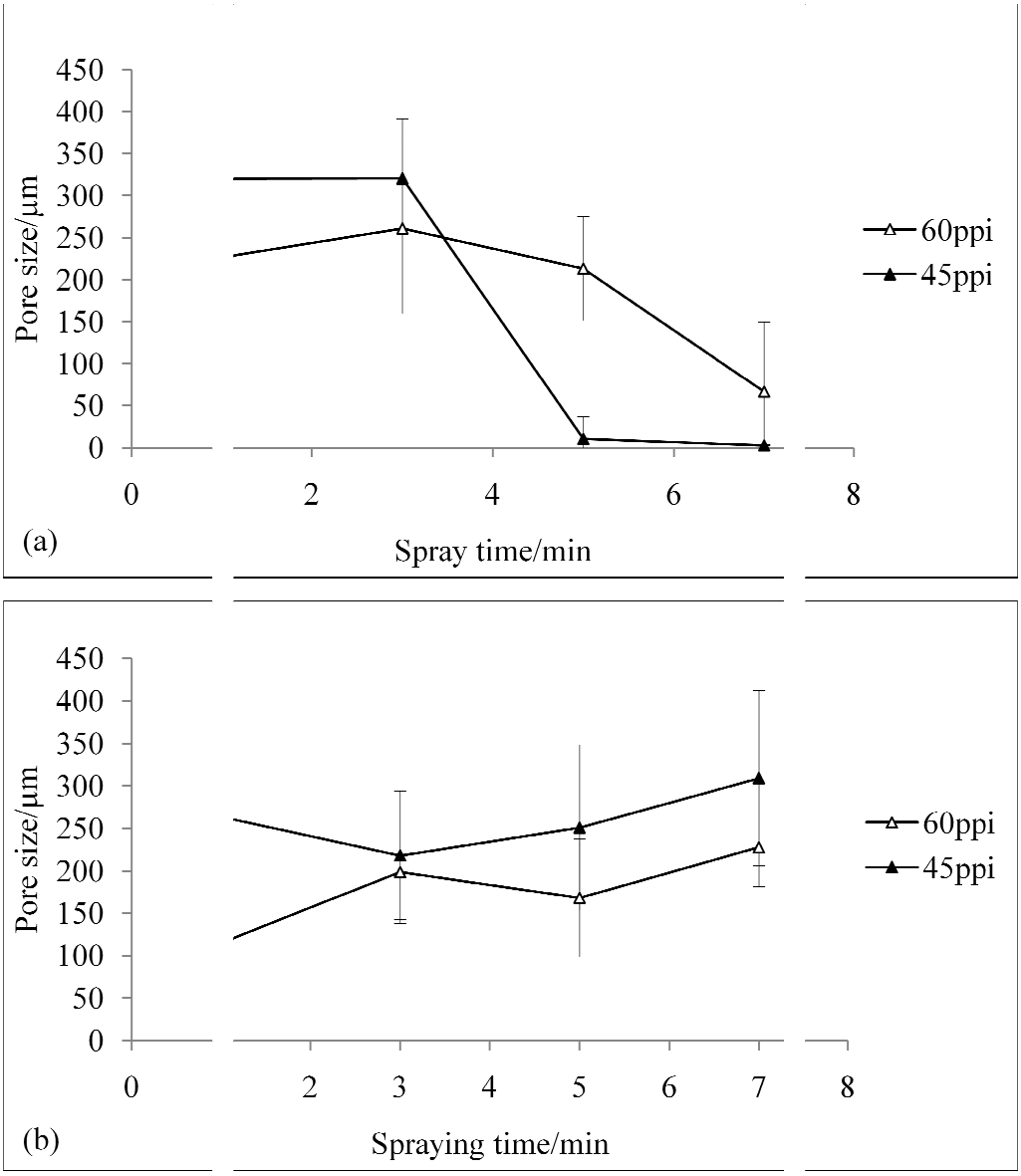

Figure 4.11 Variation of pore sizes observed as a function of spray time on the (a) sprayed and (b) inner-most surfaces using different templates (60 and 45 ppi)

4.7 Bone-like structure from zirconia

Bone is the perfect example where graded porosity occurs in nature. Lu *et al*. (2003b) have carried out scanning electron microscopy of natural bone to reveal three categories of pores. The first type is the macropores in the inner region of bone, with a large size distribution, the largest pore size of ~450 μm. The pores have been found to be interconnected, allowing the tissue to infiltrate, enabling body fluid and blood circulation, and allowing the supply of nutrients. The second type contained within the wall of the macropores are of ~0.5 μm in diameter and the third, the pores on the cortical bone ~10 μm in diameter. They further state that from a biomimetic viewpoint, such bone characteristics should be considered in the preparation of a bone substitute [Lu *et al.*, 2003b].

Taking the remarks of Lu *et al.* (2003b) into consideration, the possibility of producing structures representing bone were investigated using the EHD method and a mechanical rotating arm. This could find uses in applications such as bone grafts. For bone structure replication experiments, the polymeric template was fixed onto a mechanical rotating device that was also the ground electrode. The 45 ppi templates of dimensions 5mm × 5mm × 10mm were electrosprayed for 15 minutes under the same conditions (*i.e.* flow rate of 20 $\mu l min^{-1}$ and voltage of 5.1 kV) and were sintered to a maximum temperature of 1400°C.

4.7.1 Analysis of the structure

4.7.1.1 SEM analysis of the electrosprayed surface

SEM was carried out on the electrosprayed surface of the sintered zirconia ceramic structures to observe the structure (**Figure 4.12**). The sprayed surface looks dense and less porous and the pores were of size 130-280 µm which were scattered. There did not seem to be any interconnectivity between the pores (**Figure 4.12a**). The ceramic coating shows a rough surface and much smaller pores of size <20 µm distributed throughout the outer coating of the structure (**Figure 4.12c**). This can enhance the nutrient diffusion by enabling the passage of oxygen molecules and other nutrient molecules. Surface roughness is known to enhance attachment, proliferation and differentiation of anchorage-dependent bone forming cells [Yuan *et al.*, 1999]. Microporosity (pore size <10 µm) of scaffolds are considered to be beneficial due to the large surface area and in the case of HA, known to contribute to higher bone-inducing protein adsorption and bone-like apatite formation by dissolution and re-precipitation [Karageorgiou and Kaplan, 2005]. **Figure 4.12d** shows the individual droplets of the zirconia suspension (<10 µm in diameter being the smallest and the ~20 µm being the larger particles which could either be the larger droplets or one or more droplets coalescing).

4.7.1.2 SEM analysis of the cross-section

Due to the inconsistent ceramic coating of the scaffolds, it was not possible to fracture them using a stainless steel surgical blade to observe the cross-section in the middle. So it was decided to embed a sintered scaffold in epoxy resin to image the cross-section of the structure. The embedded sample was ground and polished to view the cross-sections

(**Figure 4.13a**). On observing the images it was deduced that this was not the best method of observing the cross section of the sample, but it does exhibit a more porous and interconnected interior (**Figure 4.13b**) and a thicker outer coating (**Figure 4.13c**) due to the increased number of zirconia particles being deposited on the sprayed surface.

Due to the three-dimensional pore arrangement of the templates (dodecahedral shape), embedding the sintered zirconia scaffold in resin did not show convincing images of the suspension penetration into the template. The graded characteristic of the structure was not clear. Since the outer coating was too strong to be fractured using a conventional surgical blade, the sintered structure was fractured using a diamond cutting wheel (RS Components, UK) to observe its internal cross-section (**Figure 4.14a**). It shows the cross section with a thick outer layer and a porous and interconnected internal structure (**Figure 4.14b**). The outer coating was about 600 – 800 µm in thickness (**Figure 4.14c**). The pore diameter was approximately 150 µm towards the edge of the structure and the pores were observed to gradually increase in size up to approximately 500 µm towards the centre. The interconnected pore network enables efficient nutrient and waste diffusion thus making electrospraying an efficient method of producing scaffolds with bone-like structure.

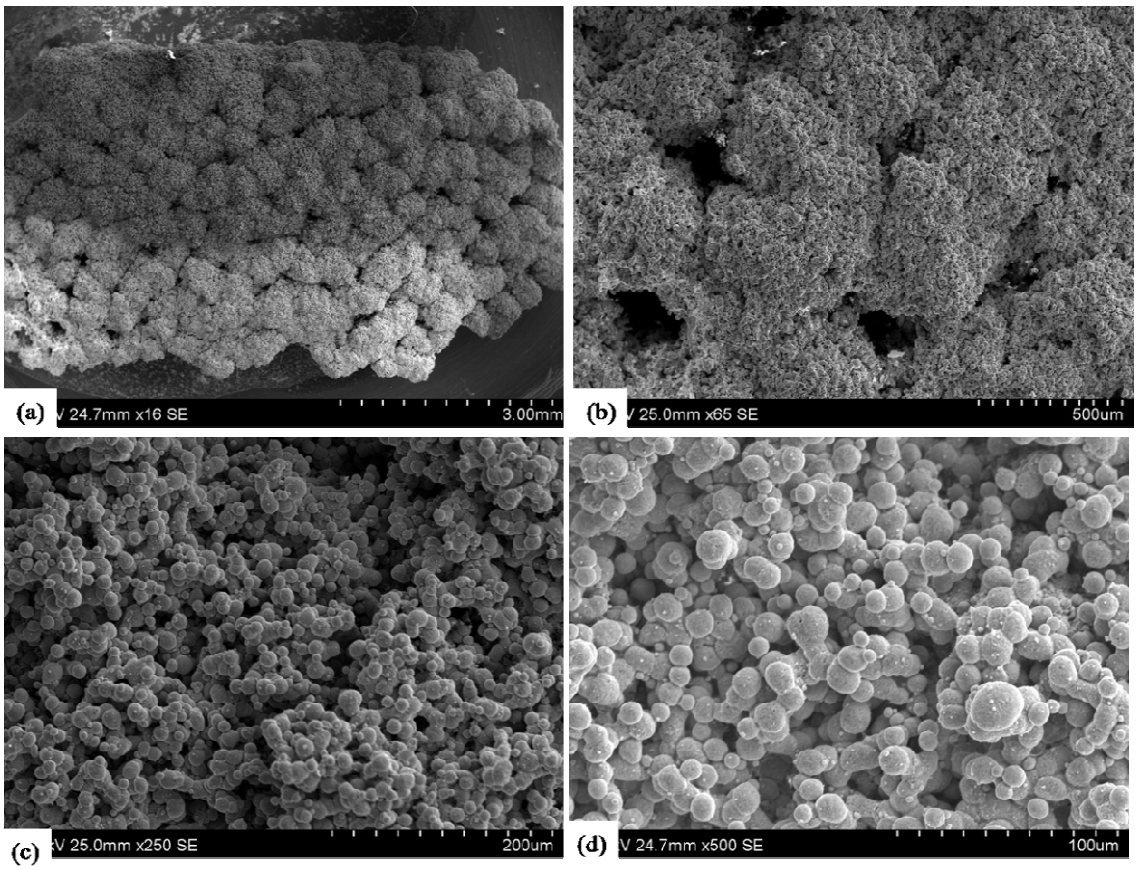

Figure 4.12 SEM images of the electrosprayed surface of the zirconia scaffold: (a) the overall surface, (b) the scattered pores at a higher resolution, (c) the ceramic coating indicating a rough surface and (d) the individual droplets of the zirconia suspension

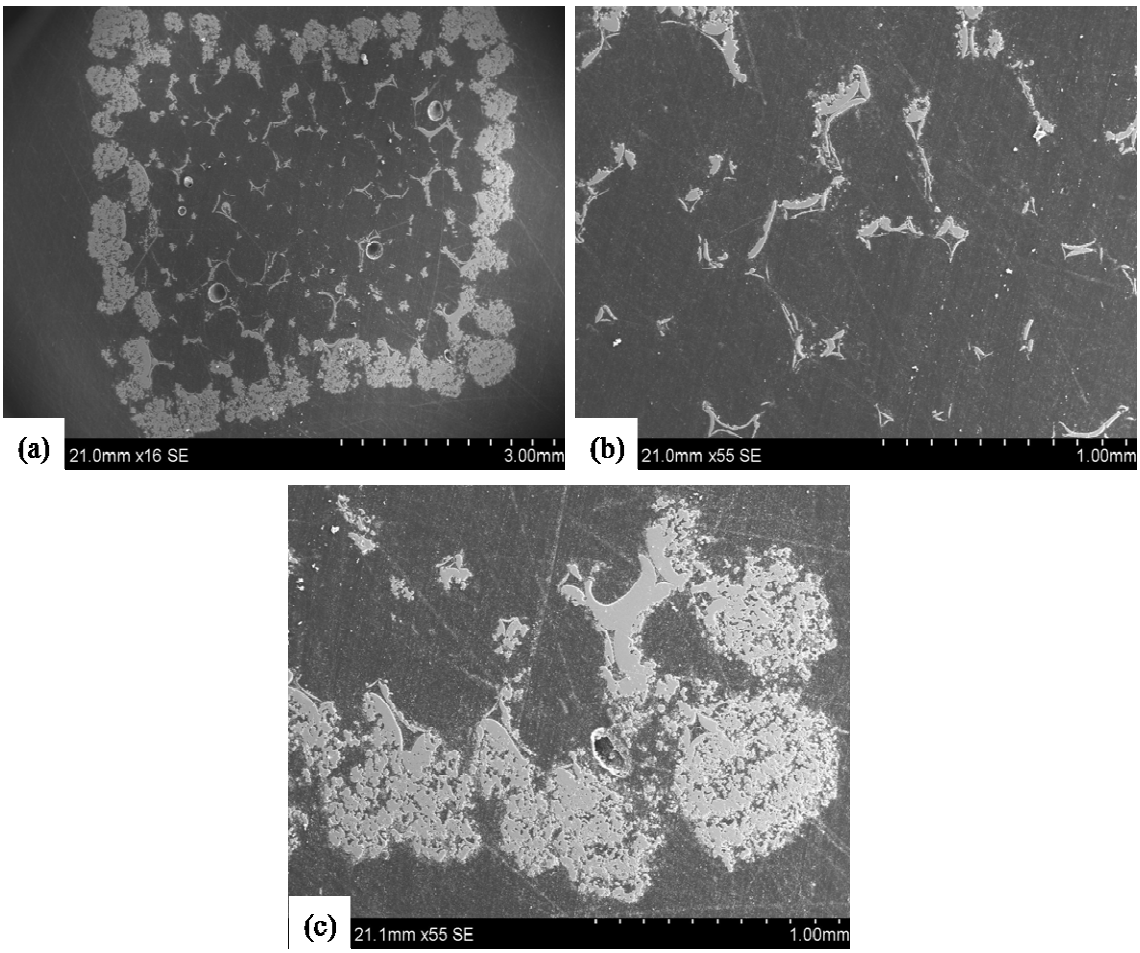

Figure 4.13 SEM images of a sintered zirconia structure which was set in resin in order to observe the cross-section: (a) The overall cross-section (b) The inner pore structure showing the interconnected pores (c) The outer coating which is denser at higher magnifications

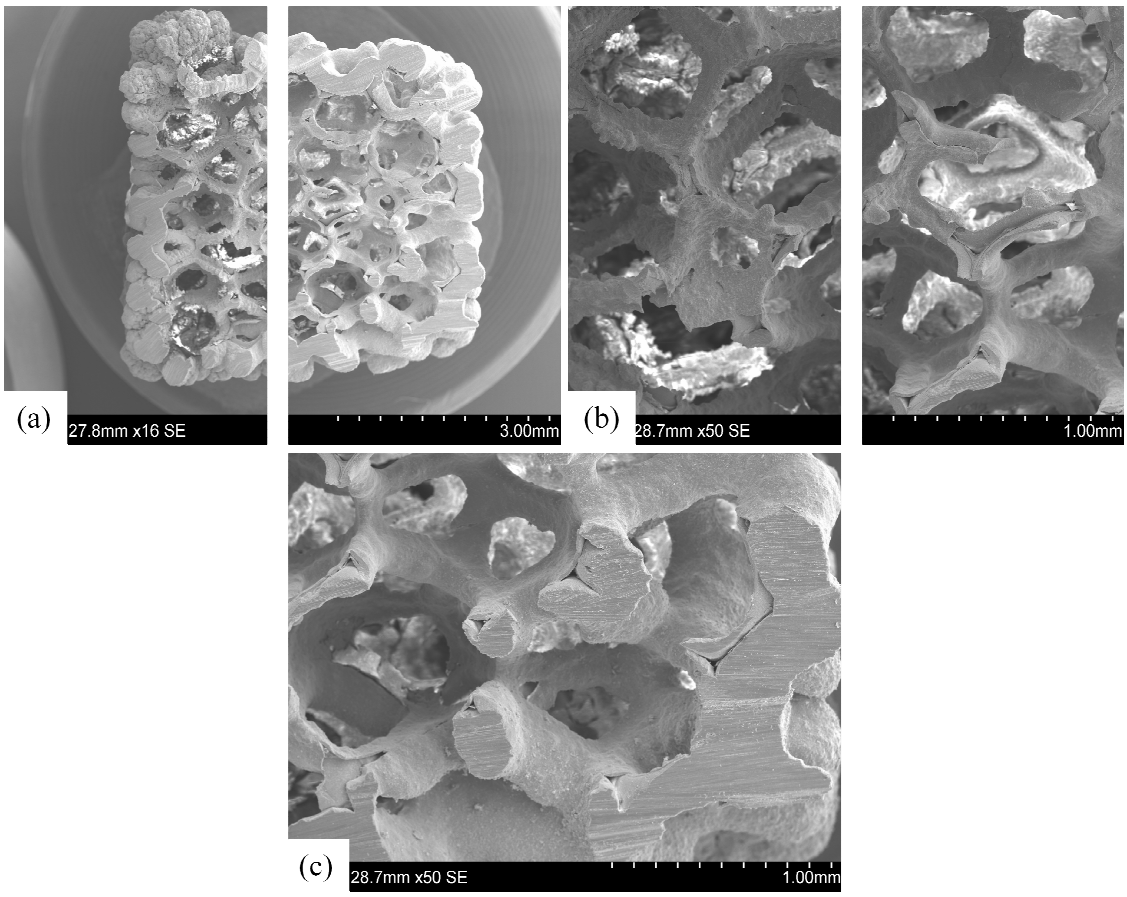

Figure 4.14 Bone-like structure replication showing: (a) the overall structure, (b) a porous and interconnected internal structure, and (c) high magnification image showing the thick outer coating

Chapter 5

Electrohydrodynamic preparation of hydroxyapatite scaffolds

Porous scaffolds are considered a key strategy in the concept of bone tissue engineering (TE). Hydroxyapatite (HA), still maintains its status as the most widely used bioceramic and has been extensively studied as a scaffold material for bone TE due to its bioactive and osteoconductive properties. Fabrication methods used for producing porous ceramics for industrial purposes have been applied to produce porous HA foam structures, from which the slurry-dipping or replication method still remains the most popular and the simplest as reviewed in the literature (**Chapter 2**). Due to the inherent brittleness of the HA and the disadvantages of the dipping method, the mechanical properties of the porous foams are very poor. There is much interest in inventing new fabrication methods and/or using combinations of one or more of the currently adopted methods, in the hope of increasing the mechanical reliability of the porous HA foams in order for them to be considered for load-bearing applications as discussed in the literature review.

It has been demonstrated in the literature, how it has been possible to create porous foam structures using the electrohydrodynamic (EHD) atomisation method. Not only is it claimed to be possible to produce void-free struts in alumina [Jayasinghe and Edirisinghe, 2002b], but also improved mechanical properties in comparison to the dipping method in zirconia foams [Chen *et al.*, 2006a] can be achieved. It is also important to note that these findings were on (more) concentrated suspensions (>60 wt%).

This research chapter investigates the feasibility of using electrospraying to produce porous HA foams. A nano-HA suspension which is water based of approximately 18wt% particle concentration (University of Cambridge) has been used which has been modified for electrospraying. The parameters for the electrospraying set-up have been optimised and in this research study, foams have been prepared using replication (dipping), electrospraying and a combination of both dipping and spraying, in an attempt to produce scaffolds with improved mechanical properties. The spraying times have also been varied. The combined method has been used as an attempt of overcoming the poor mechanical properties of the replication method and to enhance the pore interconnections. A comparison has been made in relation to the surface characteristics such as pore size and distribution, porosity and mechanical properties in order to select the most suitable foam fabricating technique that can be used to produce scaffolds for bone tissue engineering applications.

5.1 EHDA of nHA suspension

5.1.1 Nano-HA particle loading of the suspension

Initially, the original 18 wt% water-based nHA suspension was mixed with ethanol to produce a ~12 wt% nHA suspension suitable for electrospraying. It was the aim to produce an ethanol-based nHA suspension which had the highest possible particle loading to obtain a higher efficiency (*i. e.* reduced spraying time) of the ceramic coating. It was observed that it was not possible to electrospray this suspension since the jet at the needle-exit was unstable and the needle kept getting blocked. The suspension was diluted further and nHA particle loadings of 11 wt% and 9 wt% were experimented with. However, these suspensions too were unsuitable for electrospraying due to an unstable jet and nHA suspension of concentration of approximately 6 wt% was observed to be the maximum nHA particle loading for which a stable cone-jet mode could be obtained. This suspension concentration also minimised blockages in the needle when electrosprayed for extended periods of time.

5.1.2 Nano–HA suspension characterisation

Key suspension properties of the 6wt% nHA suspension such as density, surface tension, viscosity and DC electrical conductivity were measured using the equipment mentioned in **Chapter 3**. The results are shown in **Table 5.1** along with the properties obtained for ethanol.

5.1.3 Mode selection map

The flow rate of the 6 wt% nHA suspension was varied systematically and the applied voltage was varied from 0 to 7 kV. Various modes of atomisation were observed at a particular flow rate, with increasing voltage. At 0 kV, the suspension at the needle exit was in dripping mode, which changed into a micro-dripping mode with increased voltage. This mode changed into spindle, unstable cone-jet, stable cone-jet and then multi-jetting with further increase in the voltage. These modes of jetting with respect to the flow rate and the electric field were plotted (**Figure 5.1**) and the graph was then utilised to select suitable conditions for electrospraying of the nHA suspension to coat the PU templates.

Table 5.1 Properties of the nHA suspension

Property	**Ethanol**	**nHA 6wt% ethanol-based suspension**
Density /kgm^{-3}	790	945
Surface tension /mNm^{-1}	22	28
Viscosity /mPas	1.3	6.8
Electrical conductivity /Sm^{-1}	3×10^{-4}	1.1×10^{-3}

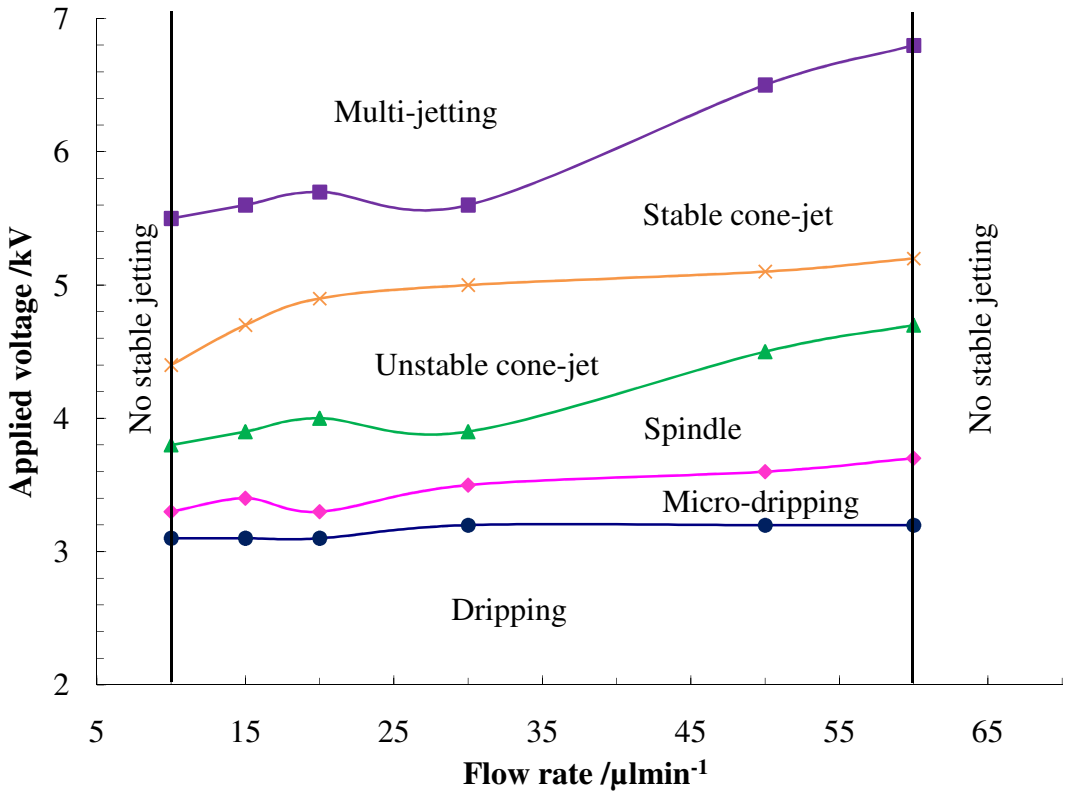

Figure 5.1 Different modes of atomisation observed with varying flow rate and the applied voltage when the 6 wt% nHA suspension was subjected to electrohydrodynamic atomisation

5.1.4 Optimisation of experimental parameters

5.1.4.1 Working distance

The distance between the exit of the needle and the foam surface was optimised experimentally to 10 mm, in order to obtain maximum coverage of the nHA coating. When the working distance (WD) was increased beyond 10 mm, the time required for spraying the polymeric template was increased. This could be due to the increased divergence of the spray with distance, causing a greater scatter of the droplets. When the

WD was less than 10 mm, the jet became unstable and this may be due to the rotating arm causing a change in the electric field, which in turn destabilised the liquid jet.

5.1.4.2 Mechanical rotating arm

It was important to continuously rotate the foam during the electrospraying procedure to ensure uniform coating of the ceramic suspension on the template. A simple mechanical rotating arm was assembled in order to ensure rotation of the foam at a constant speed. The rotating arm was operated by a multi-ratio motor gear box. The rotating speed was changed by altering the gear-sets. The minimum speed which was considered was 2 rotations/min (rpm) which was too slow and the maximum speed was set to 115 rpm which seemed too fast. It was not possible to obtain a uniform coating of the ceramic suspension using either of the above speeds and it was set to 29 rpm which resulted in satisfactory coverage of the polymeric template by the nHA suspension.

5.1.4.3 Choice of ground electrode

It was mentioned in the literature review how the geometry of the ground electrode is known to determine the trajectory of the charged droplets. While a ring-shaped ground electrode produces a conical spray that spreads out the droplets [Gañán-Calvo *et al.*, 1997], a point-like ground electrode is used to focus the majority of the droplets to a fixed area [Jayasinghe and Edirisinghe, 2004]. Since the surface area that required the nHA coating was relatively large, a spray of droplets with wider coverage was required. A stainless steel ring of diameter 25 mm was used as the ground electrode and was held approximately 10 mm below the needle exit with the polymeric template immediately

below the ring. It was observed that all the HA droplets were attracted towards the ring and there was hardly any coating on the template surface. This could be due to the charged HA droplets being attracted towards the ring which is conductive, in preference to the polymeric template which is insulative.

Therefore, the ring electrode was removed and the rotating arm to which the template was attached, was used as the ground electrode. This significantly attracted the HA droplets towards the polymeric template. A schematic of the final equipment set-up for the electrospraying of the polymeric templates is shown in **Figure 5.2**.

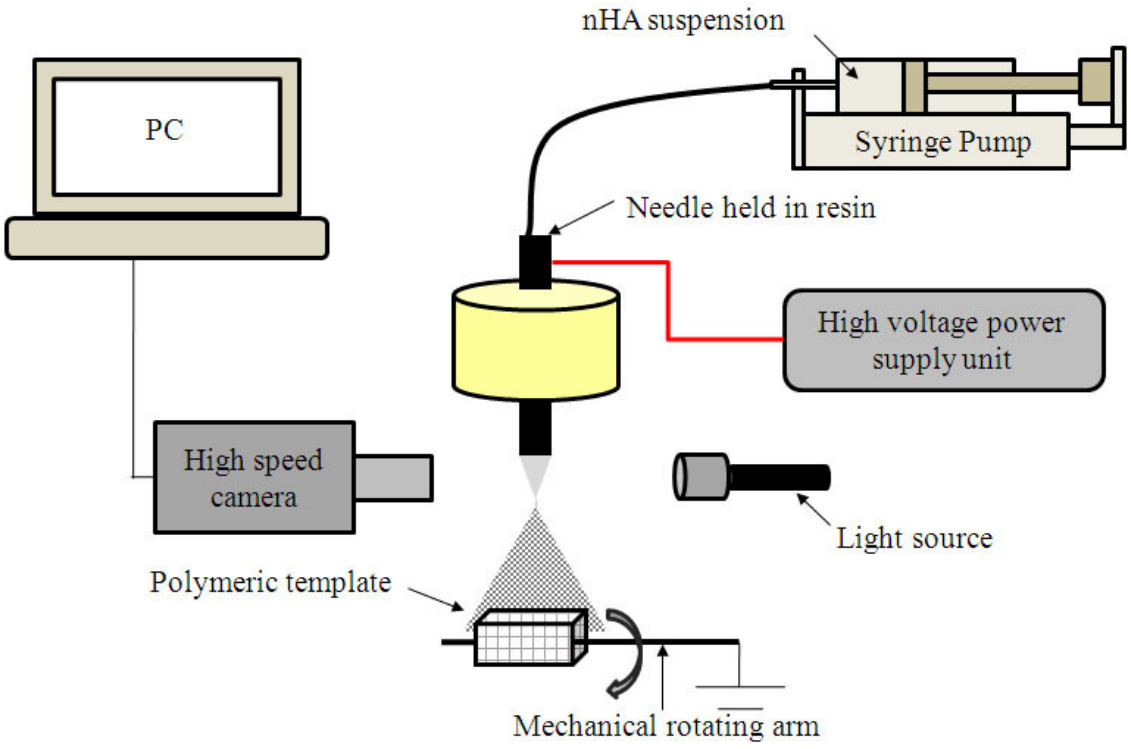

Figure 5.2 Equipment set-up for processing HA scaffolds using electrospraying method

5.1.4.4 Flow rate

The flow rate is an important parameter and can significantly influence the production of droplets. There usually exists a minimum and maximum flow rate for a given suspension to obtain a stable cone-jet and these are usually imposed experimentally. As discussed in the literature, within this stable flow rate range, relatively higher flow rates produce relatively larger droplets [Gañán-Calvo *et al.*, 1997] that tend to be polydisperse, but with a higher production frequency [Higuera, 2003]. Relatively lower flow rates within the stable cone-jet range are known to produce finer and near-monodisperse droplets and are usually utilised for nano-particle fabrication and mass spectroscopy [Grace and Marijnissen, 1994]. For this study, the flow rate of the 6 wt% nHA suspension was optimised to 10 $\mu l min^{-1}$, which was the minimum value with the ability of producing a stable cone-jet mode within a reasonable range of the applied voltage of 4.4 to 5.5 kV (**Figure 5.1**). The cone-jet mode (**Figure 5.3a**) established at this flow rate and voltage produced sufficiently fine droplets of diameter <15 μm which were observed by optical microscopy (**Figure 5.3b**) and further verified by the measurement of the droplet size distribution using the Sympatec laser diffraction system (**Figure 5.4**).

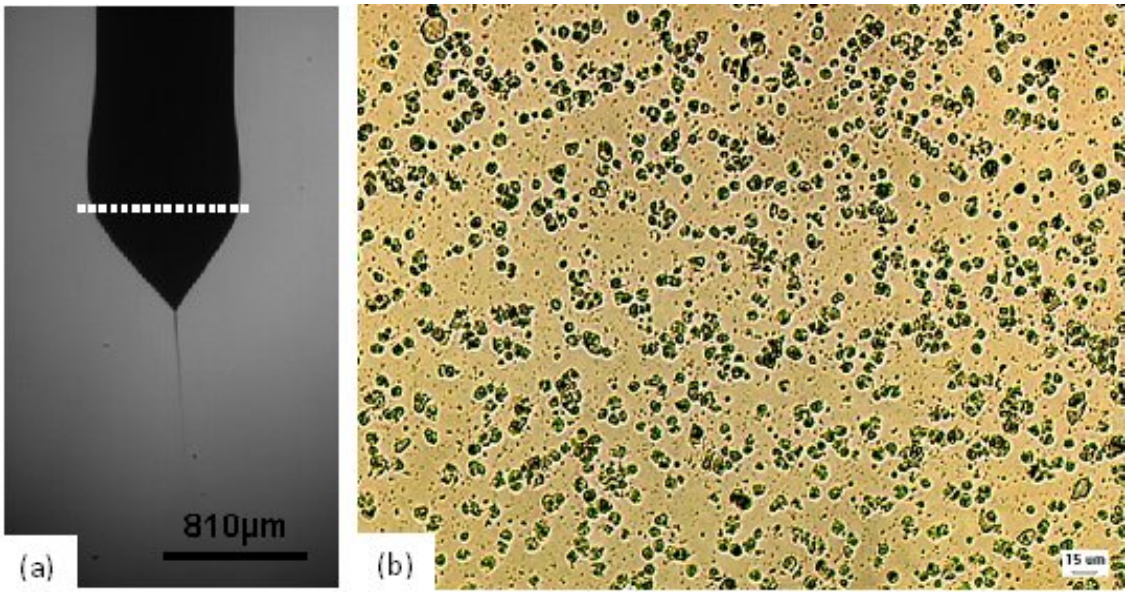

Figure 5.3 (a) Cone-jet mode of 6 wt% nHA suspension used for electrospraying and (b) near-monodisperse HA droplets of diameter <15 µm produced by electrospraying (the dotted line in (a) indicates the exit of the needle)

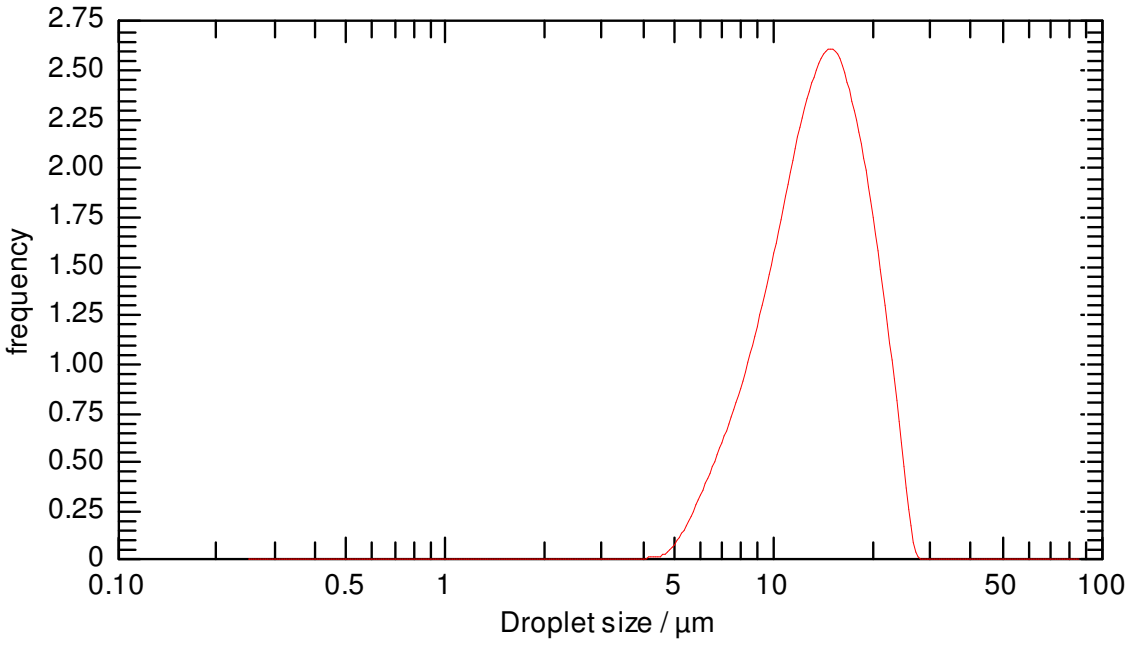

Figure 5.4 Droplet size distribution obtained for stable cone-jet mode electrohydrodynamic atomisation of 6 wt% nHA suspension

5.1.4.5 Sintering temperature

The ability of being sintered at lower temperatures was considered to be an advantage of using nanostructured ceramics according to the literature [Kalita *et al.*, 2007]. The nHA particles used in this work are rod-like in shape and are 50 – 100 nm in length and approximately 20 nm in diameter. Pyrolysis of the PU polymeric templates occurs at approximately 400°C, which was investigated by thermogravimetric analysis (TGA). For the sintering of HA, a maximum sintering temperature of 1200°C is mainly adopted in the literature. Therefore, the same heating program shown in **Figure 3.3** was used, but the maximum sintering temperature was set to 600°C instead. The green bodies were reduced to powder upon sintering and it was deduced that the sintering temperature was too low. The maximum sintering temperature was then raised to 800°C and the observation was similar to that of 600°C. The sintering temperature was then increased to 1200°C (as shown in **Figure 3.3**) and it was possible to retain the three-dimensional porous bioceramic structure on sintering.

5.2 Processing of HA scaffolds using EHDA

5.2.1 HA scaffolds produced using a 9 wt% nHA suspension

The electrospraying set-up shown in **Figure 5.2** was used to prepare the scaffolds. The 60 ppi polyurethane (PU) template dimensions of 5 mm× 5 mm× 10 mm were used for the experiments. At a solid loading of 9 wt% and a spray time of 30 minutes, the surface analysis of the green bodies exhibited an HA coating with lumps and cracks (**Figure 5.5**).

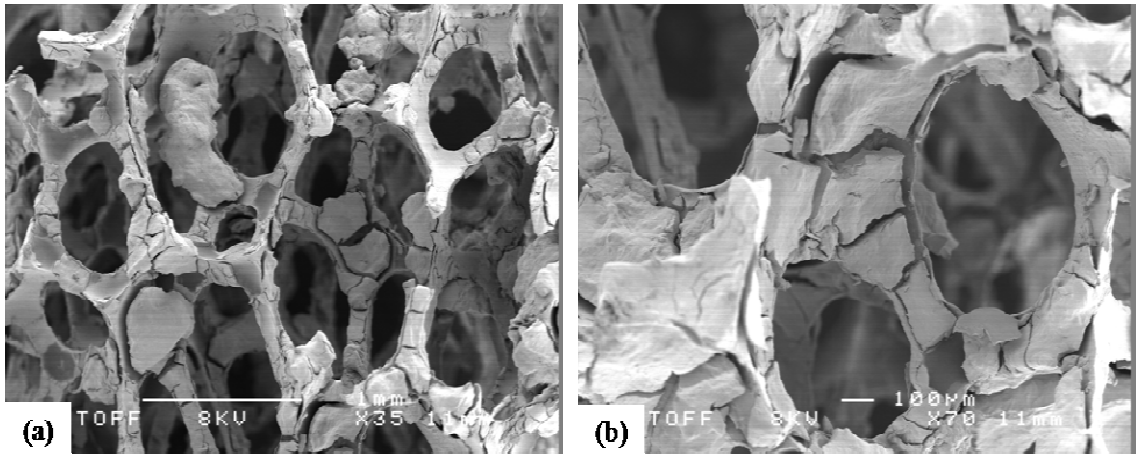

Figure 5.5 SEM images showing the surface of the HA coating on the PU template of the green bodies. The HA agglomerations and cracks are distinctly visible in both images at lower (a) and higher (b) magnifications

As mentioned in section **5.1.1**, the nHA suspension of 9 wt% nHA loading did not maintain a stable cone-jet mode. The HA lumps or agglomerations on the coating could be due to the larger droplets produced as a result of the unstable cone-jet. Due to this, a lower nHA suspension concentration was preferred, but could result in an increase in the spraying time and a weaker scaffold structure.

5.2.2 HA scaffolds produced using a 6 wt% nHA suspension

The 60 ppi PU templates were cut into 5 mm × 5 mm × 10 mm dimensions. The 6 wt% ethanol based nHA suspension was used for electrospraying. This 6 wt% nHA suspension was a modified version of the original 18 wt% (water based) nHA suspension and ethanol was added to enable the suspension to be electrosprayed. Experimental set–up shown in **Figure 5.2** was used for electrospraying and a stainless

steel needle with outer and inner diameters of 810 µm and 510 µm respectively, was used. A flow rate of 10 µlmin^{-1} and voltage in the range of 4.4-5.5 kV were the conditions at which a stable cone-jet was established (**section 5.1.4.4**). The templates were electrosprayed for 2hrs and were air-dried for ~12hrs. The green bodies were sintered to a maximum temperature of 1200℃ using the heat treatment program shown in **Figure 3.3**.

Using a nHA solid loading of 6 wt%, the PU templates had to be electrosprayed for 2 hours to obtain sintered scaffolds with some mechanical strength so they would not crumble upon handling. **Figure 5.6** shows the SEM images of the sintered scaffolds and the difference between the electrosprayed surface and the interior surface of the foam.

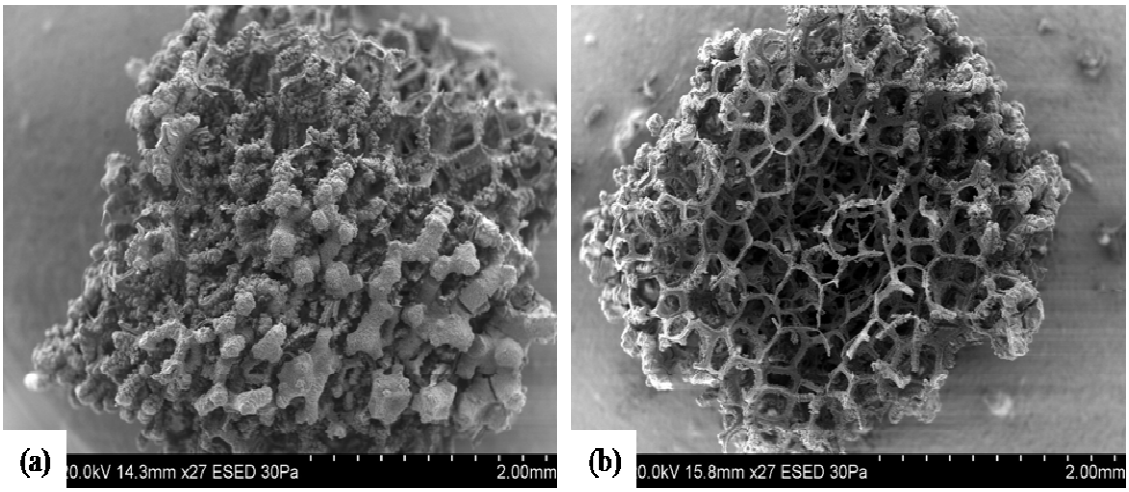

Figure 5.6 SEM images of the sintered scaffolds produced using electrospraying for 2 hours and sintered to a maximum temperature of 1200℃. (a) shows the electrosprayed surface and (b) shows the interior cross section of the structure.

These structures will be analysed in detail later on in the chapter, but the most critical observation of these SEM images is the non-homogenous nature of the sintered scaffold. During the spraying process, it was found to be difficult to spray for long periods of time due to the evaporation of ethanol leading to needle blockages and frequent replacement of the suspension due to the sedimentation effects. From the SEM images it is also clear that longer spraying time leads to a dense surface (**Figure 5.6a**), with insufficient penetration of the charged droplets into the template, thus reducing the amount of coating of the struts in the interior surfaces. This therefore, results in a weak interior structure with thin struts (**Figure 5.6b**), which is not very suitable for tissue engineering (TE) purposes.

It was clear that with a much lower solids' loading, in order to obtain complete coating of the template, the foams had to be sprayed for a longer period of time. This is not very efficient as longer spraying time causes agglomeration of suspension on the sprayed surface. Also it resulted in a structure which did not have the desirable characteristics of a scaffold for TE.

5.3 Preparation of scaffolds using a novel processing method of dipping and electrospraying

Although electrospraying has been able to produce porous foams of good mechanical properties in the literature, it was not possible to use this technique to produce the same results using a nano-HA suspension. In the literature, ceramic suspensions of high particle concentration >60 wt% were used, while only a 6 wt% nHA suspension was

used in these experiments. This obviously reduced the amount of nHA coating at a given time in comparison to that in the literature. Longer spray times is a possibility to overcome this issue, but it would make the entire processing method highly inefficient. In the foam processing methods, it seems a common procedure to combine two or more methods in order to produce scaffolds with improved surface and mechanical properties. Taking this into consideration, a novel hybrid fabrication method of dipping and then electrospraying was developed. It was the objective to make use of the advantages of both methods to overcome each other's disadvantages.

A comparison has been made in relation to the surface characteristics such as pore size and distribution, porosity and mechanical properties of the foams prepared using this combination method of dipping and electrospraying, to the foams prepared by using each method individually. This study is an attempt to produce scaffolds with enhanced pore interconnections and improved mechanical properties using slurries of low particle content for bone tissue engineering applications. This section will also describe the preparation of foams using replication method in addition to the combined method.

5.3.1 Scaffold fabrication

5.3.1.1 Replication method

Nano-HA suspensions of concentration 18 wt% (water based) and 6 wt% (ethanol based) were used. The PU templates were immersed in these suspensions for approximately five minutes. The excess slurry was squeezed out of the samples, which

were placed on a flat surface and allowed to dry at ambient temperature for at least 12 hours.

5.3.1.2 Dipping and spraying method

The samples were immersed in the respective suspensions for 5 min, the excess squeezed out and was immediately followed by electrospraying 6 wt% nHA suspension for 30 min and 1 hr time intervals. The samples were air-dried on a smooth flat surface for at least 12 hrs.

5.3.1.3 Heat treatment

The dried samples were pyrolysed and sintered to a maximum temperature of 1200℃ using the heat treatment program shown in **Figure 3.3**. The experimental conditions are identified as shown in **Table 5.2**.

Table 5.2 Identification of experiments

Label	Experimental Condition
A	18wt% dip
B	18wt% dip 6wt% 30min spray
C	18wt% dip 6wt% 1hr spray
D	6wt% dip 6wt% 30min spray
E	6wt% dip 6wt% 1hr spray
F	6wt% 2hr electrospray

5.4 Sample characterisation

X-ray diffraction (XRD) analysis was carried out on the HA powder obtained from the sintered foams and were compared to the results of the original HA suspension (**Chapter 3**).

The porosity *p* of the foam was calculated by [Gibson and Ashby, 1997b]

$$p = 1 - \frac{\rho_{foam}}{\rho_{solid}} = 1 - \rho_{relative} \qquad \textbf{(Eq. 3.3)}$$

where the density of solid HA; ρ_{solid} = 3156 kgm^{-3} [Hench and Best, 2004]. The density ρ_{foam} of the HA scaffolds was determined from the mass and dimensions of the sintered structures.

X-ray microtomography (XμT) method described in **Chapter 3** was used to image the internal pore network of the sintered foams. The porosity of these 3-D images were analysed and calculated using the CTAn software.

The microstructures of the sintered foams were characterised using a Hitachi S-3400N scanning electron microscope (SEM) as described in **Chapter 3**. Both the outer and inner surfaces of the foams were imaged to investigate the uniformity of the sintered structures.

Compression testing was carried out using a Zwick/Roell Z010 mechanical tester, using a cell load of 1 kN and a crosshead speed of 0.5 mm/min. **Chapter 3** describes the details of the method of analysis. The samples were made using the same templates that

were used for surface analysis, but the sintered dimensions were found to be on average 2.5 mm × 2.5 mm × 7 mm due to shrinkage during the sintering process.

5.5 Polymeric templates

The cellular packing of most commercial foams have a dodecahedral shape for efficient space filling [Gibson and Ashby, 1997c]. The PU foam used as the sacrificial template in this work had a cell range of 740 – 1040 µm. Each dodecahedral cell consists of 12 faces of size approximately 2 – 3 times smaller than the total size of the associated cell [Chen *et al.*, 2006a], therefore in this study the cell window size can be estimated to be 200 – 500 µm as confirmed by scanning electron microscopy (**Figure 3.1a**). The fine HA droplets (*i.e.* <15 µm) produced in cone-jet mode enabled successful penetration of the nHA suspension through the polymeric template, considering the minimum template pore size was a much larger value of ~200 µm.

5.6 X-ray diffraction

The stability and decomposition of HA at high temperatures is still under speculation in the literature. While some investigators agree that HA is stable in water vapour pressure upto 1200ºC, others report partial decomposition of HA into tri-calcium phosphate ($Ca_3(PO_4)_2$ (TCP)) in the temperature range of 800 – 1200ºC [Zhou *et al.*, 1993]. There is also speculation that the temperature range is actually 1200 – 1450ºC for the decomposition of HA into TCP [Ruys *et al.*, 1992]. In contrast, it has also been shown that HA samples sintered at 1200 – 1350℃ with a soaking time of 2 hrs did not show the presence of TCP [Zhang *et al.*, 2007].

The green bodies were soaked at the maximum sintering temperature of 1200ºC for 5 hours as an attempt to enhance the mechanical properties by, increasing the adherence of the nHA particles and decreasing the size of the central void left due to the sacrificial template. The heating ramp was set at 2ºC/min in order to minimise cracking. The original 18 wt% water based nHA suspension was produced by drying and then heat treatment at 1200°C. XRD was carried out on the sintered 18wt% nHA suspension and was compared to the HA obtained from the sintered scaffolds to observe any effects due to the polymer burn out (**Figure 5.7**). The major peaks in both graphs are similar and correspond to HA but the graph for HA from scaffolds (**Figure 5.7b**) shows a noisier spectrum due to less powder of a much coarser particle size.

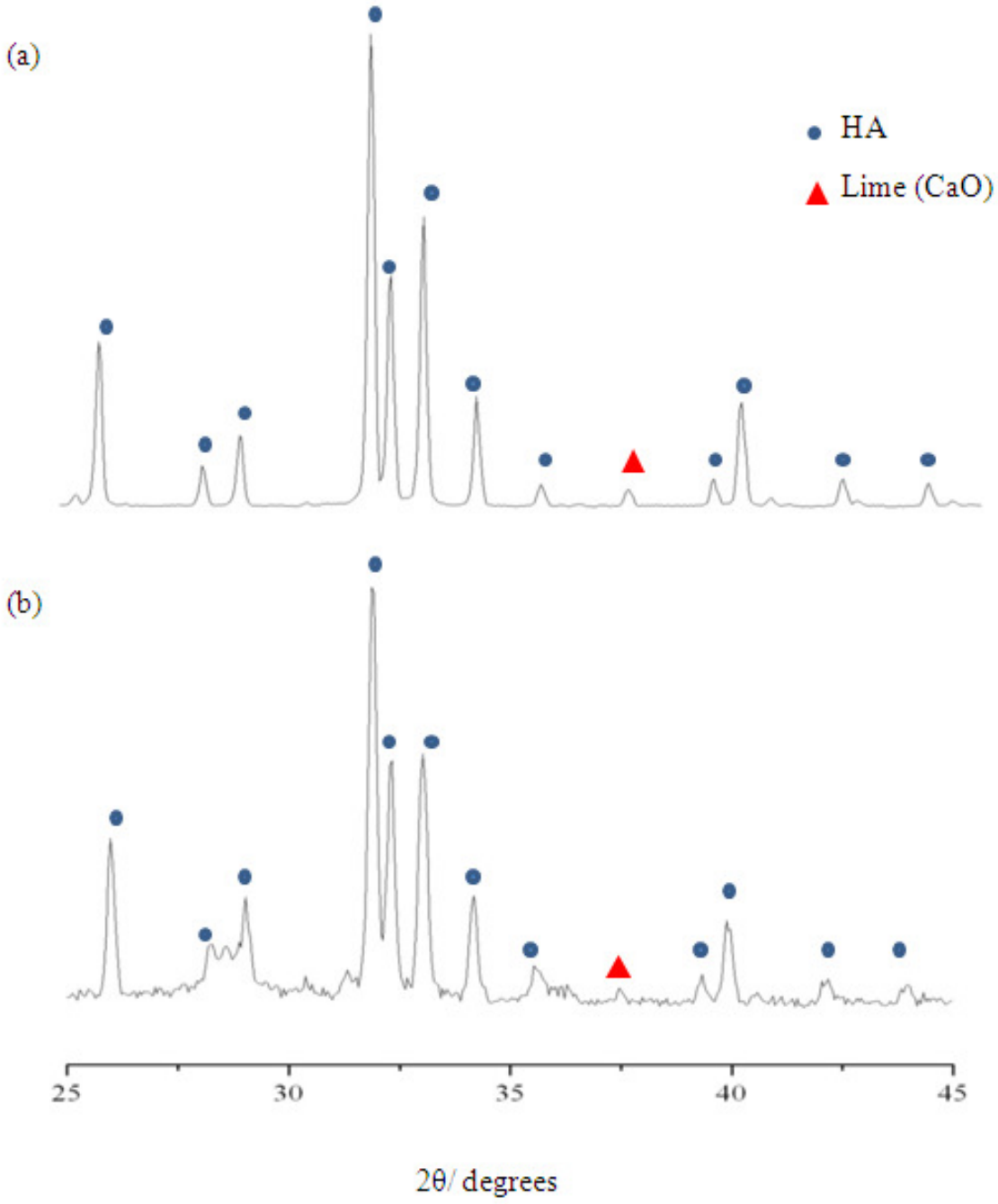

Figure 5.7 XRD results for (a) 18 wt% water-based nHA suspension which was dried and heat treated at 1200℃ and (b) HA powder obtained from the sintered scaffolds sintered to a maximum temperature of 1200℃ and soaked for 5 hrs at that temperature

5.7 Porosity

The porosities of the sintered foams were calculated using **Eq. 3.3** and the average values are shown in **Figure 5.8**. Six samples for each condition were measured and the mean porosity was calculated. All the samples had average porosities between 84 – 89% but the accuracy of this method can be questioned in relation to the porosity values obtained for the samples prepared only by electrospraying. From the surface analysis for samples that were only electrosprayed, it was observed that the outer surface was much thicker and less porous, while the centre was highly porous due to the fragile strut structure (**Figure 5.10 k, l**). These values had a large standard deviation, because the mass and dimensions of the samples showed a large variation and therefore were only an estimate due to the non-uniformity of the porous foams.

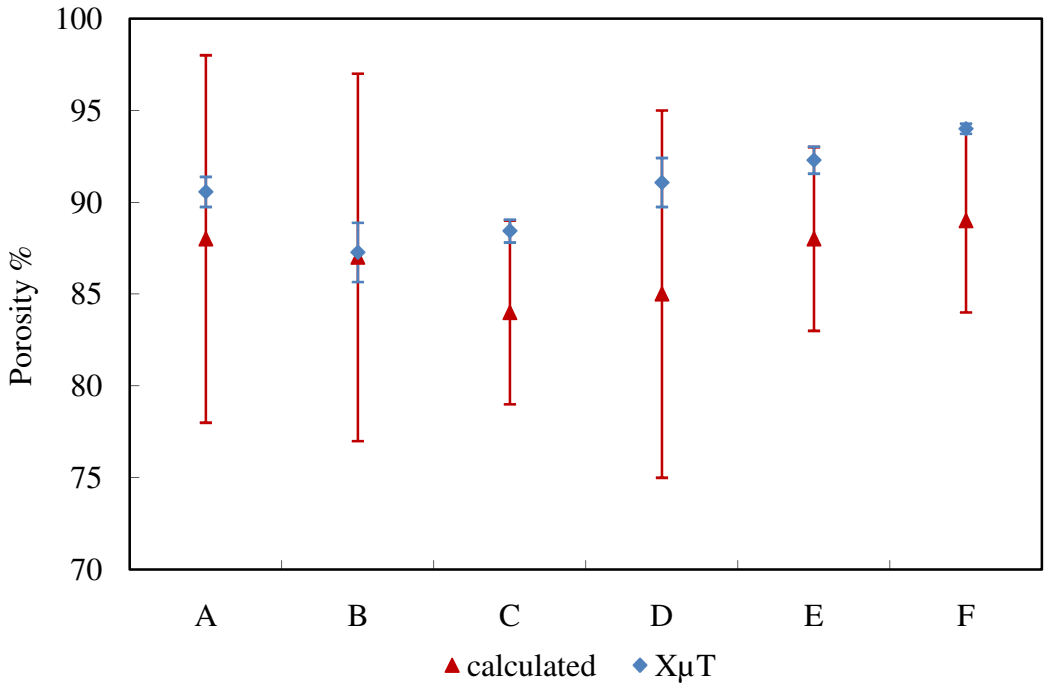

Figure 5.8 Comparison of porosities between the calculated values and the microtomography (XμT) values

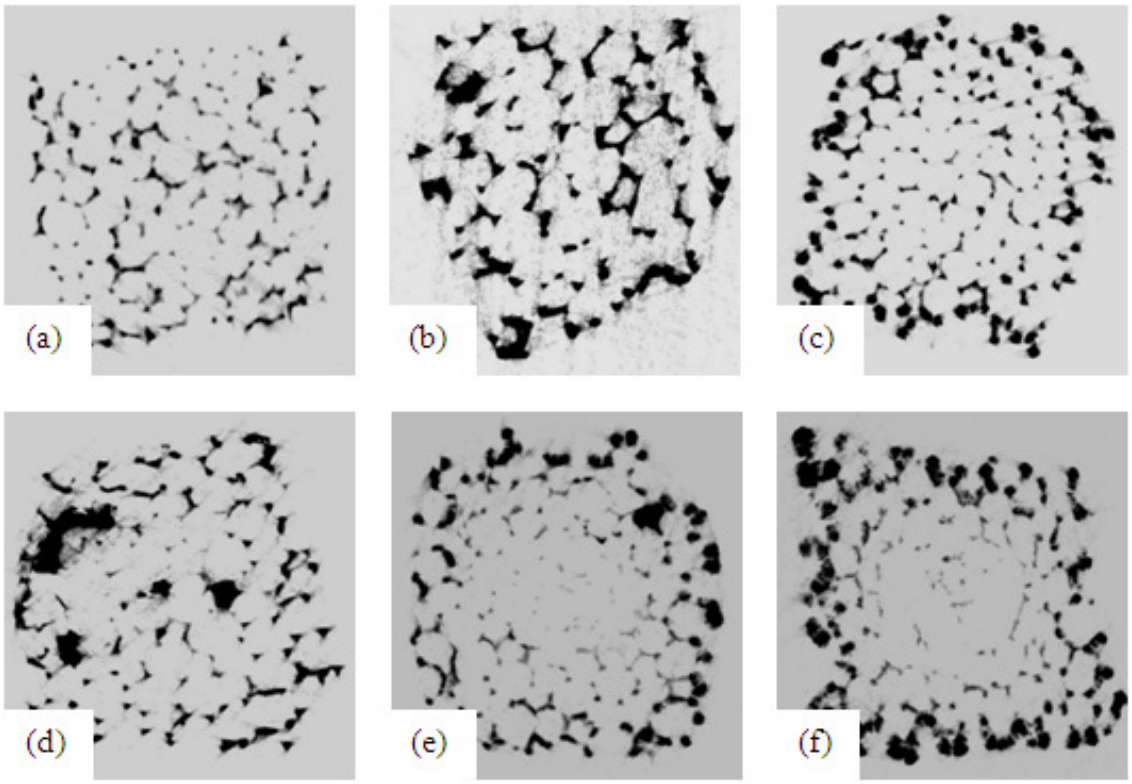

Figure 5.9 XμT images showing the cross sections of samples A-F outlining their porous structure and interconnections. The outer layer is darker (b – f) due to the electrospraying, forming a thicker coating in comparison to the centre of the foam

The calculated porosity values were compared with the values obtained using the reconstructed three-dimensional images from XμT. XμT gives a much smaller deviation and is a more accurate measurement as it considers the internal porosity of the structures. The porosities estimated using both the methods average within the range of 84 – 94% which is favourable for scaffolds for bone TE. The XμT images shown in **Figure 5.9** are cross-sections of the foam samples indicating the porosity and the interconnectivity of the structures. The dipped sample (**Figure 5.9a**) shows a

homogeneous pore structure as well as the interconnections. In the rest of the images (**Figure 5.9b-f**), where electrospraying was involved, the outer layer appears to be darker than in the centre due to the thicker coating on the sprayed surfaces.

5.8 Microstructural analysis

Scanning electron micrographs were obtained on the sintered structures for each category (A-F) on the surface and then the structures were fractured in the middle to observe the penetration of the ceramic into the template and were imaged. **Figure 5.10** shows the low magnification images of the sprayed surface and the images of the cross-section towards the centre of the foam. All the bodies retained their structures upon sintering. By using the dipping method the structure was homogeneous both on the outside and the inside (**Figure 5.10 a, b**). When the dipping and electrospraying methods were combined, denser struts were observed on the sprayed surface and the pore size was reduced (**Figure 5.10 c, g**). This characteristic was enhanced when the spray time was increased to 1hr which is expected due to the deposition of increased amounts of the HA particles (**Figure 5.10 e, i**). Complete electrospraying produced the smallest pores on the surface and the pore size was increased towards the centre of the foam (**Figure 5.10 k, l**). The struts inside the foam were reduced by approximately 70% in comparison to the strut thickness on the sprayed surface of the scaffold. This is due to the agglomerated HA particles on top of the foam reducing penetration of the slurry into interior of the foam resulting in a weak centre with poor mechanical properties.

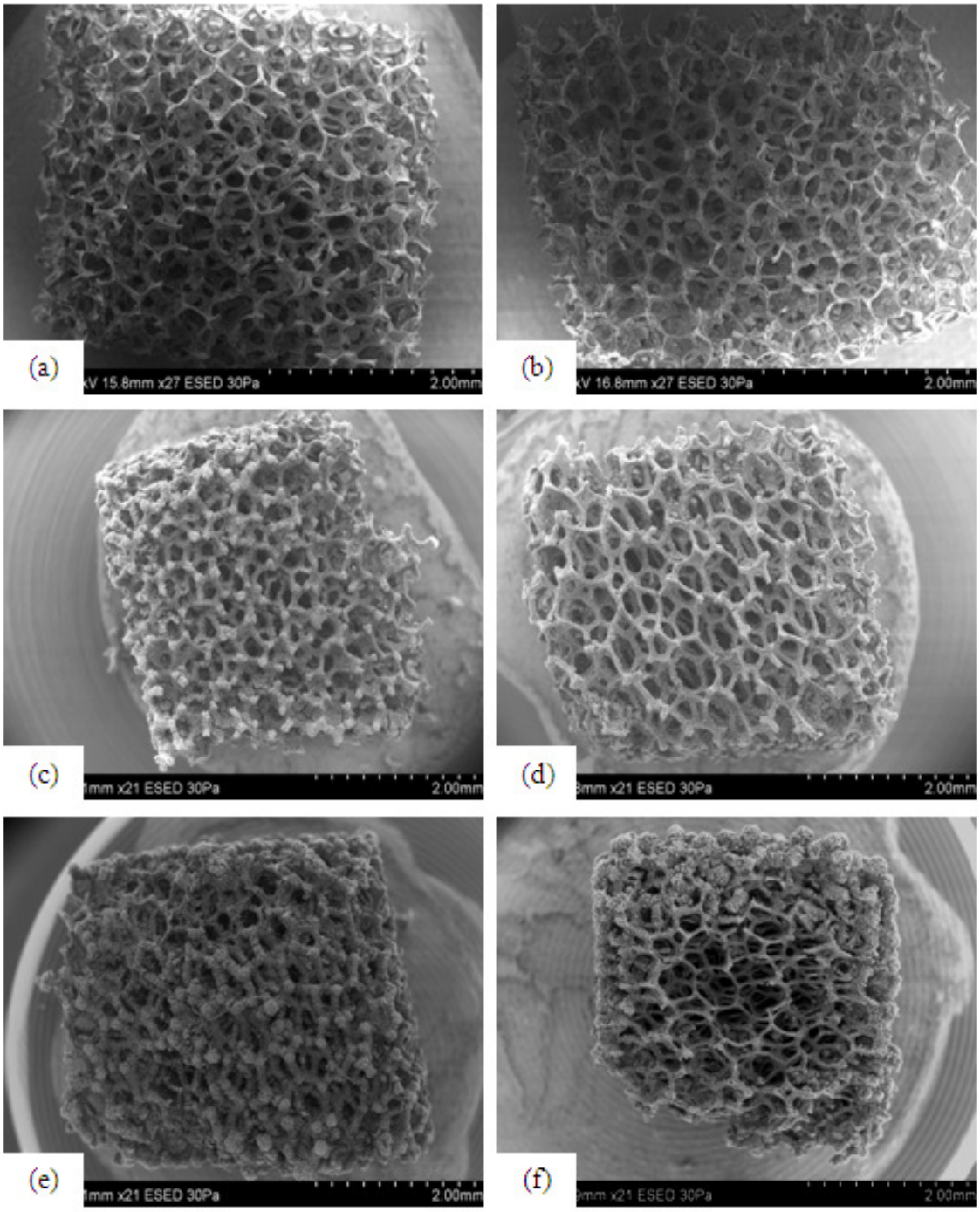
(a)
(b)
(c)
(d)
(e)
(f)

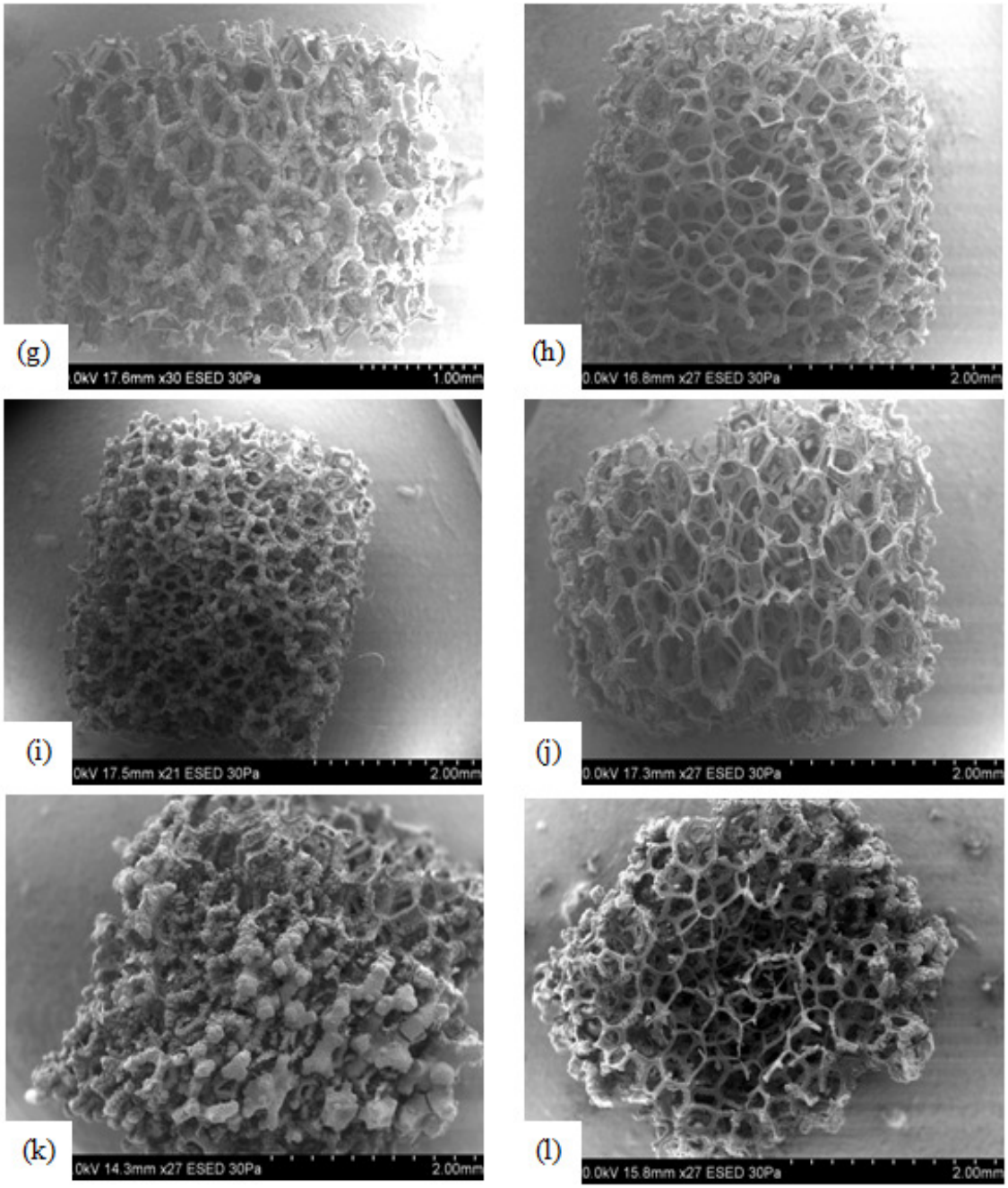

Figure 5.10 Low magnification SEM images of the sintered bodies on the surface (sprayed/ dipped/ combined) and the mid-section to observe the penetration of the slurry into the foam. Sample A (18wt% dip) (a) surface, (b) mid-section; Sample B (18wt% dip 6wt% 30min spray) (c) surface, (d) mid-section; Sample C (18wt% dip 6wt% 1hr spray) (e) surface, (f) mid-section; Sample D (6wt% dip 6wt% 30min spray) (g) surface,

(h) mid-section; Sample E (6wt% dip 6wt% 1hr spray) (i) surface, (j) mid-section; Sample F (6wt% 2hr electrospray) (k) surface, (l) mid-section.

The change in pore size and the thickness of struts for each processing route are shown in **Figure 5.11**. Approximately 100 measurements were averaged from ten samples for each category to obtain an accurate distribution of values for the pore size and strut thickness. In order to investigate the uniformity of the foams, the average pore size and the strut thickness of both the surface and the middle of the foam were analysed. The homogenous distribution of the pore size and strut thickness were obtained using only the dipping method. During the dipping method, since the template is dipped in the suspension completely, the probability of covering all the struts is very high. Since the excess is squeezed out, this results in an even spreading of the slurry over the template. An increase in the thickness of the struts is observed as a result of electrospraying on the sprayed surface. In comparison to the dipped foams (category A), the pore size has reduced in both the sprayed and cross-sectional surfaces when the foams were fabricated using the combined method (category B) and the pore size is reduced even further when the spray time is increased to 1hr (category C). This indicates that the fine droplets produced using the atomisation method have successfully penetrated deep within the PU template.

An increase in the pore size in category D is observed, even in comparison to the 18wt% dipped sample in category A. This could be due to the lower solid content in category D, since suspensions of 6wt% in ethanol were used. The pore size on the sprayed surface

has been reduced by about 42% when the spraying time was increased to 1hr (category E), but the average pore size on the inner surface seems to have increased by approximately 22%. It can be observed that the combined method of electrospraying and dipping gives rise to thicker struts and a reduced pore size in comparison to the dipped only foams. The pore size however still lies within the desired range for bone TE of 100 – 400 µm [Yoshimoto *et al.*, 2003].

Figure 5.12 shows the micrographs at higher magnification showing the strut structure and the pore interconnectivities, both on the surface and the centre of the porous foams. The foam which was prepared by only the dipping method had too many microcracks along the length of the struts compromising its mechanical properties. The foams prepared by the combined method still managed to produce interconnected pore networks and it was possible to see the HA droplets that had sintered together forming the struts via electrospraying (**Figure 5.12 c, d**). However, these images further confirm the non-uniformity of the sprayed surface and the centre of the foam in relation to the pore size, interconnectivity and strut thickness. But it can also be observed that the combination of dipping and spraying results in reduced amount of microcracks (**Figure 5.12 e, f**). This is most likely due to the finer HA droplets filling the polymeric template that were not covered sufficiently by the dipping method. It is further confirmed by the very thick struts on the outer surface with hardly any interconnectivity (**Figure 5.12 k**) and towards the centre of the foam, extremely thin, fragile struts with interconnectivity (**Figure 5.12 l**). Foams prepared under category F seem unsuitable for TE applications

not only due to its extreme fragility, but the pore size on the outer surface of the foam just reaches the minimum pore size requirement of 100 μm.

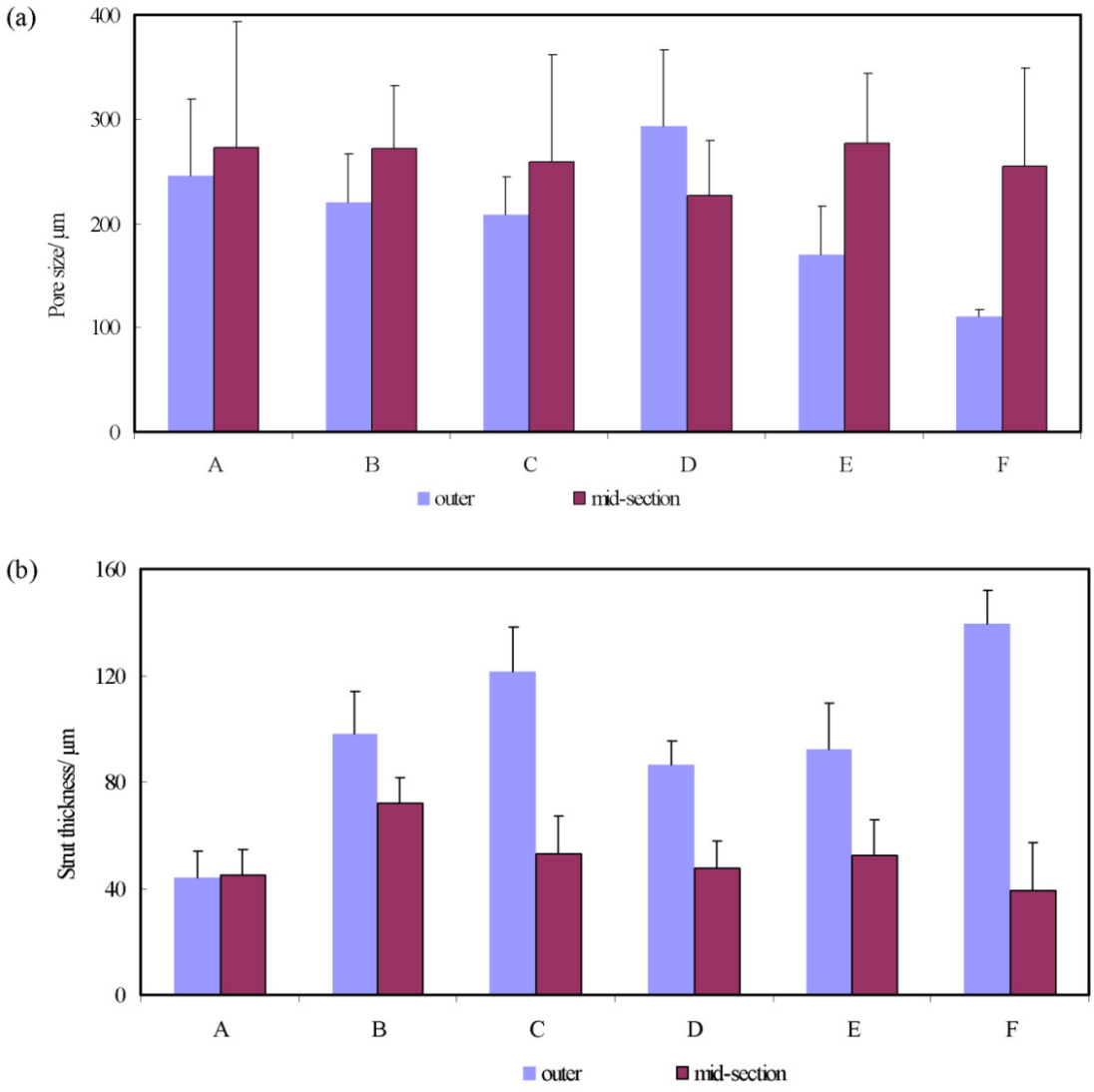

Figure 5.11 Comparison of (a) pore size and (b) strut thickness of the sintered structures obtained using different methods (A: 18wt% dip; B: 18wt% dip 6wt% 30min spray; C: 18wt% dip 6wt% 1hr spray; D: 6wt% dip 6wt% 30min spray; E: 6wt% dip 6wt% 1hr spray; F: 6wt% 2hr electrospray)

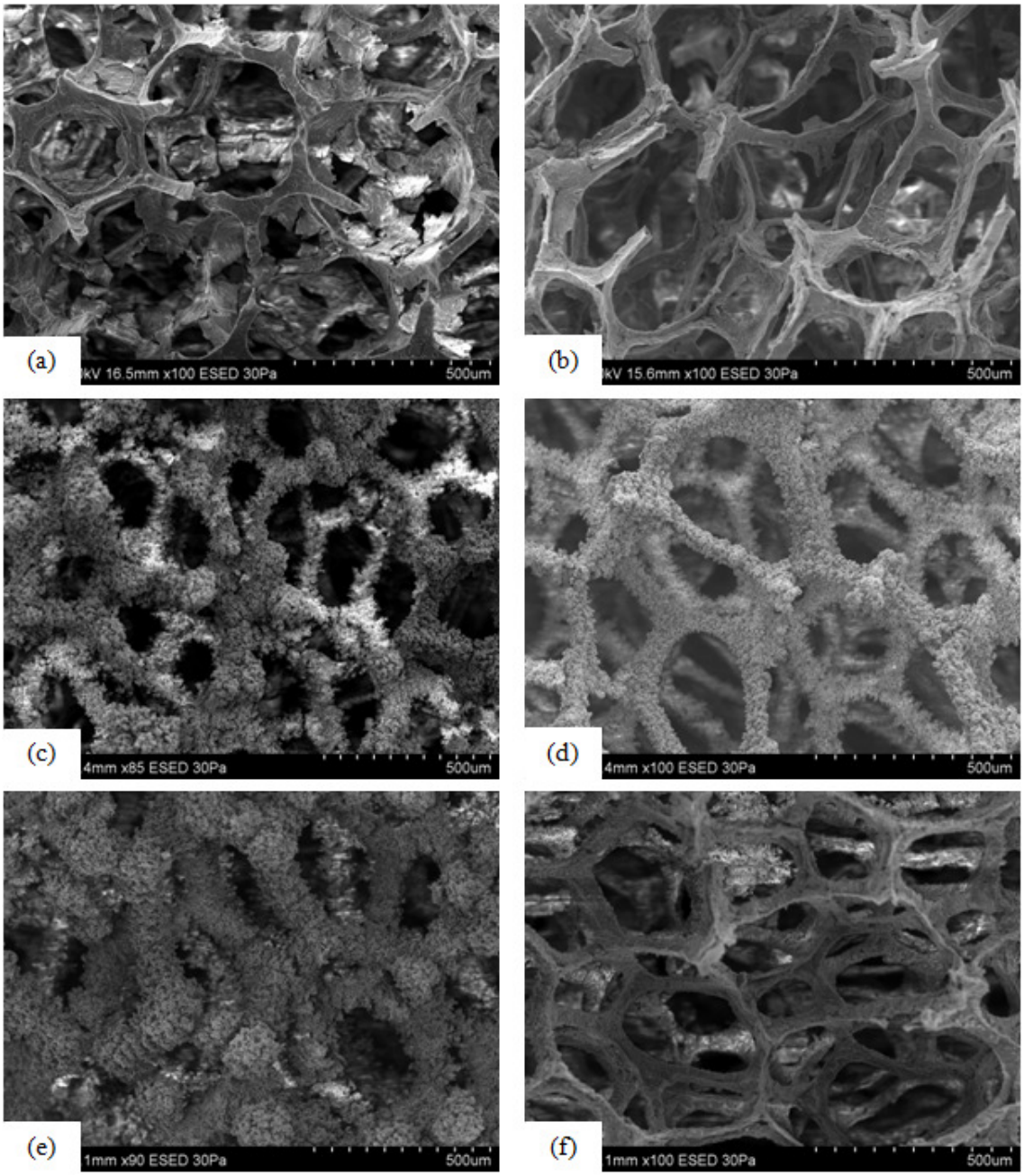
(a)
kV 16.5mm x100 ESED 30Pa
500um
(b)
kV 15.6mm x100 ESED 30Pa
500um
(c)
4mm x85 ESED 30Pa
500um
(d)
4mm x100 ESED 30Pa
500um
(e)
1mm x90 ESED 30Pa
500um
(f)
1mm x100 ESED 30Pa
500um

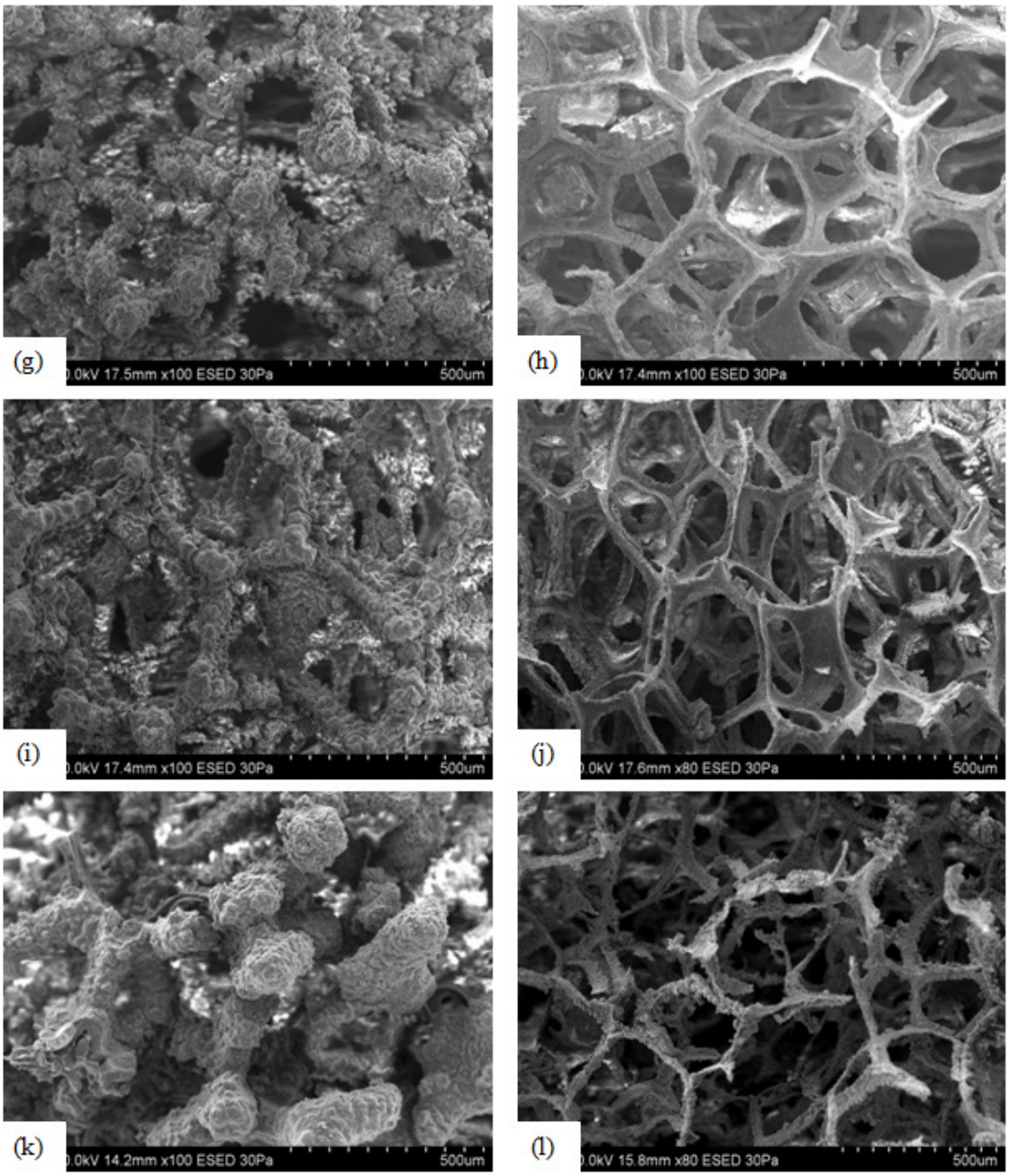

Figure 5.12 High magnification SEM images showing the strut structure and pore interconnectivity of the sintered bodies on the surface (sprayed/ dipped/ combined) and the mid-section to observe the penetration of the slurry into the foam.

Sample A [18wt% dip] (a) surface, (b) mid-section; Sample B [18wt% dip 6wt% 30min spray] (c) surface, (d) mid-section; Sample C [18wt% dip 6wt% 1hr spray] (e) surface,

(f) mid-section; Sample D [6wt% dip 6wt% 30min spray] (g) surface, (h) mid-section; Sample E [6wt% dip 6wt% 1hr spray] (i) surface, (j) mid-section; Sample F [6wt% 2hr electrospray] (k) surface, (l) mid-section

5.9 Mechanical properties

The compressive stress-strain graphs were plotted for each category as described in **Chapter 3**. **Figure 5.13a** shows the typical compressive stress-strain curves for different samples as a comparison of the mechanical behaviour in compression of foams prepared by slurry dipping, electrospraying and combination of both. The jagged curves are the result of the presence of microcracks on the strut surfaces. The microcracks on the thin struts act as stress concentration points leading to microfailures that cause a drop in stress, however the foam as a whole is still able to bear higher loads, causing the increase in stress. Due to the repetition of the rise and fall of stress, the curves show the observed jagging effect. The stress-strain curves exhibit the initial stress increase with increasing strain, followed by stress decrease or plateau, which is the typical behaviour in this type of foam [Chen *et al.*, 2006b]. **Figure 5.13a** also shows a significant improvement in the compressive mechanical properties of foams made by the combined method in comparison to foams prepared by either slurry dipping or electrospraying only. **Figure 5.13a** also indicates a further improvement of the mechanical properties with increased spraying time (*i.e.* from 30 min to 1 hour) and can be related to the increased deposition of fine HA droplets onto the template leading to thicker and stronger struts. The completely electrosprayed sample (F) had the lowest compressive strength, and could be related to the non-homogeneous nature of the structure with very

thin and fragile struts in the centre of the foam leading to poor mechanical properties. It is well known that the mechanical strength of a material decreases with increasing porosity. When the relative density is ~0.1, the compressive strength of spongy bone can be estimated to be in the range of 0.2 – 4 MPa [Gibson and Ashby, 1997a].

The maximum compressive strength obtained from the combined method of dipping and electrospraying was 0.016 MPa, which is still lower than the desired value. The low mechanical properties could be due to the low solid content of 6 – 18 wt% used in the present work in comparison to that in the literature where a solid loading of 50 wt% or higher have been used to produce HA scaffolds [Kim *et al.*, 2004c, Kim *et al.*, 2005b]. The nHA particles are of a rod-like shape [Huang *et al.*, 2004] and it is a well known fact that equiaxed shapes exhibit a better packing efficiency. Therefore, due to the lack of packing efficiency owing to the nHA particle shape during the sintering process, can lead to micropores in the sintered scaffold structure compromising the mechanical properties.

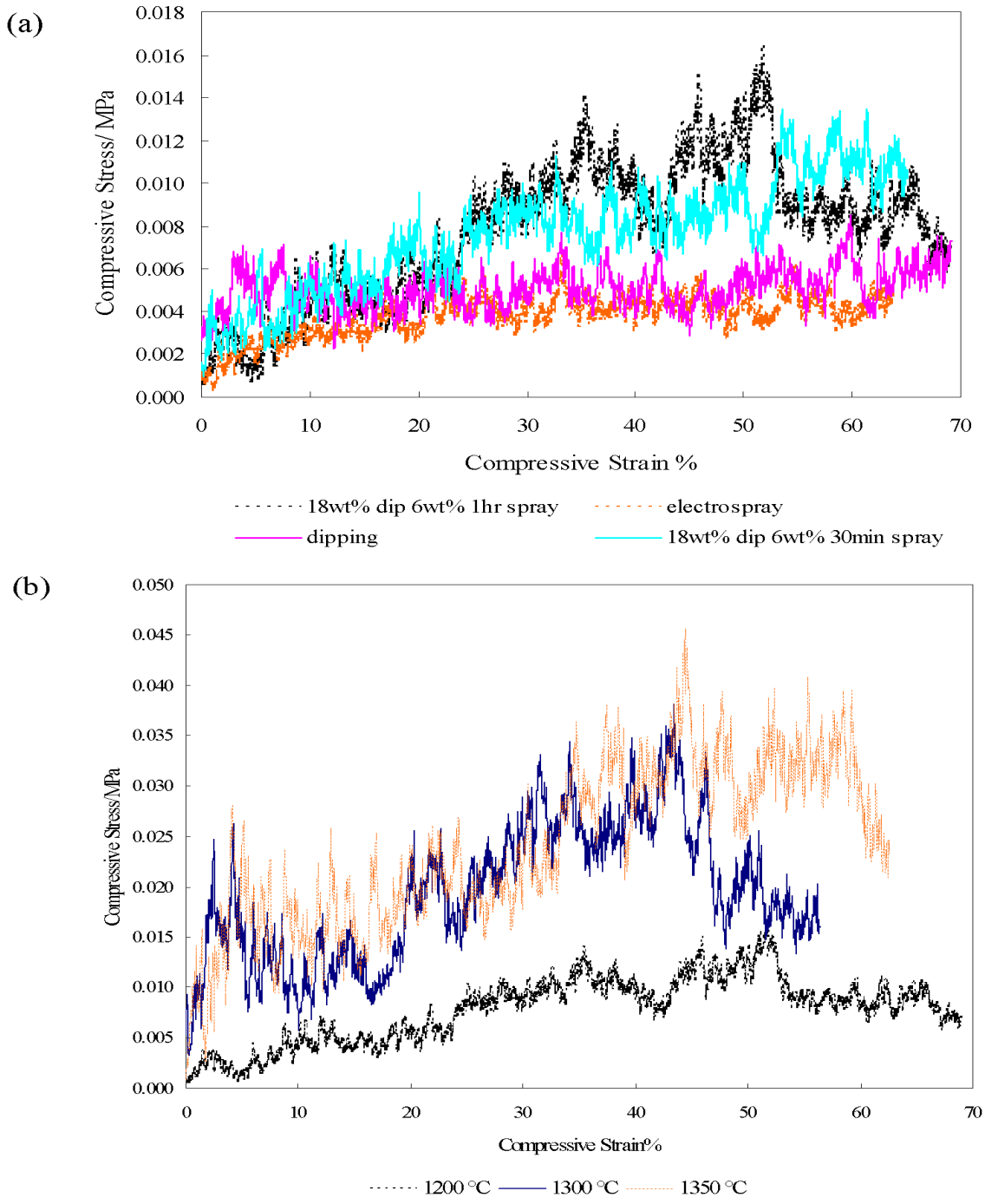

Figure 5.13 Compressive stress-strain graphs: (a) comparing dipping, electrospraying and combination method. The graph clearly indicates improved mechanical properties in the combined method which increases with spraying time; (b) improvement of mechanical properties with increasing sintering temperature. 1200 < 1300 < 1350°C

5.10 Effect of sintering temperature

It was deduced that the foams prepared using the combined method of dipping and electrospraying for 1 hr produced the best mechanical properties in comparison to the other methods. Foams were prepared using this method (condition C) but were sintered at temperatures 1200, 1300 and 1350°C to investigate the effect of sintering temperature on the pore morphology, porosity and mechanical properties. **Figure 5.14** shows the SEM images on the outer and inner surfaces of the HA foams at varying sintering temperatures. Structures of good pore interconnectivity were observed for all temperatures and the pores were in the range of 100 – 300 µm which is within the desired range for bone TE applications as specified in the literature review (**Table 5.3**). The porosity was calculated for six samples using **Eq. 3.3** and the averages were ~88% and ~84% for 1300°C and 1350°C respectively (**Table 5.3**).

Table 5.3 Effect of sintering temperature on pore diameter and porosity

Sintering temperature /°C	**Pore size on the surface /µm**	**Pore size in the interior /µm**	**Calculated porosity /%**
1200	208 ± 40	259 ± 100	84 ± 5
1300	186 ± 50	208 ± 70	88 ± 1
1350	233 ± 70	232 ± 50	84 ± 2

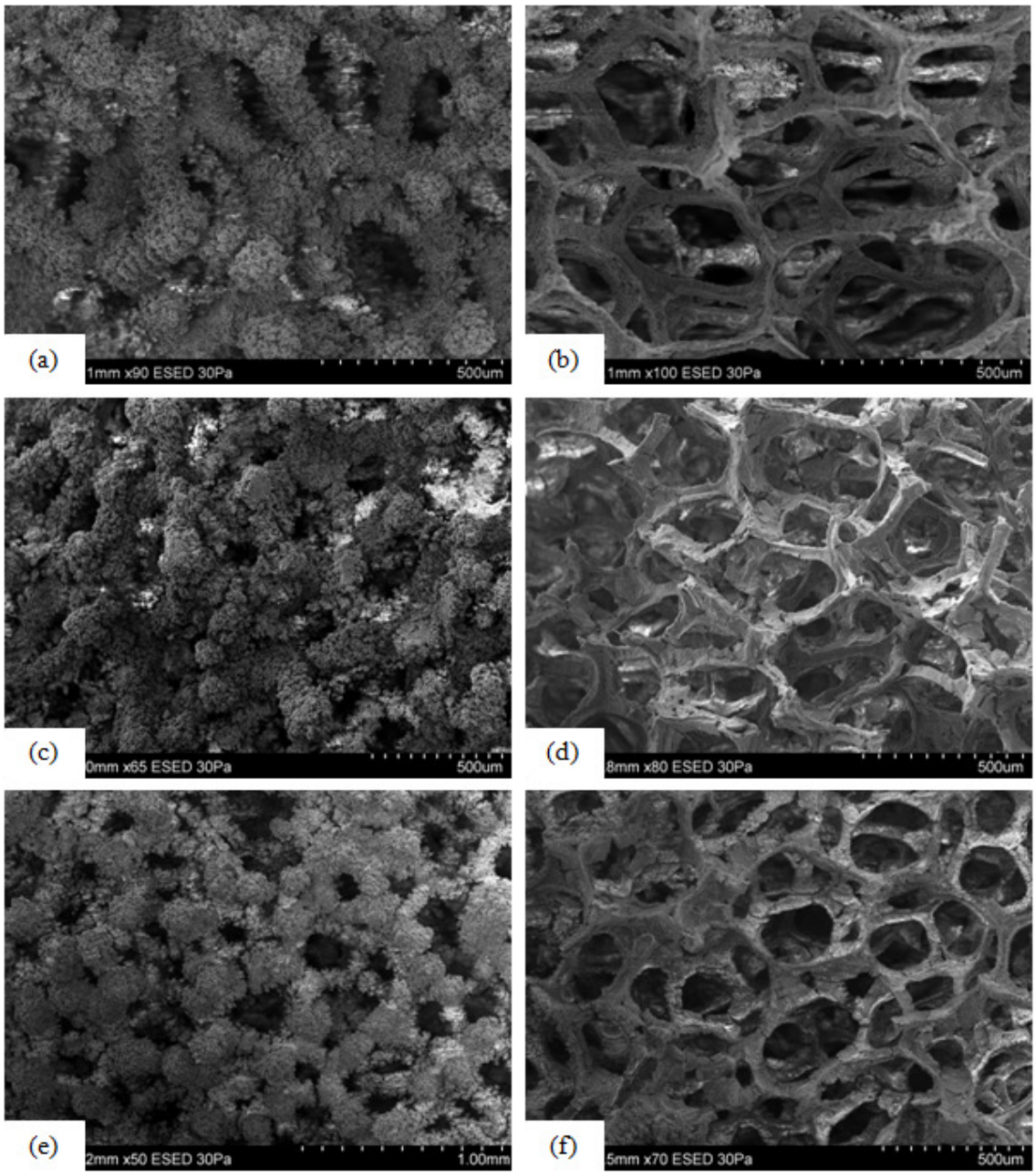

Figure 5.14 Scanning electron micrographs showing the effects of sintering temperature on the surface and cross-sections of the HA foams prepared by the combined method (condition C in **Table 5.2**). 1200°C (a) surface (b) cross-section; 1300°C (c) surface (d) cross-section; 1350°C (e) surface (f) cross-section.

The porosities of the higher temperature sintered HA scaffolds were similar to that obtained for 1200°C showing no significant change with temperature variation. However, there was a significant difference in the size of the central void in the struts. **Figure 5.15** shows a decrease in the size of the central void with increasing sintering temperature. This could be due to improved adherence of the nHA particles at higher temperatures. Also, it is important to note that there are limitations on the sintering of HA and it has been reported that at temperatures higher than 1350°C [Ruys *et al.*, 1992, Zhang *et al.*, 2007], HA can decompose into TCP, which has lower mechanical properties and an unpredictable resorption rate [Murugan and Ramakrishna, 2005]. In the literature, Fu *et al*. (2008) have sintered HA constructs at a temperature range of 1250 – 1375℃ for 3 hours to investigate the effect of sintering temperature on compressive strength of scaffolds. It was reported that there was no detectable phase change even at the maximum sintering temperature and the optimum strength was obtained at 1350℃, which they presumed was due to the HA lamellae in the porous structure reaching nearly full density [Fu *et al.*, 2008].

Even though it was shown in the literature that it is possible to produce void-free struts using electrospraying [Jayasinghe and Edirisinghe, 2002b], it was not possible to form completely solid struts using the nHA suspension. It is possible that this phenomenon not only depends on the fabrication method, but also on the ceramic material. Reduction in size of the central void should improve mechanical properties and this characteristic is observed in the average compressive stress-strain graph shown in **Figure 5.13b**, where a maximum average compressive strength of ~0.05MPa was reached.

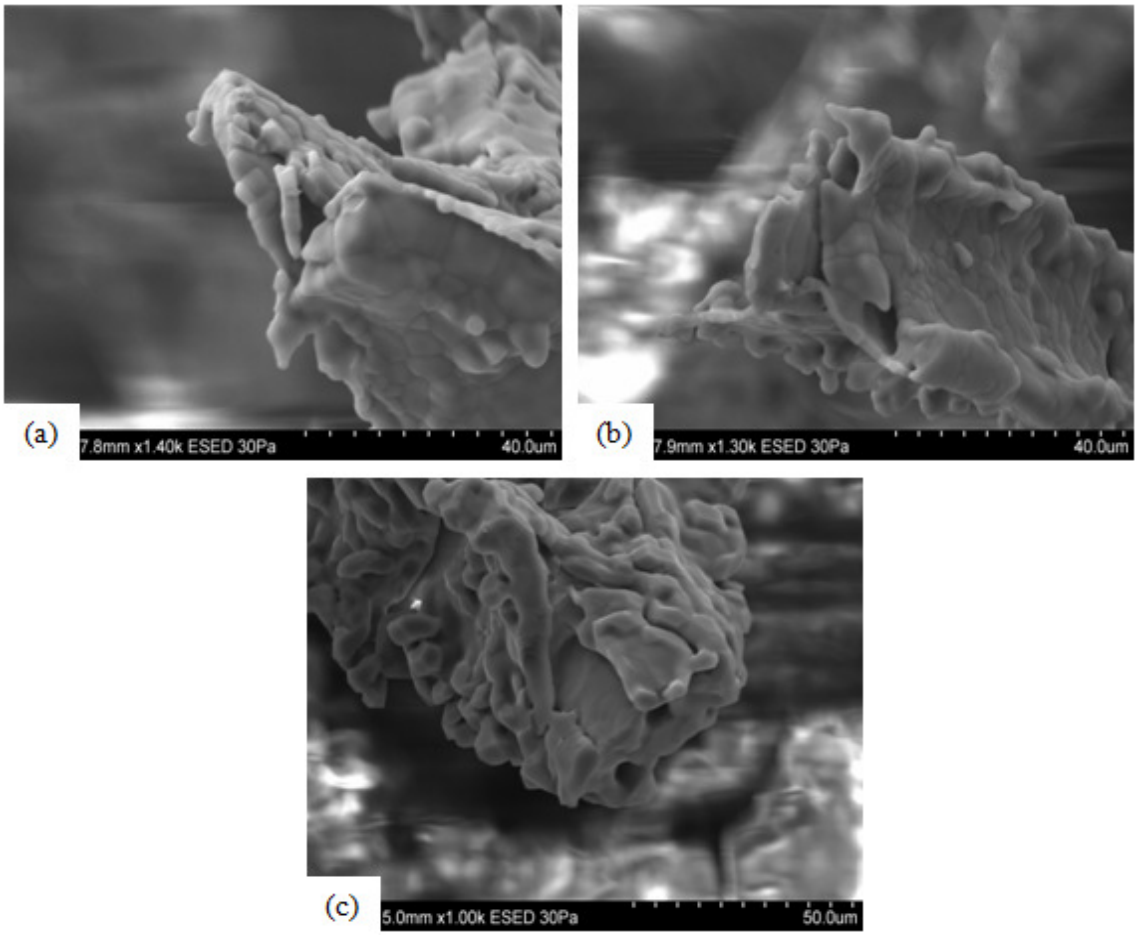

Figure 5.15 Increasing sintering temperature leading to a decrease in the size of the central void in the struts: (a) 1200℃, (b) 1300℃, (c) 1350℃. The samples were prepared under condition C (**Table 5.2**).

Chapter 6

Improvement of mechanical properties and bioactivity in bioceramic scaffolds

---

It has been possible to utilise the EHD processing method to produce scaffolds with graded as well as uniform porosity. **Chapter 4** was ended with a description of the production of a bone-like porous structure using zirconia which is a bioinert bioceramic, as the scaffold material. In **Chapter 5**, the use of bioactive hydroxyapatite (HA) to produce porous scaffolds was described. A novel processing method of combining the dipping and electrospraying was introduced. It was possible to obtain porous and interconnected pore networks satisfying some of the morphological requirements for bone tissue engineering (TE) scaffolds. However, even if the combination of dipping and electrospraying did produce scaffolds with better mechanical properties in comparison to scaffolds prepared using the processing methods individually, they were still way below the required values of 2 – 12 MPa for cancellous bone [Hench, 1998].

In this chapter, the final results and experiments of **Chapter 4** have been extended with the aim of producing scaffolds with higher mechanical properties. Zirconia is used as the scaffold material. This is because zirconia is well known for its excellent mechanical

properties in load bearing applications as discussed in the literature review of this thesis. Also with zirconia, it is possible to tailor the suspension into any appropriate concentration unlike the nano-HA suspension which had a maximum particle content of 18 wt%, which still required dilution in order to be electrosprayed. In **Chapter 4**, ultimately most experiments were carried out on a 15 vol% (57.1 wt%) ZrO_2 suspension. The zirconia suspension used in this chapter is of identical composition to that in **Chapter 4**. The suspension properties of this 15 vol% (57.1 wt%) zirconia are investigated in this chapter.

This chapter describes how electrospraying has been manipulated to enhance its efficiency and the effects of spraying time on the pore size and strut thickness of the sintered zirconia scaffolds have been investigated by examining their morphologies on the sprayed and inner-most surfaces as well as their mechanical properties. The effects of changing and modifying the sacrificial template by subjecting the templates to various pre-treatment methods, on the microstructure and mechanical properties of the sintered zirconia scaffolds are also investigated. It is the objective to achieve porous scaffolds of mechanical strength similar to that of cancellous bone.

Provided it is possible to obtain bioinert zirconia structures of desirable mechanical properties, an attempt to make these scaffolds bioactive by incorporating nano-hydroxyapatite (nHA) will be investigated. The bioactivity and biostability of these composite scaffolds are investigated using simulated body fluid (SBF).

6.1 Electrohydrodynamic atomisation of zirconia (15 vol%) suspension

6.1.1 Zirconia (15 vol%) suspension preparation

Following on from **Chapter 4**, where a 15 vol% zirconia suspension was used, it was decided to use a suspension of the same concentration and composition due to the favourable results obtained. This 15 vol% (57.1 wt%) zirconia suspension was prepared as detailed in **Chapter 3** (**Section 3.1.2**).

6.1.2 Zirconia (15 vol%) suspension characterisation

The suspension properties such as density, surface tension, viscosity and DC electrical conductivity were measured using the characterisation equipment described in **Chapter 3** (**Section 3.2**). All characterisation equipments were calibrated using ethanol and the measurements were taken at ambient temperature. **Table 6.1** compares the zirconia suspension properties with the values obtained for ethanol.

Table 6.1 Zirconia (~15 vol%) suspension properties

Property	**Ethanol**	**15vol% ZrO_2 suspension**
Density /kgm^{-3}	790	1560
Surface tension /mNm^{-1}	23	28
Viscosity /mPas	1.3	62
Electrical conductivity /Sm^{-1}	3×10^{-4}	9×10^{-4}

6.1.3 Mode selection map

The equipment set-up for electrospraying is shown in **Figure 6.1** and a stainless steel needle of outer and inner diameters 1100 µm and 810 µm respectively, was used. A stainless steel ring, 25 mm in diameter was used as the ground electrode which was placed approximately 10 mm below the needle exit, which was the same distance at which the polymeric template was rotated during the electrospraying experiments.

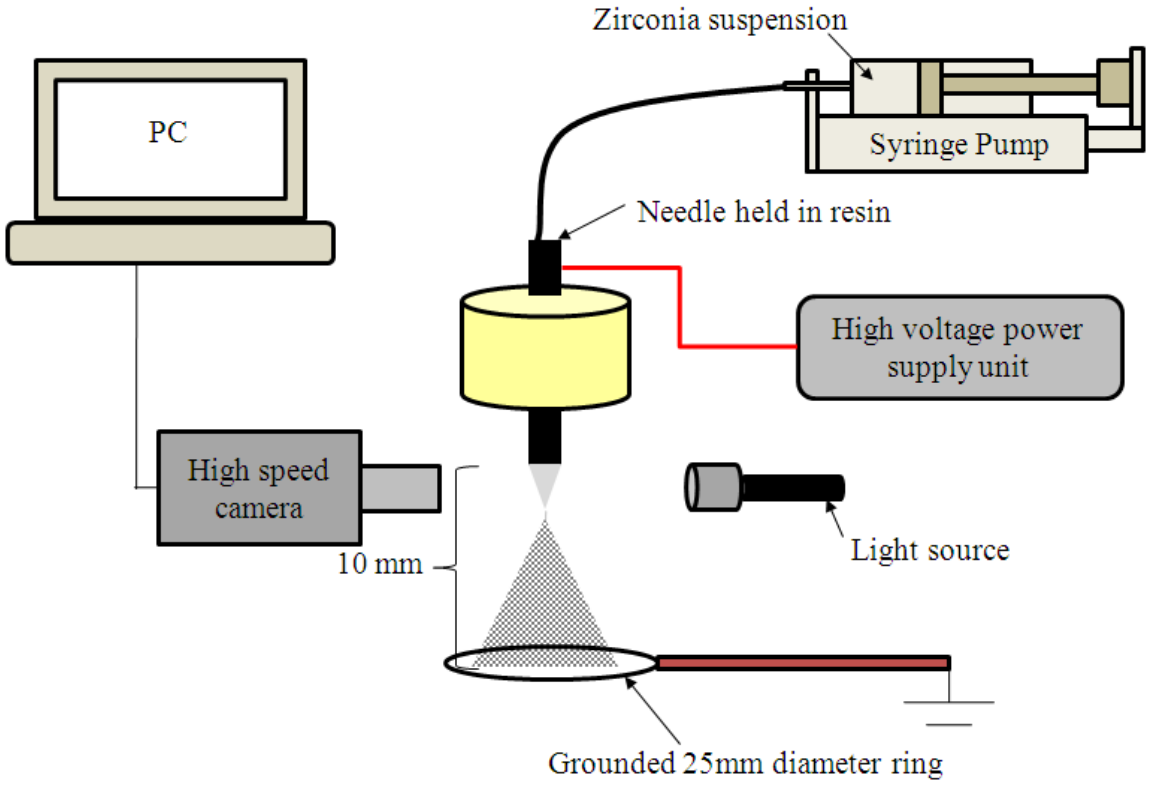

Figure 6.1 Equipment set-up for plotting the mode selection map for the 15 vol% zirconia suspension

The flow rate of the 15 vol% ZrO_2 suspension was varied systematically and different modes of atomisation were observed with increasing applied voltage. When the applied

voltage was low, dripping mode was observed and the mode was changed to microdripping mode with increasing voltage. With further increase of applied voltage, other atomisation modes, such as unstable cone-jet, stable cone-jet and multi-jetting were observed. This different mode of jetting occurring at a range of flow rates and voltages were plotted and is termed a 'mode selection map' (**Figure 6.2**). This map helps to determine a suitable flow rate and a corresponding voltage range for electrospraying experiments. The stable cone-jet mode at a flow rate of 100 µlmin^{-1} was stable over a voltage range of 6.3 - 9.4 kV.

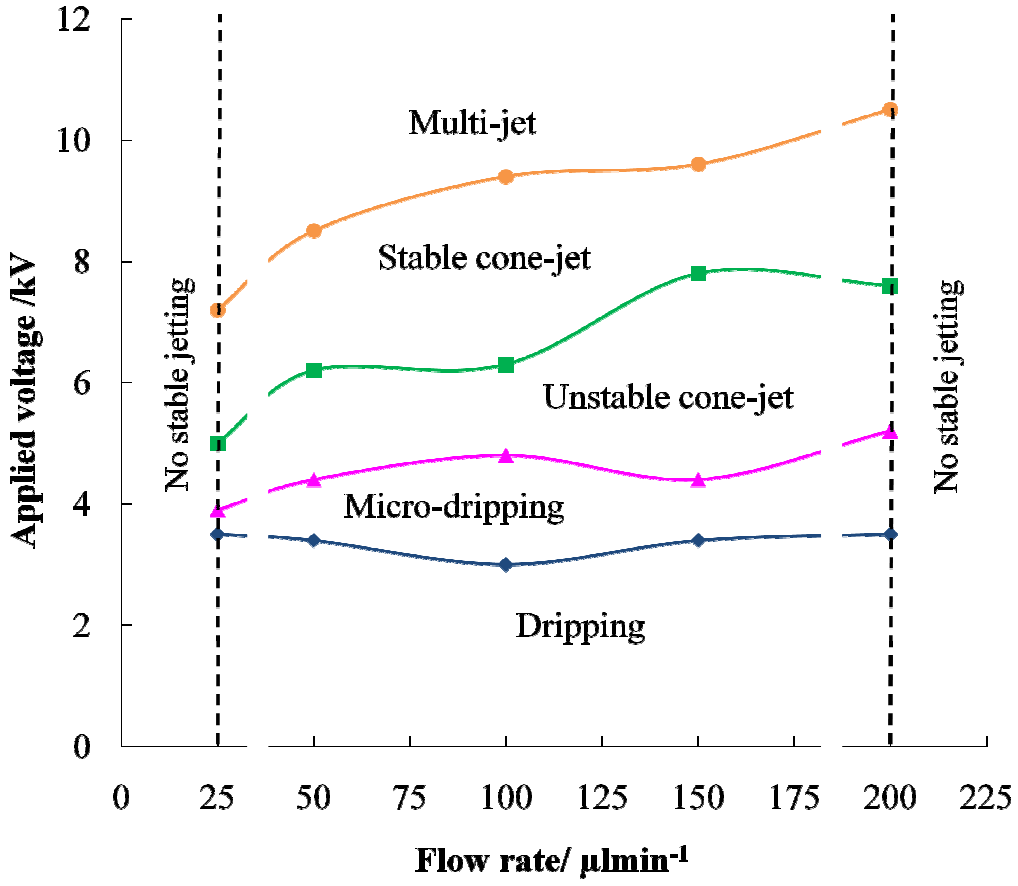

Figure 6.2 Mode selection map for 15 vol% zirconia suspension showing different modes of atomisation observed at varying voltage at a selection of flow rates

6.2 Template modification

Polyurethane (PU) templates of porosity 45 ppi and 60 ppi were cut into rectangular prismatic samples of 5 mm × 5 mm × 10 mm dimensions for all the experiments.

Gold coating: The polyurethane (PU) templates were gold sputter coated (Emscope, SC500M, Kent, UK) for 2 minutes on opposite sides, thus 4 minutes of total exposure time.

Surface hydroxylation: PU templates were immersed in a 10% (w/v) aqueous solution of potassium peroxodisulfate (PPDS) (≥ 99%, Sigma Aldrich, UK) at a temperature of 70°C for 2 hours. The immersed templates were allowed to dry completely in air for a few days prior to use in experiments.

Some of the PPDS treated and dried templates were sputter coated in gold for a total of 4 minutes. All templates were dipped in ethanol and the excess was squeezed out prior to electrospraying. PU templates dipped in ethanol were used as the control.

6.3 Set–up of the experimental parameters

The equipment set-up for electrospraying is as shown in **Figure 6.3** which is similar to that used to obtain the mode selection results. The modifications being that the ring was replaced by a mechanical rotating device to which the ethanol dipped polymeric foam was attached. This mechanical rotating arm was also grounded in order to attract the charged zirconia droplets during the atomisation. The rotating device which was battery

operated, was used to allow uniform coating of the ceramic suspension on all sides of the template. The working distance, *i.e.* the distance between the surface of the foam and needle exit was approximately 10 mm, which was the closest distance the template could be placed without interfering with the stability of the jet.

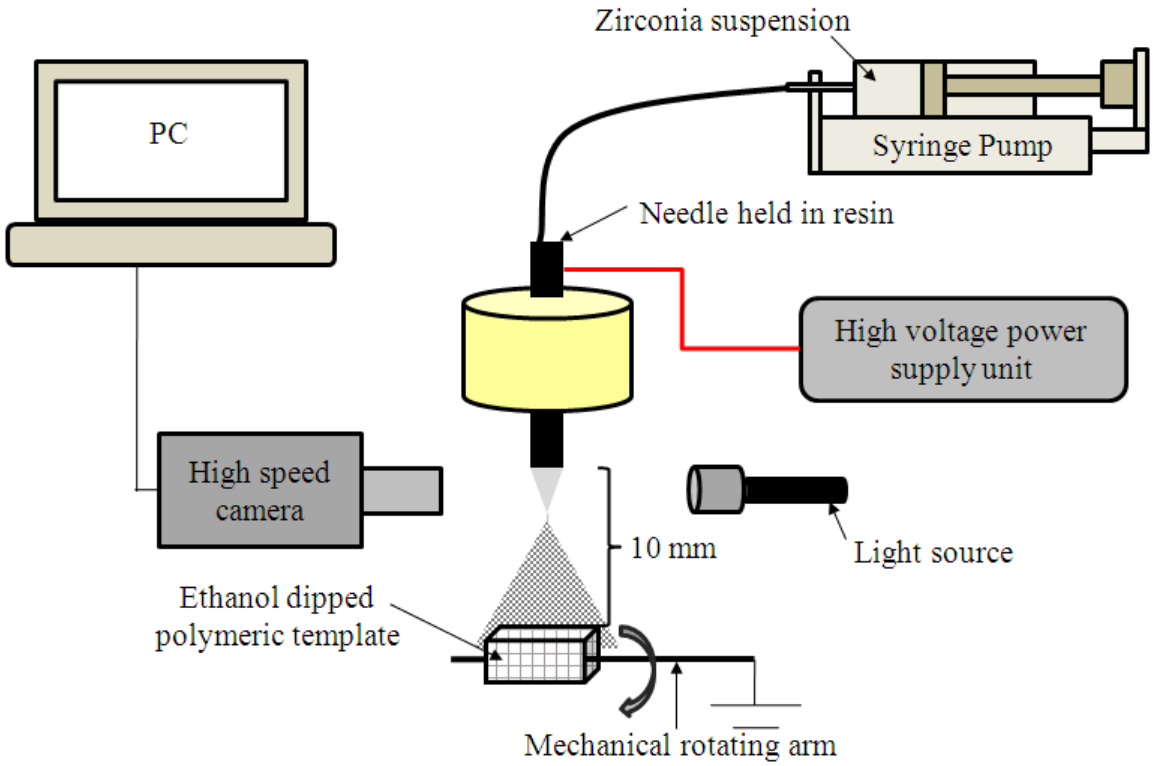

Figure 6.3 EHDA set-up for processing of zirconia scaffolds

A flow rate of 100 µlmin^{-1} and the voltage for the cone-jet mode was set at 6.3 kV. The higher flow rate of 100 µlmin^{-1} was chosen to produce charged droplets at a higher frequency which would make the process more efficient. Also from the mode map (**Figure 6.2**) it can be observed that at this flow rate, the cone-jet mode appears to be

stable over a wider voltage range. **Figure 6.4** shows an image of the cone-jet mode observed at these conditions and was obtained using a high-speed camera.

The PU templates were electrosprayed for 5 minutes and the control templates (*i.e.* ethanol dipped only) were electrosprayed for a further 10 and 15 minute intervals to investigate the effect of spray time on the morphology and mechanical properties. The electrospraying was carried out at ambient temperature. The green bodies were air-dried, the template pyrolysed at 400℃ and then sintered to a maximum temperature of 1450℃ according to the heating program described in **Chapter 3** (**Section 3.5**).

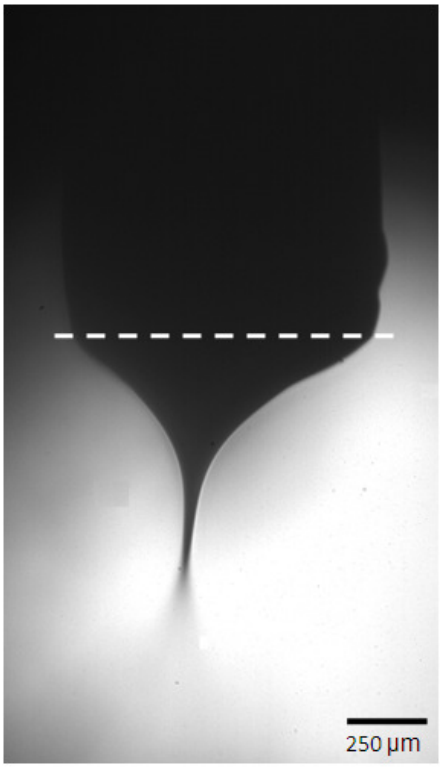

Figure 6.4 Cone-jet mode at a flow rate of 100 µlmin^{-1} and voltage of 6.3 kV. The dotted line indicates the needle exit.

6.4 Sample characterisation

6.4.1 Morphology and microstructure

The morphology and the microstructure of the sintered foams were characterised using a Hitachi S-3400N scanning electron microscope (SEM) and both the sprayed and interior surfaces of the sintered bodies were imaged at the conditions explained in **Chapter 3** (**Section 3.7.4**).

6.4.2 Porosity measurement

The total porosity (p) of scaffolds was calculated using the following equation as explained in **Chapter 3** [Gibson and Ashby, 1997b]:

$$p = 1 - \frac{\rho_{foam}}{\rho_{solid}} = 1 - \rho_{relative} \qquad \textbf{(Eq. 3.3)}$$

where ρ_{solid} = 6000 kgm^{-3} is the density of solid zirconia as supplied by the supplier. The density of the scaffolds (ρ_{foam}) was determined from the mass and dimensions of the sintered bodies.

The accuracy of these total porosity measurements was further verified by measuring the true density of the samples using a helium pycnometer, AccuPyc 1330 (Micromeritics), using a known mass of foam as explained in **Chapter 3**. The porosity was calculated using:

$$Porosity\% = 100 - \left[\frac{100 \times Bulk\ Density\ (1 - Moisture\ Content)}{True\ Density}\right] \qquad \textbf{(Eq.3.4)}$$

where the bulk density = mass of sample/ bulk volume of the sample. Moisture content of these samples was assumed to be insignificant as the samples were sintered and kept dry. The bulk volume of the samples was calculated from the dimensions.

The inner and outer porosities were roughly estimated using the SEM images. This was carried out by calculating the pore area and making a comparison to the total area.

6.4.3 Mechanical testing

The samples were tested for their compressive strength using the testing method described in **Chapter 3** (**Section 3.7.5**) using a cell load of 1 kN and a crosshead speed of 0.5 mm/min. Six samples for each category were tested to obtain an average measurement of compressive strength.

6.5 Analysis on the influence of spraying time

6.5.1 Structure

Figure 6.5 shows the change in pore structure on the electrosprayed surfaces with increased spraying time. The scaffolds sprayed for 5 minutes had a reduced amount of blocked pores and seemed to exhibit an interconnected network of pores. However, with increased spraying time, the pores on the outer surface gradually became smaller and at 15 minutes, the sprayed surface seemed to be completely covered by the ceramic coating such that it was not possible to observe any distinct struts. It can also be observed from the SEM images that the interconnectivity of the pores on the sprayed surface has an inversely proportional relationship to the spraying time.

Table 6.2 compares the variation of the average pore size and strut thickness at different spraying times, using 50 data points. The standard deviation is relatively large for the pore size. This is due to the dodecahedral shaped arrangement of the cellular packing in the PU templates. This means that each pore consists of 12 cell windows on its wall, which are about two to three times smaller than the total size of the associated cell [Chen *et al.*, 2006a]. This characteristic was explained and verified in **Chapter 3** (**Table 3.1** and **Figure 3.1**). Therefore, for each spraying condition, the maximum and minimum pore size and the strut thickness were noted to observe the general trend of the pore size distribution. The pores were larger in the samples that were sprayed for 5 minutes and the average pore size decreased with increasing spraying time. It is more than likely that this phenomenon is due to the increase in the deposition of the ceramic coating on the struts leading to an increase in the strut thickness, as shown in **Table 6.2**.

Table 6.2 Comparison of the pore sizes and the strut thickness on the electrosprayed surface with increased spraying time (45 ppi PU templates)

Spraying time (min)	**Average outer pore (µm)**	**S. D.***	**Max outer pore (µm)**	**Min outer pore (µm)**
5	509	147	869	281
10	457	175	829	153
15	298	229	728	65
Spraying time (min)	**Average outer strut (µm)**	**S.D. ***	**Max outer strut (µm)**	**Min outer strut (µm)**
5	205	45	365	130
10	429	69	614	356
15	No distinct struts observed			

*S.D.: Standard Deviation

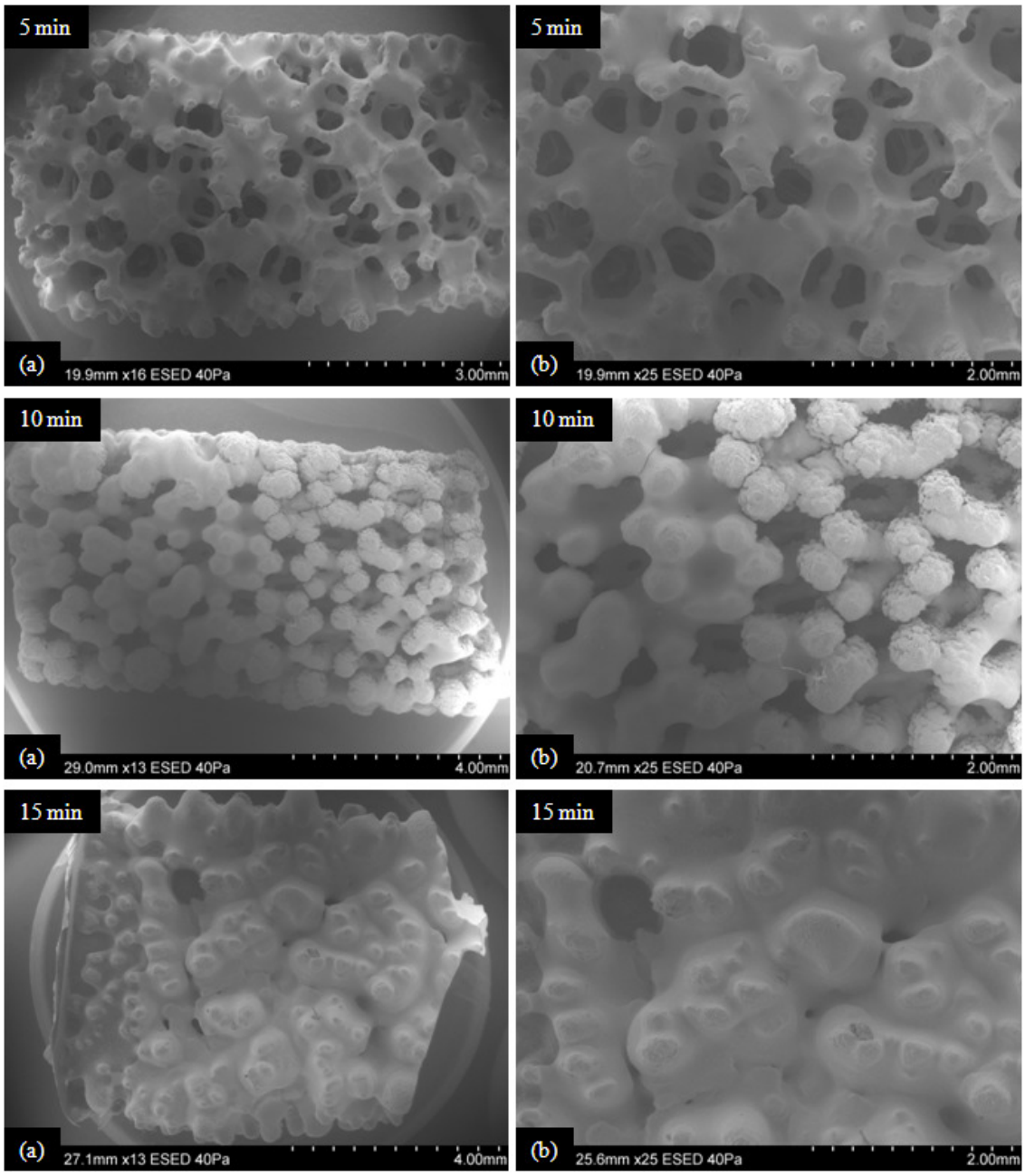

Figure 6.5 Influence of spraying time on the morphology of the sintered scaffolds. (a) indicates the overview of the sprayed surface and (b) indicates the structures at higher magnification

The sintered structures were fractured in the middle to expose the interior. **Table 6.3** shows the change in pore size and strut thickness of the interior surfaces of the sintered structures with varied spraying time. A similar trend to that of the sprayed surface was observed towards the interior, *i.e.* inverse relationship between the pore size and spraying time. The relationship between the pore size and spraying time in both the electrosprayed surface and the inner surface of the sintered scaffold can be seen clearly in **Figure 6.6**. However, the thickness of the struts seems to increase when the samples were electrosprayed for 10 minutes in comparison to the 5 minute sprayed samples, but decreased when electrosprayed for longer (**Table 6.3**). This could be due to the wide distribution of data, but it is also possible that it might be due to the increased thickness of the ceramic coating on the sprayed surface preventing sufficient coating of the inner struts. Pore networks were observed in the interior of all structures but it was clear that with increased spraying time, the outer wall thickness was increased (**Figure 6.7** and **Table 6.4**). When the samples were electrosprayed for 10 minutes it seemed to produce relatively thicker struts, but still with good interconnectivity (**Figure 6.7b**). The samples electrosprayed for 15 minutes would not find any uses as scaffolds since they would hinder the movement of cells and nutrients due to their dense (nearly non-porous) outer coating which was nearly twice that of scaffolds sprayed for 10 minutes (**Table 6.4**).

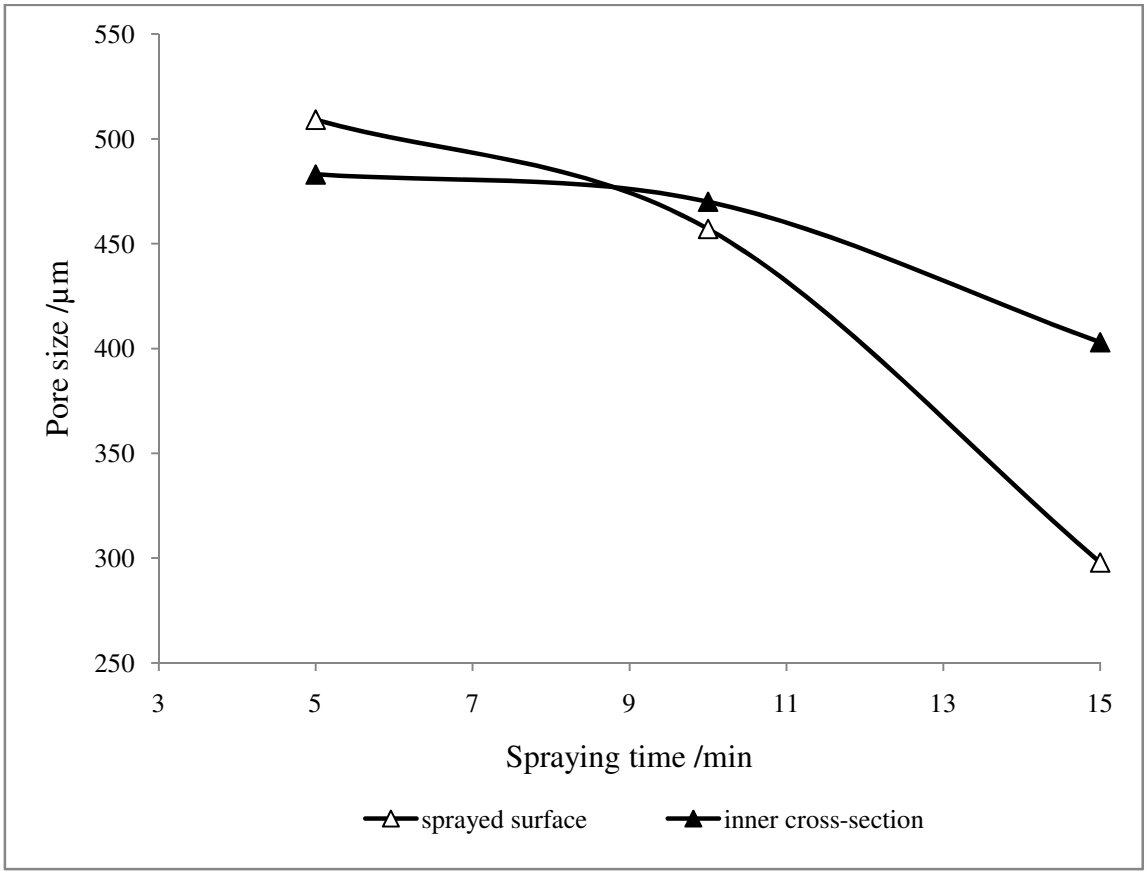

Figure 6.6 The pore size variation with increased spraying time on the electrosprayed surface and the inner cross-section of the sintered samples

Table 6.3 Comparison of the pore sizes and the strut thickness on the inner surface with increased spraying time (45 ppi PU templates)

Spraying time (min)	**Average inner pore (μm)**	**S. D.***	**Max inner pore (μm)**	**Min inner pore (μm)**
5	483	101	652	295
10	470	127	761	221
15	403	107	600	168
Spraying time (min)	**Average inner strut (μm)**	**S. D.***	**Max inner strut (μm)**	**Min inner strut (μm)**
5	103	31	204	74
10	154	35	221	96
15	114	21	161	88

*S.D.: Standard Deviation

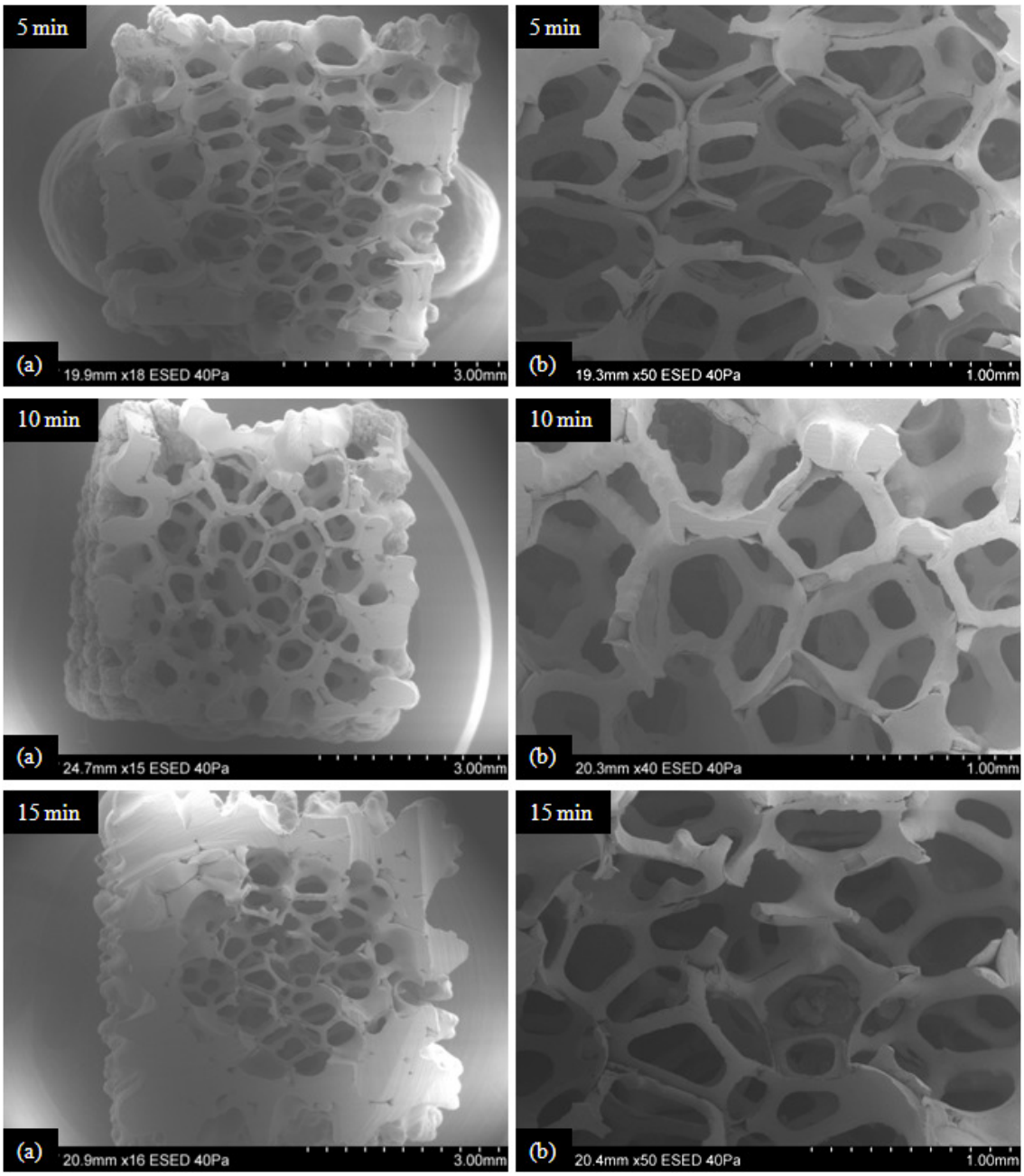

Figure 6.7 The inner surface of the sintered scaffolds with increased spraying time. (a) shows an overview of the inner structure with interconnected pores in the centre and an outer coating that increases in thickness with spraying time, while (b) shows the interconnected pore network in the centre of the scaffold at higher magnification

Table 6.4 The change in the outer wall thickness with increased spraying time (45 ppi PU templates)

Spraying time (min)	Average outer wall thickness (µm)	S. D.*
5	712	262
10	748	209
15	1338	351

*S.D.: Standard Deviation

It can be deduced using the SEM images from both the sprayed and inner surfaces of the scaffolds that the porosity would also decrease with increased spraying time. The total porosity values for the sintered structures were obtained using **Eq. 3.3** and are plotted in **Figure 6.8**. The porosity for the scaffolds sprayed for 5 minutes was calculated to be in the range of 83 – 85%, for 10 minutes to be 72 – 76% and for a 15 minute spray time, the total porosity was approximated to 60%. These values were similar to that obtained using **Eq. 3.4** from the true density measurements. The latter procedure is also an estimate since the bulk densities of the samples were calculated from the dimensions with the assumption that they were perfect rectangular cuboids.

Table 6.5 shows the inner and outer porosity values calculated using SEM images. The total pore area was deducted from the total image area and the porosity was estimated. This is only a rough estimate as it assumes that all the pores are on a two-dimensional

plane, which is not the case at all. Nevertheless, it shows that the internal porosity is much higher than that on the sprayed surface which can already be observed in **Figure 6.5** and **Figure 6.7**.

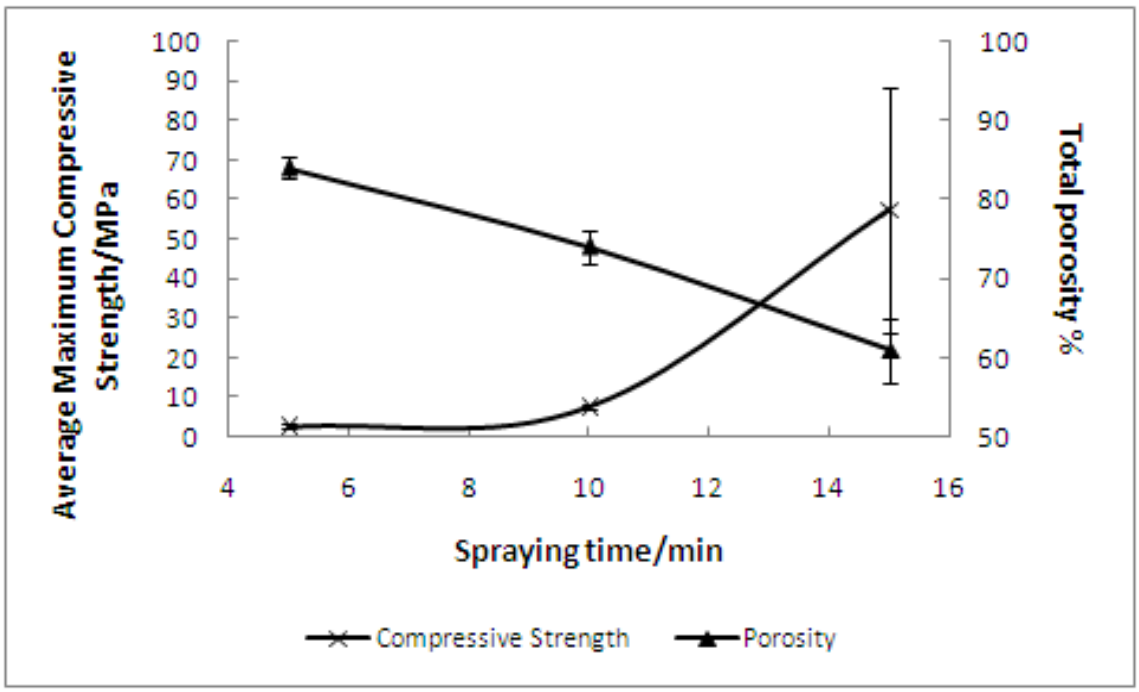

Figure 6.8 The increase in maximum compressive strength and decreased total porosity with increased spraying time (The S.D for: (i) the compressive strength values: 0.57, 0.57 and 31; (ii) total porosity values: 1.4, 2.0 and 4.0, for spraying times of 5, 10 and 15 minutes respectively, using 45 ppi templates)

Table 6.5 Estimate of inner and outer porosity with increased spraying time using the SEM images

Spraying time (min)	**Porosity on the inner surface (%)**	**Porosity on sprayed surface (%)**
5	70	37
10	62	22
15	65	8

6.5.2 Mechanical properties

The average compressive strength increased with spraying time and it was noticed that there was a large increase in the maximum compressive strength in the 15 minute sprayed samples (**Figure 6.8**). A load cell of 10 kN had to be used instead of the 1 kN and these samples withstood the force and failed at approximately 15% of the applied strain. This extreme increase in the mechanical strength is due to the thick and nearly non-porous coating on the sprayed surface of these samples (**Figure 6.5**). The standard deviation is also quite high as it seems that increase in spraying time leads to an increase in the non-uniformity of the outer coating which is the major contributor towards the increased compressive strength.

However, the samples that were prepared by electrospraying for 10 minutes, had a maximum compressive strength value averaged at 7.5 MPa (**Figure 6.8**). This is rather impressive for a ceramic scaffold with a reasonable porosity averaging 74%. The

relatively high compressive strength value is likely due to the relatively denser outer coating on these scaffolds, but they still maintain the desirable scaffold characteristics such as pore size and interconnectivity (**Figure 6.7**). **Figure 6.8** also shows the inverse relationship between the average maximum compressive strength and the total porosity.

6.6 Analysis on the influence of template

6.6.1 Structure

Two different types of PU templates, 45 ppi and 60 ppi were used, and this time, the surface of the template was subjected to modification. All the templates were electrosprayed for 5 minutes and sintered to a maximum temperature of 1450℃. The effects of modifying the templates and change of template on the pore structure and distribution were investigated. **Figure 6.9** shows the SEM images of the sintered scaffold structures under varied experimental conditions. **Table 6.6** shows the pore size range for each experimental condition which clearly shows the effects that would proceed to contribute to the mechanical properties discussed in the next section.

60 ppi foams seem to be more prone to blockages and this is due to the templates having a much smaller pore size in comparison to 45 ppi, thus covering and blocking the pores faster with identical spraying times (**Figure 6.9 a, b**).

Methods such as sputtering or evaporating a thin layer of a metallic bond–coating onto the polymeric foam to make the template conductive in order to enhance the attraction of the charged ceramic particles to increase the deposition and hence, further improve the microstructures is a suitable pre-treatment strategy. However, the metallic coating

should not impair the mechanical properties, toxicity and the bioactivity of the ceramic foam by reacting with it and has to be chosen with care. Gold has been used in dentistry for fillings, crowns and bridges, and has been used as early as 700 B.C. It is known to be chemically inert and is now being increasingly investigated for its use in medicine, especially in cancer diagnostics and therapeutics [Huang *et al.*, 2007]. It has been shown for gold to be biosafe and *in-vitro* studies have shown that gold nanoparticles do not cause cytotoxicity in human cells [Huang *et al.*, 2007, Connor *et al.*, 2005]. Therefore, the polymeric templates were sputter-coated with gold as a pre-treatment prior to being electrosprayed. It was observed that the structures produced using this method had a smaller pore size range compared to the control. A gold sputter-coater used to coat samples for SEM imaging was used for this investigation and the 4 minute exposure time gave a thin coating of gold on the PU template, improving its conductivity. Thus there is improved attraction of the charged zirconia droplets towards the more conductive PU templates thereby producing a thicker coating on the template struts.

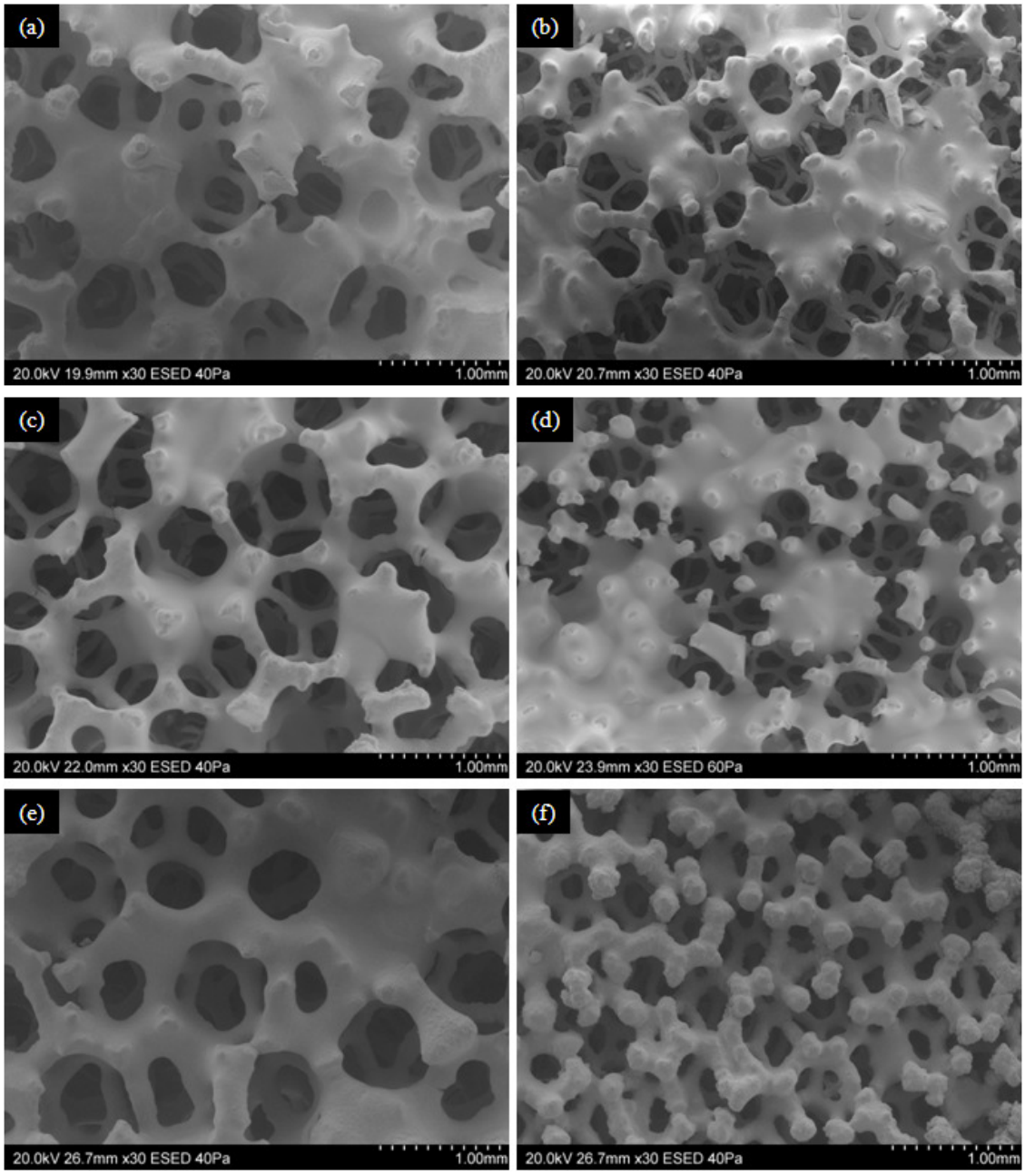
(a)
20.0kV 19.9mm x30 ESED 40Pa
1.00mm
(b)
20.0kV 20.7mm x30 ESED 40Pa
1.00mm
(c)
20.0kV 22.0mm x30 ESED 40Pa
1.00mm
(d)
20.0kV 23.9mm x30 ESED 60Pa
1.00mm
(e)
20.0kV 26.7mm x30 ESED 40Pa
1.00mm
(f)
20.0kV 26.7mm x30 ESED 40Pa
1.00mm

45 ppi 60 ppi

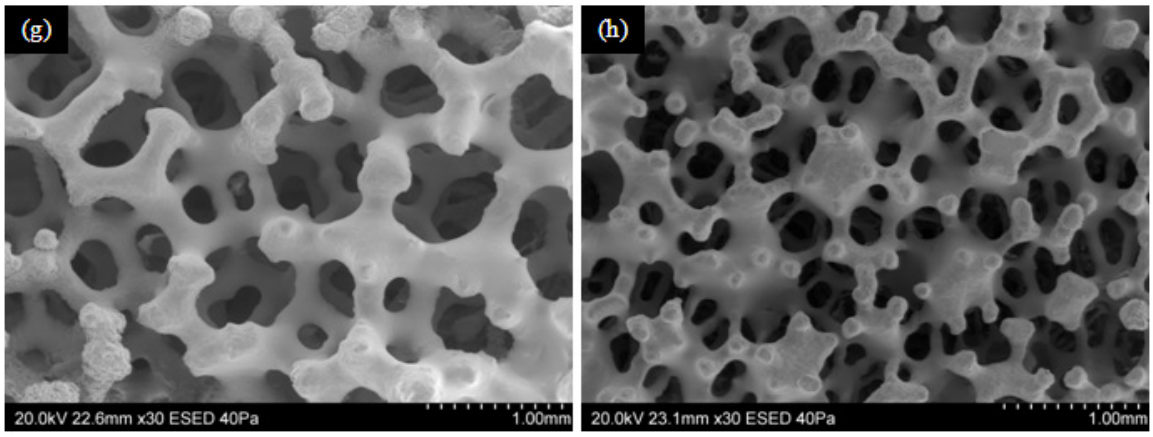

45 ppi 60 ppi

Figure 6.9 SEM images of the sintered structures showing the microstructures of the electrosprayed surfaces at different experimental conditions. Ethanol dipped (a, b); Gold+ethanol (c, d); PPDS+ethanol (e, f); PPDS+gold+ethanol (g, h)

Table 6.6 Effect of modification and type of polymeric template on the pore size of the sintered scaffolds (All samples electrosprayed for 5 minutes, n = 5, 50 data points averaged)

Experimental condition	**Average pore size range (µm)**	
	45 ppi	**60 ppi**
Ethanol (control)	280-870	260-650
Gold+Ethanol	298-650	200-450
PPDS+Ethanol	190-700	200-560
PPDS+Gold+Ethanol	250-600	190-380

Pre–treatment of the PU templates with PPDS seems to have encouraged a more uniform coating on the sprayed surface of the sintered structure (**Figure 6.9 e, f**). It also seems to have reduced the amount of blocked pores on the surface in comparison to the ethanol dipped and gold coated samples. This characteristic is seen clearly in the scaffolds made from 60 ppi templates comparing **Figure 6.9f** with **Figure 6.9b, d**. When the PPDS treated templates were gold sputter-coated, it lead to a reduction in the pore size (**Table 6.6**), due to the improved attraction of the charged ceramic droplets, but the amount of pore blocking was still less than the control and the structures prepared using gold coated templates (**Figure 6.9h**, compared with **Figure 6.9b, d**).

6.6.2 Mechanical properties

Figure 6.10 compares the average maximum compressive strength values obtained for the sintered zirconia scaffolds which were prepared by using two types of templates (45 and 60 ppi), subjected to different types of surface modification and electrosprayed for 5 minutes.

For the ethanol dipped 60 ppi templates, the maximum compressive strength was in the range of 1.1 – 1.3 MPa. When the templates were gold coated, the mechanical strength was increased in the resulting sintered structure and was in the range 1 – 2 MPa. The templates which were pre-treated with PPDS resulted in even better mechanical properties ranging between 1.4 – 3 MPa. When the PPDS treated templates were gold sputter coated and then electrosprayed, the mechanical properties were further improved to range between 2.5 – 6 MPa.

A similar trend was followed by the sintered structures that were produced using 45 ppi polymeric templates. It was also observed that 45 ppi templates had increased mechanical strength in comparison to their experimentally matching counterparts of 60 ppi templates. This is most likely due to 45 ppi having a larger cell range, thus enabling more ceramic droplets to penetrate into the template. The time taken to block the sprayed surface is longer than for the 60 ppi templates, therefore again increasing the amount of charged droplets penetrating into the interior of the 45 ppi template. It can also be pointed out that the 60 ppi templates have higher porosity in comparison to the 45 ppi templates of identical size. Increased porosity in the template could pose another likely cause for the reduction in mechanical strength compared to the samples prepared using the 45 ppi templates.

In the research carried out in **Chapter 4**, the improvement of coating ability of the ceramic slurry on the template by immersing the template in ethanol, prior to electrospraying was demonstrated. This has made the electrospraying method more efficient by significantly reducing the spraying time to a few minutes rather than the 1 – 2 hours as in the literature [Jayasinghe and Edirisinghe, 2002b, Chen *et al.*, 2006a]. This method has also managed to produce porous foams with an average compressive strength of 7.5 MPa, with good pore interconnectivity, within 10 minutes in comparison to the 0.4 – 3 MPa values obtained from foams, electrosprayed for 2 hours using a 20 vol% zirconia suspension [Chen *et al.*, 2006a].

By sputter coating the templates with gold, the templates are made conductive and it can be assumed the charged ceramic droplets are more attracted towards the foam. This could be the reason for the increase in the average mechanical strength in comparison to scaffolds only dipped in ethanol. Pre-treatment of the polymeric templates using PPDS (10% w/v) increased the mechanical strength in comparison to the gold coated scaffolds. PPDS is known to hydroxylate the polymeric template and has been used in the literature to improve the coating on polymeric surfaces [Korematsu *et al.*, 2002]. The increase in mechanical properties is more obvious between the gold coated and PPDS treated 60 ppi templates than the 45 ppi. This could also be due to a reduced amount of blocked pores and a near-uniform coating on the surface of the structures from (**Figure 6.9f**) PPDS treated 60 ppi templates.

Electrospraying was also carried out on templates which were treated with PPDS and then gold sputter coated. It was observed that the average maximum compressive strength increased by a factor of 2, for the 45 ppi and 60 ppi templates, in comparison to the templates only treated with PPDS. The hydroxylated template surface ensures that the coating of the ceramic suspension is near-uniform, while the introduction of gold improves the conductivity of the templates, thus increasing the attraction of the charged zirconia droplets. This results in a structure with thicker struts and smaller pores, but they are well within the range to be considered for tissue engineering applications (**Table 6.6**).

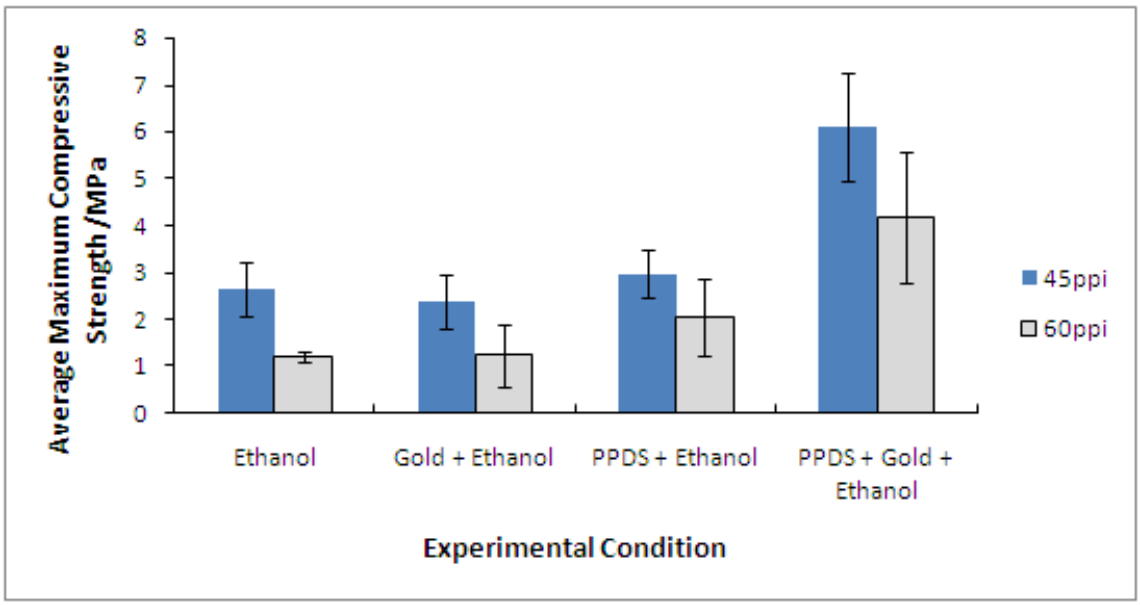

Figure 6.10 Comparison of the average maximum compressive strength (in MPa) for the sintered scaffolds obtained by electrospraying on two types of templates subjected to different types of surface modification (n = 6, electrospraying time = 5 min)

6.7 Introduction of bioactivity into zirconia scaffolds

It was explained in the literature review how HA continues to receive much attention in bone TE area due to its excellent osteoconduction and bone bonding ability to the surrounding tissue but HA is also however inherently brittle. Due it being the major inorganic component of natural bone, HA is often used in conjunction with another material which fulfills the mechanical property requirement in a bone TE scaffold. There has been extensive research into incorporating HA into chitosan [Kong *et al.*, 2006], collagen [Wahl and Czernuszka, 2006], synthetic polymers [Kim *et al.*, 2007b, Zhao *et al.*, 2008] and even other bioceramics such as zirconia [Kim *et al.*, 2004a, Kim *et al.*, 2004b, Kim *et al.*, 2003, Quan *et al.*, 2008] to make composite scaffolds in order to attempt to fulfill the bioactivity criteria as well as mechanical integrity.

It was discussed in the literature review of this thesis how it is believed that HA in its nano–scale form would have better osteoblast adhesion, differentiation and proliferation due to their resemblance to the morphology of the mineral crystals found in bone, than microcrystalline HA. The nano-HA for the research in **Chapter 5** has been characterised and utilised successfully in previous work [Thian *et al.*, 2008a] and has shown favourable cellular responses.

It has been possible to produce porous zirconia scaffolds of compressive strength in the desirable range of 2 – 12 MPa by electrospraying for only 10 minutes. In comparison to the literature, the mechanical properties of the scaffolds produced in this research are much higher and the process was made much more efficient by incorporating a medley of modifications such as template modification and ground electrode configuration. Despite meeting the mechanical strength requirement, for these scaffolds to be considered for bone TE applications, it is desired for the scaffold to be able to positively interact with the host tissue and promote tissue growth. However, zirconia is a bioinert material which does not interact with the surrounding tissue. Therefore, it was attempted to coat the sintered zirconia scaffolds with a nHA suspension in order to introduce the bioactive component to these mechanically strong scaffolds.

A suspension of suitable nHA particle concentration had to be chosen, which had to be kept low as it should not block the existing pores on the sintered zirconia scaffold. The bioactivity of the nano-HA coated zirconia scaffolds was investigated using simulated body fluid (SBF). The SBF testing is a standard procedure for evaluating the bone-

bonding ability of a material by examining the ability to form apatite on its surface upon immersion in SBF with ion concentrations nearly equal to that found in human blood plasma [Kokubo and Takadama, 2006].

6.7.1 Sample preparation

6.7.1.1 Zirconia scaffolds

45 ppi PU templates of dimensions, 5 mm × 5 mm × 10 mm were electrosprayed with a 15 vol% zirconia suspension for 10 minutes at a flow rate of 100 $\mu l min^{-1}$ and voltage of 6.3 kV. The equipment set-up shown in **Figure 6.3** was used for the electrospraying. The green bodies were air-dried, the template pyrolysed at 400℃ and then sintered to a maximum temperature of 1450℃ according to the heat treatment programme described in **Chapter 3** (**Section 3.5**).

6.7.1.2 Zirconia–HA composite scaffolds

The original nHA 18 wt% aqueous suspension was diluted in ethanol to obtain a suspension of 2 wt% nHA loading. The sintered zirconia scaffolds were dipped in the nHA suspension for 5 minutes, were heat treated to a maximum temperature of 600°C at a heating rate of 2℃/min, with a dwelling time of 2 hours before the scaffolds were cooled to room temperature at a cooling rate of 5℃/min.

The nHA particle concentration was further increased to 4 wt%. The already sintered zirconia scaffolds were then immersed for 10 minutes in the nHA suspension, air-dried

and heat treated to a maximum temperature of 600°C at a rate of 2°C/min with a dwelling time of 2 hours and then cooled down to room temperature at 5°C/min.

6.7.2 Assessment of bioactivity in SBF

The SBF solution was prepared as instructed by Kokubo and his colleagues and is described in **Chapter 3** (**Section 3.1.4**). Each foam was placed in a centrifuge tube separately, and 30ml of SBF was added and placed in an incubator at a controlled temperature of 37°C. The volume of SBF for testing was calculated using the following equation [Kokubo and Takadama, 2006]:

$$Vs = S_a/10 \qquad \textbf{(Eq. 6.1)}$$

where V_s is the volume of SBF (ml) and S_a is the surface area of the specimen (mm^2). Using the dimensions of the templates, the volume of SBF was calculated to be 25 ml but according to Kokubo and co-workers (2006), the SBF volume should be greater than the calculated volume. Thus, an SBF volume of 30 ml was used for each foam.

Ten samples from each type (zirconia and zirconia-HA) were extracted after 7, 14 and 28 days, rinsed with distilled water three times and then allowed to dry naturally. SBF was replaced weekly since the cation concentration is known to decrease due to the changes in the chemistry of the samples.

Also as a control for monitoring the apatite growth on the surface of the structure, bioglass scaffolds which were prepared by dip–coating were also immersed in SBF

solution and were extracted after 7, 14 and 28 days, rinsed with distilled water and allowed to dry naturally.

6.7.3 Sample characterisation

The morphology and microstructure were observed for the apatite growth using the field emission scanning electron microscope described in **Chapter 3**. The samples were gold sputter coated for 2 minutes and an accelerating voltage of 5 kV was used for imaging.

The porosity of the zirconia and the composite scaffolds were calculated using helium pycnometry and **Eq. 3.4** (**Chapter 3**).

The crystalline phase present in the zirconia and composite scaffolds as well as detection of any apatite growth in the latter was observed using X-ray diffraction described in **Chapter 3**.

The samples were tested for their compressive strength using the testing method described in **Chapter 3** (**Section 3.7.5**) using a cell load of 1 kN and a crosshead speed of 0.5 mm/min. Six samples for each category were tested to obtain an average measurement of compressive strength.

6.7.4 Results and discussion on the bioactivity assessment of the composite scaffolds

The as-received nHA suspension was water based and had approximately 18 wt% nHA particle loading. Even though the solid content of this nHA aqueous suspension was

relatively low, it had a paste-like consistency. The nHA suspension was modified to contain a lower solid loading because the nHA was only used to make the scaffolds more cell-friendly due to its osteoconductive nature, without extensively blocking the pores. Also, the sintered zirconia scaffolds that were to be infiltrated by the nHA, which unlike the polymeric templates, would not allow squeezing out the excess slurry and the nHA suspension required the ability to reach the interior of the sintered zirconia scaffolds.

Initially, the modified nHA ethanol based suspension had a particle content of 2 wt% and the sintered zirconia scaffolds were immersed in this nHA suspension for 5 minutes. After sintering again up to 600°C, SEM was carried out to investigate the HA coating on the zirconia scaffold. It was observed that the coating was not uniform which was verified by an elemental map and analysed using INCA software. Thus, the nHA particle content of the suspension was increased to 4 wt% and the scaffolds were immersed for 10 minutes prior to sintering up to a maximum temperature of 600°C.

If there is a mismatch in the thermal expansion coefficient, the materials are known to contract at different rates during the cooling process after sintering. This will generate thermal stresses and cause cracking. Thus, it is preferred to use materials with similar thermal expansion coefficients. The thermal expansion coefficient for HA is ~ 16.9×10^{-6} /℃, compared to ~10×10^{-6} /℃ for yittria stabilised zirconia [Guo *et al.*, 2003]. In a simple model of a bilayer structure, the layer with a higher thermal expansion coefficient will experience a tensile stress during cooling and the layer with a lower

thermal expansion coefficient will experience a compressive stress [Guo *et al.*, 2003]. So basically, during cooling, tensile stress tends to be developed in the HA layer [Guo *et al.*, 2003]. However, in the composite scaffolds, the zirconia was sintered at a high temperature of 1400°C prior to the nano-HA coating. According to Kalita *et al*. (2007) nanostructured ceramics could have the advantage of being sintered at lower temperatures. This theory did not work for the sintering of HA scaffolds in **Chapter 5**, but since in this work, we are only trying to attach the nHA onto the already sintered zirconia scaffold, it was decided to sinter the nHA coated zirconia scaffold to a maximum temperature of 600°C. Therefore, due to this much lower temperature, there should not be any thermal stresses and cracking due to the thermal expansion coefficient mismatch.

Although it is expected that pure HA will remain stable until above 1300°C, it is believed that the HA tends to decompose into TCP second phases well below 1300°C in the presence of zirconia (ZrO_2) [Kim *et al.*, 2002, Evis, 2007]. This characteristic was investigated by Evis (2007) where it was reported that the decomposition of HA during sintering at 1100°C and 1300°C was increased with the addition of zirconia. It was believed that this decomposition involved the exchange of Ca^{2+} and ZrO^{2+} ions between HA and zirconia, where the larger ZrO^{2+} ions cause swelling of the HA structure, which induces strain, thus increasing the rate of decomposition of HA [Evis, 2007]. It is also important to add that water, which is generated as a by-product of the HA decomposition leads to increased porosity of the sintered composites, reducing their mechanical properties [Evis, 2007]. It was also reported in 2006 by Evis *et al*. that

increased osteoblast adhesion could be achieved on HA-zirconia ceramic composites which were sintered at lower temperatures of 900°C for 1 hour [Evis *et al.*, 2006].

Porosities of the sintered scaffolds were calculated by measuring the true density and using **Eq. 3.4**. Five samples were evaluated and average porosities were obtained for each category of zirconia and zirconia-HA composite scaffolds. For the zirconia–HA composite scaffolds, the porosities were evaluated before and after coating with the nHA suspension. The sintered zirconia scaffolds which were prepared by electrospraying for 10 minutes had an average porosity of 74% (±2). Before coating the sintered scaffolds, the porosities of the zirconia scaffolds were maintained at an average of 74% (±2) and this value was reduced to 68% (±2.2) after coating with nHA suspension and sintering at 600°C again. The reduction in porosity could be due to the repeated sintering of the bioceramic scaffolds increasing the densification of the structures and also some of the pores in the zirconia scaffold getting blocked as a result of the nHA coating.

6.7.4.1 Mechanical properties

Figure 6.11 shows the average maximum compressive strength observed in the zirconia and zirconia-HA composite scaffolds after immersion in SBF for 0, 7, 14 and 28 days. The mechanical properties of the zirconia scaffolds remain similar ranging between 7 – 7.6 MPa throughout the experiment, showing the inert nature of the scaffold material. Overall, the compressive strength for the composite scaffold has been increased in comparison to that of zirconia-only scaffolds. This increase could be the result of one or

many of the following factors. The introduction of an additional material (HA) will increase the density of the structure and sintering twice even at a lower temperature could make the scaffolds much stronger due to increased densification of the structure. This could also result in compromising the porosity of the scaffold, but there was not an extreme reduction in the porosity values as calculated using helium pycnometry. It is also possible that the slight increase in the mechanical properties with increased days immersed in the SBF could be a result of the additional apatite formation of the scaffold making the scaffolds stronger.

6.7.4.2 X-Ray diffraction

X-ray diffraction was carried out on the two types of scaffolds to observe any phase changes due to any reaction with SBF. **Figure 6.12** shows the XRD spectra for the zirconia scaffolds immersed in SBF. All the major peaks correspond to zirconia and the spectra seem unchanged and the SBF seems to have made no impact on scaffold structure. This further reinforces the bioinert characteristic of zirconia.

Figure 6.13 shows the XRD spectra for the zirconia-HA composite scaffolds. At 0 days, HA peaks are detected due to the nHA coating. At 7 days, there are some additional HA peaks, which could be due to the extra apatite growth on the scaffold surface due to the interaction with the SBF. Most of these extra apatite peaks are maintained at 14 and 28 days. Therefore, it can be deduced that the introduction of HA (4 wt%) into bioinert zirconia has made the scaffold bioactive and positively responsive towards the physiological environment.

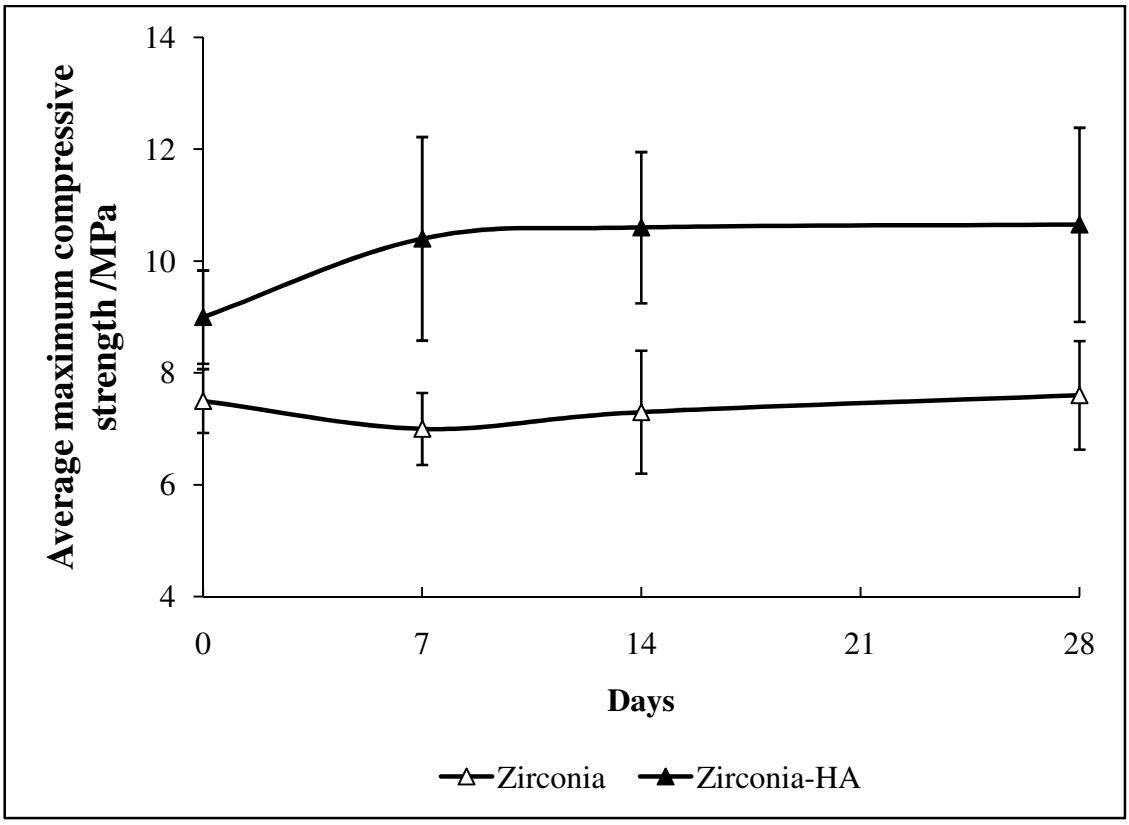

Figure 6.11 Investigation of the average maximum compressive strength of the zirconia and zirconia-HA composite scaffolds immersed in SBF for 0, 7, 14 and 28 days (The S.D. for the (i) zirconia scaffolds: 0.57, 0.64, 1.1 and 1; and (ii) zirconia-HA scaffolds: 0.83, 1.8, 1.3 and 1.7)

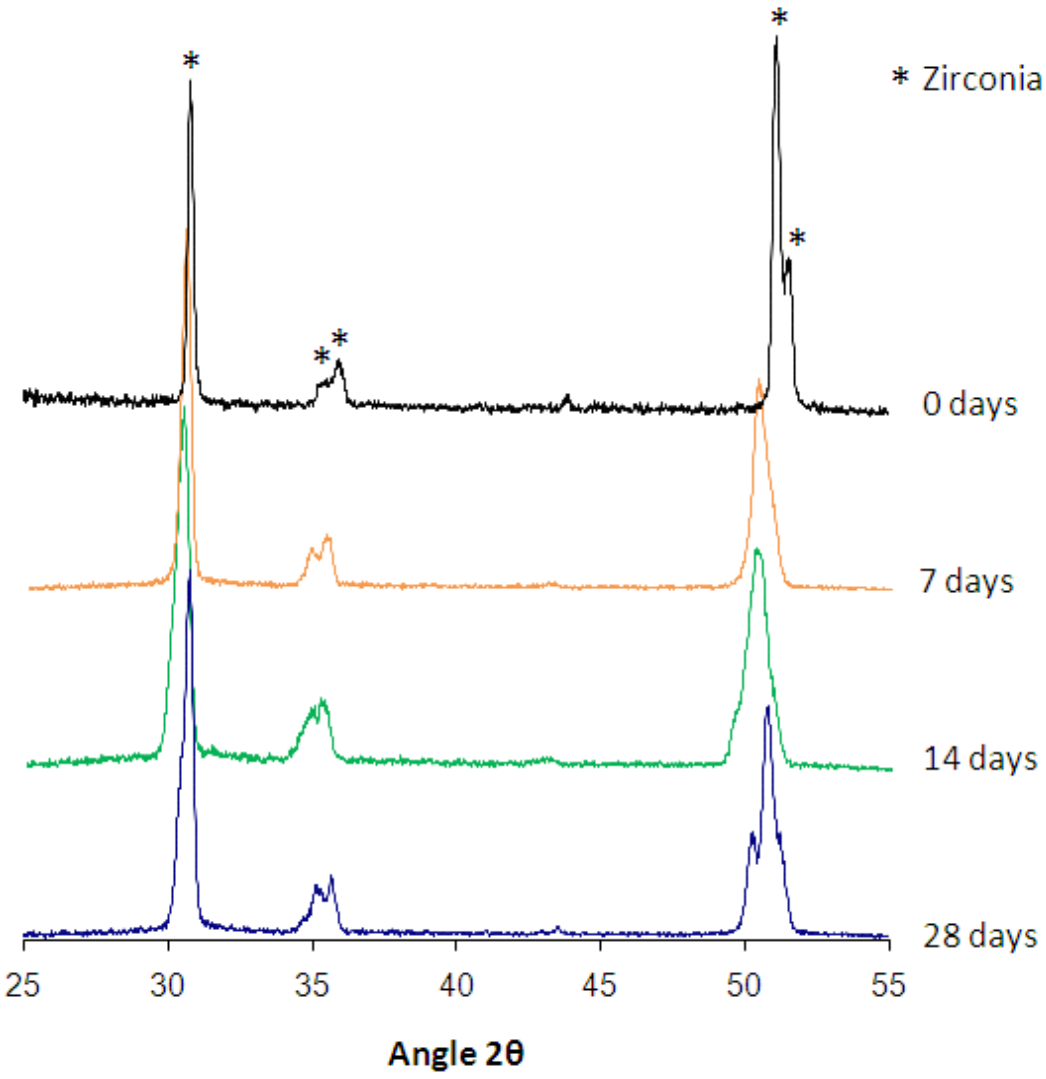

Figure 6.12 XRD spectra of the zirconia scaffolds immersed in SBF for 0, 7, 14 and 28 days. All the major peaks were identified as zirconia with no other phase present.

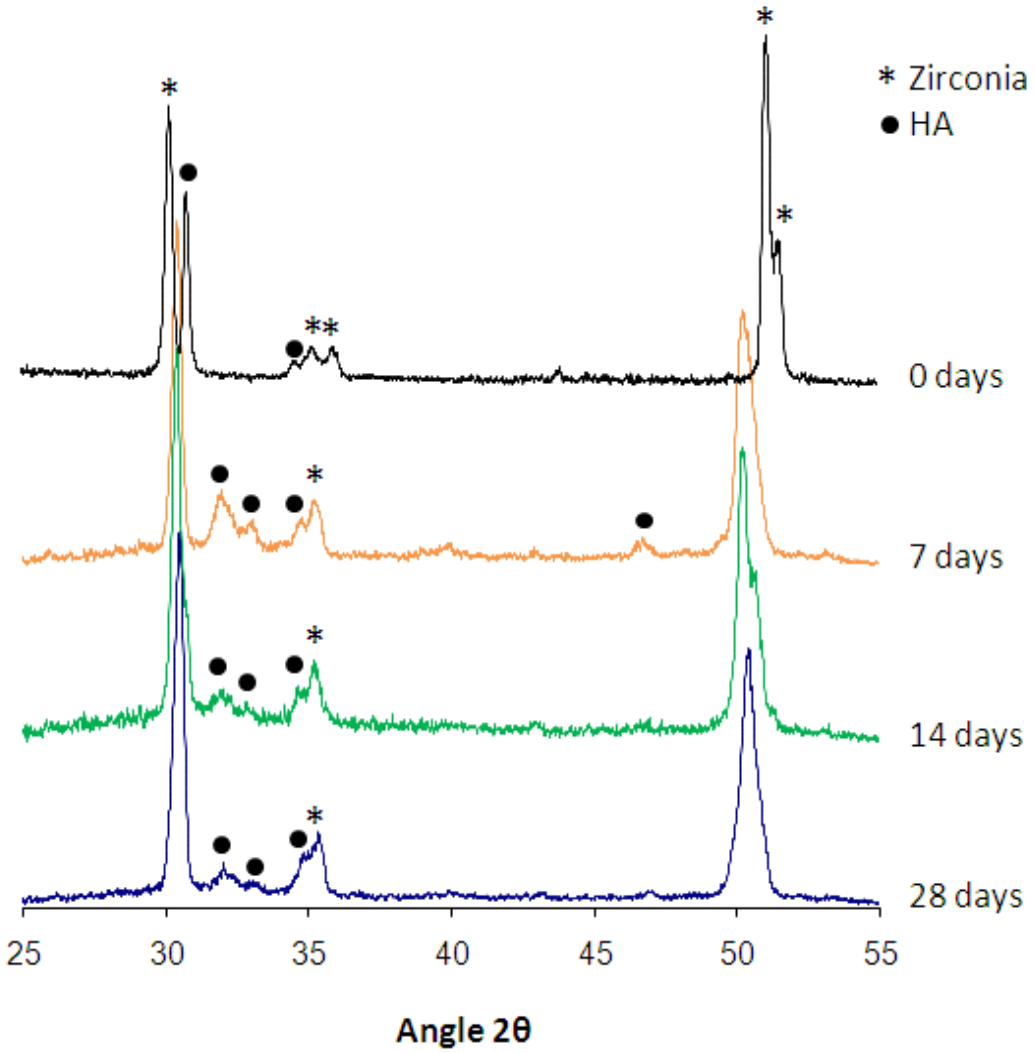

Figure 6.13 XRD spectra of zirconia-HA composite scaffolds immersed in SBF for 0, 7, 14 and 28 days. All the major peaks of zirconia and apatite have been identified.

6.7.4.3 Morphology and microstructure

A field emission scanning electron microscope was used to observe and obtain high resolution images of the surfaces of the sintered scaffolds and the SBF immersed

structures. **Figure 6.14** shows the SEM images of the as-sintered scaffolds. The zirconia scaffold prepared by electrospraying for 10 minutes shows a porous structure (**Figure 6.14a**) even on its electrosprayed surface which means that the nHA slurry could infiltrate towards the interior of the scaffold. At higher magnification, the zirconia grain structure can be observed (**Figure 6.14b**) and did not show any micro-pores after the sintering process, meaning that the mechanical properties should not be affected.

Figure 6.14c shows the porous structure of the sintered zirconia scaffold after coating with 4 wt% nHA suspension and sintering again at 600℃. It can be observed that the porous structure is still intact, but there are also cracks visible on the surface of the struts. This could be a result of un-even coating of the zirconia scaffolds with the nHA slurry. In the dipping method as described in the literature review (**Chapter 2**), after dipping in the slurry, the excess slurry needs to be squeezed out to obtain a homogenous coating on the foam struts. However in this case, the excess slurry could not be squeezed out as the foams were already sintered. But from the mechanical testing results, it is clear that these cracks had not made much of an impact on the compressive strength (**Figure 6.11**). **Figure 6.14d** shows the nHA coating after firing at 600℃. Upon closer inspection (**inset image-Figure 6.14d**) it is possible to see some of the individual nHA particles. This shows that the sintering temperature of 600℃ is not sufficient to sinter these nHA particles but this should not have any effect on the cell growth. Work has been carried out on investigating the osteoblast growth on electrosprayed apatite nanocrystals, where the samples were not sintered after electrospraying and this still demonstrated patterned cell growth and differentiation [Thian *et al.*, 2008b]. Therefore,

it is fair to assume that this feature should not have a negative impact on the bioactivity investigation but actually a positive impact as it is believed that nHA particles could in fact accentuate the osteoconductivity due to its similarity to the mineral crystals found in bone and is discussed in the literature review section of this thesis (**Chapter 2**).

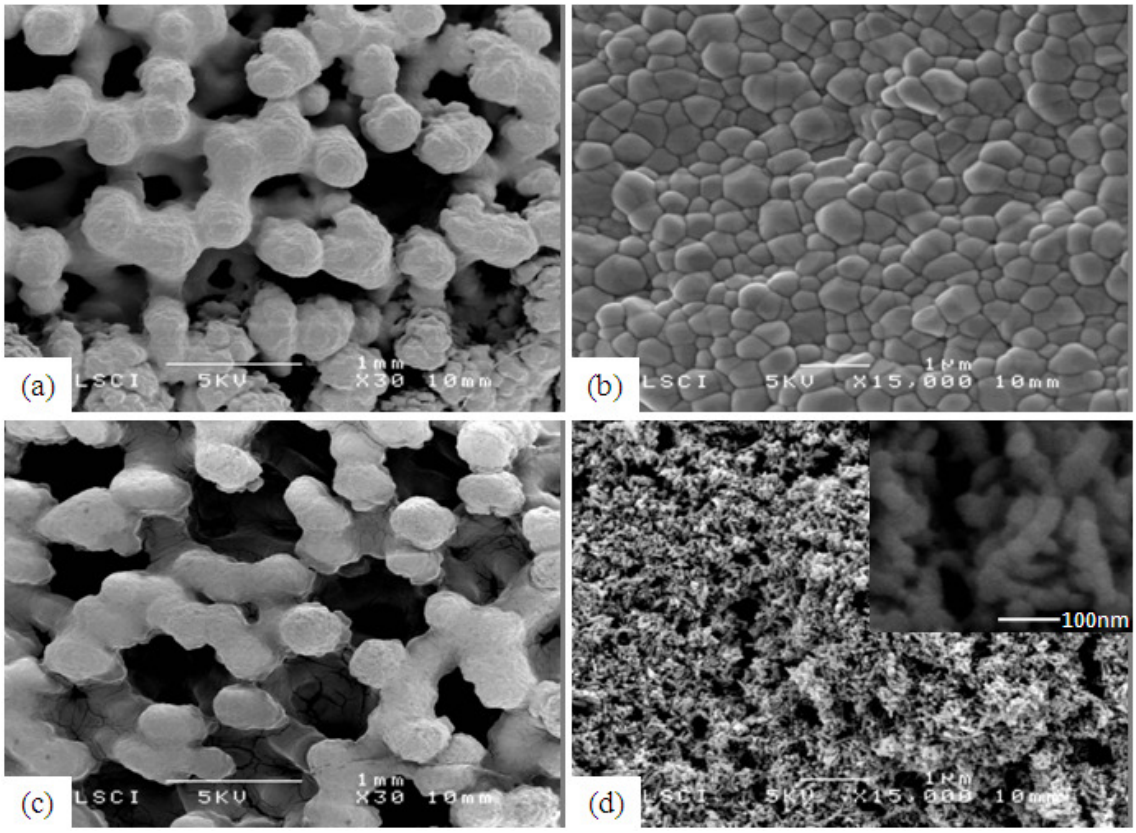

Figure 6.14 SEM images of the zirconia and zirconia-HA composite scaffolds prior to SBF testing (0 days); (a) sintered zirconia scaffold at low maginification showing the porous structure, (b) the grain structure of the zirconia scaffold at high magnification, (c) sintered zirconia scaffold coated with 4 wt% nHA suspension after sintering again at 600℃ and (d) the HA coating on the zirconia-HA composite scaffold, showing some of the individual nHA particles (inset image)

It was decided to use bioglass® scaffolds as a control experiment for the investigation of apatite growth upon immersion in SBF solution. Bioglass is known to grow an apatite layer by interacting with SBF and it is this characteristic that makes these bioceramics bond to bone (**Chapter 2**). There was a dramatic change in the morphology of the bioglass structure after 7 days of immersion in SBF. The signature 'cauliflower' structure of apatite growth was clearly observed in the bioglass scaffolds. The zirconia-HA composite scaffold had some distinct growth of the rough apatite as well as some smoother sections (**Figure 6.15**).

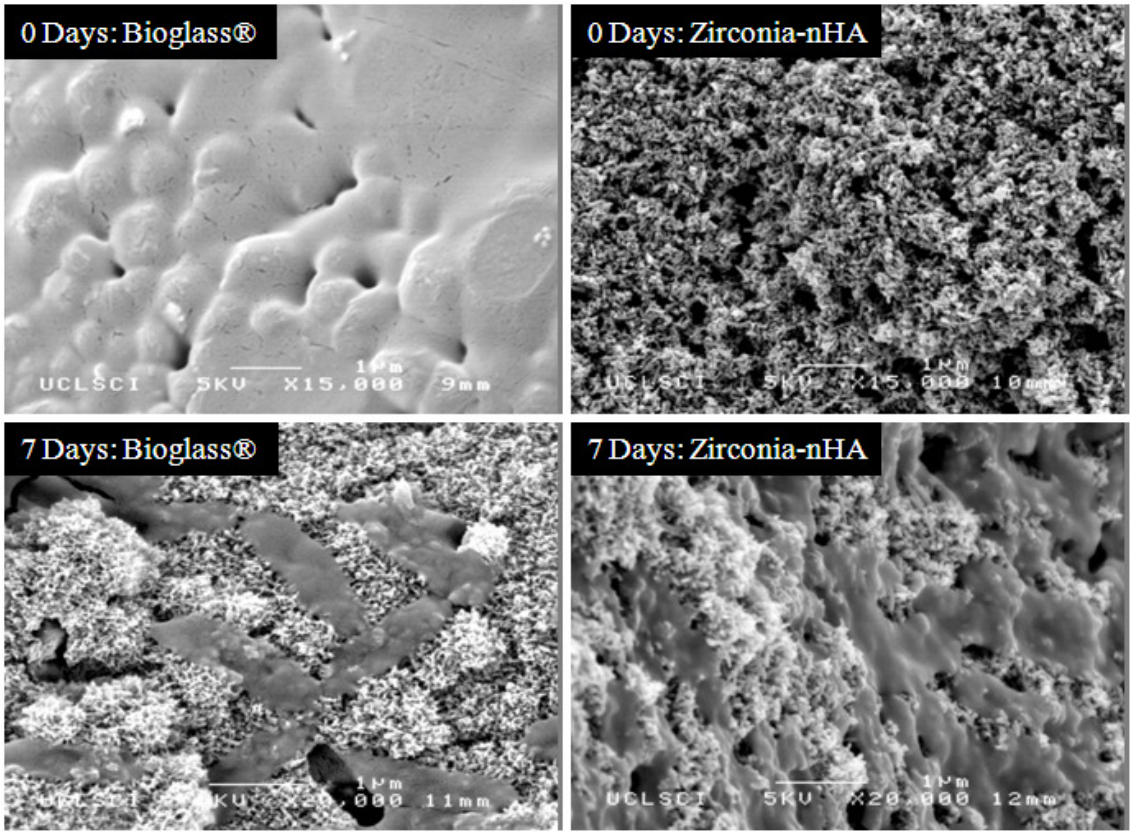

Figure 6.15 Surface morphology of the scaffolds after immersion in SBF for 7 days compared to 0 days. The images clearly show the apatite growth on the structures and have been compared to bioglass® scaffolds

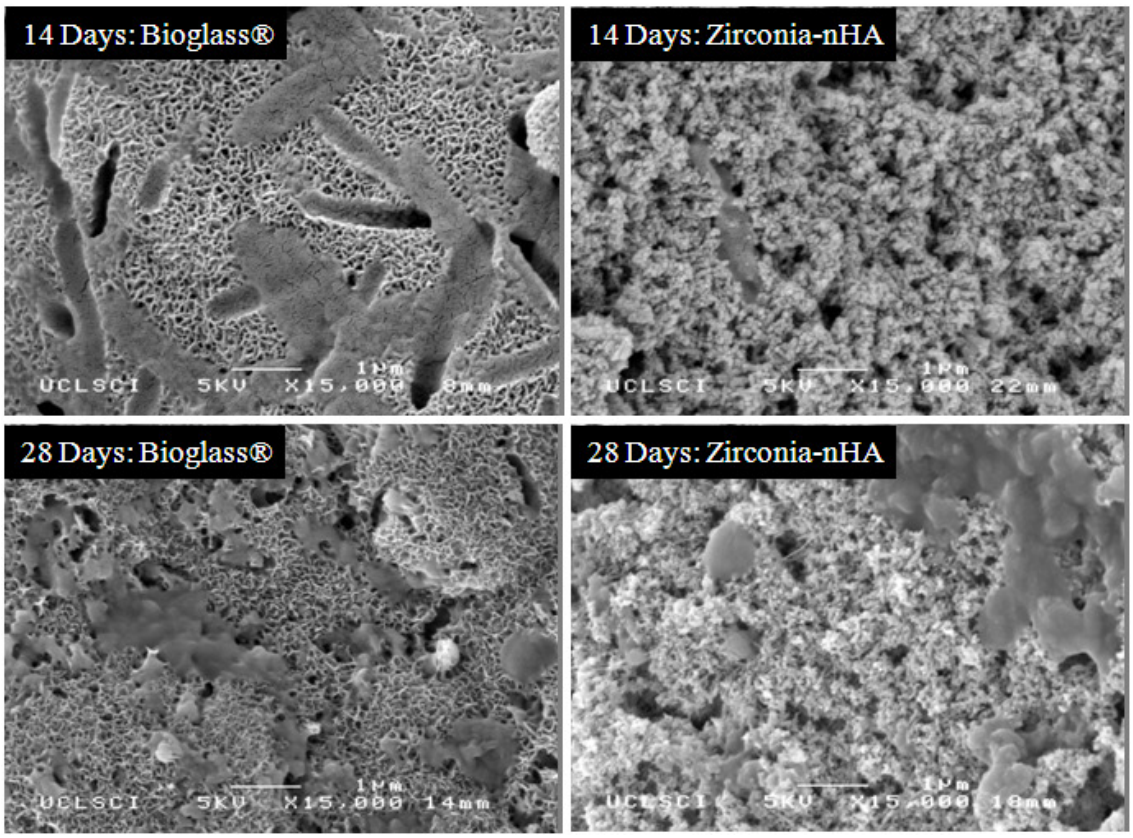

Figure 6.16 Surface morphology of the scaffolds after immersion in SBF for 14 and 28 days

Figure 6.16 shows the surface morphologies of the scaffolds after immersion in SBF for 14 and 28 days. There is an increase in the apatite growth in the zirconia-HA composite scaffolds but this growth is much more obvious in the bioglass® scaffolds. However, it is possible that there is significant apatite growth on the zirconia-HA composite scaffold according to the additional HA peaks observed in XRD spectra and the increase in mechanical properties.

On close examination of the SEM images, there is a relatively smooth section scattered on the SBF immersed samples on both the bioglass and the zirconia-HA composite scaffolds. It was initially hypothesised to be some salt remnants after washing, therefore elemental analysis was carried out on both the rough and smooth sections of a 14-day SBF immersed composite structure (**Figure 6.17**). Upon carrying out elemental analysis, it was also found that the elements found on the smooth surface were similar to those found on the rough surface and also to be the formation of apatite.

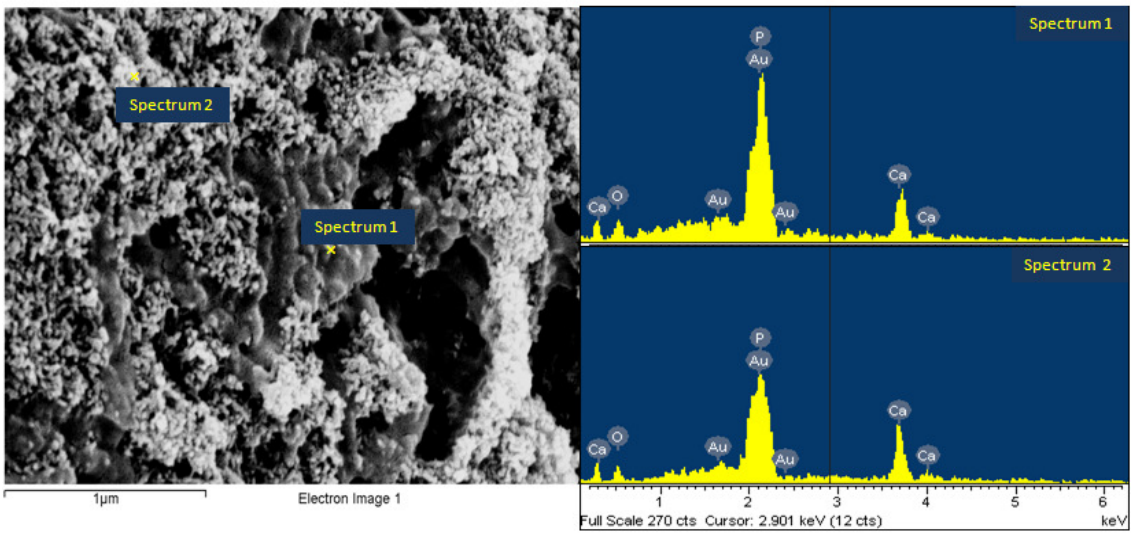

Figure 6.17 Elemental analysis of the smooth and rough surfaces observed on the zirconia-HA composite scaffold

It has been mentioned in the literature of SBF testing, that the degree of ability for apatite formation on the surface of a material in SBF could predict the degree of *in-vivo* bone bioactivity of a material [Kokubo and Takadama, 2006]. Therefore, a material having the ability to form apatite on its surface in SBF within a short period bonds to

living bone in a short period, which means that within a living body this apatite formation will also occur within a short period [Kokubo and Takadama, 2006].

Chapter 7

Conclusions and Future work

7.1 Conclusions

The following conclusions can be drawn from the investigations carried out in this thesis.

On the processing of structures with graded porosity;

- It has been possible to manipulate the electrohydrodynamic method to obtain a range of zirconia ceramic structures with graded porosity, crucial for medical engineering and technology development.

- Fixing the foam on a pin electrode which was also grounded proved to be a successful experimental set–up for obtaining foams with graded porosity as it seemed to converge the charged droplets towards the polymeric template.

- Dipping the polymeric templates in ethanol significantly improved the attraction and adherence of the zirconia particles into the template, reducing the spraying time.

- It was expected that the porosity would gradually increase away from the sprayed surface. However, microscopy shows that the pore size increases towards the middle of the foam and then reduces in size in the inner–most surfaces of the foam. Micropores of less than 10 µm in size were observed on the sprayed surface, while the middle of the foam consisted of pores of approximately 300 µm in diameter and then were reduced to approximately 100 µm at the inner surface. It was observed that the sintered foams had an inverted-pyramid shaped structure gradually narrowing towards the inner-end. With increased spraying time, a pyramid shaped structure was formed on top of the sprayed surface.

- The electrohydrodynamic spraying process has proved to be a very effective and efficient 'one-step' method of fabricating ceramic structures with graded porosity over other methods as it only takes a few minutes and no multiple or repetitive steps are involved in fabrication.

- The porosity, pore size and depth of penetration can be tailored as desired by changing one or more of parameters such as, sintering temperature, spraying time and sacrificial template.

- The sintered structures excluding the sprayed surface had interconnected pore networks which are desired in scaffolds for bone tissue engineering applications.

- The porosity graded foams prepared in this work can find uses as scaffolds that can provide anchorage to osteoblasts in bone tissue engineering applications.

- If the external coating is not permitted to form a pyramidal-shape, it is possible to obtain structures that resemble bone (*i.e.* dense exterior and, porous and interconnected interior).

- Therefore, by rotating the polymeric template, the possibility of obtaining bone-like structures, which can be used as a bone substitute, with the porous internal structure providing a framework for cell migration and growth, while the dense exterior provides the mechanical support, has been demonstrated in this work.

On the feasibility study of using electrospraying to produce bioactive HA scaffolds;

- The original 18 wt% aqueous nHA suspension could not be electrosprayed due to its paste-like consistency and had to be diluted in ethanol in order to make a nHA suspension suitable for electrospraying. After experimenting with different nHA particle loadings, a suspension of 6 wt% particle content was able to produce a stable cone–jet mode.

- It has been possible to electrospray a suspension of nano-hydroxyapatite (nHA) onto polymeric templates to produce porous scaffolds. Contrary to the belief that nano-scale particles would sinter at low temperatures, a temperature of 600℃ seemed to be too low for the sintering of HA scaffolds since they did not retain the structures upon

sintering. However, by increasing the sintering temperature to 1200℃, it was possible to obtain three dimensional porous HA scaffolds. But the scaffolds produced by electrospraying had a dense outer surface and a highly porous interior with extremely thin struts leading to a weak structure which is undesirable.

- A novel method of fabricating HA scaffolds with open pores was developed, which is a combination of slurry dipping and electrospraying. The porosity for the combined method ranged between 84 – 94% and the pore size was within the desired range of 100 – 350 μm for bone tissue engineering applications.

- There has been an improvement in the mechanical properties of the scaffolds without compromising the porosity or the pore size in the foams produced by the combined method in comparison to the individual methods of dipping and electrospraying.

- The mechanical properties have been improved further by increasing the sintering temperature, thus decreasing the size of the central void in the struts.

- Due to the osteoconductive nature of HA, it is fair to assume that these foams can be used for guided bone regeneration, but the mechanical properties still need to be improved for these scaffolds to be considered for load bearing applications.

On producing mechanically strong ceramic scaffolds which are also bioactive;

- Zirconia was used as the ceramic material as unlike the nHA, preparation of suspensions of high particle concentration was made possible and EHDA or electrospraying proved to be an efficient method of producing porous and mechanically strong scaffolds.

- The porosity on the sprayed surface decreases as a function of time and the mechanical properties increase. A spray time of 10 minutes seem to be better as it still produces scaffolds that are porous and are also mechanically strong since its compressive strength lies between the recommended region of 2 – 12 MPa for cancellous bone. Even if the mechanical properties are excellent at 15 minute spray time, these scaffolds cannot be used as matrices to guide tissue growth due to their non-porous characteristic on the sprayed surface.

- The scaffolds produced using 45 ppi templates are mechanically stronger in comparison to the scaffolds prepared from 60 ppi templates at identical experimental conditions, due to their larger pore size, increasing the droplet penetration towards the interior of the template.

- Hydroxylating the PU template surface seems to ensure a more uniform coating of the ceramic suspension and a reduction in blocked pores, thus leading to improved mechanical properties. By increasing the conductivity of the hydroxylated template, the

mechanical properties are improved even further due to the increased attraction of the charged ceramic droplets towards the polymeric templates.

- This investigation has proved that it is possible to produce mechanically strong scaffolds using zirconia. This has been accomplished by varying the spraying time and investigating the effects of modifying template surfaces. There has been a significant effect on the pore size, the morphology of the foams and mechanical properties by making slight modifications to the polymeric template.

- It has been shown in this thesis that by dipping the templates prior to electrospraying improves the ceramic coating, thus making the production process more efficient. It was observed that a spray time of 10 minutes produced scaffolds of compressive strength approximating 7.5 MPa. However, by using pre-treatment methods for the templates, the mechanical properties were further improved especially when the templates were subjected to surface hydroxylation and a conductive gold coating. Within 5 minutes, it was possible to nearly achieve the same compressive strength as that of the templates treated only with ethanol and electrosprayed for 10 minutes.

- Introduction of nHA into these mechanically stronger zirconia scaffolds was carried out by dipping a sintered zirconia scaffold into a nano-HA slurry of low particle content. It was the concept to introduce a bioactive component to the mechanically strong, yet bioinert zirconia scaffolds. The mechanical properties were increased as a

result of this additional layer (nHA) and the repetitive sintering even if it was at a low temperature of 600℃.

- The SBF testing proved the bioinert characteristic of zirconia as it did not exhibit any changes in forming apatite phases or changes to the mechanical properties, which remained constant throughout the 28 days.

- The SBF results proved to be favourable and apatite growth was observed on the zirconia-HA composite scaffolds using SEM images, additional apatite peaks on the XRD spectra and the increase in the mechanical properties.

7.2 Future Work

Based on the research carried out and the outcome of this thesis, the following recommendations are made for future work.

- Functionally graded porous ceramics have a vast number of applications ranging from industry to medicine. In the work presented in this thesis, zirconia is used only as an example, and it is possible to use other ceramics such as alumina (for industry) and hydroxyapatite (for biomedical) for producing functionally graded materials using the electrohydrodynamic method.

- In the effect of replacing zirconia with a new material, it is essential to investigate the suitability of that material for electrospraying. It will be necessary to

experiment with different concentrations of suspensions and plotting a mode selection map will be required as the conditions for the stable cone-jet mode will depend on the material.

- In the investigations conducted in this thesis, two types of templates (60 and 45 ppi) of varying porosity ranges were used. This work could be further extended to include a variety of templates in order to observe the effect of template on the pore size and strut thickness.

- The effects of two types of sintering temperatures on producing graded porous structures were investigated and a range of sintering temperatures could be investigated to observe the effects on the porous structure such as the pore size and porosity due to shrinkage.

- By combining the effects of a range of polymeric templates and sintering temperatures, it will be possible to experimentally further optimise the fabrication process to produce functionally graded porous structures of more desirable properties tailored to the specific application.

- It is necessary to develop an understanding of the pyramidal shrinkage of structures with graded porosity and an investigation into other possible explanations for the occurrence of this phenomenon than that discussed in this thesis.

- Even if it was possible to produce porous HA scaffolds using a combined method of dipping and electrospraying, and the structures proved to be stronger than the scaffolds produced by using each method individually, the mechanical properties still need to be improved in the HA foam structures if they are to be considered for applications where load bearing is required.

- Using a biopolymer such as Poly(D-L, lactic acid) or P4HB to coat the sintered scaffolds could be considered. This method has improved mechanical properties in bioglass® ceramic scaffolds. A range of polymers maybe considered, and a systematic investigation is therefore needed to determine the appropriate polymer type and concentration suitable for the coating. There is the likelihood that the polymer may suppress the osteoconductive properties of HA, and it is also important to examine the degradation and the mechanical properties of the polymer in comparison to the HA.

- In the literature, for reasonable mechanical strength of HA scaffolds, hydroxyapatite concentration of at least 50 wt% have been used in the slurries. Using a higher nHA particle loading in the suspension could be investigated as it will increase the probability of improving the mechanical properties of the foams.

- The nHA particles used in this investigation have a rod-like shape, making the packing efficiency low, leading to micropores during the sintering process compromising the mechanical properties. Therefore, it is likely if sphere shaped nHA

particles are used, the packing efficiency will be improved leading to improved porous structures.

- It will be beneficial to develop a better understanding of the rheology of the suspensions and control of suspension properties might lead to improved coating and enhanced mechanical properties.

- The zirconia scaffolds produced by the pre-treatment of polymeric templates need to be fractured in the centre and the internal cross-sections need to be examined in order to observe if there is an improvement on the internal structure due to these pre-treatment methods based on the pore size, the strut thickness and the outer wall thickness.

- Pre-treatment methods for the polymeric templates have improved mechanical properties; however a more detailed study needs to follow this work such as the effects of changing the PPDS concentration and the exposure time for the gold coating and their effects on the coating of the bioceramic and how it leads to any changes in the mechanical properties.

- A range of polymeric templates undergoing pre-treatment methods should be investigated, or at least templates of pore size 50 – 55 ppi in order to optimise the porosity as well as the mechanical strength of these bioceramic scaffolds.

- The pre-treated template sizes need to be increased (for the replacement of potentially larger bone defects) and the depth of penetration of the charged ceramic droplets need to be investigated, as well as its effect on the mechanical properties.

- A systematic study is required of the effects of the nHA concentration which is used to coat the zirconia scaffolds in order to obtain an optimum concentration of nHA particle loading which is dilute enough to permeate towards the interior of the porous scaffold and not have too much of an effect on its porosity, but be of sufficient concentration to effectively coat the zirconia structure so that bone tissue growth is well promoted.

- The zirconia structures that were coated with the nHA (4 wt%) need to be fractured in the centre to observe the penetration of the nHA coating on this area of the scaffold. SEM and XRD analysis will be required to examine the bioactive coating on the struts, by imaging and the presence of phases, respectively.

- The bioactivity of the composite scaffolds due to SBF were only examined on the electrosprayed surfaces in this thesis and again, SEM and XRD analysis need to be carried out on the interior surfaces to observe the apatite formation.

- The scaffolds produced using surface hydroxylation and improved conductivity and a spray time of 5 minutes exhibited good mechanical properties. These scaffolds could be coated with nHA, as they might prove to be more accommodating to a nano-

HA concentration of high particle loading than 4 wt% due to the reduced number of blocked pores. SBF testing need to be carried out and the bioactivity needs to be investigated and compared to the scaffolds prepared using ethanol dipped templates electrosprayed for 10 minutes, sintered and dipped in nHA, *i.e.* the work produced in this thesis.

- The SBF work carried out on the zirconia-HA composite scaffolds in this thesis showed increased apatite formation which is an indication of its ability to promote tissue growth and the ability to bond to living bone *in-vivo*. However, this needs to be verified by carrying out a systematic set of experiments involving cell culture work. Osteoblast cells could be seeded into these zirconia-HA composite scaffolds and experiments need to be carried out over about a three-month period to observe the cell attachment, viability, proliferation and mineralization in order to confirm its suitability to promote bone tissue growth.

REFERENCES

Abe, Y., Kawashita, M., Kokubo, T. & Nakamura, T. (2001) Effects of solution on apatite formation on substrate in biomimetic process. *Journal of the Ceramic Society of Japan,* **109**, 106-109.

Albee, F. & Morrison, H. (1920) Studies in bone growth. *Annals of Surgery,* **71**, 32-38.

Almirall, A., Larrecq, G., Delgado, J. A., Martinez, S., Ginebra, M. P. & Planell, J. A. (2004) Fabrication of low temperature hydroxyapatite foams. *Key Engineering Materials,* **254-2**, 1001-1004.

Bailliez, S. & Nzihou, A. (2004) The kinetics of surface area reduction during isothermal sintering of hydroxyapatite adsorbent. *Chemical Engineering Journal,* **98**, 141-152.

Baksh, D., Davies, J. E. & Kim, S. (1998) Three-dimensional matrices of calcium polyphosphates support bone growth in vitro and in vivo. *Journal of Materials Science-Materials in Medicine,* **9**, 743-748.

Becker, B. S. & Bolton, J. D. (1997) Corrosion behaviour and mechanical properties of functionally gradient materials developed for possible hard-tissue applications. *Journal of Materials Science-Materials in Medicine,* **8**, 793-797.

Ben-Nissan, B. & Pezzotti, G. (2004) Bioceramics: An Introduction. IN TEOH, S. H. (Ed.) *Engineering Materials for Biomedical Applications.* Singapore; London, World Scientific p. 6:1-6:36.

Binner, J. G. P. & Reichert, J. (1996) Processing of hydroxyapatite ceramic foams. *Journal of Materials Science,* **31**, 5717-5723.

Boccaccini, A. R., Notingher, I., Maquet, V. & Jerome, R. (2003) Bioresorbable and bioactive composite materials based on polylactide foams filled with and coated by Bioglass® particles for tissue engineering applications. *Journal of Materials Science-Materials in Medicine,* **14**, 443-450.

Bohner, M. (2000) Calcium orthophosphates in medicine: from ceramics to calcium phosphate cements. *Injury-International Journal of the Care of the Injured,* **31**, S37-S47.

Bouler, J. M., Trecant, M., Delecrin, J., Royer, J., Passuti, N. & Daculsi, G. (1996) Macroporous biphasic calcium phosphate ceramics: Influence of five synthesis parameters on compressive strength. *Journal of Biomedical Materials Research,* **32**, 603-609.

Brown, K. L. B. & Cruess, R. L. (1982) Bone and cartilage transplantation surgery. *Journal of Bone and Joint Surgery,* **64A**, 270-279.

Burg, K. J. L., Porter, S. & Kellam, J. F. (2000) Biomaterial developments for bone tissue engineering. *Biomaterials,* **21**, 2347-2359.

Callcut, S. & Knowles, J. C. (2002) Correlation between structure and compressive strength in a reticulated glass-reinforced hydroxyapatite foam. *Journal of Materials Science-Materials in Medicine,* **13**, 485-489.

Carson, R. S. & Hendrick, C. D. (1965) Natural Pulsations in Electrical Spraying of Liquids. *AIAA Journal,* **3**, 1072-1075.

Castillo, M., Moore, J. J., Schowengerdt, F. D., Ayers, R. A., Zhang, X., Umakoshi, M., Yi, H. C. & Guigne, J. Y. (2003) Effects of gravity on combustion synthesis of functionally graded biomaterials. *Advances in Space Research,* **32**, 265-270.

Cesarano, J., Dellinger, J. G., Saavedra, M. P., Gill, D. D., Jamison, R. D., Grosser, B. A., Sinn-Hanlon, J. M. & Goldwasser, M. S. (2005) Customization of load-bearing hydroxyapatite lattice scaffolds. *International Journal of Applied Ceramic Technology,* **2**, 212-220.

Chen, Q. Z., Boccaccini, A. R., Zhang, H. B., Wang, D. Z. & Edirisinghe, M. J. (2006a) Improved mechanical reliability of bone tissue engineering (Zirconia) scaffolds by electrospraying. *Journal of the American Ceramic Society,* **89**, 1534-1539.

Chen, Q. Z. Z., Thompson, I. D. & Boccaccini, A. R. (2006b) 45S5 Bioglass®-derived glass-ceramic scaffolds for bone tissue engineering. *Biomaterials,* **27**, 2414-2425.

Christel, P., Meunier, A., Dorlot, J. M., Crolet, J. M., Witvolet, J., Sedel, L. & Boutin, P. (1988) Biomechanical compatibility and design of ceramic implants for orthopedic surgery. IN DUCHEYNE, P. & LEMONS, J. (Eds.) *Bioceramics: material characteristics versus in vivo behaviour.* New York, Annals of New York Academy of Sciences, p. 234-256.

Chu, T. M. G., Halloran, J. W., Hollister, S. J. & Feinberg, S. E. (2001) Hydroxyapatite implants with designed internal architecture. *Journal of Materials Science-Materials in Medicine,* **12**, 471-478.

Chu, T. M. G., Hollister, S. J., Halloran, J. W., Feinberg, S. E. & Orton, D. G. (2002a) Manufacturing and characterization of 3-D hydroxyapatite bone tissue engineering scaffolds. *Reparative Medicine: Growing Tissues and Organs.* p. 114-117.

Chu, T. M. G., Orton, D. G., Hollister, S. J., Feinberg, S. E. & Halloran, J. W. (2002b) Mechanical and in vivo performance of hydroxyapatite implants with controlled architectures. *Biomaterials,* **23**, 1283-1293.

Cima, L. G. & Cima, M. J. (1996) Preparation of medical devices by solid free-form fabrication methods. US Patent No. 5490962.

Cloupeau, M. & Prunet-Foch, B. (1989) Electrostatic Spraying of Liquids in Cone-Jet Mode. *Journal of Electrostatics,* **22**, 135-159.

Cloupeau, M. & Prunet-Foch, B. (1990) Electrostatic spraying of liquids. Main functioning modes. *Journal of Electrostatics,* **23**, 165-184.

Cloupeau, M. & Prunet-Foch, B. (1994) Electrohydrodynamic Spraying Functioning Modes - a Critical-Review. *Journal of Aerosol Science,* **25**, 1021-1036.

Connor, E. E., Mwamuka, J., Gole, A., Murphy, C. J. & Wyatt, M. D. (2005) Gold nanoparticles are taken up by human cells but do not cause acute cytotoxicity. *Small,* **1**, 325-327.

Corbin, S. F., Zhao-Jie, X., Henein, H. & Apte, P. S. (1999) Functionally graded metal/ceramic composites by tape casting,lamination and infiltration. *Materials Science and Engineering -A,* **262**, 192-203.

Correia, R. N., Magalhaes, M. C. F., Marques, P. & Senos, A. M. R. (1996) Wet synthesis and characterization of modified hydroxyapatite powders. *Journal of Materials Science-Materials in Medicine,* **7**, 501-505.

Cullinane, D. M. & Salisbury, K. T. (2004) Biomechanics. IN HOLLINGER, J. O., EINHORN, T. A., DOLL, B. A. & SFEIR, C. (Eds.) *Bone Tissue Engineering.* Boca Raton (US), CRC Press, p. 261-263.

Dariel, M. P., Levin, L. & Frage, N. (2001) Graded ceramic preforms: various processing approaches. *Materials Chemistry and Physics,* **67**, 192-198.

De Sousa, F. C. G. & Evans, J. R. G. (2003) Sintered hydroxyapatite latticework for bone substitute. *Journal of the American Ceramic Society,* **86**, 517-519.

Dellinger, J. G., Cesarano, J. & Jamison, R. D. (2007) Robotic deposition of model hydroxyapatite scaffolds with multiple architectures and multiscale porosity for bone tissue engineering. *Journal of Biomedical Materials Research Part A,* **82A**, 383-394.

Dellinger, J. G., Wojtowicz, A. M. & Jamison, R. D. (2006) Effects of degradation and porosity on the load bearing properties of model hydroxyapatite bone scaffolds. *Journal of Biomedical Materials Research Part A,* **77A**, 563-571.

Deville, S., Saiz, E. & Tomsia, A. P. (2006) Freeze casting of hydroxyapatite scaffolds for bone tissue engineering. *Biomaterials,* **27**, 5480-5489.

Devin, J. E., Attawia, M. A. & Laurencin, C. T. (1996) Three-dimensional degradable porous polymer-ceramic matrices for use in bone repair. *Journal of Biomaterials Science-Polymer Edition,* **7**, 661-669.

Dhara, S., Pradhan, M., Ghosh, D. & Bhargava, P. (2005) Nature inspired novel processing routes for ceramic foams. *Advances in Applied Ceramics,* **104**, 9-21.

Dong, Y. S., Liu, B., Lin, P. H., Zhang, Q. G. & Pu, Y. P. (2005) Macroporous hydroxyapatite scaffold fabricated by foam impregnation. *Key Engineering Materials,* **288-289**, 565-568.

Downey, P. A. & Siegel, M. I. (2006) Bone biology and the clinical implications for osteoporosis. *Physical Therapy,* **86**, 77-91.

Du, C., Cui, F. Z., Zhu, X. D. & De Groot, K. (1999) Three-dimensional nano-HAp/collagen matrix loading with osteogenic cells in organ culture. *Journal of Biomedical Materials Research,* **44**, 407-415.

Enneking, W. F., Eady, J. L. & Burchardt, H. (1980) Autogenous cortical bone grafts in the reconstruction of segmental skeletal defects. *Journal of Bone and Joint Surgery,* **62A**, 1039-1058.

Evis, Z. (2007) Reactions in hydroxylapatite-zirconia composites. *Ceramics International,* **33**, 987-991.

Evis, Z., Sato, M. & Webster, T. J. (2006) Increased osteoblast adhesion on nanograined hydroxyapatite and partially stabilized zirconia composites. *Journal of Biomedical Materials Research Part A,* **78A**, 500-507.

Fenn, J. B., Mann, M., Meng, C. K., Wong, S. F. & Whitehouse, C. M. (1989) Electrospray Ionization for Mass-Spectrometry of Large Biomolecules. *Science,* **246**, 64-71.

Fernandez De La Mora, J. (1992) The effect of charge emission from electrified liquid cones. *Journal of Fluid Mechanics,* **243**, 561-574.

Freyman, T. M., Yannas, I. V. & Gibson, L. J. (2001) Cellular materials as porous scaffolds for tissue engineering. *Progress in Materials Science,* **46**, 273-282.

Fu, Q., Rahaman, M. N., Dogan, F. & Bal, B. S. (2008) Freeze casting of porous hydroxyapatite scaffolds. II. Sintering, microstructure, and mechanical behavior. *Journal of Biomedical Materials Research Part B-Applied Biomaterials,* **86B**, 514-522.

Fukasawa, T., Deng, Z. Y., Ando, M., Ohji, T. & Goto, Y. (2001) Pore structure of porous ceramics synthesized from water-based slurry by freeze-dry process. *Journal of Materials Science,* **36**, 2523-2527.

Gañán-Calvo, A. M. (1995) The role of the viscosity in the EHD spraying of liquids in cone-jet mode. *Electrostatics 1995.* p. 61-68.

Gañán-Calvo, A. M. (1999) The electrohydrodynamic atomization of liquids today. *Journal of Aerosol Science,* **30**, S547-S548.

Gañán-Calvo, A. M., Davila, J. & Barrero, A. (1997) Current and droplet size in the electrospraying of liquids. Scaling laws. *Journal of Aerosol Science,* **28**, 249-275.

Gañán-Calvo, A. M., Lasheras, J. C., Davila, J. & Barrero, A. (1994) The electrostatic spray emitted from an electrified conical meniscus. *Journal of Aerosol Science,* **25**, 1121-1142.

Garvie, R. C., Hannink, R. H. & Pascoe, R. T. (1975) Ceramic Steel. *Nature,* **258**, 703-704.

Gibson, L. J. & Ashby, M. F. (1997a) Cellular solids, structure and properties. 2nd ed. Cambridge, Cambridge University Press, p. 429-452.

Gibson, L. J. & Ashby, M. F. (1997b) Cellular solids, structure and properties. 2nd ed. Cambridge, Cambridge University Press, p. 15.

Gibson, L. J. & Ashby, M. F. (1997c) Cellular Solids, structure and properties. 2nd ed. Cambridge, Cambridge University Press, p. 26-33.

Glowacki, J. & Mulliken, J. B. (1985) Demineralized Bone Implants. *Clinics in Plastic Surgery,* **12**, 233-241.

Gomez, A. & Tang, K. Q. (1994) Charge and Fission of Droplets in Electrostatic Sprays. *Physics of Fluids,* **6**, 404-414.

Grace, J. M. & Marijnissen, J. C. M. (1994) A Review of Liquid Atomization by Electrical Means. *Journal of Aerosol Science,* **25**, 1005-1019.

Grigorev, A. I. & Shiryaeva, S. O. (1994) The Theoretical Consideration of Physical Regularities of Electrostatic Dispersion of Liquids as Aerosols. *Journal of Aerosol Science,* **25**, 1079-1091.

Grigoriev, D. A. & Edirisinghe, M. J. (2002) Evaporation of liquid during cone-jet mode electrospraying. *Journal Applied Physics,* **91**, 437-439.

Guo, H., Khor, K. A., Boey, Y. C. & Miao, X. (2003) Laminated and functionally graded hydroxyapatite/yttria stabilized tetragonal zirconia composites fabricated by spark plasma sintering. *Biomaterials,* **24**, 667-675.

Haldeman, K. & Moore, J. (1934) Influence of a local excess of calcium and phosphorous on the healing of fractures. *Archives of Surgery,* **29**, 385-396.

Hancox, N. M. (1972) Generalities. *Biology of Bone (Biological Structure and Function No. 1).* Cambridge, Cambridge University Press, p. 3-5.

Hartman, R. P. A., Borra, J.-P., Marijnissen, J. C. M. & Scarlett, B. (1996) Development of electrohydrodynamic sprays related to space charge effects. *Journal of Aerosol Science,* **27**, S177-S178.

Hartman, R. P. A., Borra, J. P., Brunner, D. J., Marijnissen, J. C. M. & Scarlett, B. (1999a) The evolution of electrohydrodynamic sprays produced in the cone-jet mode, a physical model. *Journal of Electrostatics,* **47**, 143-170.

Hartman, R. P. A., Brunner, D. J., Camelot, D. M. A., Marijnissen, J. C. M. & Scarlett, B. (1999b) Electrohydrodynamic atomization in the cone - jet mode physical modelling of the liquid cone and jet. *Journal of Aerosol Science,* **30**, 823-849.

Hartman, R. P. A., Brunner, D. J., Camelot, D. M. A., Marijnissen, J. C. M. & Scarlett, B. (2000) Jet break-up in electrohydrodynamic atomization in the cone-jet mode. *Journal of Aerosol Science,* **31**, 65-95.

Hayati, I., Bailey, A. & Tadros, T. F. (1987a) Investigations into the Mechanism of Electrohydrodynamic Spraying of Liquids .2. Mechanism of Stable Jet Formation and Electrical Forces Acting on a Liquid Cone. *Journal of Colloid and Interface Science,* **117**, 222-230.

Hayati, I., Bailey, A. I. & Tadros, T. F. (1986) Mechanism of Stable Jet Formation in Electrohydrodynamic Atomization. *Nature,* **319**, 41-43.

Hayati, I., Bailey, A. I. & Tadros, T. F. (1987b) Investigations into the Mechanisms of Electrohydrodynamic Spraying of Liquids .1. Effect of Electric-Field and the Environment on Pendant Drops and Factors Affecting the Formation of Stable Jets and Atomization. *Journal of Colloid and Interface Science,* **117**, 205-221.

Helmer, J. D. & Driskell, T. D. (1969) Research on bioceramics. *Symposium on Use of Ceramics in Surgical Implants.* Clemson University, South Carolina (USA).

Hench, L. L. (1991) Bioceramics - from Concept to Clinic. *Journal of the American Ceramic Society,* **74**, 1487-1510.

Hench, L. L. (1998) Bioceramics. *Journal of the American Ceramic Society,* **81**, 1705-1728.

Hench, L. L. & Best, S. M. (2004) Ceramics, glasses and glass-ceramics. IN RATNER, D., SCHOEN, F. J., HOFFMAN, A. S. & LEMONS, J. E. (Eds.) *Biomaterials Science: An Introduction to Materials in Medicine.* 2nd ed., Elsevier Academic Press, p. 153-170.

Higuera, F. J. (2003) Flow rate and electric current emitted by a Taylor cone. *Journal of Fluid Mechanics,* **484**, 303-327.

Hing, K. A., Best, S. M. & Bonfield, W. (1999) Characterization of porous hydroxyapatite. *Journal of Materials Science-Materials in Medicine,* **10**, 135-145.

Hollinger, J. O. & Battistone, G. C. (1986) Biodegradable bone repair materials. Synthetic polymers and ceramics. *Clinical Orthopaedics and Related Research,* **207**, 290-305.

Hollister, S. J., Maddox, R. D. & Taboas, J. M. (2002) Optimal design and fabrication of scaffolds to mimic tissue properties and satisfy biological constraints. *Biomaterials,* **23**, 4095-4103.

Hollister, S. J., Taboas, J. M., Schek, R. M., Lin, C.-Y. & Chu, T. M. (2004) Design and Fabrication of Bone Tissue Engineering Scaffolds. IN HOLLINGER, J. O., EINHORN, T. A., DOLL, B. A. & SFEIR, C. (Eds.) *Bone Tissue Engineering.* US, CRC Press, p. 167-192.

Holtappels, P., Sorof, C., Verbraeken, M. C., Rambert, S. & Vogt, U. (2006) Preparation of porosity-graded SOFC anode substrates. *Fuel Cells,* **6**, 113-116.

Hu, Y. F. & Miao, X. G. (2004) Comparison of hydroxyapatite ceramics and hydroxyapatite/borosilicate glass composites prepared by slip casting. *Ceramics International,* **30**, 1787-1791.

Huang, J., Best, S. M., Bonfield, W., Brooks, R. A., Rushton, N., Jayasinghe, S. N. & Edirisinghe, M. J. (2004) In vitro assessment of the biological response to nano-sized hydroxyapatite. *Journal of Materials Science-Materials in Medicine,* **15**, 441-445.

Huang, X. & Miao, X. (2007) Novel porous hydroxyapatite prepared by combining H_2O_2 foaming with PU sponge and modified with PLGA and bioactive glass. *Journal of Biomaterials Applications,* **21**, 351-374.

Huang, X. H., Jain, P. K., El-Sayed, I. H. & El-Sayed, M. A. (2007) Gold nanoparticles: interesting optical properties and recent applications in cancer diagnostic and therapy. *Nanomedicine,* **2**, 681-693.

Hulbert, S. F. (1993) The use of Alumina and Ziconia in Surgical Implants. IN HENCH, L. L. & WILSON, J. (Eds.) *An Introduction to Bioceramics.* Singapore; London, World Scientific, p. 25-40.

Hulbert, S. F., Young, F. A., Mathews, R. S., Klawitter, J. J., Talbert, C. D. & Stelling, F. H. (1970) Potential of ceramic materials as permanently implantable skeletal prostheses. *Journal of Biomedical Materials Research,* **4**, 433-456.

Hutmacher, D. W. (2000) Scaffolds in tissue engineering bone and cartilage. *Biomaterials,* **21**, 2529-2543.

Itala, A. I., Ylanen, H. O., Ekholm, C., Karlsson, K. H. & Aro, H. T. (2001) Pore diameter of more than 100 μm is not requisite for bone ingrowth in rabbits. *Journal of Biomedical Materials Research,* **58B**, 679-683.

Jarcho, M. (1981) Calcium-Phosphate Ceramics as Hard Tissue Prosthetics. *Clinical Orthopaedics and Related Research*, 259-278.

Jaworek, A. & Krupa, A. (1999) Classification of the modes of EHD spraying. *Journal of Aerosol Science,* **30**, 873-893.

Jayasinghe, S. N. & Edirisinghe, M. J. (2002a) Effect of viscosity on the size of relics produced by electrostatic atomization. *Journal of Aerosol Science,* **33**, 1379-1388.

Jayasinghe, S. N. & Edirisinghe, M. J. (2002b) A novel method of forming open cell ceramic foam. *Journal of Porous Materials,* **9**, 265-273.

Jayasinghe, S. N. & Edirisinghe, M. J. (2004) Electrostatic atomisation of a ceramic suspension. *Journal of the European Ceramic Society,* **24**, 2203-2213.

Jayasinghe, S. N., Edirisinghe, M. J. & De Wilde, T. (2002) A novel ceramic printing technique based on electrostatic atomization of a suspension. *Materials Research Innovations,* **6**, 92-95.

Jones, J. R. & Hench, L. L. (2003) Regeneration of trabecular bone using porous ceramics. *Current Opinion in Solid State & Materials Science,* **7**, 301-307.

Jones, J. R. & Hench, L. L. (2004) Factors affecting the structure and properties of bioactive foam scaffolds for tissue engineering. *Journal of Biomedical Materials Research Part B-Applied Biomaterials,* **68B**, 36-44.

Jones, J. R., Lee, P. D. & Hench, L. L. (2006) Hierarchical porous materials for tissue engineering. *Philosophical Transactions of the Royal Society A-Mathematical Physical and Engineering Sciences,* **364**, 263-281.

Jun, I. K., Koh, Y. H., Song, J. H. & Kim, H. E. (2006) Fabrication and characterization of dual-channeled zirconia ceramic scaffold. *Journal of the American Ceramic Society,* **89**, 2021-2026.

Kalita, S. J., Bhardwaj, A. & Bhatt, H. A. (2007) Nanocrystalline calcium phosphate ceramics in biomedical engineering. *Materials Science & Engineering C-Biomimetic and Supramolecular Systems,* **27**, 441-449.

Karageorgiou, V. & Kaplan, D. (2005) Porosity of 3D biomaterial scaffolds and osteogenesis. *Biomaterials,* **26**, 5474-5491.

Khan, Y. M., Katti, D. S. & Laurencin, C. T. (2004) Novel polymer-synthesized ceramic composite-based system for bone repair: An in vitro evaluation. *Journal of Biomedical Materials Research Part A,* **69A**, 728-737.

Kim, H.-W., Noh, Y.-J., Koh, Y.-H., Kim, H.-E. & Kim, H.-M. (2002) Effect of CaF_2 on densification and properties of hydroxyapatite-zirconia composites for biomedical applications. *Biomaterials,* **23**, 4113-4121.

Kim, H. W., Kim, H. E. & Knowles, J. C. (2004a) Hard-tissue-engineered zirconia porous scaffolds with hydroxyapatite sol-gel and slurry coatings. *Journal of Biomedical Materials Research Part B-Applied Biomaterials,* **70B**, 270-277.

Kim, H. W., Kim, H. E., Salih, V. & Knowles, J. C. (2004b) Dissolution control and cellular responses of calcium phosphate coatings on zirconia porous scaffold. *Journal of Biomedical Materials Research Part A,* **68A**, 522-530.

Kim, H. W., Knowles, J. C. & Kim, H. E. (2004c) Development of hydroxyapatite bone scaffold for controlled drug release via poly(epsilon-caprolactone) and hydroxyapatite hybrid coatings. *Journal of Biomedical Materials Research Part B-Applied Biomaterials,* **70B**, 240-249.

Kim, H. W., Knowles, J. C. & Kim, H. E. (2005a) Hydroxyapatite and gelatin composite foams processed via novel freeze-drying and crosslinking for use as temporary hard tissue scaffolds. *Journal of Biomedical Materials Research Part A,* **72A**, 136-145.

Kim, H. W., Knowles, J. C. & Kim, H. E. (2005b) Hydroxyapatite porous scaffold engineered with biological polymer hybrid coating for antibiotic Vancomycin release. *Journal of Materials Science-Materials in Medicine,* **16**, 189-195.

Kim, H. W., Lee, S. Y., Bae, C. J., Noh, Y. J., Kim, H. E., Kim, H. M. & Ko, J. S. (2003) Porous ZrO_2 bone scaffold coated with hydroxyapatite with fluorapatite intermediate layer. *Biomaterials,* **24**, 3277-3284.

Kim, J. Y., Lee, J. W., Lee, S. J., Park, E. K., Kim, S. Y. & Cho, D. W. (2007a) Development of a bone scaffold using HA nanopowder and micro-stereolithography technology. *Microelectronic Engineering,* **84**, 1762-1765.

Kim, S. S., Ahn, K. M., Park, M. S., Lee, J. H., Choi, C. Y. & Kim, B. S. (2007b) A poly(lactide-co-glycolide)/hydroxyapatite composite scaffold with enhanced osteoconductivity. *Journal of Biomedical Materials Research Part A,* **80A**, 206-215.

Kim, S. S., Park, M. S., Jeon, O., Choi, C. Y. & Kim, B. S. (2006) Poly(lactide-co-glycolide)/hydroxyapatite composite scaffolds for bone tissue engineering. *Biomaterials,* **27**, 1399-1409.

Kim, Y. U., Kim, M. C., Kim, K. N., Kim, K. M., Choi, S. H., Kim, C. K., Legeros, R. Z. & Lee, Y. K. (2005c) Effect of calcium phosphate glass on compressive strength of macroporous hydroxyapatite scaffold. *Key Engineering Materials,* **284-286**, 313-316.

Klawitter, J. J. & Hulbert, S. F. (1971) Application of porous ceramics for the attachment of load bearing internal orthopedic applications. *Journal of Biomedical Materials Research Symposium,* **2**, 161-229.

Kokubo, T. & Takadama, H. (2006) How useful is SBF in predicting in vivo bone bioactivity? *Biomaterials,* **27**, 2907-2915.

Kong, L., Gao, Y., Lu, G., Gong, Y., Zhao, N. & Zhang, X. (2006) A study on the bioactivity of chitosan/nano-hydroxyapatite composite scaffolds for bone tissue engineering. *European Polymer Journal,* **42**, 3171-3179.

Korematsu, A., Takemoto, Y., Nakaya, T. & Inoue, H. (2002) Synthesis, characterization and platelet adhesion of segmented polyurethanes grafted phospholipid analogous vinyl monomer on surface. *Biomaterials,* **23**, 263-271.

Lakes, R. (1993) Materials with Structural Hierarchy. *Nature,* **361**, 511-515.

Langer, R. & Vacanti, J. P. (1993) Tissue Engineering. *Science,* **260**, 920-926.

Lee, K.-Y., Park, M., Kim, H.-M., Lim, Y.-J., Chun, H.-J., Kim, H. & Moon, S.-H. (2006) Ceramic bioactivity:progresses, challenges and perspectives. *Biomedical Materials,* **1**, R31-R37.

Lee, Y. M., Park, Y. J., Lee, S. J., Ku, Y., Han, S. B., Choi, S. M., Klokkevold, P. R. & Chung, C. P. (2000) Tissue engineered bone formation using chitosan/tricalcium phosphate sponges. *Journal of Periodontology,* **71**, 410-417.

Legeros, R. Z. (2002) Properties of osteoconductive biomaterials: Calcium phosphates. *Clinical Orthopaedics and Related Research*, 81-98.

Leukers, B., Gulkan, H., Irsen, S. H., Milz, S., Tille, C., Schieker, M. & Seitz, H. (2005) Hydroxyapatite scaffolds for bone tissue engineering made by 3D printing. *Journal of Materials Science-Materials in Medicine,* **16**, 1121-1124.

Li, S. H., De Wijn, J. R., Layrolle, P. & De Groot, K. (2002) Synthesis of macroporous hydroxyapatite scaffolds for bone tissue engineering. *Journal of Biomedical Materials Research,* **61**, 109-120.

Lin, C. Y., Kikuchi, N. & Hollister, S. J. (2004) A novel method for biomaterial scaffold internal architecture design to match bone elastic properties with desired porosity. *Journal of Biomechanics,* **37**, 623-636.

Liu, D. M. (1997a) Fabrication of hydroxyapatite ceramic with controlled porosity. *Journal of Materials Science-Materials in Medicine,* **8**, 227-232.

Liu, D. M. (1997b) Influence of porosity and pore size on the compressive strength of porous hydroxyapatite ceramic. *Ceramics International,* **23**, 135-139.

Lu, H. H., El-Amin, S. F., Scott, K. D. & Laurencin, C. T. (2003a) Three-dimensional, bioactive, biodegradable, polymer-bioactive glass composite scaffolds with improved mechanical properties support collagen synthesis and mineralization of human osteoblast-like cells in vitro. *Journal of Biomedical Materials Research Part A,* **64A**, 465-474.

Lu, W. W., Zhao, F., Luk, K. D. K., Yin, Y. J., Cheung, K. M. C., Cheng, G. X., Yao, K. D. & Leong, J. C. Y. (2003b) Controllable porosity hydroxyapatite ceramics as spine cage: fabrication and properties evaluation. *Journal of Materials Science-Materials in Medicine,* **14**, 1039-1046.

Luyten, J., Thijs, I., Vandermeulen, W., Mullens, S., Wallaeys, B. & Mortelmans, R. (2005) Strong ceramic foams from polyurethane templates. *Advances in Applied Ceramics,* **104**, 4-8.

Malmstrom, J., Adolfsson, E., Emanuelsson, L. & Thomsen, P. (2008) Bone ingrowth in zirconia and hydroxyapatite scaffolds with identical macroporosity. *Journal of Materials Science-Materials in Medicine,* **19**, 2983-2992.

Mastrogiacomo, M., Scaglione, S., Martinetti, R., Dolcini, L., Beltrame, F., Cancedda, R. & Quarto, R. (2006) Role of scaffold internal structure on in vivo bone formation in macroporous calcium phosphate bioceramics. *Biomaterials,* **27**, 3230-3237.

Meesters, G. M. H., Vercoulen, P. H. W., Marijnissen, J. C. M. & Scarlett, B. (1992) Generation of Micron-Sized Droplets from the Taylor Cone. *Journal of Aerosol Science,* **23**, 37-49.

Miao, X., Hu, Y., Liu, J., Tio, B., Cheang, P. & Khor, K. A. (2003) Highly interconnected and functionally graded porous bioceramics. *Bioceramics 15.* p. 595-598.

Miao, X., Hu, Y., Liu, J. & Wong, A. P. (2004) Porous calcium phosphate ceramics prepared by coating polyurethane foams with calcium phosphate cements. *Materials Letters,* **58**, 397-402.

Michelson, D. (1990) Electrostatic Atomization. *Bristol and New York; Adam Hilger Press*.

Michna, S., Wu, W. & Lewis, J. A. (2005) Concentrated hydroxyapatite inks for direct-write assembly of 3-D periodic scaffolds. *Biomaterials,* **26**, 5632-5639.

Mikos, A. G., Lyman, M. D., Freed, L. E. & Langer, R. (1994) Wetting of Poly(L-Lactic Acid) and Poly(Dl-Lactic-Co-Glycolic Acid) Foams for Tissue-Culture. *Biomaterials,* **15**, 55-58.

Min, S. H., Jin, H. H., Park, H. Y., Park, I. M., Park, H. C. & Yoon, S. Y. (2006) Preparation of porous hydroxyapatite scaffolds for bone tissue engineering. *Eco-Materials Processing & Design Vii.* p. 754-757.

Muller, L., Muller, F. A., Zeschky, J., Fey, T. & Greil, P. (2005) Fabrication of hydroxyapatite ceramics with interconnected macro porosity. *Key Engineering Materials,* **284-286**, 277-280.

Munch, E., Franco, J., Deville, S., Hunger, P., Saiz, E. & Tomsia, A. P. (2008) Porous ceramic scaffolds with complex architectures. *JOM: Journal of Minerals, Metals and Materials Society,* **60**, 54-58.

Murugan, R. & Ramakrishna, S. (2005) Development of nanocomposites for bone grafting. *Composites Science and Technology,* **65**, 2385-2406.

Nagornyi, V. S. & Bezrukov, V. I. (1980) Droplet emission in an electrostatic field. *Magnetohydrodynamics,* **16**, 315-319.

Neo, M., Nakamura, T., Ohtsuki, C., Kokubo, T. & Yamamuro, T. (1993) Apatite Formation on 3 Kinds of Bioactive Material at an Early-Stage in-Vivo - a Comparative-Study by Transmission Electron-Microscopy. *Journal of Biomedical Materials Research,* **27**, 999-1006.

Netz, D. J. A., Sepulveda, P., Pandolfelli, V. C., Spadaro, A. C. C., Alencastre, J. B., Bentley, M. V. L. B. & Marchetti, J. M. (2001) Potential use of gelcasting hydroxyapatite porous ceramic as an implantable drug delivery system. *International Journal of Pharmaceutics,* **213**, 117-125.

Ohtsuki, C., Kushitani, H., Kokubo, T., Kotani, S. & Yamamuro, T. (1991) Apatite Formation on the Surface of Ceravital-Type Glass-Ceramic in the Body. *Journal of Biomedical Materials Research,* **25**, 1363-1370.

Okii, N., Nishimura, S., Kurisu, K., Takeshima, Y. & Uozumi, T. (2001) In vivo histological changes occurring in hydroxyapatite cranial reconstruction - Case report. *Neurologia Medico-Chirurgica,* **41**, 100-104.

Ota, Y., Kasuga, T. & Abe, Y. (1997) Preparation and compressive strength behavior of porous ceramics with β-$Ca(PO_3)_2$ fiber skeletons. *Journal of the American Ceramic Society,* **80**, 225-231.

Patka, P., Otto, T. E., Van Der Elst, M., Haarmann, H. J. T. M. & Bakker, F. C. (1998) Bioresorbable Polymers as Materials in Osteosynthesis. IN WALENKAMP, G. H. I. M. (Ed.) *Biomaterials in Surgery.* Germany, Georg Thieme Verlag, p. 102-105.

Peltier, L. F., Bickel, E. Y., Lillo, R. & Thein, M. S. (1957) The use of Plaster of Paris to fill defects in Bone. *Annals of Surgery,* **146**, 61-69.

Pereira, M. M., Jones, J. R. & Hench, L. L. (2005) Bioactive glass and hybrid scaffolds prepared by sol-gel method for bone tissue engineering. *Advances in Applied Ceramics,* **104**, 35-42.

Peters, M. C. & Mooney, D. J. (1997) Synthetic Extracellular Matrices for Cell Transplantation. IN LIU, D. M. & DIXIT, V. (Eds.) *Porous Materials for Tissue Engineering, Materials Science Forum Vol 250.* Trans tech publications, Switzerland, p. 43-52.

Piconi, C. & Maccauro, G. (1999) Zirconia as a ceramic biomaterial. *Biomaterials,* **20**, 1-25.

Pompe, W., Worch, H., Epple, M., Friess, W., Gelinsky, M., Greil, P., Hempel, U., Scharnweber, D. & Schulte, K. (2003) Functionally graded materials for biomedical applications. *Materials Science and Engineering: A,* **362**, 40-60.

Quan, R. F., Yang, D. S., Wu, X. C., Wang, H. B., Miao, X. D. & Li, W. (2008) In vitro and in vivo biocompatibility of graded hydroxyapatite-zirconia composite bioceramic. *Journal of Materials Science-Materials in Medicine,* **19**, 183-187.

Ramay, H. R. & Zhang, M. Q. (2003) Preparation of porous hydroxyapatite scaffolds by combination of the gel-casting and polymer sponge methods. *Biomaterials,* **24**, 3293-3302.

Ray, R., Degge, J., Gloyd, P. & Mooney, G. (1952) Bone regneration:An experimental study of bone-grafting materials. *Journal of Bone and Joint Surgery,* **34**, 638-647.

Rayleigh, Lord (1878) On the instability of jets. *The Proceedings of the London Mathematical Society,* **10**, 4-13.

Rayleigh, Lord (1879) On the capillary phenomena in jets. *The Proceedings of the Royal Society,* **29**, 71-97.

Rayleigh, Lord (1882) On the equilibrium of liquid conducting masses charged with electricity. *Philosophical Magazine,* **14**, 184.

Rezwan, K., Chen, Q. Z., Blaker, J. J. & Boccaccini, A. R. (2006) Biodegradable and bioactive porous polymer/inorganic composite scaffolds for bone tissue engineering. *Biomaterials,* **27**, 3413-3431.

Rho, J. Y., Kuhn-Spearing, L. & Zioupos, P. (1998) Mechanical properties and the hierarchical structure of bone. *Medical Engineering & Physics,* **20**, 92-102.

Robinson, J. H., Best, S. M., Ahmad, Z. & Edirisinghe, M. J. (2008) The effect of reaction conditions on hydroxyapatite particle morphology and applications to the reticulated foam method of scaffold production. *Key Engineering Materials,* **361-363**, 3-6.

Roether, J. A., Boccaccini, A. R., Hench, L. L., Maquet, V., Gautier, S. & Jerome, R. (2002) Development and in vitro characterisation of novel bioresorbable and bioactive composite materials based on polylactide foams and Bioglass® for tissue engineering applications. *Biomaterials,* **23**, 3871-3878.

Roy, D. M. & Linnehan, S. K. (1974) Hydroxyapatite Formed from Coral Skeletal Carbonate by Hydrothermal Exchange. *Nature,* **247**, 220-222.

Rulison, A. J. & Flagan, R. C. (1994) Synthesis of Yttria Powders by Electrospray Pyrolysis. *Journal of the American Ceramic Society,* **77**, 3244-3250.

Ruys, A. J., Zeigler, K. A., Standard, O. C., Brandwood, A., Milthorpe, B. K. & Sorrell, C. C. (1992) Hydroxyapatite sintering phenomena: densification and dehydration behaviour. IN BANNISTER, M. J. (Ed.) *Ceramics: Adding the Value, Volume 2. Proceedings of the International Ceramic Conference, Austerceram92.* Melbourne, CSIRO, p. 605-610.

Sachlos, E., Reis, N., Ainsley, C., Derby, B. & Czernuszka, J. T. (2003) Novel collagen scaffolds with predefined internal morphology made by solid freeform fabrication. *Biomaterials,* **24**, 1487-1497.

Saiz, E., Gremillard, L., Menendez, G., Miranda, P., Gryn, K. & Tomsia, A. P. (2007) Preparation of porous hydroxyapatite scaffolds. *Materials Science & Engineering C-Biomimetic and Supramolecular Systems,* **27**, 546-550.

Schwartzwalder, K., Somers, H. & Somers, A. V. (1963) Method of making porous ceramic articles. US Patent No. 3090094.

Seal, B. L., Otero, T. C. & Panitch, A. (2001) Polymeric biomaterials for tissue and organ regeneration. *Materials Science & Engineering R-Reports,* **34**, 147-230.

Seitz, H., Rieder, W., Irsen, S., Leukers, B. & Tille, C. (2005) Three-dimensional printing of porous ceramic scaffolds for bone tissue engineering. *Journal of Biomedical Materials Research Part B-Applied Biomaterials,* **74B**, 782-788.

Sepulveda, P. (1997) Gelcasting foams for porous ceramics. *American Ceramic Society Bulletin,* **76**, 61-65.

Sepulveda, P., Binner, J. G. P., Rogero, S. O., Higa, O. Z. & Bressiani, J. C. (2000a) Production of porous hydroxyapatite by the gel-casting of foams and cytotoxic evaluation. *Journal of Biomedical Materials Research,* **50**, 27-34.

Sepulveda, P., Ortega, F. S., Innocentini, M. D. M. & Pandolfelli, V. C. (2000b) Properties of highly porous hydroxyapatite obtained by the gelcasting of foams. *Journal of the American Ceramic Society,* **83**, 3021-3024.

Shea, J. E. & Miller, S. C. (2005) Skeletal function and structure: Implications for tissue-targeted therapeutics. *Advanced Drug Delivery Reviews,* **57**, 945-957.

Shin, H. I., Kim, K. H., Kang, I. K. & Oh, K. S. (2005) Successful osteoinduction by cell-macroporous biphasic HA-TCP ceramic matrix. *Key Engineering Materials,* **288-289**, 245-248.

Shiryaeva, S. O. & Grigorev, A. I. (1995) The Semiphenomenological Classification of the Modes of Electrostatic Dispersion of Liquids. *Journal of Electrostatics,* **34**, 51-59.

Simon, J. L., Michna, S., Lewis, J. A., Rekow, E. D., Thompson, V. P., Smay, J. E., Yampolsky, A., Parsons, J. R. & Ricci, J. L. (2007) In vivo bone response to 3D periodic hydroxyapatite scaffolds assembled by direct ink writing. *Journal of Biomedical Materials Research Part A,* **83A**, 747-758.

Simske, S. J., Ayers, R. A. & Bateman, T. A. (1997) Porous Materials for Bone Engineering. IN LIU, D.-M. & DIXIT, V. (Eds.) *Porous Materials for Tissue Engineering, Materials Science Forum.* Switzerland, Trans tech publications, p. 151-182.

Sittinger, M. (2003) Engineering Cartilage Structures. IN HENDRICH, C., NÖTH, U. & EULERT, J. (Eds.) *Cartilage Surgery and Future Perspectives.* NY, Springer, p. 67-73.

Smith, D. P. H. (1986) The Electrohydrodynamic Atomization of Liquids. *IEEE Transactions on Industry Applications,* **22**, 527-535.

Steffens, H.-D., Babiaka, Z. & Gramlicha, M. (1999) Some aspects of thick thermal barrier coating lifetime prolongation. *Journal of Thermal Spray Technology,* **8**, 517-522.

Studart, A. R., Gonzenbach, U. T., Tervoort, E. & Gauckler, L. J. (2006) Processing routes to macroporous ceramics: A review. *Journal of the American Ceramic Society,* **89**, 1771-1789.

Taboas, J. M., Maddox, R. D., Krebsbach, P. H. & Hollister, S. J. (2003) Indirect solid free form fabrication of local and global porous, biomimetic and composite 3D polymer-ceramic scaffolds. *Biomaterials,* **24**, 181-194.

Tampieri, A., Celotti, G., Sprio, S., Delcogliano, A. & Franzese, S. (2001) Porosity-graded hydroxyapatite ceramics to replace natural bone. *Biomaterials,* **22**, 1365-1370.

Tanahashi, M., Yao, T., Kokubo, T., Minoda, M., Miyamoto, T., Nakamura, T. & Yamamuro, T. (1994) Apatite Coating on Organic Polymers by a Biomimetic Process. *Journal of the American Ceramic Society,* **77**, 2805-2808.

Tang, K. Q. & Gomez, A. (1996) Monodisperse electrosprays of low electric conductivity liquids in the cone-jet mode. *Journal of Colloid and Interface Science,* **184**, 500-511.

Taylor, G. (1969) Electrically Driven Jets. *Proceedings of the Royal Society of London Series A-Mathematical and Physical Sciences,* **313**, 453-475.

Taylor, G. I. (1964) Disintegration of water drops in an electrical field. *The Proceedings of the Royal Society,* **280A**, 383-397.

Thian, E. S., Ahmad, Z., Huang, J., Edirisinghe, M. J., Jayasinghe, S. N., Ireland, D. C., Brooks, R. A., Rushton, N., Bonfield, W. & Best, S. M. (2008a) Electrosprayed nanoapatite: A new generation of bioactive material. *Key Engineering Materials,* **361-363**, 597-600.

Thian, E. S., Ahmad, Z., Huang, J., Edirisinghe, M. J., Jayasinghe, S. N., Ireland, D. C., Brooks, R. A., Rushton, N., Bonfield, W. & Best, S. M. (2008b) The role of electrosprayed apatite nanocrystals in guiding osteoblast behaviour. *Biomaterials,* **29**, 1833-1843.

Thomas, V., Dean, D. R. & Vohra, Y. K. (2006) Nanostructured Biomaterials for regenerative medicine. *Current Nanoscience,* **2**, 155-177.

Thomson, R. C., Shung, A. K., Yaszemski, M. J. & Mikos, A. G. (2000) Polymer Scaffold Processing. IN LANZA, R., LANGER, R. & VACANTI, J. (Eds.) *Principles of Tissue Engineering*. NY, Academic Press, p. 251-262.

Thomson, R. C., Yaszemski, M. J., Powers, J. M. & Mikos, A. G. (1998) Hydroxyapatite fiber reinforced poly(alpha-hydroxy ester) foams for bone regeneration. *Biomaterials,* **19**, 1935-1943.

Tian, J. M., Wang, X. Y., Dong, L. M., Wang, C. & Xu, W. (2005) Preparation of porous hydroxyapatite scaffolds. *Key Engineering Materials,* **280-283**, 1541-1544.

Tian, J. T. & Tian, J. M. (2001) Preparation of porous hydroxyapatite. *Journal of Materials Science,* **36**, 3061-3066.

Tsuruga, E., Takita, H., Itoh, H., Wakisaka, Y. & Kuboki, Y. (1997) Pore size of porous hydroxyapatite as the cell-substratum controls BMP-induced osteogenesis. *Journal of Biochemistry,* **121**, 317-324.

Tulliani, J. M., Montanaro, L., Bell, T. J. & Swain, M. V. (1999) Semiclosed-cell mullite foams: Preparation and macro- and micromechanical characterization. *Journal of the American Ceramic Society,* **82**, 961-968.

Van Der Elst, M., Dijkema, A. R. A., Klein, C., Patka, P. & Haarman, H. (1995) Tissue Reaction on PLLA Versus Stainless-Steel Interlocking Nails for Fracture Fixation - an Animal Study. *Biomaterials,* **16**, 103-106.

Vats, A., Tolley, N. S., Polak, J. M. & Gough, J. E. (2003) Scaffolds and biomaterials for tissue engineering: a review of clinical applications. *Clinical Otolaryngology,* **28**, 165-172.

Vaz, L., Lopes, A. B. & Almeida, M. (1999) Porosity control of hydroxyapatite implants. *Journal of Materials Science-Materials in Medicine,* **10**, 239-242.

Vedula, V. R., Green, D. J. & Hellman, J. R. (1999) Thermal shock resistance of ceramic foams. *Journal of the American Ceramic Society,* **82**, 649-656.

Vonnegut, B. & Neubauer, R. L. (1952) Production of monodisperse liquid particles by electrical atomization. *Journal of Colloidal Science,* **7**, 616-620.

Wahl, D. A. & Czernuszka, J. T. (2006) Collagen-hydroxyapatite composites for hard tissue repair. *European Cells & Materials,* **11**, 43-56.

Webster, T. J., Ergun, C., Doremus, R. H., Siegel, R. W. & Bizios, R. (2000) Enhanced functions of osteoblasts on nanophase ceramics. *Biomaterials,* **21**, 1803-1810.

Webster, T. J., Ergun, C., Doremus, R. H., Siegel, R. W. & Bizios, R. (2001) Enhanced osteoclast-like cell functions on nanophase ceramics. *Biomaterials,* **22**, 1327-1333.

Wei, G. B. & Ma, P. X. (2004) Structure and properties of nano-hydroxyapatite/polymer composite scaffolds for bone tissue engineering. *Biomaterials,* **25**, 4749-4757.

Werner, J., Linner-Krcmar, B., Friess, W. & Greil, P. (2002) Mechanical properties and in vitro cell compatibility of hydroxyapatite ceramics with graded pore structure. *Biomaterials,* **23**, 4285-4294.

Xu, J. L., Khor, K. A., Dong, Z. L., Gu, Y. W., Kumar, R. & Cheang, P. (2004) Preparation and characterization of nano-sized hydroxyapatite powders produced in a radio frequency (rf) thermal plasma. *Materials Science and Engineering A-Structural Materials Properties Microstructure and Processing,* **374**, 101-108.

Yoon, J. J. & Park, T. G. (2001) Degradation behaviors of biodegradable macroporous scaffolds prepared by gas foaming of effervescent salts. *Journal of Biomedical Materials Research,* **55**, 401-408.

Yoshida, K., Hashimoto, K., Toda, Y., Udagawa, S. & Kanazawa, T. (2006) Fabrication of structure-controlled hydroxyapatite/zirconia composite. *Journal of the European Ceramic Society,* **26**, 515-518.

Yoshimoto, H., Shin, Y. M., Terai, H. & Vacanti, J. P. (2003) A biodegradable nanofiber scaffold by electrospinning and its potential for bone tissue engineering. *Biomaterials,* **24**, 2077-2082.

Younger, E. M. & Chapman, M. W. (1989) Morbidity at bone graft donor site. *Journal of Orthopaedic Trauma,* **3**, 192-195.

Yuan, H., Kurashina, K., De Bruijn, J. D., Li, Y., De Groot, K. & Zhang, X. (1999) A preliminary study on osteoinduction of two kinds of calcium phosphate ceramics. *Biomaterials,* **20**, 1799-1806.

Yuan, H. P., De Bruijn, J. D., Zhang, X. D., Van Blitterswijk, C. A. & De Groot, K. (2001) Bone induction by porous glass ceramic made from Bioglass® (45S5). *Journal of Biomedical Materials Research,* **58**, 270-276.

Zeleny, J. (1914) The electrical discharge from liquid points and a hydrostatic method of measuring the electric intensity at their surfaces. *The Physical Review,* **3**, 69-91.

Zeleny, J. (1915) On the conditions of instability of electrified drops with applications to the electrical discharge from liquid points. *The Proceedings of the Cambridge Philosophy Society,* **18**, 71-83.

Zeleny, J. (1917) Instability of electrified liquid surfaces. *The Physical Review,* **10**, 1-6.

Zeschky, J., Hofner, T., Arnold, C., Weissmann, R., Bahloul-Hourlier, D., Scheffler, M. & Greil, P. (2005) Polysilsesquioxane derived ceramic foams with gradient porosity. *Acta Materialia,* **53**, 927-937.

Zhang, J. X., Tanaka, H., Ye, F., Jiang, D. L. & Iwasa, M. (2007) Colloidal processing and sintering of hydroxyapatite. *Materials Chemistry and Physics,* **101**, 69-76.

Zhang, R. Y. & Ma, P. X. (1999) Poly(alpha-hydroxyl acids) hydroxyapatite porous composites for bone-tissue engineering. I. Preparation and morphology. *Journal of Biomedical Materials Research,* **44**, 446-455.

Zhao, J., Guo, L. Y., Yang, X. B. & Weng, J. (2008) Preparation of bioactive porous HA/PCL composite scaffolds. *Applied Surface Science,* **255**, 2942-2946.

Zhou, J. M., Zhang, X. D., Chen, J. Y., Zeng, S. X. & Degroot, K. (1993) High-Temperature Characteristics of Synthetic Hydroxyapatite. *Journal of Materials Science-Materials in Medicine,* **4**, 83-85.